INSTITUTO DE TECNOLOGÍA QUÍMICA

EXCELENCIA SEVERO OCHOA

CSIC
CONSEJO SUPERIOR DE INVESTIGACIONES CIENTÍFICAS

UNIVERSITAT POLITÈCNICA DE VALÈNCIA

Catalytic valorization of natural gas and biomass-derived feedstocks by metal oxides

PhD Thesis

Presented by:

Daniel Delgado Muñoz

Supervisor:

Prof. José Manuel López Nieto

Valencia, May 2019

Agradecimientos

Quiero expresar mi más sincero agradecimiento a todas las personas que, en mayor o menor medida, me han acompañado durante estos años en Valencia, y que han hecho posible este trabajo.

En primer lugar, quiero dar las gracias a mi director de tesis, el Prof. José Manuel López Nieto, por ofrecerme la oportunidad de realizar el presente trabajo en su grupo de investigación; por sus enseñanzas, dedicación, consejos y, sobre todo, por su confianza, capacidad de trabajo, apoyo y motivación. Ha sido un placer (y en gran medida una suerte) poder compartir estos primeros años en el mundo de la investigación contigo. Quiero extender este agradecimiento al Prof. Benjamín Solsona de la Universidad de Valencia, por su ayuda y compromiso con este trabajo. También me gustaría agradecerle al Prof. Avelino Corma, investigador principal del proyecto SEV-2012-0267, a través del cual he podido realizar mi tesis doctoral en el Instituto de Tecnología Química (SVP-2014-068669).

Quisiera darles particularmente las gracias a todos los compañeros de grupo que me han acompañado y ayudado durante estos años en el ITQ: Dolo, Alessandro, Amada, Lidia, Cristina, Segundo, Nathalia, Maria José, Mario, Andrea, Borja, Lamia, Yousra, Jose y Agustín. También agradecer a Alberto y al Dr. Marcelo Domine del ITQ, cuyo trabajo, esfuerzo y constancia también están plasmados en esta tesis, así como a todo el personal de administración, caracterización y taller; y a todos mis compañeros de laboratorio en el Instituto. También al Prof. Agustín Martínez, posiblemente uno de los mejores profesores de química que he tenido el gusto de conocer.

A su vez, quiero agradecer a la Dra. Annette Trunschke y a todo su grupo de investigación del Departamento de Química Inorgánica en el Instituto Fritz Haber de la Sociedad Max Planck en Berlín, por su acogida y hospitalidad durante la realización de mi estancia. También a todos mis amigos en Berlín, Nacho, Penélope y Belén; también a Javi, Kike y Dani, que me hicieron sentir como en casa durante los tres meses que pasé en Alemania. Vuestra valentía nos inspira a los que en su día decidimos aguantar.

Agradecer también al Prof. Alfonso Caballero, por acogerme en su grupo del Instituto de Ciencia de Materiales de Sevilla e introducirme al mundo de la Espectroscopía de Absorción de Rayos X; así como al Prof. Enrique Rodríguez Castellón, por su compañía durante las semanas en el sincrotrón y sus consejos

sobre XPS. También a la Prof. Ester García González de la Universidad Complutense, por ayudarnos a entender nuestros materiales.

Quisiera hacer una mención especial al Prof. Miguel Ángel Alario y Franco, quien supo transmitirme su pasión por la ciencia y la investigación durante mi último año de estudios en la Universidad Complutense. También a Mariche, Florent y Milo, por acogerme las primeras semanas que pasé en Valencia, y por todas esas noches de música y tertulias; y a Sento, por su poesía.

Cuatro años de estudio y trabajo me han traído grandes amigos que echaré mucho en falta, pero que quedarán para siempre. Luismi, Jaime, Pascual, Yannick, Ferran, Zaher, Silvia, Marvin, Jorge, Marta, Sara, Evgeni, Vincent, Julio, Janine, Carmencita, Rocío, Iván, Ruth... Gracias por vuestra compañía y por todos los buenos momentos que hemos pasado. Por todo ello también formáis parte de esta tesis. También a todos mis amigos madrileños (y gallegos), a los que he echado de menos. Gracias por seguir recibiéndome como si no me hubiese marchado.

No quiero dejar de expresar mi más profundo agradecimiento a toda mi familia en Madrid, especialmente a mis padres (Antonia y Félix), a Ana (gracias) y a mis abuelos (sobre todo a mi abuela Asun). Gracias por confiar siempre en mí, por cuidarme, y por vuestro amor incondicional, catalizadores de todo este trabajo. Vuestra perseverancia y optimismo me han servido y me servirán siempre de inspiración, especialmente en los momentos en los que un plus de esfuerzo es el factor determinante.

También quiero agradecerles a mis tíos (Alfonso, Espe, Ana, Toño, Fili, Paco, Polo, Nela, Alberta…), a mis primos (Javi, Víctor, Rubén, Cristina, Agustina, Luismi, Alfon, Antonio…) y a toda mi familia en Bilbao (Fredes, Patxi, Asun, Igor y Sandra). Gracias por vuestro cariño y por lo bien que me habéis cuidado siempre.

Finalmente, quiero dedicarle expresamente este trabajo a mi familia en Valencia: Antonio, Rosa, Eva, Jesús, Marc y Leire, por quererme tanto; y especialmente a Lorena, por su apoyo incondicional y por ser la mejor compañera de aventuras. Sois el verdadero regalo que me ha dejado esta tesis doctoral.

Daniel Delgado Muñoz

“La realidad, pues, se ofrece en perspectivas individuales. *Lo que para uno está en último plano, se halla para otro en primer término.”*

Verdad y perspectiva, José Ortega y Gasset, 1916.

Summary

The present doctoral thesis is set within the scope of the current energy transition, which considers the progressive substitution of non-renewable fossil sources by renewable feedstocks for the production of chemicals and fuels. In this context of gradual transition, and according to recent energy outlooks, fossil sources (especially natural gas) and biomass feedstocks will play a key role during the shift.

A study on the use of metal oxides (based on tungsten bronzes or nickel oxides) as catalysts for different reactions has been conducted. Particularly, they have been studied as catalytic materials for: i) the transformation of biomass-derived feedstocks: glycerol transformation into acrolein/acrylic acid, and the transformation of short-chain oxygenates present in aqueous effluents (derived from extraction processes of pyrolysis bio-oils) into fuels; and ii) the valorization of natural gas components, i.e. the transformation of ethane into ethylene by oxidative dehydrogenation. The work is presented from a materials chemistry perspective, emphasizing the physicochemical characteristics of the different catalytic systems by using conventional and *in situ* characterization techniques and model reactions (gas phase methanol and ethanol transformation); with the aim of understanding the specific catalytic functionalities present in each case.

For both gas phase glycerol transformation and the valorization of short-chain oxygenates aqueous mixtures, catalysts based on tungsten oxide bronzes have been used. The compositional and structural versatility of this structural types (with the subsequent control of their functional properties) will be highlighted.

In this sense, the acid-redox properties of W-V-O catalysts can be modulated by controlling the crystalline phase composition in the materials (i.e. hexagonal and monoclinic polymorphs of tungsten oxide) at a fixed V concentration. This effect has been studied by using the gas-phase aerobic transformation of methanol as a surface test reaction. The concentration of the hexagonal and monoclinic polymorphs in the catalysts

has also an important influence in the gas-phase transformation of glycerol into acrylic acid.

Also, it is possible to control the Brönsted/Lewis acid nature of the surface by the isomorphic substitution of Nb for W in WO_3-Nb_2O_5 system. On the one hand, catalysts showing a higher proportion of Brönsted acid sites are more effective in the glycerol dehydration to acrolein. On the other hand, materials with a higher concentration of Lewis acid sites display high yields to condensation products in the aqueous phase valorization of short chain oxygenates.

Additionally, the differences between W-V-O and W-Nb-O catalysts prepared by both reflux and hydrothermal methods have been studied. Also the effect of adding a mesoporous KIT-6 silica as support on the catalytic performance in the gas-phase transformation of ethanol and glycerol will be underlined.

Considering the transformation of natural gas components, nickel oxide-based materials were chosen (either supported on different oxides and/or promoted with different metals) to perform the oxidative dehydrogenation (ODH) of ethane. In this case the study has been focused on elucidating the effects of both promoters and supports on the nature and physicochemical features of nickel oxide, which lead to a drastic change in the catalytic behavior of these materials. This way, it has been observed that by the modification of the reducibility and the chemical nature of nickel oxide, it is possible to transform an apparently non-selective catalyst in the ODH of ethane (like NiO, showing a selectivity to ethylene of ca. 30 %) into one of the most selective catalysts reported in the literature (presenting a selectivity to ethylene of ca. 90 %).

Resumen

La presente tesis doctoral se sitúa en el marco de la actual transición energética, que plantea la sustitución progresiva de materias primas de origen fósil por fuentes renovables, tanto para la obtención de productos químicos como para la producción de combustibles. En este contexto de transición paulatina a las renovables, y teniendo en cuenta los últimos pronósticos, las fuentes fósiles (fundamentalmente gas natural) y derivados de la biomasa, jugarán un papel fundamental durante el cambio.

Se ha llevado a cabo un estudio sobre el empleo de óxidos metálicos (basados en bronces de wolframio o en óxido de níquel), como catalizadores para: i) la transformación de derivados de biomasa: de glicerol a acroleína/ácido acrílico; y de compuestos oxigenados de cadena corta presentes en efluentes acuosos (procedentes de tratamientos de extracción de bio-aceites de pirolisis) a combustibles; y ii) la transformación de componentes del gas natural, concretamente la obtención de etileno a partir de etano, mediante deshidrogenación oxidativa. El trabajo se presenta desde una perspectiva de la química de materiales, haciendo hincapié en las propiedades fisicoquímicas de los distintos sistemas catalíticos, empleando técnicas de caracterización convencionales e *in situ*, además de reacciones modelo (transformación de metanol y etanol en fase gaseosa), con el objetivo de entender las funciones catalíticas presentes en cada caso.

Tanto para la transformación de glicerol en fase gas, como para la valorización de mezclas acuosas de compuestos oxigenados de cadena corta, se han utilizado catalizadores basados en bronces de wolframio. Se ha tratado de poner de manifiesto la gran versatilidad composicional y estructural (con el consiguiente control de las propiedades funcionales), que presentan este tipo de materiales.

En este sentido, las propiedades ácidas y redox de catalizadores W-V-O pueden ser moduladas, para una misma concentración de vanadio, mediante el control de la relación de fases cristalinas (hexagonal y monoclínica) del óxido de wolframio. Este efecto se ha estudiado empleando la transformación aeróbica de metanol como reacción “test”, y tiene una gran influencia en la deshidratación oxidativa de glicerol a ácido acrílico.

A su vez, mediante la sustitución isomórfica de wolframio por niobio (en el sistema WO_3-Nb_2O_5) es posible controlar la relación de centros ácidos de tipo Brönsted y Lewis en la superficie de los materiales. Por un lado, los catalizadores con una alta relación Brönsted/Lewis se han mostrado más efectivos en la deshidratación de glicerol a acroleína, mientras que los catalizadores con altas concentraciones de centros de tipo Lewis presentan altos rendimientos a productos de condensación de compuestos oxigenados de cadena corta.

Adicionalmente se han estudiado las diferencias entre catalizadores (bien óxidos mixtos W-V-O o W-Nb-O) preparados mediante un método hidrotermal o mediante reflujo, así como el efecto de la utilización de un soporte mesoporoso inerte (KIT-6), sobre sus propiedades catalíticas en la transformación aeróbica en fase gaseosa de etanol y glicerol.

Finalmente, en lo que concierne a la transformación de componentes del gas natural, se han empleado materiales basados en óxido de níquel (soportado sobre distintos óxidos y/o promovido con distintos metales) como catalizadores para la deshidrogenación oxidativa de etano. En este caso el estudio se ha centrado fundamentalmente en dilucidar los efectos de promotores y soportes en la naturaleza y propiedades fisicoquímicas del óxido de níquel, los cuales dan lugar a un cambio drástico en sus propiedades catalíticas. Así, se ha observado que modificando la reducibilidad y las características superficiales del óxido de níquel es posible transformar un catalizador muy poco selectivo en la deshidrogenación oxidativa de etano (como es el NiO, con una selectividad a etileno del 30 %) en uno de los catalizadores más selectivos para llevar a cabo esta reacción (con una selectividad a etileno del 90 %).

Resum

Aquesta tesi doctoral es situa dins del marc de l’actual transició energètica, la qual planteja la substitució progressiva de les primeres matèries d’origen fòssil per fonts renovables, tant per a l’obtenció de productes químics com per a la producció de combustibles. En aquest context de transició gradual a les renovables, i tenint en compte els últims pronòstics, les fonts fòssils (principalment el gas natural) i els derivats de la biomassa, exerciran un paper fonamental durant aquest canvi.

S’ha dut a terme un estudi sobre la utilització d’òxids metàl·lics (basats en bronzes de wolframi o en òxid de níquel), com a catalitzadors per a: i) la transformació de derivats de la biomassa: de glicerol a acroleïna/àcid acrílic; i de compostos oxigenats de cadena curta presents en efluents aquosos (procedents de tractaments d’extracció de bio-olis de la piròlisi) a combustibles; i ii) la transformació de components del gas natural, concretament l’obtenció d’etilè a partir d’età, mitjançant la deshidrogenació oxidativa.

El treball es presenta des del punt de vista de la química de materials, posant l’accent en les propietats fisicoquímiques dels diferents sistemes catalítics, utilitzant tècniques de caracterització convencionals i *in situ*, a més de reaccions model (com per exemple, la transformació de metanol i etanol en fase gasosa), amb l’objectiu d’entendre les funcions catalítiques presents en cadascun dels casos.

Tant per a la transformació del glicerol en fase gasosa com per a la valorització de les mescles aquoses de compostos oxigenats de cadena curta, s’han utilitzat catalitzadors basats en bronze de wolframi. S’ha intentat posar de manifest la gran versatilitat de composicions i estructures (amb el conseqüent control de les propietats funcionals) que presenten aquest tipus de materials.

En aquest sentit, les propietats àcides i redox dels catalitzadors de W – V – O poden ser modulades, per a una mateixa concentració de vanadi, mitjançant el control de la relació de fases cristal·lines (hexagonal i monoclínica) de l’òxid de wolframi. Aquest efecte s’ha estudiat utilitzant la transformació aeròbica de metanol com a reacció “test”, i presenta una gran influència en la deshidratació oxidativa de glicerol a àcid acrílic.

Al mateix temps, mitjançant la substitució isomòrfica de wolframi per niobi (en el sistema WO_3 – Nb_2O_5), és possible controlar la relació de centres àcids de tipus Brönsted i Lewis en la superfície dels materials. Per una part, els catalitzadors que presenten una relació Brönsted / Lewis alta s’han mostrat més efectius en la deshidratació de glicerol a acroleïna, mentre que els catalitzadors amb unes altes concentracions de tipus Lewis presenten alts rendiments a productes de condensació de compostos oxigenats de cadena curta.

Addicionalment, s’han estudiat les diferències entre catalitzadors (ja siguin òxids mixtos W-V-O o W-Nb-O) preparats mitjançant un mètode hidrotermal o mitjançant un mètode de reflux, així com l’efecte que presenta la utilització d’un suport mesoporós inert (KIT-6), sobre les seves propietats catalítiques en la reacció de transformació aeròbica en fase gasosa d’etanol i glicerol.

Finalment, pel que fa referència a la transformació de components del gas natural, s’han utilitzat materials basats en òxid de níquel (suportat sobre diferents òxids i/o promoguts amb diferents metalls) i catalitzadors per a la deshidrogenació oxidativa d’età. En aquest cas, l’estudi s’ha focalitzat principalment en dilucidar els efectes de promotors i suports en la naturalesa i propietats fisicoquímiques de l’òxid de níquel, els quals impliquen un canvi dràstic en les seves propietats catalítiques. Així doncs, s’ha observat que modificant la reductibilitat i les característiques superficials de l’òxid de níquel és possible transformar un catalitzador molt poc selectiu en la deshidrogenació oxidativa de l’età (com és el cas del NiO, amb una selectivitat a l’etilè del 30%) en un dels catalitzadors més selectius per portar a terme aquesta reacció amb una selectivitat a l’etilè del 90%.

Index

Page

Chapter 1. Introduction

1.1. The energy transition to renewables………………................. 3

1.2. Current industrial production of olefins: steam-cracking……………………………………………………… 5

1.3. Oxidative dehydrogenation (ODH) of ethane as an alternative to steam cracking processes for the production of ethylene… 8

1.4. Bio-fuels and chemicals from biomass. The bio-refinery concept…………………………………………………….. 12

  1.4.1. Glycerol as raw material for chemicals………………… 15

  1.4.2. Upgrading aqueous solutions derived from fast pyrolysis of lignocellulosic biomass…………………………… 19

1.5. Heterogeneous catalysis as a tool to meet green chemistry principles……………………………………………………... 20

1.6. Metal oxide bronzes: multifunctional materials………………. 25

1.7. Nickel oxide-based materials for the ODH of ethane…………. 30

1.8. Objectives…………………………………………………….. 33

1.9. References…………………………………………………… 35

Chapter 2. Experimental procedure

2.1. Catalyst synthesis……………………………………………... 57

  2.1.1. Materials…………………………………………………….. 57

2.1.2. Hydrothermal synthesis of W-Nb-O and W-V-O mixed oxides……………………………………………………... 57

2.1.3. Reflux synthesis of W-Nb-O and W-V-O mixed oxides. Preparation of supported catalysts……………………… 60

2.1.4. Synthesis of promoted and supported NiO-based catalysts……………………………………………… 61

2.2. Catalyst characterization…………………………………. 62

2.2.1. Powder X-Ray Diffraction……………………………... 62

2.2.2. Scanning electron microscopy (SEM)…………………. 64

2.2.3. Transmission electron microscopy (TEM)……………... 65

2.2.4. Energy-Dispersive X-ray spectroscopy (XEDS)………. 67

2.2.5. X-ray photoelectron spectroscopy (XPS)………………. 68

2.2.6. X-Ray Absorption Spectroscopy (XAS)……………….. 70

2.2.7. Fourier-transform infrared spectroscopy (FTIR)………. 75

2.2.8. Raman spectroscopy…………………………………… 76

2.2.9. N_2-physisorption……………………………………….. 77

2.2.10. Pulse chemisorption and temperature programmed desorption of ammonia (TPD-NH_3)…………………… 79

2.2.11. Fourier-transform infrared (FTIR) spectroscopy of adsorbed pyridine………………………………………. 80

2.2.12. Fourier-transform infrared (FTIR) spectroscopy of adsorbed CO at low temperature……………………….. 81

2.2.13. Temperature-programmed reduction (TPR)………….. 82

2.2.14. Thermogravimetric analysis (TG-DTA)……………… 83

2.3. Catalytic tests……………………………………………… 83

2.3.1. Gas phase aerobic transformation of glycerol………….. 84

2.3.2. Gas phase aerobic transformation of methanol and ethanol………………………………………………….. 87

2.3.3. Oxidative dehydrogenation of ethane (ODH)………….. 87

2.3.4. Aqueous phase catalytic transformation of biomass-derived short-chain oxygenates………………………… 88

2.4. References……………………………………………….. 90

Chapter 3. W-V-O catalysts: Influence of phase composition on their multifunctional acid-redox properties

3.1. Previous considerations……………………………………… 95

3.2. Physicochemical characterization of W-V-O oxides………… 96

3.3. Catalytic properties in the gas phase aerobic transformation of methanol and glycerol…………………………………… 107

3.3.1. Gas phase aerobic transformation of methanol……….. 107

3.3.2. Gas phase aerobic transformation of glycerol………… 112

3.4. General Remarks…………………………………………….. 115

3.5. References…………………………………………………… 117

Chapter 4. W-Nb-O bronzes as catalysts for the valorization of biomass-derived feedstocks

4.1. Previous considerations……………………………………… 125

4.2. Physicochemical characterization of W-Nb-O oxides……….. 126

4.2.1. Structural features of W-Nb-O materials……………... 127

4.2.2. Textural features of W-Nb-O mixed oxides. N_2-adsorption study………………………………………… 136

4.2.3. Acid properties of W-Nb-O oxides. Temperature-programmed desorption and FTIR spectroscopy studies…………………………………………………… 138

4.3. Catalytic behavior in the transformation of biomass-derived feedstocks…………………………………………………… 149

4.3.1. Gas-phase aerobic transformation of glycerol………… 149

4.3.2. Catalytic properties in the valorization of aqueous effluents via C-C bond formation reactions…………… 153

4.4. General Remarks……………………………………………….. 160

4.5. References…………………………………………………… 162

Chapter 5. Reflux-synthesized bulk and supported W-Nb-O and W-V-O oxide bronzes: Aerobic transformation of alcohols

5.1. Previous considerations……………………………………… 169

5.2. Physicochemical characterization bulk and supported materials……………………………………………………….. 170

5.3. Gas-phase aerobic transformation of ethanol………………... 178

5.4. Gas-phase aerobic transformation of glycerol……………….. 183

5.5. General Remarks……………………………………………….. 187

5.6. References…………………………………………………… 189

Chapter 6. Promoted NiO catalysts: Studies on the redox and catalytic properties in the ODH of ethane

6.1. Previous considerations…………………………………… 195
6.2. Catalytic properties of promoted NiO catalysts in the ODH of ethane……………………………………………………….. 196
6.3. Characterization of promoted NiO catalysts…………………. 201
6.4. General Remarks……………………………………………….. 219
6.5. References……………………………………………………… 221

Chapter 7. Supported NiO catalysts: Study on the effect of the support on NiO active phase

7.1. Previous considerations…………………………………… 227
7.2. Catalytic properties of supported NiO catalysts in the ODH of ethane……………………………………………………….. 228
7.3. Characterization of supported NiO catalysts……………….. 230
7.4. General Remarks……………………………………………….. 244
7.5. References……………………………………………………… 246

Chapter 8. Overall conclusions…………………………… **253**

Appendix I. Index of Figures.. **259**
Appendix II. Index of Tables……………………………… **279**
Appendix III. List of patents……………………………… **285**
Appendix IV. List of publications and selected conferences……………………………….. **289**

Chapter 1

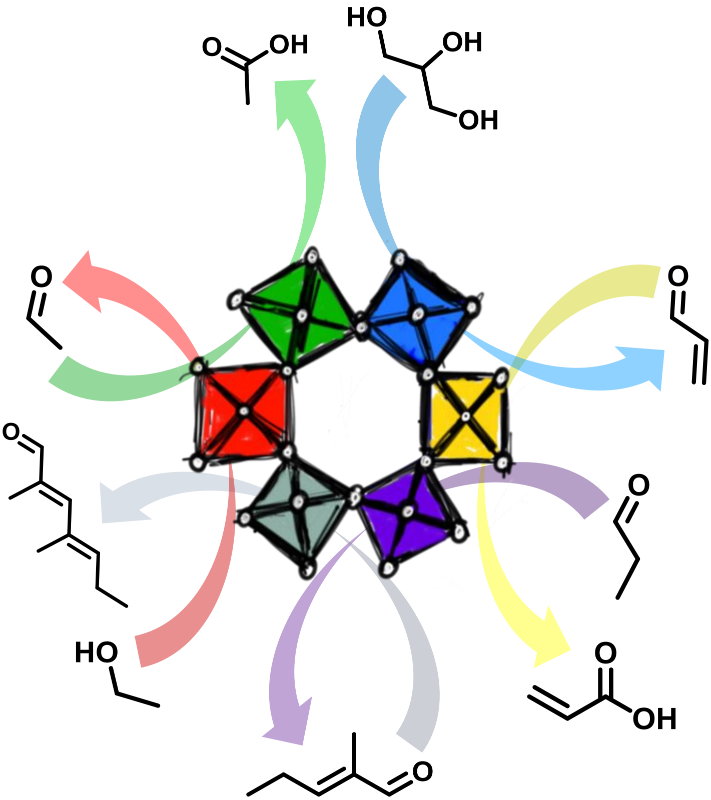

O
OH
HO
OH
OH
O
O
O
O
O
OH
HO
O

Introduction

1.1. The energy transition to renewables

The Nobel laureate in physics Richard P. Feynman pointed out in his public speech “The Value of Science” in 1955: “Our responsibility is to do what we can, learn what we can, improve the solutions, and pass them on. It is our responsibility to leave the people of the future a free hand” [1]. In the near future, one of the central challenges that our species will need to face is the search for more efficient and sustainable energy forms. The responsibility to improve the solutions lies again with scientific community.

The history of human being have gone hand in hand with the continuous discovery and exploitation of new energy sources and raw materials [2-7]. During the last 200 years, two energy transitions took place, which have shaped the whole human society, prompting and leading to technological, economic, social and environmental changes (**Fig. 1.1**) [4].

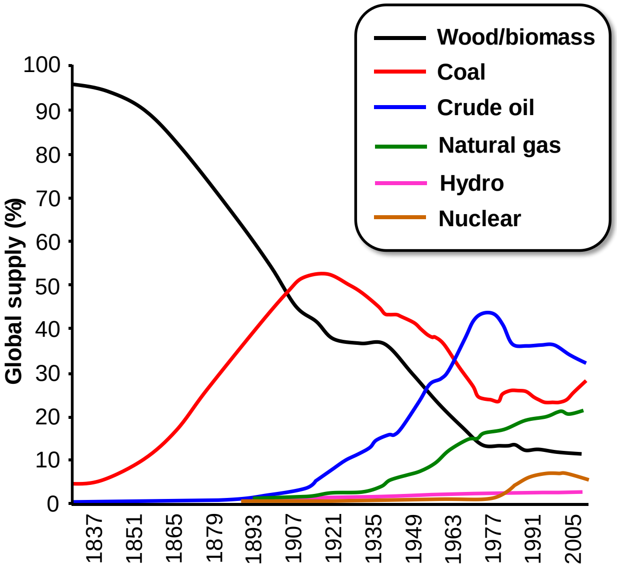

Figure 1.1. Global energy supply in percentages from 1830 to 2007. Source: Reference [4].

The transition from wood to coal drove the emerging industrial revolution in 19th century, meanwhile coal to oil transition paved the way for the development of a vast variety of industries (automobile, polymer, pharmaceutical, etc.). This had a capital importance in the creation of the modern world and welfare state in developed countries. During the 20th century, refining and petrochemical industries have been the main fuels and consumption goods suppliers in our societies. Driven, among others, by the exponential population growth, low price and the expansion of the consumer society, an overexploitation of fossil resources took place in the second half of the last century. For instance, considering all non-renewable energy sources in 1990 (i.e. coal, oil and natural gas), they represented an approximated share of 80 % of the global energy supply (**Fig. 1.1**) [8].

Promoted by environmental issues associated with global gas emissions and climate warming (i.e. the greenhouse effect), the World is now immersed in the next energy transition, which will consist on the way from non-renewable fossil sources to renewables [2-5]. Focusing on energy shifts occurred along the human history, it is obvious that they were not addressed swiftly, being closely linked with social and technological advances and breakthroughs. For example, the shift from wood to coal as the main energy supplier was extended along approximately 100 years, in unison with the development of the steam engine and transportation [2, 5]. This can be extrapolated to coal to oil transition in 20th century, closely associated with the development of gasoline and diesel engines and refining industry, in which catalysis science played a central role [9].

Accordingly, the overcoming energy transition will take place gradually, with fossil feedstocks playing a key role during the transition. In fact, even in fast transition scenarios, recent energy outlooks forecast an increase of production and consumption of both renewables and natural gas by 2040-2050 (**Fig. 1.2**) [7, 8, 10-12]. If these predictions hold true, natural gas will surpass coal in the mid 2020´s and will converge on oil by 2040, arriving to an unseen situation, in which the World will move to a highly diversified energy mix, i.e. coal, oil, natural gas and non-fossil sources will provide ca. a 25 % of global energy needs (**Fig. 1.2**). In addition, biomass, as renewable source of fuels and chemicals, is expected to play and important role during and after the energy transition to non-fossil sources [13, 14]. As in the case of refining industry in the past century, catalytic science is forecasted to be essential to drive the transition [9].

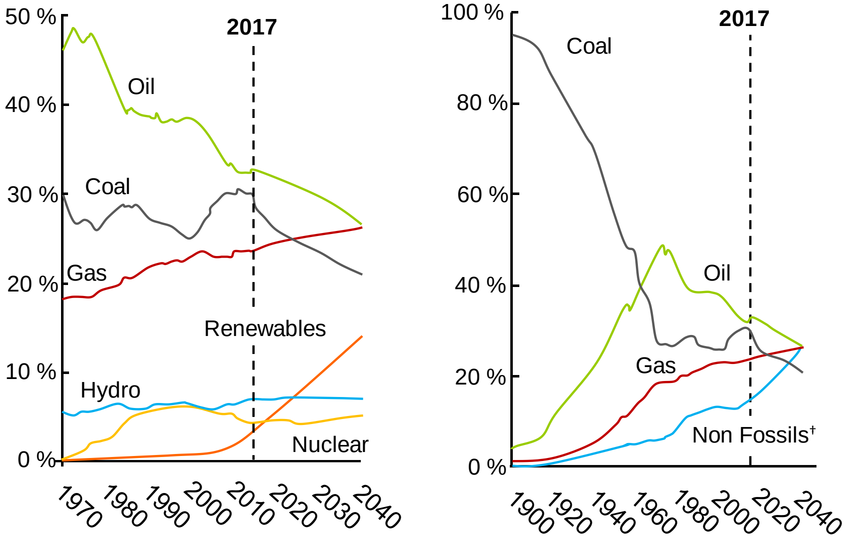

Figure 1.2. Shares of primary energy by feedstock with projection to 2040. Source: Reference [8]. $^+$ Non-fossils: nuclear, hydro and renewables.

1.2. Current industrial production of olefins: steam-cracking

Considering recent energy outlooks, it is predicted that the non-combusted uses of oil and natural gas will increase by 2040-2050, particularly as feedstock for petrochemicals [8, 10-12]. This is not surprising, since the chemical richness of both resources is clearly wasted when they are burned. For instance, in the U.S. only the 2 % of oil went for petrochemical uses in 2017, being gasoline, jet-fuel and fuel oil the majority products (ca. 85 wt.%) [15].

Among all the chemical products provided by the petrochemical industry, olefins can be considered the most important ones. Particularly, ethylene is one of its key compounds, with an annual production of 150 million tons in 2015, displaying a growth rate of ca. 3.5 % per year [16]. It is used directly as building block in the production of polyethylene resins (70 MT/year), which constitute the basis of polymer industry. It is also a basic feedstock for the production of commodity chemicals such as vinyl chloride, ethylene oxide or styrene [17-19].

The main industrial route for the production of ethylene (and, in part, propylene) is steam cracking, which accounts for the 72 % of total production of olefins [20-23]. This technology has been applied for more than 50 years, and consists in the high temperature treatment of hydrocarbons in the presence of steam. Interestingly, feedstocks have been changing over the years. Naphtha used to be the main raw material for the production of ethylene through this process, although the current trend is moving to ethane as feedstock for two main reasons: i) favorable production costs of ethane crackers and; ii) increasing available amounts of ethane derived from shale gas extraction. Furthermore, ethane leads to a lower formation of byproducts than naphtha in steam cracking units [8, 10, 23]. In spite of being a well stablished technology, steam cracking is probably the most intensive process in terms of energy consumption (the reaction is carried out in the 700-850 ºC temperature range) and CO_2 emissions (ca. 1.2 kg CO_2/$kg_{ethylene}$) [20-22, 24]. Aligned with the increasing annual demand of olefins, the search for alternative and more sustainable methods for their production is a recurring topic in catalysis science.

In the last decades, several approaches have been proposed to face this issue, like maximizing the selectivity to olefins in current processes like FCC [25]. Other approximations to the problem consist in the production of either the olefin or their derived commodity chemicals by other routes, using cheaper or renewable biomass-derived feedstocks [26, 27].

Both natural gas (cheap and abundant) (**Fig. 1.3**) and biomass (renewable) (**Fig. 1.4**) constitute ideal raw materials for the development of new chemical routes to olefins and derivatives, meeting the requirements of the green and sustainable chemistry. Natural gas is a major energy source in the planet, accounting for 21% of the World's energy supply in 2010. It consists mainly of methane (ca. 70-90%) but contains also small amounts of C_2-C_4 hydrocarbons (ethane, propane and butane; ca. 0-20%), and nonhydrocarbon gases [28]. On the other hand, biomass refer to any organic material that comes from animals and/or plants. In the case of plants, they store solar energy in a chemical form, by the so-called photosynthesis process. It can be considered a renewable feedstock for the production of fuels and chemicals [29, 30], although its transformation to fuels is more extended. For example, biomass provided ca. 5 % of the total primary energy in the U.S. in 2017 [31].

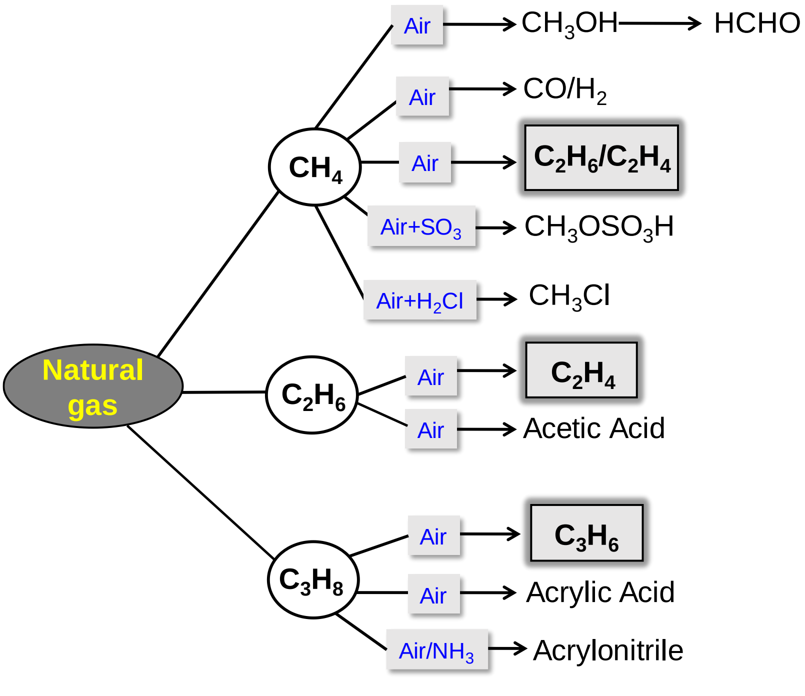
Natural gas
CH_4
Air
CH_3OH
HCHO
Air
CO/H_2
Air
C_2H_6/C_2H_4
Air+SO_3
CH_3OSO_3H
Air+H_2Cl
CH_3Cl
C_2H_6
Air
C_2H_4
Air
Acetic Acid
C_3H_8
Air
C_3H_6
Air
Acrylic Acid
Air/NH_3
Acrylonitrile

Figure 1.3. Proposed pathways for the valorization of natural gas via oxidative processes. Source: reference [27].

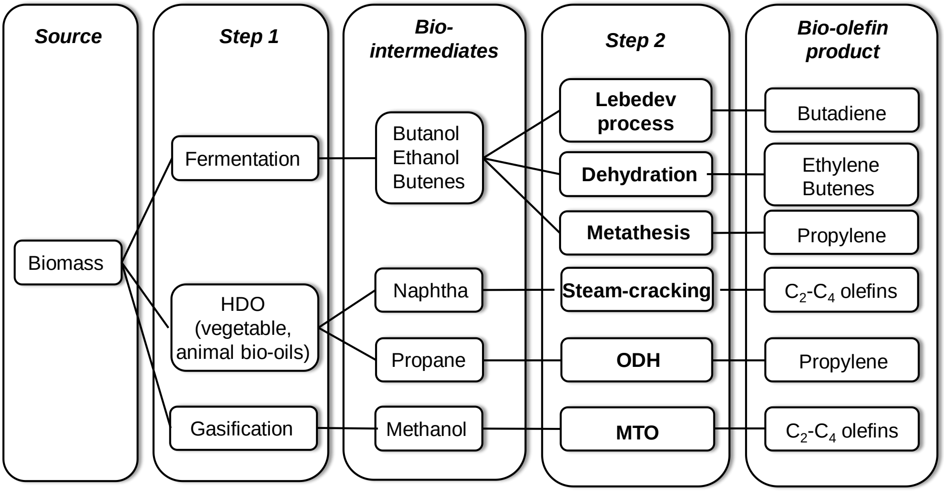
Source
Step 1
Bio-intermediates
Step 2
Bio-olefin product
Biomass
Fermentation
HDO (vegetable, animal bio-oils)
Gasification
Butanol
Ethanol
Butenes
Naphtha
Propane
Methanol
Lebedev process
Dehydration
Metathesis
Steam-cracking
ODH
MTO
Butadiene
Ethylene
Butenes
Propylene
C2-C4 olefins
Propylene
C2-C4 olefins

Figure 1.4. Proposed routes for the production of olefins from biomass. Adapted from reference [26].

The present doctoral thesis will provide some examples of how materials chemistry can help us to understand and develop new catalysts for the transformation of both type of feedstocks in valuable chemical commodities and fuels.

1.3. Oxidative dehydrogenation (ODH) of ethane as an alternative to steam cracking processes for the production of ethylene

Among all the alternative pathways proposed for the synthesis of ethylene, the oxidative dehydrogenation (ODH) of ethane constitutes the most promising one, in view to an industrial implementation [32]. The process consists in the reaction of ethane in the presence of a solid catalyst and oxygen in the feed (**Fig. 1.5**). It is an exothermic reaction, since the abstracted hydrogen is instantaneously oxidized to give H_2O, what allows to work at relatively low temperatures (350-500 ºC). Unlike catalytic dehydrogenation, no coke is formed during the process, and no regeneration of the catalyst is needed [27, 33].

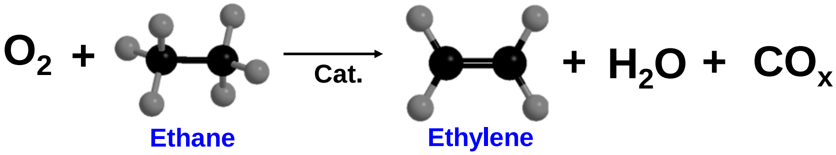

Figure 1.5. Reaction scheme of the oxidative dehydrogenation of ethane.

Three catalytic systems have shown promising results in the ODH of ethane: i) Vanadium oxide-based materials [34, 35]; ii) Nickel oxide-based materials [36-39] and; iii) Multicomponent MoVTe(Sb)NbO mixed metal oxide bronzes with an orthorhombic structure, the so-called M1-type phase [40-43] (**Fig. 1.6**).

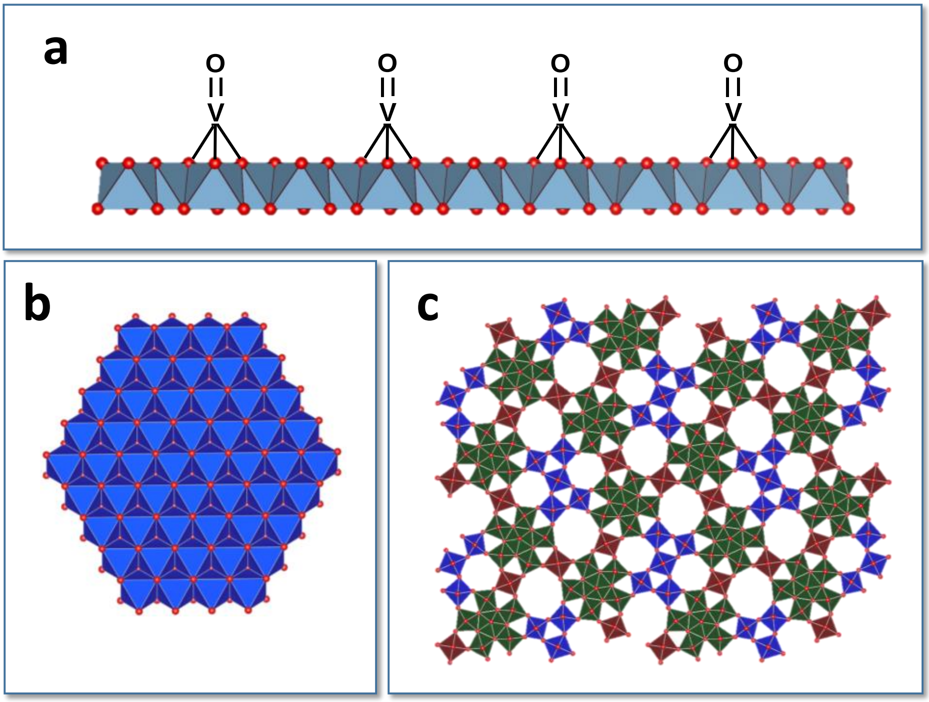

Figure 1.6. a) Supported vanadium oxide; b) NiO with a sodium chloride-type structure viewed along [111] direction; c) Mo-V mixed oxide with an M1-type structure viewed along [001] direction.

All these systems are able to transform ethane to ethylene by oxidative dehydrogenation. However, the variation of the selectivity to ethylene with ethane conversion strongly depends on the characteristics of the catalyst. Thus, only MoVTe(Sb)NbO mixed metal oxides show very high yields to ethylene (up to 75%) [40]. We must indicate that both Mo-V-O and NiO-based catalysts can maintain a high selectivity to ethylene at increasing ethane conversions, i.e. up to 80% ethane conversion for MoVTe(Sb)NbO mixed metal oxides, or up to 40% ethane conversion in the case of NiO-based catalysts; which leads to possible technological applications [44-48].

The catalytic behavior of these materials in ODH reactions follows a Mars-van Krevelen (MvK) redox mechanism (**Fig. 1.7**), which is generalized for most of gas-phase partial oxidation reactions [49]. According to this mechanism, O^{2-} nucleophilic species on the catalyst surface are responsible for the partial oxidation of the substrate, leading to the formation of partial oxidation products, or the olefin and water in the case of ODH.

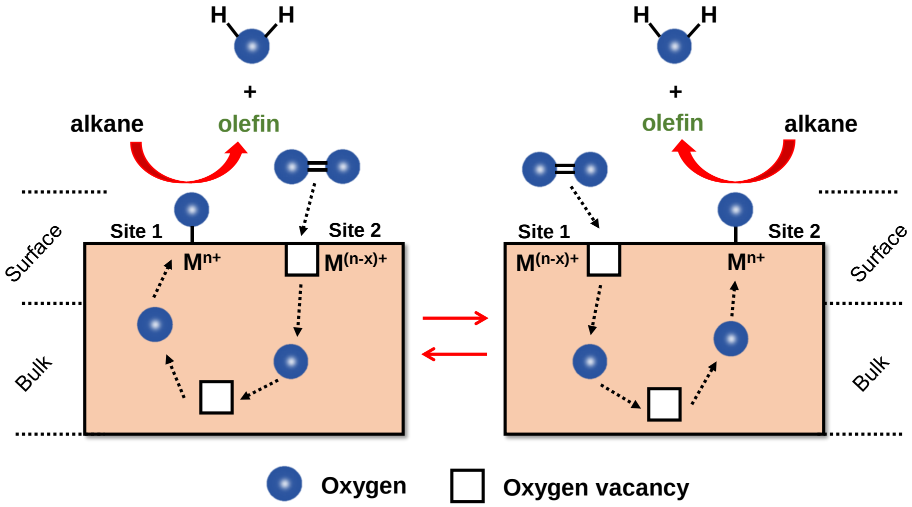

Figure 1.7. Schematic representation of the Mars-van Krevelen redox mechanism during the oxidative dehydrogenation of alkanes.

Particularly, these lattice surface oxygen species are responsible for the activation of the hydrocarbon C-H bond, and are incorporated into the final products, or into water molecules generated during the oxidative dehydrogenation of the alkane. Subsequently, a surface oxygen vacancy (associated with a reduced metal center) is left behind after each catalytic cycle. Then, these anionic vacant sites are replenished by molecular oxygen, with the consequent reoxidation of the metal center. The reoxidation of the catalyst usually implies migration of the aforementioned vacancies near the surface, with the associated transport of O^{2-} species into the bulk of the material. In turn, partial oxidation reaction (i.e. the reduction of the catalysts) implies O^{2-} transport from the bulk to the surface.

This mechanism is widely reported in the literature, and has been demonstrated by using isotopic labeled $^{18}O_2$ in the feed [50, 51]. Reactivity tests under these conditions show that only ^{16}O atoms are inserted into the final products. This means that only lattice oxygen is taking part in the oxygen insertion during partial oxidation by this mechanism. Only at long reaction times ^{18}O is detected in the products, due to a partial substitution of original ^{16}O species in the catalysts.

Assuming this partial oxidation mechanism, two very important variables arise, which have a pivotal role in the catalytic behavior in partial oxidation and ODH, i.e. the strength of the surface metal-oxygen bond, and the stability of reactants and products. In the first case, M-O should be weak enough to liberate surface oxygen, but strong enough in order to avoid total oxidation [52]. On the contrary, very strong M-O bond would lead to inactive materials. These assumptions are in line with the classical Sabatier´s principle for catalytic phenomena.

The stability of reactants, partial oxidation and/or ODH products constitutes another key aspect in these reactions. The stability can be estimated from the dissociation enthalpies of the weakest C-H or C-C bonds in both reactants and products [49]. This way, when the weakest bond of the reactant is stronger that the weakest one in the product of interest, we can achieve high yields in partial oxidation and ODH reactions. Otherwise, products are prone to consecutive reactions and overoxidation to carbon oxides, especially at high alkane conversion. Hence, the highest yields to the olefin in the ODH of short chain alkanes have been found in the transformation of ethane to ethylene. This is not surprising, since both compounds (i.e ethane and ethylene) are the only ones that meet these requirements, being the dissociation energy of the weakest C-H bond for ethane and ethylene, 419.5 and 444 kJ/mol respectively [49]. On the other hand, both propylene and butene present an allylic C-H bond which is weaker that the weakest C-H bond of their corresponding alkane. Consequently, they tend to give consecutive reactions, and it is more difficult to obtain high yields to the olefin in ODH processes.

1.4. Bio-fuels and chemicals from biomass. The bio-refinery concept

Biomass can be considered as the main renewable carbon source in planet Earth, at least assuming CO_2 neutrality in the production-consumption cycle (in an optimistic way) [53-55]. Then, the use of biomass derivatives in substitution of fossil feedstocks for the production of commodities stands as a good alternative to drive the energy transition to renewables. Despite this, the use of biomass for the production of consumer goods raises a number of ethical problems beyond energy and gas emissions issues [56]. In this sense, sustainability assessments of the use of bio-resources as raw materials have to take into consideration not only the energy equilibrium and net emissions, but also the type of crop, and social and environmental issues related with the use of land.

Nowadays biomass sources can be classified in three groups or generations, depending on its origin [57, 58]. First generation biomass includes standard crops, such as corn, sugar cane or soy. Its utilization is mainly focused on the production of bio-fuels, like bio-ethanol (by fermentation processes) or biodiesel (by transesterification of vegetable oils), which are already available for consumers. The use of such crops generated several ethical problems, since they strongly compete with food. Conversely, second generation sources are centered in the exploitation of non-edible crops, lignocellulosic biomass, agricultural waste and other residues (like, for example, cooking oil or animal fats). The third generation would be based on the utilization of algae as raw material, which are able to generate more energy per crop unit area that in the case of terrestrial biomass. For example, the production rates of triglycerides from algae is 45-220 times higher than in the case of conventional crops [29]. First and second generation biomass already have technological applications, meanwhile the applicability of third generation biomass is still under development. The work related with biomass transformation presented in this doctoral thesis is focused on the valorization of waste streams generated during thermal and chemical treatments of second generation biomass. The valorization of waste effluents is closely connected with the integrated bio-refinery concept, as it is discussed below.

The production of either fuels or chemicals from biomass-derived feedstocks has been widely addressed in literature in the last decades [29, 30]. Nevertheless, the integrated bio-refinery concept is envisaged to be the most sustainable way to carry out biomass conversion into valuable products. Unlike more restricted conceptions, in which a specific bio-refinery would be dedicated to the production of specific consumer goods (like for example, fuel-driven or chemical-driven bio-refineries), an integrated bio-refinery would include: innovative plant resources (genetically modified biomass), fuels, chemicals, and bio-power production [53]. In fact, this will imply a multidisciplinary approach based on the collaboration between biochemists, chemical engineers and fundamental and materials chemists. The production of such a variety of valuable products helps to minimize both the risk associated with price fluctuations and the operational costs of each process [59]. Moreover, in an integrated conception of a bio-refinery, the valorization of residues will be an important step in the global process, since it appears very difficult to avoid waste generation when dealing with such a complicated and heterogeneous raw material as biomass [53].

Currently, there exist a huge number of available strategies for the transformation of biomass into value added products, which comprise thermal and chemical processes [55]. General schemes of the transformation of lignocellulosic biomass and vegetable oils are depicted in **Figure 1.8** and **Figure 1.9**, respectively. Since it is out of the scope of this work, we will not get into a detailed description of each route, and we will pay attention to the production of biodiesel from vegetable oils and animal fats; and bio-oils by lignocellulosic biomass fast pyrolysis. Specifically, this thesis deals with the catalytic transformation of waste streams derived from both processes, i.e. glycerol and short chain oxygenates respectively, and the discussion hereafter will be focused on how those residues are generated.

Both vegetable and fast pyrolysis oils, although presenting different chemical nature, share a common point, i.e. they show undesirable physicochemical properties that prevent their direct use as fuels in combustion engines. Therefore, upgrading approaches are necessary in both cases, in order to make them suitable for their utilization as automotive fuels [58, 60, 61].

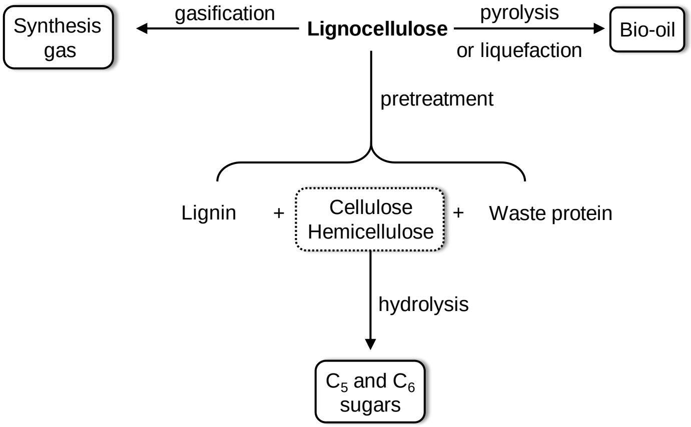
Synthesis gas
gasification
Lignocellulose
pyrolysis
or liquefaction
Bio-oil
pretreatment
Lignin
+
Cellulose Hemicellulose
+
Waste protein
hydrolysis
C_5 and C_6 sugars

Figure 1.8. General scheme of primary treatments of lignocellulosic biomass.

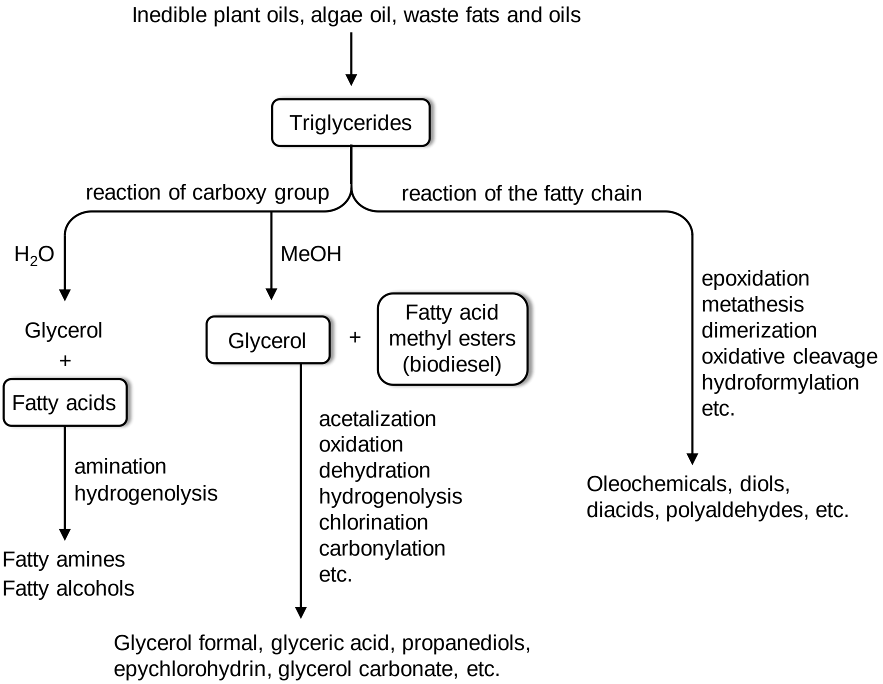
Inedible plant oils, algae oil, waste fats and oils
Triglycerides
reaction of carboxy group
reaction of the fatty chain
H2O
MeOH
Glycerol
+
Fatty acids
amination
hydrogenolysis
Fatty amines
Fatty alcohols
Glycerol
+
Fatty acid methyl esters (biodiesel)
acetalization
oxidation
dehydration
hydrogenolysis
chlorination
carbonylation
etc.
Glycerol formal, glyceric acid, propanediols, epychlorohydrin, glycerol carbonate, etc.
epoxidation
metathesis
dimerization
oxidative cleavage
hydroformylation
etc.
Oleochemicals, diols, diacids, polyaldehydes, etc.

Figure 1.9. General scheme the transformation of triglycerides into chemicals and fuels.

1.4.1. Glycerol as raw material for chemicals

In the case of vegetable oils, they actually could be directly used in engines, but their high viscosity leads to problems due to deposits formed after combustion [61]. This high viscosity derives from its chemical nature, characterized by the presence of triglyceride mixtures. The upgrading approach in this specific case consist in the elimination of the glycerin part form triglycerides, which is responsible for the viscosity and deposit formation. It is currently carried out by a transesterification reaction in basic media, using methanol and NaOH. The process leads to the liberation of fatty acid methyl esters (FAMEs, also known as bio-diesel) and the generation of high amounts of glycerol as a by-product (10 wt.% of the total production) (**Fig. 1.10**) [62]. The amount of glycerol provided by this transesterification technology is high enough to satisfy all the pharmaceutical, cosmetics and food industry needs. Indeed, this fact provoked the obsolescence of the traditional technology for the production of glycerol from propene [59]. Nevertheless, according to the volumes generated by biodiesel industry, which are expected to reach ca. 3.6 MT in 2020 [63], there are still high amounts of glycerol which are discarded [64].

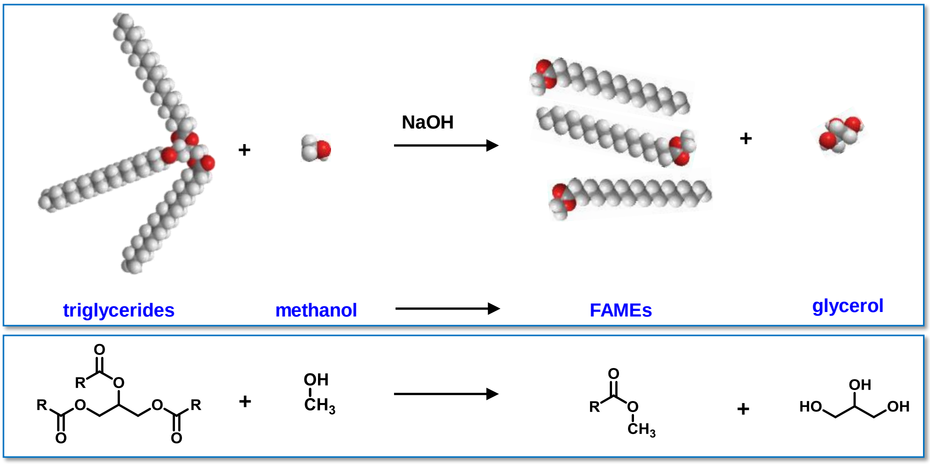

Figure 1.10. Scheme of the transesterification of triglycerides in basic media.

Thereby, this available low-price glycerol stock has generated an increasing interest in the development of new routes involving its transformation into platform chemicals and value-added products [59, 62]. **Figure 1.11** summarizes some of the suggested pathways for the transformation of glycerol into a wide range of products. Indeed, some of those transformations have already been implemented in industry, like the synthesis of epichlorohydrin (process by Solvay) [65-67] or 1,2-propanediol (commercialized by Synergy Chemicals) [64].

An interesting building block than can be obtained through the catalytic transformation of glycerol is acrolein [64, 68, 69], which is currently obtained by partial oxidation of propene using bismuth molybdate-based catalysts [70]. The main use of acrolein is the production of acrylic acid (by oxidation catalysis), which is the basic feedstock for the production of acrylic resins or superabsorbent polymers like sodium polyacrylate (annual production of 1.9 MT in 2010) [64, 69].

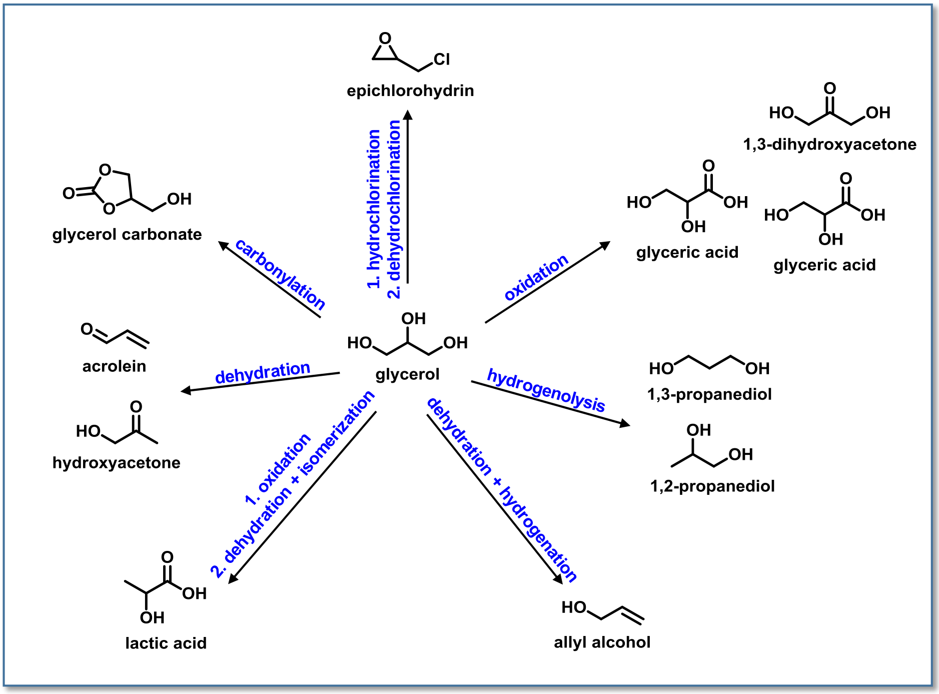
epichlorohydrin
1. hydrochlorination
2. dehydrochlorination
1,3-dihydroxyacetone
glyceric acid
glyceric acid
oxidation
glycerol carbonate
carbonylation
acrolein
dehydration
glycerol
hydroxyacetone
hydrogenolysis
1,3-propanediol
1,2-propanediol
1. oxidation
2. dehydration + isomerization
dehydration + hydrogenation
lactic acid
allyl alcohol

Figure 1.11. Different strategies for glycerol transformation into valuable chemicals

Acrolein can be synthesized from glycerol through a double dehydration route using Brönsted-type acid catalysts (**Fig. 1.12**) [64, 69, 71, 72]. Despite the relatively high yields to acrolein reported in the literature (up to ca. 90 %), the process has not yet been implemented at an industrial scale. There are several reasons that explain this aspect: deactivation of the catalysts due to the deposition of coke and high molecular weight products, glycerol price volatility or high costs of glycerol purification [64, 69, 72].

In turn, acrylic acid can also be synthesized from glycerol through a two-step approximation in which: i) glycerol is transformed into acrolein in a first stage and; ii) acrolein is subsequently oxidized to acrylic acid in a separated second step [63] **(Fig. 1.13)**. This multi-reactor approach would present higher costs, since two reactors are needed two perform the double-step process. A more elegant approach to attack the problem would be to incorporate both acid and redox functions able to work under the same reaction conditions in the same crystal phase (**Fig. 1.13**). In this respect, metal oxide bronzes constitute an excellent matrix to incorporate different functionalities, as it will be explained in section 1.6.

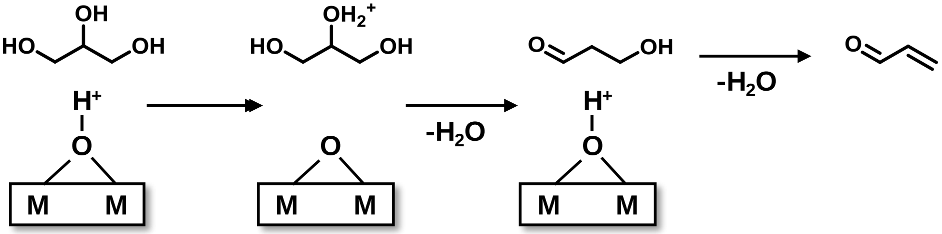
OH
HO
OH
H+
O
M M
OH2+
HO
OH
O
M M
-H2O
O
OH
H+
O
M M
-H2O
O

Figure 1.12. Scheme of glycerol dehydration to acrolein on Brönsted acid sites.

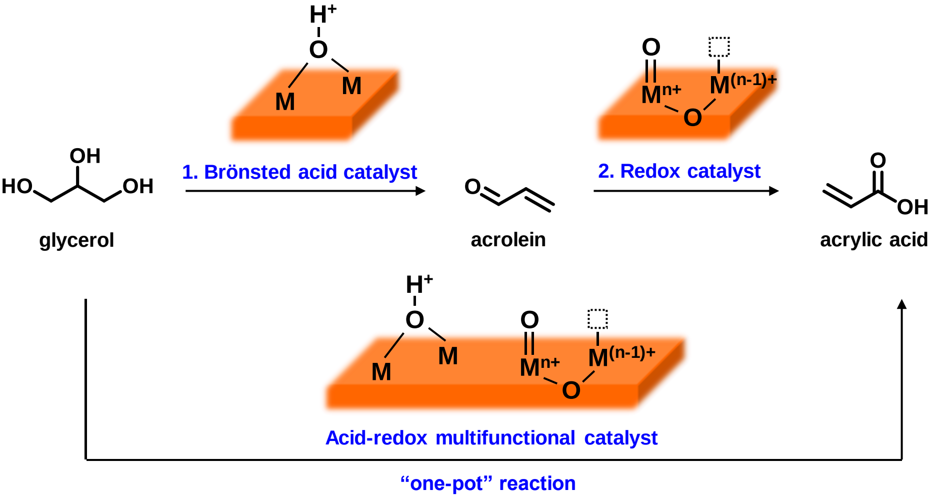
H+
O
M
M
OH
HO
OH
glycerol
1. Brönsted acid catalyst
O
acrolein
O
Mn+
M(n-1)+
O
2. Redox catalyst
O
OH
acrylic acid
H+
O
M
M
O
Mn+
M(n-1)+
O
Acid-redox multifunctional catalyst
"one-pot" reaction

Figure 1.13. Schematic representation of glycerol transformation on acid, redox and on multifunctional acid-redox catalysts.

1.4.2. Upgrading aqueous solutions derived from fast pyrolysis of lignocellulosic biomass

Considering bio-oils, obtained by fast pyrolysis of lignocellulosic biomass (thermal treatments in the absence of oxygen), they also display undesired physicochemical properties for their direct use as fuel, like high viscosity, low pH and high corrosiveness [60, 73]. Moreover, in this case these features also prevent their storage for long-term uses. Thus, their application is mostly limited to their combustion in boilers and furnaces for electricity and heat generation [74, 75]. Its composition resembles that of biomass rather than petroleum oils. In fact, it could be defined as a mixture of depolymerization products of biomass constituents, i.e. cellulose, hemicellulose and lignin [60, 76]. In particular, the obtained pyrolytic oil displays an extremely heterogeneous composition, which highly depends on the type of biomass used, and pyrolysis conditions [77]. In general, they show a high content of carboxylic acids, responsible for their low pH (pH = 1-3), water (15-30 wt.%) and light oxygenates (C_1-C_4, 10-40 wt.%); apart from oligomers, phenols, sugars, etc. [77-79]. Accordingly, this implies a high oxygen content in the bio-oil. Due to this, upgrading approaches are mandatory in order to extend their application as transportation fuels.

The most extended upgrading strategy is based on hydrotreating, which implies bio-oil treatment at high temperatures and high hydrogen pressures (> 60 bar) in the presence of a catalysts (generally CoMo, NiMo and/or NiW-based materials) [80-82]. Supported on HDS, hydrogenation and hydrocracking technologies, which are well stablished in conventional refineries, it has experimented a fast development during the last years [83-85]. Hydrodeoxygenation (HDO), hydrocracking and hydrogenation reactions improve those physicochemical features of the bio-oil (decrease its acidity, oxygen content or corrosiveness), allowing their blending with conventional fuels [60, 86]. Nonetheless, these approach presents other drawbacks, like a high hydrogen consumption or relatively low atom economy (most of the short-chain compounds are transformed into gases) [87].

In the recent years, a new upgrading approach has raised increasing interest in both academia and industry, which consist in the phase separation by water addition [85, 88-90]. Instead of considering the presence of high water contents as a disadvantage, the addition of water to the bio-oil can promote phase separation into an aqueous and an organic phase. Short chain oxygenates (acids, ketones, alcohols, etc.) are displaced within the aqueous phase, whereas the organic fraction can be further upgraded by conventional methods to obtain a bio-oil which meets the requirements for blending with fossil fuels [85, 88, 91]. It is worth noting that the aqueous phase would remain as a waste stream in this case. Then, the valorization of this mixture would help to increase the efficiency of the global process. Most of the literature on this topic deals with the transformation of model compounds through ketonization and/or aldol condensation reactions, obviating the high water content or the presence of different organic functions in the mixture [92-98]. Accordingly, a more realistic approximation to the problem would be to carry out the valorization of the whole aqueous mixture in one-pot [99]. Assuming high water contents and low pH (high acetic acid concentration) of the aqueous residue, the transformation must be performed using water and acid-resistant catalysts.

1.5. Heterogeneous catalysis as a tool to meet green chemistry principles

In the late 90´s Paul Anastas and John Warner introduced the twelve principles of Green Chemistry, which are summarized in **Figure 1.14** [100, 101]. Leaving aside terminological discussions about the meaning of green or sustainable chemistry, catalysis can be considered as the meeting point at which most of these principles converge. Despite catalysis is only mentioned in terms of using “catalytic reagents rather than stoichiometric ones”, it is closely related with most of the Green Chemistry principles, which in fact were not new. For example, the concept “atom economy” is nothing but selectivity in catalysis science; or “design for energy efficiency” is closely linked with catalytic activity.

The 12 Principles of Green Chemistry

1. **Prevention**
2. **Atom Economy**
3. **Less Hazardous Chemical Synthesis**
4. **Designing Safer Chemicals**
5. **Safer Solvents and Auxiliaries**
6. **Design for Energy Efficiency**
7. **Use of Renewable Feedstocks**
8. **Reduce Derivatives**
9. **Catalysis**
10. **Design for Degradation**
11. **Real-Time Analysis for Pollution Prevention**
12. **Inherently Safer Chemistry for Accident Prevention**

Figure 1.14. The 12 principles of Green Chemistry as listed by Anastas *et al.* Source: reference [100].

The paradigmatic case of butane oxidation to maleic anhydride underlines this connection between catalysis (in particular heterogeneous catalysis) and the development of "greener" or more sustainable processes for the production of chemicals [102-105]. The industrial process starting from benzene was substituted about 30 years ago by the one using butane as raw material (**Fig. 1.15**), which presented substantial improvements: i) Two carbon atoms are lost in the case of benzene-based technology; ii) carbon oxides and small amount of acetic acid are the only by products in butane-based process and; iii) toxicity issues related to the use of benzene and the generation of higher amounts of residues in the case of the former technology [104].

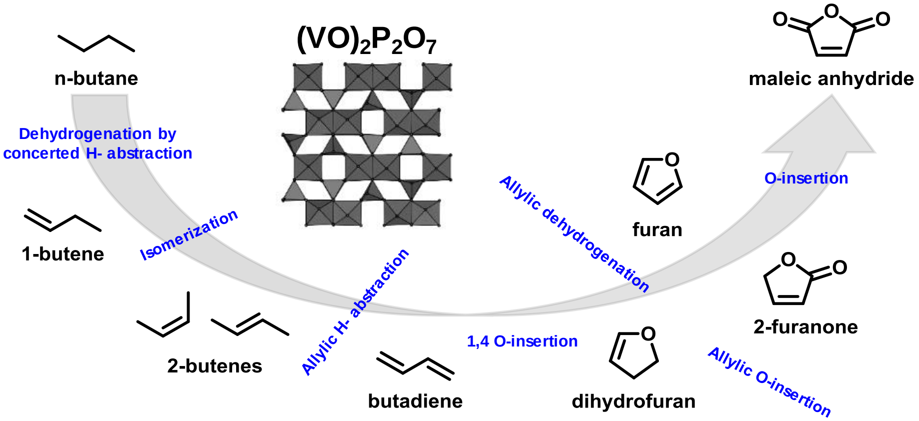
(VO)$_2$P$_2$O$_7$
n-butane
Dehydrogenation by concerted H- abstraction
1-butene
Isomerization
2-butenes
Allylic H- abstraction
butadiene
1,4 O-insertion
dihydrofuran
Allylic dehydrogenation
furan
Allylic O-insertion
2-furanone
O-insertion
maleic anhydride

Figure 1.15. Reaction scheme of partial oxidation of n-butane to maleic anhydride. Adapted from reference [106].

The partial oxidation of n-butane to maleic anhydride (with yields of ca. 70 %) is the only process based on the partial oxidation of a light alkane that has been industrially implemented, and fully meets the pillars of Green Chemistry: the process uses non-toxic reagents and presents an improved atom economy, minimizing waste formation. In fact, most of the worldwide production of maleic anhydride is currently carried out by this method. More importantly, this industrial shift towards a more sustainable production was driven by the development of vanadyl pyrophosphate (VPP) based catalysts (**Fig. 1.16**) [107], which is able to perform the multistep reaction selectively (**Fig. 1.15**).

Specifically, it can carry out the abstraction of eight H, the insertion of three O atoms and the transfer of 14 e$^-$ (**Fig. 1.15**), with high activity and selectivity [102, 105]. Indeed, this catalytic system meets all the requirements proposed by Grasselli as “the seven pillars of oxidation catalysis” (**Fig. 1.17**) which can be summarized in: i) the presence of nucleophile lattice oxygen; ii) redox properties; iii) a structurally stable host structure; iv) phase cooperation; v) multifunctionality; vi) active site isolation and; vii) M-O bonds with an intermediate strength (Sabatier´s principle) [52, 108].

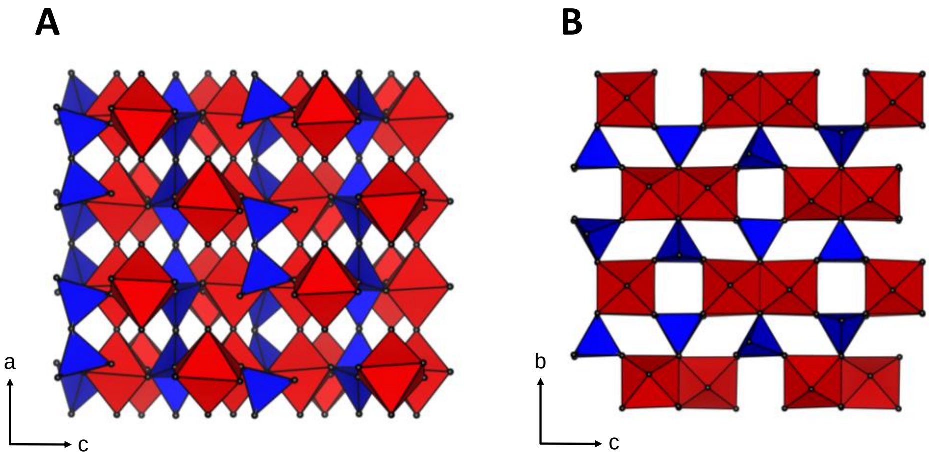

Figure 1.16. Crystal structure of vanadyl pyrophosphate (VPP) viewed along [010] (A) and [100] (B) directions. Blue tetrahedra and red octahedra correspond to $[PO_4]_{Td}$ and $[VO_6]_{Oh}$ units respectively.

Grasselli´s seven pillars point out the importance of catalyst design, which allows to deal with such complicated reaction pathways. In fact, they could be considered as the rationalization of the fundamentals of solid catalyst design for the specific case of oxidation reactions. These fundamentals can be summed up in: the design of functional /multifunctional materials with well-defined catalytic properties, in which the active sites are located at interatomic distances and preferably in the same crystal structure. Particularly, this thesis work is focused on the use bulk and supported tungsten oxide bronzes and nickel oxide as host structures.

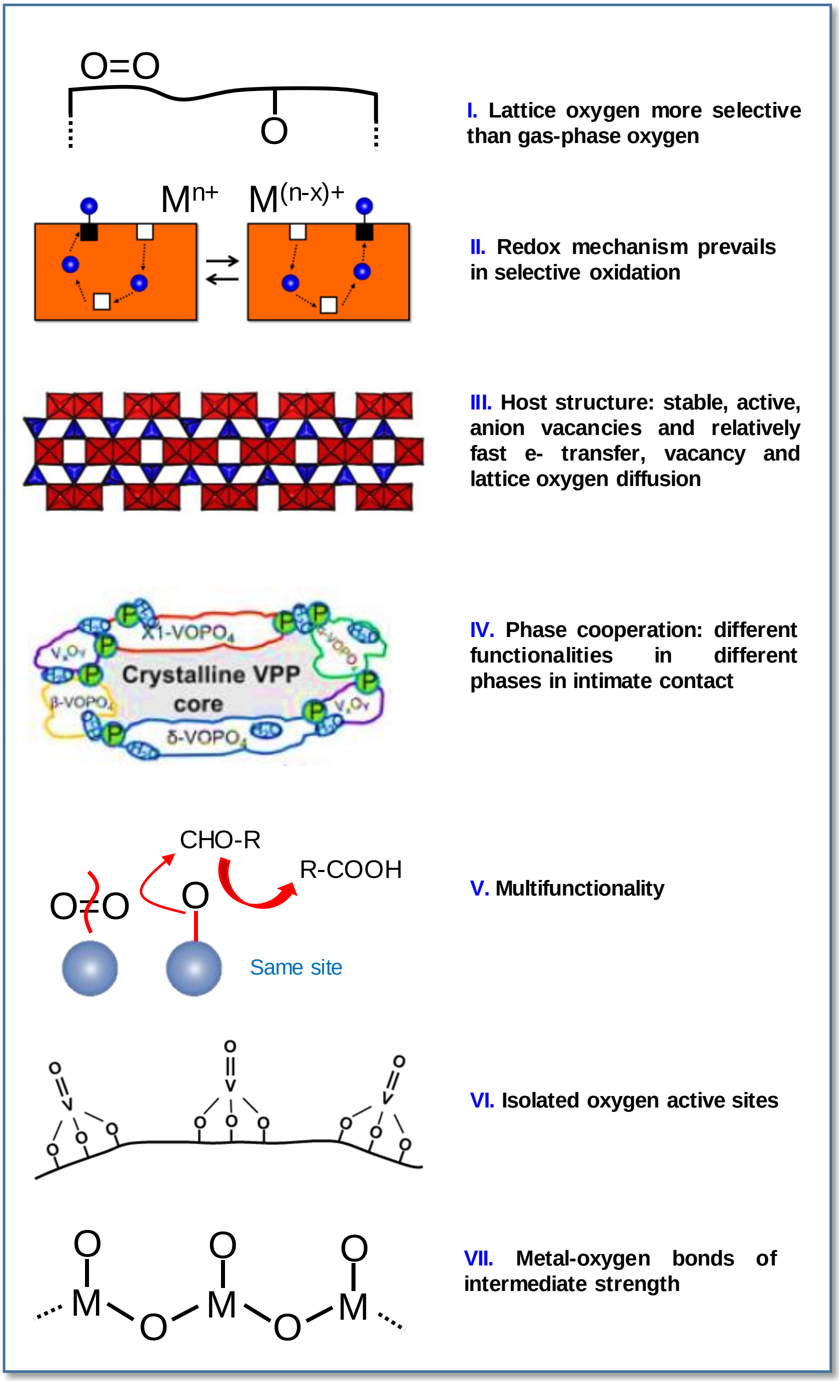
O=O
O
I. Lattice oxygen more selective than gas-phase oxygen
Mn+
M(n-x)+
II. Redox mechanism prevails in selective oxidation
III. Host structure: stable, active, anion vacancies and relatively fast e- transfer, vacancy and lattice oxygen diffusion
X1-VOPO4
Crystalline VPP core
VxOy
β-VOPO4
δ-VOPO4
P
IV. Phase cooperation: different functionalities in different phases in intimate contact
CHO-R
R-COOH
O=O
O
Same site
V. Multifunctionality
O
V
VI. Isolated oxygen active sites
O
M
VII. Metal-oxygen bonds of intermediate strength

Figure 1.17. Schematic representation of Grasselli´s seven pillars of oxidation catalysis. Adapted from reference [106].

1.6. Metal oxide bronzes: multifunctional materials

First reported by Wohler in the first quarter of 19th century, the term metal oxide "bronze" derives from the brilliant and colored crystals (reminding metal alloys) that were obtained after treating sodium tungstate in hydrogen at high temperature [109]. The term is usually generalized to describe oxides with the general formula of A_xMO_n, being A an electropositive element (classically alkaline or alkaline-earth metals) [110, 111] and M a transition metal (M: W, Mo, Ti, Ta, Re, etc.) [112]. In addition, other types of A cations can be inserted in the oxide framework, rare earths [113, 114], also transition metals [115, 116] and metals [117-119], and even ammonium ions [120], pointing out their compositional richness. Moreover, the partial substitution of M by other transition metals is also possible [112, 121, 122].

Formally, they can be understood as intercalation compounds, in which A^{m+} cations are incorporated within the MO_n oxide matrix [123, 124]. This fact implies a partial reduction of M^{n+} cations in the pristine MO_n oxide. Due to this, they can be also classified as partially reduced phases. Thereby, it is also possible to obtain the corresponding materials with no A element incorporated, by selecting the appropriate precursors and heat treatments under reducing, inert or oxidative conditions. These changes in the average oxidation state of M gives rise to structural modifications leading to new crystal phases [125].

This structural versatility is exemplified by the whole family of Magneli phases (with the presence of Wadsley defects) (**Fig. 1.18 a**) [126, 127], and the observation of rotational faults, with the formation of tunnel structures (**Fig. 1.18 b**) [128, 129], which correlate different structural types along these oxide bronze systems. As far as these defects get ordered, new crystalline materials are obtained. All this features are found in the tungsten oxide system, which is shown in **Figure 1.19**.

It is worth noting the key role of the oxygen content in the crystals, which has a great influence on the structural type obtained after synthesis (**Fig. 1.19**). By performing typical solid state reactions at high temperatures under controlled atmospheres (reducing, inert or oxidant), and by selecting the appropriate precursors (metals, metal salts or metal oxides), it is relatively easy to modulate the specific oxidation states in the final materials. This determines metal/oxygen ratio and, consequently, the final structural type. On the other hand, the ability to control these variables is not so evident when alternative synthesis methods are used, like hydrothermal or slurry methodologies.

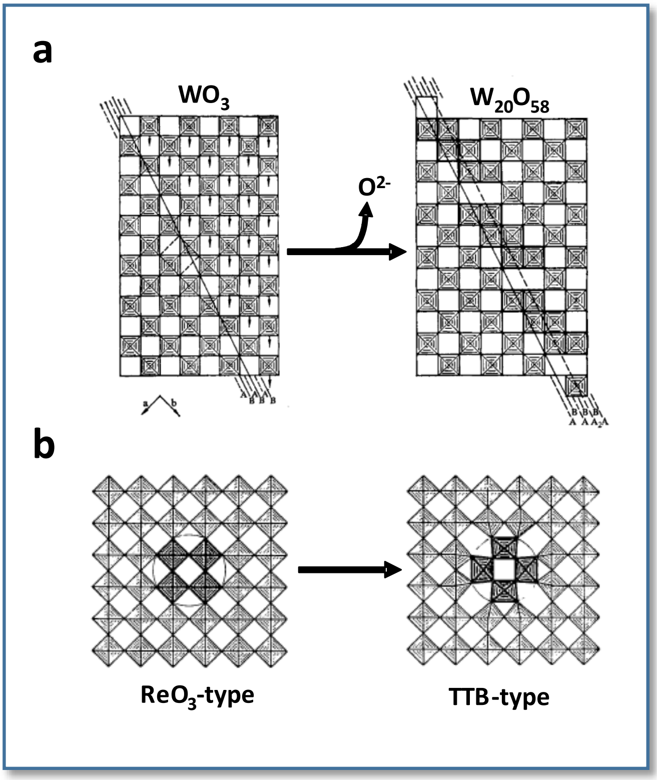

Figure 1.18. a) Representation of the formation of the Magneli phase $W_{20}O_{58}$ through the generation of crystallographic shear planes (ordered Wadsley defects) by loss of oxygen. Source: reference [127]. b) Scheme of the rotational fault generated in ReO_3-type tungsten oxide phase which correlates its structure with the tetragonal tungsten bronze (TTB) polymorph. Source: reference [128].

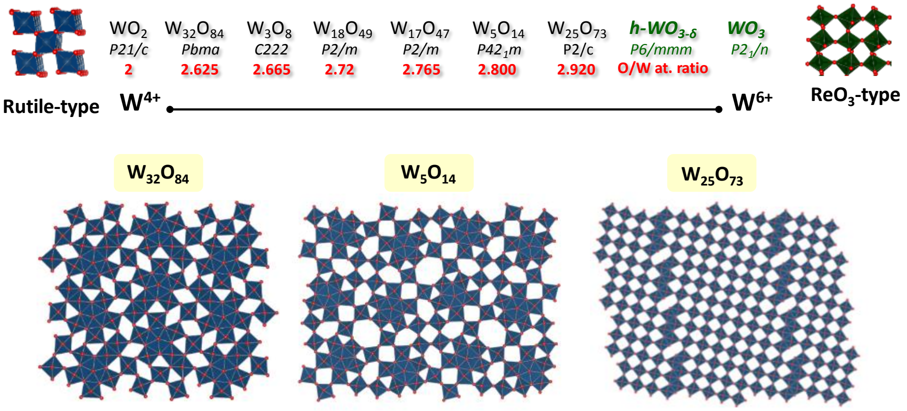
WO2
P21/c
2
W32O84
Pbma
2.625
W3O8
C222
2.665
W18O49
P2/m
2.72
W17O47
P2/m
2.765
W5O14
P421m
2.800
W25O73
P2/c
2.920
h-WO3-δ
P6/mmm
O/W at. ratio
WO3
P21/n
Rutile-type
W4+
W6+
ReO3-type
W32O84
W5O14
W25O73

Figure 1.19. Representation of some of tungsten oxide crystal phases in the system WO_2-WO_3, highlighting their oxygen/tungsten ratio, related with the proportion of W^{4+}, W^{5+} and W^{6+} in the structure.

Because of their extremely adaptive features (i.e. compositional and structural versatility, that in fact allows the modulation of their functional properties), metal oxide bronze-based materials have aroused a great interest in diverse fields, including magnetic materials [130], conductors [131], superconductors [132], optical materials [133] or gas sensors [134]. However, their catalytic applications were somehow limited, especially due to their extremely low surface areas derived from high temperature synthesis methods. It was not until the development of synthesis procedures based on “soft chemistry” or “chimie douce” that it was possible to obtain mixed oxide bronzes with interesting catalytic properties [135].

Several reported examples suggest that *in situ* formation of polyoxometalates (POM´s) could play a key role during the preparation by this soft methods (especially by hydrothermal synthesis), being responsible for providing the building blocks that generate the oxide framework [136-140]. For instance, this aspect has been demonstrated by Ueda *et al.* for the synthesis of Mo-V-O bronzes under hydrothermal conditions, in which a $[Mo_{72}V_{30}]$ POM provides the $[Mo_6O_{21}]^{6-}$ pentagonal units characteristic of the M1-type phase [139] (**Fig. 1.20**).

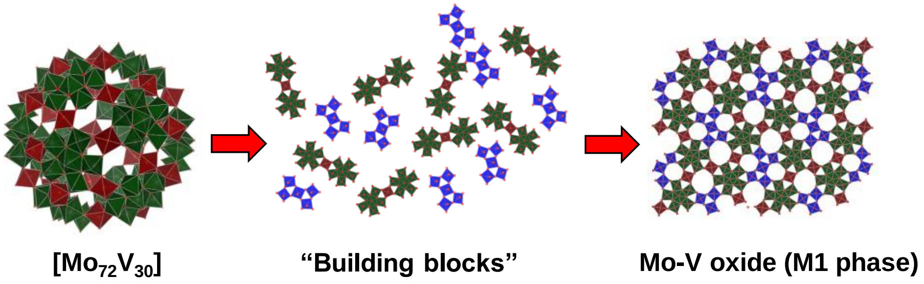

$[Mo_{72}V_{30}]$ **"Building blocks"** **Mo-V oxide (M1 phase)**

Figure 1.20. Scheme of the formation mechanism of a Mo-V oxide with a M1-type structure under hydrothermal conditions. Source: reference [139].

This M1-type structure presents 6 and 7-member ring channels in which we can introduce other elements [141]. Moreover, it also admits the isomorphic substitution in the octahedral matrix. In fact, this material is isostructural with MoVNbTe(Sb)O catalysts for the ODH of ethane and the partial oxidation/ammoxidation of propane [142]. In the latter case, Te/Sb atoms are located within the 6-member ring channels of the structure, while the pentagonal units are formed by $[Nb_6O_{21}]^{12-}$ clusters [143, 144]. This catalyst exemplifies the importance of both structure and location of the active sites in bronze-type materials [145, 146]. On the one hand, blocking the hexagonal channel (by the incorporation of Te^{4+} or Sb^{3+}) and introducing $[Nb_6O_{21}]^{12-}$ bipyramids in the framework increases the degree of active site isolation (V-O sites in the 7-member ring channel) [147, 148]. On the other hand, it is suggested that the mere existence of those 7-member channels could stabilize the reaction intermediates in the ODH ethane via van der Waals interactions, acting as an active "hole" for ethane activation [149, 150].

Another example of oxide bronzes with interesting catalytic properties is the case of hexagonal tungsten bronze-based materials (HTBs) (**Fig. 1.21**). As in the case of Mo-V based oxides, they can be obtained by hydrothermal synthesis [151-154]. Also the incorporation of different functionalities can be carried out by the selection of the appropriate precursors to effectively substitute W atoms in *h*-WO_3 lattice, or by inserting additional elements inside the hexagonal tunnels [155]. Recently, it was demonstrated that the incorporation of V within HTB matrix in octahedral coordination gives rise to a multifunctional acid-redox material, able to transform glycerol into acrylic acid in one-pot (**Fig. 1.22**) [151]. Subsequent studies showed that the incorporation of Nb or Mo within this host structure have effects in their structural and catalytic features, leading to the modulation of their acid-redox properties, which give rise to higher acrylic acid yields (up to 50 % yield) [153, 154]. The technological interest of this family of materials is illustrated by the several number of patents published in the last years [156-159].

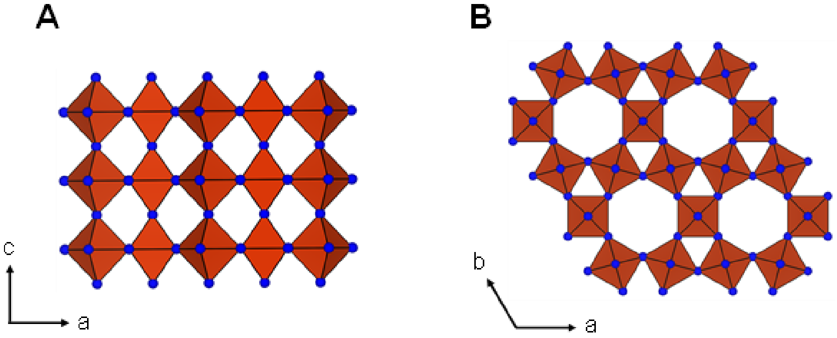

Figure 1.21. Representation of the hexagonal tungsten bronze structure (also known HTB or *h*-WO_3) along [010] (A) and [001] (B) directions.

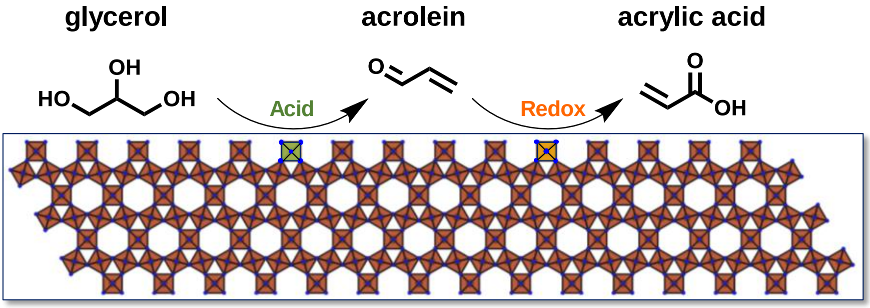

Figure 1.22. Simplified reaction scheme of the gas-phase transformation of glycerol on a multifunctional acid-redox hexagonal tungsten bronze-based catalyst.

1.7. Nickel oxide-based materials for the ODH of ethane

As it was commented in section 1.3, besides Mo-V-based catalysts, nickel oxide-based materials present also an outstanding catalytic performance in the ODH of ethane [33]. Both systems show the ability to maintain the selectivity to ethylene in a wide range of ethane conversions. In the case of the best NiO-based catalysts, a selectivity to ethylene of ca. 90 % is observed up to ethane conversions of approximately 40 % [160, 161]. This feature makes them able to achieve high ethylene yields in the ODH of ethane (up to 30-40 %). Interestingly these catalysts do not show the formation of CO (or at least it is not detected in the output stream), fact that is not observed in the case of supported V_2O_5 catalysts. This can be explained because ethylene formed is less reactive than ethane [34].

Despite unmodified NiO can activate ethane molecule in the presence of oxygen, it displays a low selectivity to ethylene (ca. 30 %), being CO_2 the main reaction product. In their pioneering work in the field, Lemonidou´s group observed that the incorporation of Nb^{5+} into nickel oxide framework drastically shifted the selectivity towards ethylene formation [160, 161]. This way, it was possible to transform an apparently total oxidation catalyst in one of the most selective materials for the oxidative dehydrogenation of ethane, presenting an ethylene selectivity of ca. 90 %.

The case of Nb-doped catalysts observed by Lemonidou was not an isolated case. During the last decade several examples of NiO promoted by other elements have been reported. Interestingly when the metal promoter shows a high valence, like in the case of Nb^{5+}, W^{6+}, Ce^{4+}, Sn^{4+}, Al^{3+} or Ta^{5+} [36, 37, 162-167], the selectivity to ethylene notably increases. On the other hand, when the promoter displays a low valence, like Li^+ or K^+ [36, 37], the selectivity to ethylene is unaltered, or even decreases. This observation has been explained in terms of the specific oxygen and nickel species present in each type of catalyst. It has been suggested that the incorporation of elements in a high oxidation state would push Ni to the lowest oxidation state (i.e. Ni^{2+}), decreasing NiO non-stoichiometry, i.e. by the elimination of Ni^{3+} species [168, 169]. This Ni^{3+} provides positive holes (h^+) that are associated with the presence of electrophilic oxygen species ($O^{2-} + h^+ \rightarrow O^{\cdot -}$) responsible for deep oxidation of the alkane (**Fig. 1.23**). The correlation between electrical conductivity, which is dependent on h^+ concentration, and the selectivity to ethylene, goes in line with these assumptions [170]. In addition, not only the number of electrophilic oxygen species decreases when high valence dopants are used, but also their lability is substantially reduced, preventing total oxidation reactions [37].

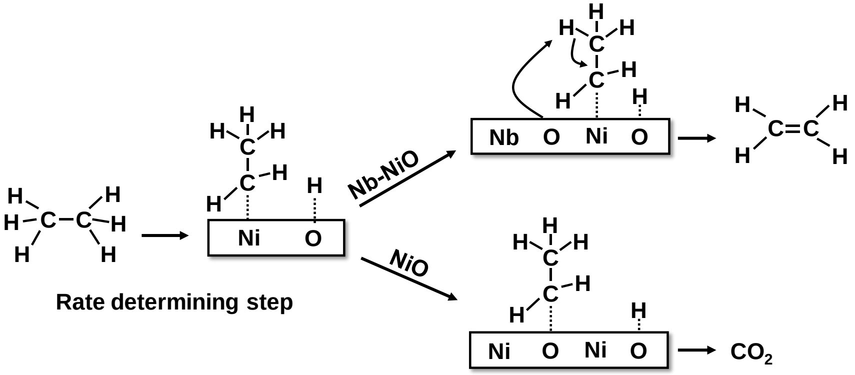

Figure 1.23. Schematized reaction pathway on undoped and Nb-doped NiO catalysts during the ODH of ethane. Adapted from reference [171].

Interestingly, the use of specific supports also changes drastically the catalytic properties of NiO in the ODH of ethane. In this sense, similar shifts in the selectivity profiles are observed in comparison to promoted-NiO catalysts. Specifically, the use of Al_2O_3 [38], porous clay heterostructures (PCH) [39] and TiO_2 [172] as NiO supports increases the selectivity to ethylene to levels comparable to the best promoted catalysts (ethylene selectivity in the range 80-90 %). The main difference between both types of materials (i.e. supported and promoted) lies in the amount of active phase found in optimized catalysts. While the selectivity to ethylene achieved in both cases is comparable (ca. 90 %), promoted catalysts present an optimum amount of NiO of 90-95 at. % (i.e. a promoter concentration of 5-10 at. %) [160, 161, 166, 167], whereas the optimum amount found for supported catalysts lies between 5-50 wt.% NiO loading [39, 172]. In this sense, the specific concentration of active phase in supported catalysts has been reported to be very dependent on the surface area of the specific support [172] (**Fig. 1.24**).

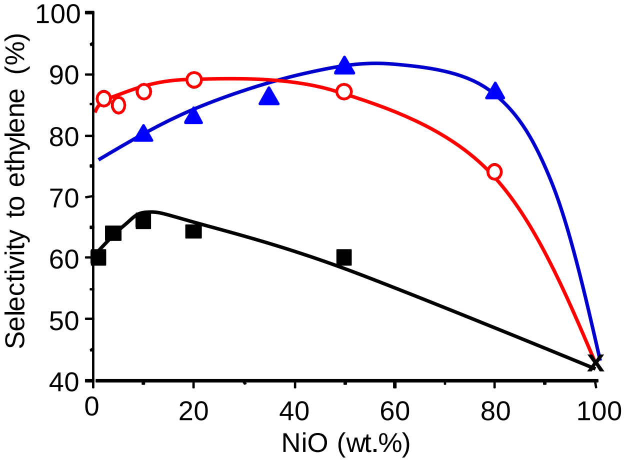

Figure 1.24. Selectivity to ethylene in the ODH of ethane at 400 °C as a function of NiO loading for a series of TiO_2-supported catalysts presenting different support surface areas. Symbols: (■) 11 $m^2 g^{-1}$ TiO_2; (○) 55 $m^2 g^{-1}$ TiO_2; (▲) 85 $m^2 g^{-1}$ TiO_2. Adapted from reference [172].

In general, an inverse correlation between the reducibility of the catalyst (measured by means of temperature-programmed reduction experiments) and the selectivity to ethylene is observed in both promoted and supported materials [165-167, 172]. Accordingly, the lower the reducibility of Ni species in the catalysts, the higher the selectivity to ethylene achieved. Nevertheless, in some cases this is not so direct, for instance Nb-promoted catalysts show some discrepancies in this respect [160]. A similar correlation has been found with particle size of NiO catalysts, showing increasing ethylene selectivity trends when NiO particle size decreases [36, 165]. This suggest that the dispersion of NiO particles (and their crystal sizes) strongly influences the catalytic behavior.

Particularly, the assumption that a decrease in the non-stoichiometry of the catalysts is the only factor affecting the catalytic behavior of the catalyst (mainly the shift in the selectivity to ethylene) could be debated. Non-stoichiometry degree of NiO depends fundamentally on the amount of Ni^{3+} and cation vacancies, which determines the final oxygen content in the material. Unfortunately, the characterization of these variables is not a trivial task, and differences in the concentration of defects depending on the applied technique are reported in the literature [173-175]. For example, it is surprising that the elimination of such electrophilic species, associated with Ni^{3+}, whose concentration is assumed to be very low (2-4 at. %), may give rise to such an increase in the selectivity to ethylene (from ca. 30 % to 90 %).

1.8. Objectives

The present doctoral thesis falls within the scope of the current energy transition to renewables, in which both fossil (like natural gas) and renewable (i.e. biomass) sources will play pivotal roles. Specifically, it can be divided in two parts: i) the development of tungsten bronze-based materials for the valorization of biomass feedstocks and, ii) nickel oxide-based materials for the oxidative dehydrogenation (ODH) of ethane. The results will be presented from the materials chemistry point of view, trying to link materials properties and catalytic behavior.

A study of the incorporation of V and Nb into h-WO_3 framework by hydrothermal and reflux methods will be presented in the first chapters of this thesis. Insights on the effect of supports, atomic and phase composition into structural and catalytic properties are given. Examples of the use of methanol and ethanol as model reactions for the characterization of the acid-redox properties of these materials are also presented. Considering catalytic applications, tungsten bronze based materials have been studied as catalysts for the valorization of biomass-derived waste streams; i.e. glycerol, and aqueous mixtures of short chain oxygenates. In the case of glycerol, the use of acid and multifunctional acid-redox materials to obtain acrolein and acrylic acid is proposed. An in-depth characterization study of WO_3-Nb_2O_5 system has been also performed in order to extend its application to the valorization of an aqueous mixture of short-chain oxygenates via C-C bond formation reactions.

The second part of this work deals with gaining further insights into the catalytic properties of nickel oxide-based materials for the ODH of ethane. With this purpose, series of promoted and supported nickel oxides presenting low, intermediate and high selectivity to ethylene in the ODH of ethane have been prepared, which were subsequently characterized by a wide variety of physicochemical techniques. The results include time-resolved *in situ* measurements of redox kinetics under oxidative and reducing conditions by *in situ* X-ray Absorption Spectroscopy. In the case of supported catalysts, the specific coordination environment of nickel species has been studied by analyzing the EXAFS region in XAS spectra.

1.9. References

[1] R.P. Feynman, R. Leighton, *“What do you care what other people think?": Further adventures of a curious character*, W. W. Norton 2011.

[2] S. Pain, *Power through the ages*, Nature, 551 (2017) S134-S139.

[3] R. Fouquet, *Make low-carbon energy an integral part of the knowledge economy*, Nature, 551 (2017) S141.

[4] B.K. Sovacool, *How long will it take? Conceptualizing the temporal dynamics of energy transitions*, Energy Research & Social Science, 13 (2016) 202-215.

[5] A.P. Connor, J.C. Cleveland, *U.S. Energy Transitions 1780–2010*, Energies, 7 (2014).

[6] R. Fouquet, P.J.G. Pearson, *Past and prospective energy transitions: Insights from history*, Energy Policy, 50 (2012) 1-7.

[7] D. Elliot, *Energy, Society and Environment*, Routledge, London and New York, (1997).

[8] BP Energy Outlook, 2018 Edition.

[9] J.M. Thomas, J.M. Thomas, W.J. Thomas, *Principles and Practice of Heterogeneous Catalysis*, John Wiley & Sons Ltd. 2015.

[10] U.S. Energy Information Administration, *Annual Energy Outlook 2018, with projections to 2050*.

[11] ExxonMobil, *2018 Outlook for Energy: A view to 2040*.

[12] *Shell energy scenarios to 2050*.

[13] in: F. Cavani, S. Albonetti, F. Basile, A. Gandini (Eds.) *Chemicals and Fuels from Bio-Based Building Blocks*, Wiley-VCH Verlag GmbH & Co. KGaA 2016.

[14] in: J. Clark, F. Deswarte (Eds.) *Introduction to Chemicals from Biomass*, John Wiley & Sons, Ltd. 2015.

[15] U.S. Energy Information Administration, *Petroleum & other liquids. Refinery Yield.*

www.eia.gov/dnav/pet/PET_PNP_PCT_DC_NUS_PCT_A.htm.

[16] D. Lippe, *Planned maintenance to slow first-half 2016 ethylene production*, Oil & Gas Journal, 114 (2016) 62-70.

[17] T.J. Farmer, M. Mascal, *Platform Molecules*, in: *Introduction to chemicals from biomass*, John Wiley & Sons, Ltd. 2014, pp. 89-155.

[18] J.J.H.B. Sattler, J. Ruiz-Martinez, E. Santillan-Jimenez, B.M. Weckhuysen, *Catalytic dehydrogenation of light alkanes on metals and metal oxides*, Chemical Reviews, 114 (2014) 10613-10653.

[19] R.A. Collins, A.F. Russell, P. Mountford, *Group 4 metal complexes for homogeneous olefin polymerisation: a short tutorial review*, Applied Petrochemical Research, 5 (2015) 153-171.

[20] T. Ren, M.K. Patel, K. Blok, *Steam cracking and methane to olefins: Energy use,* CO_2 *emissions and production costs*, Energy, 33 (2008) 817-833.

[21] T. Ren, M. Patel, K. Blok, *Olefins from conventional and heavy feedstocks: Energy use in steam cracking and alternative processes*, Energy, 31 (2006) 425-451.

[22] S.M. Sadrameli, *Thermal/catalytic cracking of hydrocarbons for the production of olefins: A state-of-the-art review. I: Thermal cracking review*, Fuel, 140 (2015) 102-115.

[23] R.W. Heinz Zimmermann, *Ethylene, Ullmann's Encyclopedia of Industrial Chemistry*, Wiley-VCH Verlag GmbH & Co. KGaA: Weinheim, Germany, 2009.

[24] J.-L. Dubois, *Selective oxidation of hydrocarbons and the global warming problem*, Catalysis Today, 99 (2005) 5-14.

[25] A. Corma, E. Corresa, Y. Mathieu, L. Sauvanaud, S. Al-Bogami, M.S. Al-Ghrami, A. Bourane, *Crude oil to chemicals: light olefins from crude oil*, Catalysis Science & Technology, 7 (2017) 12-46.

[26] A. Chieregato, J.V. Ochoa, F. Cavani, *Olefins from biomass*, in: *Chemicals and Fuels from Bio-Based Building Blocks*, John Wiley & Sons, Ltd. 2016.

[27] F. Ivars, J.M.L. Nieto, *Light Alkanes Oxidation: Targets reached and current challenges*, in: *Handbook of Advanced Methods and Processes in Oxidation Catalysis*, pp. 767-834.

[28] R. Webster, *What's the difference between natural gas, liquid natural gas, shale gas, shale oil and methane? An oil and gas glossary*, www.carbonbrief.org/whats-the-difference-between-natural-gas-liquid-natural-gas-shale-gas-shale-oil-and-methane-an-oil-and-gas-glossary, (2013).

[29] G.W. Huber, S. Iborra, A. Corma, *Synthesis of transportation fuels from biomass: Chemistry, catalysts, and engineering*, Chemical Reviews, 106 (2006) 4044-4098.

[30] A. Corma, S. Iborra, A. Velty, *Chemical routes for the transformation of biomass into chemicals*, Chemical Reviews, 107 (2007) 2411-2502.

[31] U. S. Energy Information Administration,

https://www.eia.gov/energyexplained/?page=biomass_home.

[32] F. Cavani, N. Ballarini, A. Cericola, *Oxidative dehydrogenation of ethane and propane: How far from commercial implementation?*, Catalysis Today, 127 (2007) 113-131.

[33] C.A. Gärtner, A.C. van Veen, J.A. Lercher, *Oxidative dehydrogenation of ethane: common principles and mechanistic aspects*, ChemCatChem, 5 (2013) 3196-3217.

[34] T. Blasco, J.M.L. Nieto, *Oxidative dyhydrogenation of short chain alkanes on supported vanadium oxide catalysts*, Applied Catalysis A: General, 157 (1997) 117-142.

[35] H.H. Kung, M.C. Kung, *Oxidative dehydrogenation of alkanes over vanadium-magnesium-oxides*, Applied Catalysis A: General, 157 (1997) 105-116.

[36] J.M. López Nieto, B. Solsona, R.K. Grasselli, P. Concepción, *Promoted NiO catalysts for the oxidative dehydrogenation of ethane*, Topics in Catalysis, 57 (2014) 1248-1255.

[37] E. Heracleous, A.A. Lemonidou, *Ni–Me–O mixed metal oxides for the effective oxidative dehydrogenation of ethane to ethylene – Effect of promoting metal Me,* Journal of Catalysis, 270 (2010) 67-75.

[38] E. Heracleous, A.F. Lee, K. Wilson, A.A. Lemonidou, *Investigation of Ni-based alumina-supported catalysts for the oxidative dehydrogenation of ethane to ethylene: structural characterization and reactivity studies*, Journal of Catalysis, 231 (2005) 159-171.

[39] B. Solsona, P. Concepcion, J.M. López Nieto, A. Dejoz, J.A. Cecilia, S. Agouram, M.D. Soriano, V. Torres, J. Jimenez-Jimenez, E. Rodriguez Castellon, *Nickel oxide supported on porous clay heterostructures as selective catalysts for the oxidative dehydrogenation of ethane*, Catalysis Science & Technology, 6 (2016) 3419-3429.

[40] J.M. López Nieto, P. Botella, M.I. Vázquez, A. Dejoz, *The selective oxidative dehydrogenation of ethane over hydrothermally synthesised MoVTeNb catalysts*, Chemical Communications, (2002) 1906-1907.

[41] N. Fang Chen, W. Ueda, K. Oshihara, *Hydrothermal synthesis of Mo–V–M–O complex metal oxide catalysts active for partial oxidation of ethane*, Chemical Communications, (1999) 517-518.

[42] T. Konya, T. Katou, T. Murayama, S. Ishikawa, M. Sadakane, D. Buttrey, W. Ueda, *An orthorhombic* Mo_3VO_x *catalyst most active for oxidative dehydrogenation of ethane among related complex metal oxides*, Catalysis Science & Technology, 3 (2013) 380-387.

[43] P. Botella, A. Dejoz, J.M. López Nieto, P. Concepción, M.I. Vázquez, *Selective oxidative dehydrogenation of ethane over MoVSbO mixed oxide catalysts*, Applied Catalysis A: General, 298 (2006) 16-23.

[44] J.M. López Nieto, P. Botella, B. Solsona, Patent, WO/2003/008096, (2002).

[45] A.M. Gaffney, R. Ghosh, R. Song, C.Y. Yeh, T. Langner, Patent, US8105971B2, (2009).

[46] A.M. Gaffney, R. Song, Patent, US7718568B2, (2002).

[47] Y. Liu, Patent, US6436871B1, (2002).

[48] Y. Liu, Patent, US6417422B1, (1999).

[49] C. Batiot, B.K. Hodnett, *The role of reactant and product bond energies in determining limitations to selective catalytic oxidations*, Applied Catalysis A: General, 137 (1996) 179-191.

[50] L.C. Glaeser, J.F. Brazdil, M.A. Hazle, M. Mehicic, R.K. Grasselli, *Identification of active oxide ions in a bismuth molybdate selective oxidation catalyst*, Journal of the Chemical Society, Faraday Transactions 1: Physical Chemistry in Condensed Phases, 81 (1985) 2903-2912.

[51] Y. Moro-oka, D.-H. He, W. Ueda, *Catalyst oxide support oxide interaction to prepare multifunctional oxidation catalysts*, in: R.K. Grasselli, A.W. Sleight (Eds.) Studies in Surface Science and Catalysis, Elsevier 1991, pp. 57-66.

[52] R.K. Grasselli, *Fundamental Principles of Selective Heterogeneous Oxidation Catalysis*, Topics in Catalysis, 21 (2002) 79-88.

[53] A.J. Ragauskas, C.K. Williams, B.H. Davison, G. Britovsek, J. Cairney, C.A. Eckert, W.J. Frederick, J.P. Hallett, D.J. Leak, C.L. Liotta, J.R. Mielenz, R. Murphy, R. Templer, T. Tschaplinski, *The path forward for biofuels and biomaterials,* Science, 311 (2006) 484-489.

[54] C.O. Tuck, E. Pérez, I.T. Horváth, R.A. Sheldon, M. Poliakoff, *Valorization of biomass: deriving more value from waste*, Science, 337 (2012) 695-699.

[55] R.A. Sheldon, *Green and sustainable manufacture of chemicals from biomass: state of the art*, Green Chemistry, 16 (2014) 950-963.

[56] J.P.W. Scharlemann, W.F. Laurance, *How green are biofuels?*, Science, 319 (2008) 43-44.

[57] J. Moncada, J.A. Tamayo, C.A. Cardona, *Integrating first, second, and third generation biorefineries: Incorporating microalgae into the sugarcane biorefinery*, Chemical Engineering Science, 118 (2014) 126-140.

[58] S.N. Naik, V.V. Goud, P.K. Rout, A.K. Dalai, *Production of first and second generation biofuels: A comprehensive review*, Renewable and Sustainable Energy Reviews, 14 (2010) 578-597.

[59] G.M. Lari, G. Pastore, M. Haus, Y. Ding, S. Papadokonstantakis, C. Mondelli, J. Pérez-Ramírez, *Environmental and economical perspectives of a glycerol biorefinery*, Energy & Environmental Science, 11 (2018) 1012-1029.

[60] K. Jacobson, K.C. Maheria, A. Kumar Dalai, *Bio-oil valorization: A review*, Renewable and Sustainable Energy Reviews, 23 (2013) 91-106.

[61] T. Issariyakul, A.K. Dalai, *Biodiesel from vegetable oils*, Renewable and Sustainable Energy Reviews, 31 (2014) 446-471.

[62] C.-H. Zhou, J.N. Beltramini, Y.-X. Fan, G.Q. Lu, *Chemoselective catalytic conversion of glycerol as a biorenewable source to valuable commodity chemicals*, Chemical Society Reviews, 37 (2008) 527-549.

[63] D. Sun, Y. Yamada, S. Sato, W. Ueda, *Glycerol as a potential renewable raw material for acrylic acid production*, Green Chemistry, 19 (2017) 3186-3213.

[64] B. Katryniok, S. Paul, V. Bellière-Baca, P. Rey, F. Dumeignil, *Glycerol dehydration to acrolein in the context of new uses of glycerol*, Green Chemistry, 12 (2010) 2079-2098.

[65] E. Santacesaria, R. Tesser, M. Di Serio, L. Casale, D. Verde, *New process for producing epichlorohydrin via glycerol chlorination*, Industrial & Engineering Chemistry Research, 49 (2010) 964-970.

[66] *Solvay to build world-class Epicerol plant in Thailand*, Pump Industry Analyst, 2007 (2007) 3.

[67] https://www.solvay.us/en/markets-and-products/featured-products/epicerol.html.

[68] D. Cespi, F. Passarini, G. Mastragostino, I. Vassura, S. Larocca, A. Iaconi, A. Chieregato, J.L. Dubois, F. Cavani, *Glycerol as feedstock in the synthesis of chemicals: a life cycle analysis for acrolein production*, Green Chemistry, 17 (2015) 343-355.

[69] B. Katryniok, S. Paul, F. Dumeignil, *Recent developments in the field of catalytic dehydration of glycerol to acrolein*, ACS Catalysis, 3 (2013) 1819-1834.

[70] L. Liu, X.P. Ye, J.J. Bozell, *A comparative review of petroleum-based and bio-based acrolein production*, ChemSusChem, 5 (2012) 1162-1180.

[71] G.S. Foo, D. Wei, D.S. Sholl, C. Sievers, *Role of Lewis and Brønsted acid sites in the dehydration of glycerol over niobia*, ACS Catalysis, 4 (2014) 3180-3192.

[72] A. Talebian-Kiakalaieh, N.A.S. Amin, H. Hezaveh, *Glycerol for renewable acrolein production by catalytic dehydration*, Renewable and Sustainable Energy Reviews, 40 (2014) 28-59.

[73] R.H. Venderbosch, W. Prins, *Fast pyrolysis of biomass for energy and chemicals: Technologies at various scales*, in: *Sustainable Development in the Process Industries*, John Wiley & Sons Ltd. 2010, pp. 109-155

[74] R. Venderbosch, W. Prins, *Fast pyrolysis technology development*, Biofuels, Bioproducts and Biorefining, 4 (2010) 178-208.

[75] M. Balat, *An overview of the properties and applications of biomass pyrolysis oils*, Energy Sources, Part A: Recovery, utilization, and environmental effects, 33 (2011) 674-689.

[76] S. Czernik, A.V. Bridgwater, *Overview of applications of biomass fast pyrolysis oil*, Energy & Fuels, 18 (2004) 590-598.

[77] Z. Luo, J. Zhou, *Thermal Conversion of Biomass*, in: W.-Y. Chen, J. Seiner, T. Suzuki, M. Lackner (Eds.) *Handbook of Climate Change Mitigation*, Springer US, New York, NY, 2012, pp. 1001-1042.

[78] C. Branca, C.D. Blasi, R. Elefante, *Devolatilization and heterogeneous combustion of wood fast pyrolysis oils*, Industrial & Engineering Chemistry Research, 44 (2005) 799-810.

[79] E.E. Iojoiu, M.E. Domine, T. Davidian, N. Guilhaume, C. Mirodatos, *Hydrogen production by sequential cracking of biomass-derived pyrolysis oil over noble metal catalysts supported on ceria-zirconia*, Applied Catalysis A: General, 323 (2007) 147-161.

[80] A. Pinheiro, D. Hudebine, N. Dupassieux, C. Geantet, *Impact of oxygenated compounds from lignocellulosic biomass pyrolysis oils on gas oil hydrotreatment*, Energy & Fuels, 23 (2009) 1007-1014.

[81] V.N. Bui, G. Toussaint, D. Laurenti, C. Mirodatos, C. Geantet, *Co-processing of pyrolisis bio oils and gas oil for new generation of bio-fuels: Hydrodeoxygenation of guaïacol and SRGO mixed feed*, Catalysis Today, 143 (2009) 172-178.

[82] D.C. Elliott, T.R. Hart, G.G. Neuenschwander, L.J. Rotness, M.V. Olarte, A.H. Zacher, Y. Solantausta, *Catalytic hydroprocessing of fast pyrolysis bio-oil from pine sawdust*, Energy & Fuels, 26 (2012) 3891-3896.

[83] G.W. Huber, A. Corma, *Synergies between bio- and oil refineries for the production of fuels from biomass*, Angewandte Chemie International Edition, 46 (2007) 7184-7201.

[84] H. Wang, J. Male, Y. Wang, *Recent advances in hydrotreating of pyrolysis bio-oil and its oxygen-containing model compounds*, ACS Catalysis, 3 (2013) 1047-1070.

[85] A.H. Zacher, M.V. Olarte, D.M. Santosa, D.C. Elliott, S.B. Jones, *A review and perspective of recent bio-oil hydrotreating research*, Green Chemistry, 16 (2014) 491-515.

[86] A.V. Bridgwater, D. Meier, D. Radlein, *An overview of fast pyrolysis of biomass*, Organic Geochemistry, 30 (1999) 1479-1493.

[87] D.E. Resasco, S.P. Crossley, *Implementation of concepts derived from model compound studies in the separation and conversion of bio-oil to fuel*, Catalysis Today, 257 (2015) 185-199.

[88] D. Radlein, A. Quignard, US Patent, 2014/028833, 2014.

[89] L.K.-E. Park, S. Ren, S. Yiacoumi, X.P. Ye, A.P. Borole, C. Tsouris, *Separation of switchgrass bio-oil by water/organic solvent addition and pH adjustment*, Energy & Fuels, 30 (2016) 2164-2173.

[90] J. Xu, J. Jiang, W. Lv, W. Dai, Y. Sun, *Rice husk bio-oil upgrading by means of phase separation and the production of esters from the water phase, and novolac resins from the insoluble phase*, Biomass and Bioenergy, 34 (2010) 1059-1063.

[91] S. Zhang, Y. Yan, T. Li, Z. Ren, *Upgrading of liquid fuel from the pyrolysis of biomass*, Bioresource Technology, 96 (2005) 545-550.

[92] S. Wang, K. Goulas, E. Iglesia, *Condensation and esterification reactions of alkanals, alkanones, and alkanols on* TiO_2*: Elementary steps, site requirements, and synergistic effects of bifunctional strategies*, Journal of Catalysis, 340 (2016) 302-320.

[93] S. Wang, E. Iglesia, *Experimental and theoretical assessment of the mechanism and site requirements for ketonization of carboxylic acids on oxides,* Journal of Catalysis, 345 (2017) 183-206.

[94] A. Gangadharan, M. Shen, T. Sooknoi, D.E. Resasco, R.G. Mallinson, *Condensation reactions of propanal over* $Ce_xZr_{1-x}O_2$ *mixed oxide catalysts*, Applied Catalysis A: General, 385 (2010) 80-91.

[95] C.A. Gaertner, J.C. Serrano-Ruiz, D.J. Braden, J.A. Dumesic, *Catalytic coupling of carboxylic acids by ketonization as a processing step in biomass conversion*, Journal of Catalysis, 266 (2009) 71-78.

[96] J.N. Chheda, J.A. Dumesic, *An overview of dehydration, aldol-condensation and hydrogenation processes for production of liquid alkanes from biomass-derived carbohydrates*, Catalysis Today, 123 (2007) 59-70.

[97] L. Faba, E. Díaz, S. Ordóñez, *One-pot aldol condensation and hydrodeoxygenation of biomass-derived carbonyl compounds for biodiesel synthesis*, ChemSusChem, 7 (2014) 2816-2820.

[98] T.N. Pham, T. Sooknoi, S.P. Crossley, D.E. Resasco, Ketonization of carboxylic acids: *Mechanisms, catalysts, and implications for biomass conversion*, ACS Catalysis, 3 (2013) 2456-2473.

[99] A. Fernández-Arroyo, D. Delgado, M.E. Domine, J.M. López-Nieto, *Upgrading of oxygenated compounds present in aqueous biomass-derived feedstocks over* NbO_x*-based catalysts*, Catalysis Science & Technology, 7 (2017) 5495-5499.

[100] P. Anastas, N. Eghbali, *Green Chemistry: Principles and Practice*, Chemical Society Reviews, 39 (2010) 301-312.

[101] P.T. Anastas, J.C. Warner, *Green Chemistry: Theory and Practice*, Oxford University Press 1998.

[102] G. Centi, S. Perathoner, C*atalysis and sustainable (green) chemistry*, Catalysis Today, 77 (2003) 287-297.

[103] R.M. Contractor, D.I. Garnett, H.S. Horowitz, H.E. Bergna, G.S. Patience, J.T. Schwartz, G.M. Sisler, *A new commercial scale process for n-butane oxidation to maleic anhydride using a circulating fluidized bed reactor*, in: V.C. Corberán, S.V. Bellón (Eds.) Studies in Surface Science and Catalysis, Elsevier 1994, pp. 233-242.

[104] M. Malow, *Maleic anhydride via butane oxidation*, Environmental Progress, 4 (1985) 151-154.

[105] G. Centi, F. Trifiro, J.R. Ebner, V.M. Franchetti, *Mechanistic aspects of maleic anhydride synthesis from* C_4 *hydrocarbons over phosphorus vanadium oxide*, Chemical Reviews, 88 (1988) 55-80.

[106] J.M. López Nieto, B. Solsona, *Gas phase heterogeneous partial oxidation reactions*, in: J.C. Védrine (Ed.) *Metal Oxides in Heterogeneous Catalysis*, Elsevier 2018, pp. 211-286.

[107] G. Centi, *Vanadyl Pyrophosphate - A Critical Overview*, Catalysis Today, 16 (1993) 5-26.

[108] R. Schlögl, *Selective Oxidation: From a still immature technology to the roots of catalysis science*, Topics in Catalysis, 59 (2016) 1461-1476.

[109] F. Wöhler, *Ueber das Wolfram*, Annalen der Physik, 78 (1824) 345-358.

[110] A. Magnéli, B. Blomberg, *Contribution to the knowledge of the alkali tungsten bronzes*, Acta Chemica Scandinavica, 5 (1951) 372-378.

[111] A. Magnéli, *Studies on the hexagonal tungsten bronzes of potassium, rubidium, and cesium*, Acta Chemica Scandinavica, 7 (1953) 315-324.

[112] P. Hagenmuller, *Tungsten bronzes, vanadium bronzes and related compounds*, in: D.J.M. Bevan, P. Hagenmuller (Eds.) *Non-Stoichiometric Compounds*, Pergamon 1973, pp. 541-605.

[113] W. Ostertag, *Rare earth tungsten bronzes*, Inorganic Chemistry, 5 (1966) 758-760.

[114] W. Ostertag, C.V. Collins, *Electrical resistivity of cubic rare earth, thorium and uranium tungsten bronzes*, Materials Research Bulletin, 2 (1967) 217-221.

[115] L.E. Conroy, M.J. Sienko, *A copper analog of the alkali tungsten bronzes*, Journal of the American Chemical Society, 79 (1957) 4048-4051.

[116] M.J. Sienko, B.R. Mazumder, *Some solid state studies of silver-doped* WO_3, Journal of the American Chemical Society, 82 (1960) 3508-3510.

[117] A.B. Swanson, J.S. Anderson, *Indium tungsten bronze,* Materials Research Bulletin, 3 (1968) 149-152.

[118] D. Vandeven, J. Galy, M. Pouchard, P. Hagenmuller, *Evolution structurale en fonction de la temperature de quelques bronzes oxygenes de tungstene pauvres en element d'insertion*, Materials Research Bulletin, 2 (1967) 809-817.

[119] M.J. Sienko, *Thallium-tungsten bronze: A solid state defect structure*, Journal of the American Chemical Society, 81 (1959) 5556-5559.

[120] I.M. Szilágyi, J. Madarász, G. Pokol, P. Király, G. Tárkányi, S. Saukko, J. Mizsei, A.L. Tóth, A. Szabó, K. Varga-Josepovits, *Stability and controlled composition of hexagonal* WO_3, Chemistry of Materials, 20 (2008) 4116-4125.

[121] F. Galasso, L. Katz, R. Ward, *Tantalum analogs of the tetragonal tungsten bronzes*, Journal of the American Chemical Society, 81 (1959) 5898-5899.

[122] P.R. Slater, J.T.S. Irvine, *Niobium based tetragonal tungsten bronzes as potential anodes for solid oxide fuel cells: synthesis and electrical characterisation*, Solid State Ionics, 120 (1999) 125-134.

[123] J.S. Anderson, *Reactions in crystallographic shear structures*, in: M.S. Whittingham, A.J. Jacobson (Eds.) *Intercalation Chemistry*, Academic Press 1982, pp. 503-538.

[124] P.G. Dickens, M.F. Pye, *Oxide insertion compounds*, in: M.S. Whittingham, A.J. Jacobson (Eds.) *Intercalation Chemistry*, Academic Press 1982, pp. 539-561.

[125] J.S. Anderson, B.G. Hyde, *On the possible role of dislocations in generating ordered and disordered shear structures*, Journal of Physics and Chemistry of Solids, 28 (1967) 1393-1408.

[126] A. Magneli, *Non-stoichiometry and structural disorder in some families of inorganic compounds,* Pure and Applied Chemistry, 1978, pp. 1261.

[127] D.J.M. Bevan, *Non-stoichiometric compounds: an introductory essay*, in: D.J.M. Bevan, P. Hagenmuller (Eds.) *Non-Stoichiometric Compounds*, Pergamon 1973, pp. 453-540.

[128] B.G. Hyde, M. O'Keeffe, *Relations between the DO9(ReO3) structure type and some `bronze' and `tunnel' structures*, Acta Crystallographica Section A, 29 (1973) 243-248.

[129] L.A. Bursill, B.G. Hyde, *Rotation faults in crystals*, Nature Physical Science, 240 (1972) 122.

[130] M. Greenblatt, *Monophosphate tungsten bronzes. A new family of low-dimensional, charge-density-wave oxides*, Accounts of Chemical Research, 29 (1996) 219-228.

[131] A.F. Arif, R. Balgis, T. Ogi, F. Iskandar, A. Kinoshita, K. Nakamura, K. Okuyama, *Highly conductive nano-sized Magnéli phases titanium oxide* (TiO_x)*,* Scientific Reports, 7 (2017) 3646.

[132] M. Greenblatt, *Molybdenum and tungsten bronzes*, in: C. Schlenker, J. Dumas, M. Greenblatt, S. van Smaalen (Eds.) *Physics and Chemistry of Low-Dimensional Inorganic Conductors*, Springer US, Boston, MA, 1996, pp. 15-43.

[133] Y. Lee, T. Lee, W. Jang, A. Soon, *Unraveling the intercalation chemistry of hexagonal tungsten bronze and its optical responses*, Chemistry of Materials, 28 (2016) 4528-4535.

[134] O. Merdrignac-Conanec, P.T. Moseley, *Gas sensing properties of the mixed molybdenum tungsten oxide*, $W_{0.9}Mo_{0.1}O_3$, Journal of Materials Chemistry, 12 (2002) 1779-1781.

[135] M.S. Whittingham, *Hydrothermal synthesis of transition metal oxides under mild conditions*, Current Opinion in Solid State and Materials Science, 1 (1996) 227-232.

[136] H. Tsuji, Y. Koyasu, *Synthesis of* $MoVNbTe(Sb)O_x$ *composite oxide catalysts via reduction of polyoxometalates in an aqueous medium*, Journal of the American Chemical Society, 124 (2002) 5608-5609.

[137] M. Sadakane, K. Yamagata, K. Kodato, K. Endo, K. Toriumi, Y. Ozawa, T. Ozeki, T. Nagai, Y. Matsui, N. Sakaguchi, W.D. Pyrz, D.J. Buttrey, D.A. Blom, T. Vogt, W. Ueda, *Synthesis of orthorhombic Mo-V-Sb oxide species by assembly of pentagonal* Mo_6O_{21} *polyoxometalate building blocks*, Angewandte Chemie International Edition, 48 (2009) 3782-3786.

[138] R. Canioni, C. Marchal-Roch, N. Leclerc-Laronze, M. Haouas, F. Taulèlle, J. Marrot, S. Paul, C. Lamonier, J.-F. Paul, S. Loridant, J.-M.M. Millet, E. Cadot, *Selective conversion of* $\{Mo_{132}\}$ *Keplerate ion into 4-electron reduced crown-capped Keggin derivative* $[Te_5Mo_{15}O_{57}]^{8-}$. *A key intermediate to single-phase M1 multielement MoVTeO light-alkanes oxidation catalyst*, Chemical Communications, 47 (2011) 6413-6415.

[139] M. Sadakane, K. Endo, K. Kodato, S. Ishikawa, T. Murayama, W. Ueda, *Assembly of a pentagonal polyoxomolybdate building block,* $[Mo_6O_{21}]^{6-}$, *into crystalline MoV oxides*, European Journal of Inorganic Chemistry, 2013 (2012) 1731-1736.

[140] H. Tsuji, K. Oshima, Y. Koyasu, *Synthesis of molybdenum and vanadium-based mixed oxide catalysts with metastable structure:*

Easy access to the MoVNbTe(Sb)O_x catalytically active structure using reductant and oxoacid, Chemistry of Materials, 15 (2003) 2112-2114.

[141] W.D. Pyrz, D.A. Blom, M. Sadakane, K. Kodato, W. Ueda, T. Vogt, D.J. Buttrey, *Atomic-level imaging of Mo-V-O complex oxide phase intergrowth, grain boundaries, and defects using HAADF-STEM*, Proceedings of the National Academy of Sciences, 107 (2010) 6152-6157.

[142] J.T. Grant, J.M. Venegas, W.P. McDermott, I. Hermans, *Aerobic oxidations of light alkanes over solid metal oxide catalysts*, Chemical Reviews, 118 (2018) 2769-2815.

[143] P. DeSanto, J. Buttrey Douglas, K. Grasselli Robert, G. Lugmair Claus, F. Volpe Anthony, H. Toby Brian, T. Vogt, *Structural aspects of the M1 and M2 phases in MoVNbTeO propane ammoxidation catalysts*, Zeitschrift für Kristallographie - Crystalline Materials, 2004, pp. 152.

[144] W.D. Pyrz, D.A. Blom, T. Vogt, D.J. Buttrey, *Direct imaging of the MoVTeNbO M1 phase using an aberration-corrected high-resolution scanning transmission electron microscope*, Angewandte Chemie International Edition, 47 (2008) 2788-2791.

[145] R.K. Grasselli, A.F. Volpe, *Catalytic consequences of a revised distribution of key elements at the active centers of the M1 phase of the MoVNbTeO_x System*, Topics in Catalysis, 57 (2014) 1124-1137.

[146] R.K. Grasselli, C.G. Lugmair, A.F. Volpe, *Towards an understanding of the reaction pathways in propane ammoxidation based on the distribution of elements at the active centers of the M1 phase of the MoV(Nb,Ta)TeO system*, Topics in Catalysis, 54 (2011) 595-604.

[147] R.K. Grasselli, *Site isolation and phase cooperation: Two important concepts in selective oxidation catalysis: A retrospective*, Catalysis Today, 238 (2014) 10-27.

[148] A.C. Sanfiz, T.W. Hansen, D. Teschner, P. Schnörch, F. Girgsdies, A. Trunschke, R. Schlögl, M.H. Looi, S.B.A. Hamid, *Dynamics of the MoVTeNb oxide M1 phase in propane oxidation,* The Journal of Physical Chemistry C, 114 (2010) 1912-1921.

[149] L. Annamalai, Y. Liu, S. Ezenwa, Y. Dang, S.L. Suib, P. Deshlahra, *Influence of tight confinement on selective oxidative dehydrogenation of ethane on MoVTeNb mixed oxides,* ACS Catalysis, 8 (2018) 7051-7067.

[150] M. Aouine, T. Epicier, J.-M.M. Millet, *In situ environmental STEM study of the MoVTe Oxide M1 phase catalysts for ethane oxidative dehydrogenation,* ACS Catalysis, 6 (2016) 4775-4781.

[151] M.D. Soriano, P. Concepción, J.M. López Nieto, F. Cavani, S. Guidetti, C. Trevisanut, *Tungsten-Vanadium mixed oxides for the oxidehydration of glycerol into acrylic acid,* Green Chemistry, 13 (2011) 2954-2962.

[152] A. Chieregato, F. Basile, P. Concepción, S. Guidetti, G. Liosi, M.D. Soriano, C. Trevisanut, F. Cavani, J.M. López Nieto, *Glycerol oxidehydration into acrolein and acrylic acid over W–V–Nb–O bronzes with hexagonal structure,* Catalysis Today, 197 (2012) 58-65.

[153] A. Chieregato, M.D. Soriano, F. Basile, G. Liosi, S. Zamora, P. Concepción, F. Cavani, J.M. López Nieto, *One-pot glycerol oxidehydration to acrylic acid on multifunctional catalysts: Focus on the influence of the reaction parameters in respect to the catalytic performance,* Applied Catalysis B: Environmental, 150-151 (2014) 37-46.

[154] A. Chieregato, M.D. Soriano, E. García-González, G. Puglia, F. Basile, P. Concepción, C. Bandinelli, J.M. López Nieto, F. Cavani, *Multielement crystalline and pseudocrystalline oxides as efficient catalysts for the direct transformation of glycerol into acrylic acid*, ChemSusChem, 8 (2014) 398-406.

[155] M.D. Soriano, E. García-González, P. Concepción, C.B. Rodella, J.M. López Nieto, *Self-organized transformation from hexagonal to orthorhombic bronze of Cs–Nb–W–O mixed oxides prepared hydrothermally*, Crystal Growth & Design, 17 (2017) 6320-6331.

[156] S. Paul, F. Dumeignil, B. Katryniok, M.M. Araque, T. Murayama, W. Ueda, Patent, WO2016203283A1, (2015).

[157] J.-F. Devaux, J.-L. Dubois, Patent, US9296676B2, (2011).

[158] Y. Magatani, K. Okumura, Patent, US20110112330A1, (2008).

[159] W. Ueda, Y. Magatani, K. Okumura, T. Kawaguchi, Patent, WO2012005348, (2012).

[160] E. Heracleous, A.A. Lemonidou, *Ni–Nb–O mixed oxides as highly active and selective catalysts for ethene production via ethane oxidative dehydrogenation. Part I: Characterization and catalytic performance*, Journal of Catalysis, 237 (2006) 162-174.

[161] E. Heracleous, A.A. Lemonidou, *Ni–Nb–O mixed oxides as highly active and selective catalysts for ethene production via ethane oxidative dehydrogenation. Part II: Mechanistic aspects and kinetic modeling*, Journal of Catalysis, 237 (2006) 175-189.

[162] B. Solsona, F. Ivars, A. Dejoz, P. Concepción, M.I. Vázquez, J.M. López Nieto, *Supported Ni–W–O Mixed oxides as selective catalysts for the oxidative dehydrogenation of ethane*, Topics in Catalysis, 52 (2009) 751-757.

[163] B. Solsona, J.M. López Nieto, P. Concepción, A. Dejoz, F. Ivars, M.I. Vázquez, *Oxidative dehydrogenation of ethane over Ni–W–O mixed metal oxide catalysts*, Journal of Catalysis, 280 (2011) 28-39.

[164] B. Solsona, P. Concepción, S. Hernández, B. Demicol, J.M. López Nieto, *Oxidative dehydrogenation of ethane over NiO–CeO_2 mixed oxides catalysts*, Catalysis Today, 180 (2012) 51-58.

[165] B. Solsona, J.M. López Nieto, S. Agouram, M.D. Soriano, A. Dejoz, M.I. Vázquez, P. Concepción, *Optimizing both catalyst*

preparation and catalytic behaviour for the oxidative dehydrogenation of ethane of Ni–Sn–O catalysts, Topics in Catalysis, 59 (2016) 1564-1572.

[166] B. Solsona, P. Concepción, B. Demicol, S. Hernández, J.J. Delgado, J.J. Calvino, J.M. López Nieto, *Selective oxidative dehydrogenation of ethane over* SnO_2*-promoted NiO catalysts*, Journal of Catalysis, 295 (2012) 104-114.

[167] Z. Skoufa, G. Xantri, E. Heracleous, A.A. Lemonidou, *A study of Ni–Al–O mixed oxides as catalysts for the oxidative conversion of ethane to ethylene*, Applied Catalysis A: General, 471 (2014) 107-117.

[168] B. Savova, S. Loridant, D. Filkova, J.M.M. Millet, *Ni–Nb–O catalysts for ethane oxidative dehydrogenation*, Applied Catalysis A: General, 390 (2010) 148-157.

[169] H. Zhu, D.C. Rosenfeld, M. Harb, D.H. Anjum, M.N. Hedhili, S. Ould-Chikh, J.-M. Basset, *Ni–M–O (M = Sn, Ti, W) Catalysts prepared by a dry mixing method for oxidative dehydrogenation of ethane*, ACS Catalysis, 6 (2016) 2852-2866.

[170] I. Popescu, E. Heracleous, Z. Skoufa, A. Lemonidou, I.-C. Marcu, *Study by electrical conductivity measurements of semiconductive and redox properties of M-doped NiO (M = Li, Mg, Al, Ga, Ti, Nb) catalysts for the oxidative dehydrogenation of ethane*, Physical Chemistry Chemical Physics, 16 (2014) 4962-4970.

[171] Z. Skoufa, E. Heracleous, A.A. Lemonidou, *On ethane ODH mechanism and nature of active sites over NiO-based catalysts via isotopic labeling and methanol sorption studies*, Journal of Catalysis, 322 (2015) 118-129.

[172] R. Sanchis, D. Delgado, S. Agouram, M.D. Soriano, M.I. Vázquez, E. Rodríguez-Castellón, B. Solsona, J.M. López Nieto, *NiO diluted in high surface area* TiO_2 *as an efficient catalyst for the oxidative*

dehydrogenation of ethane, Applied Catalysis A: General, 536 (2017) 18-26.

[173] P. Dubey, N. Kaurav, R.S. Devan, G.S. Okram, Y.K. Kuo, *The effect of stoichiometry on the structural, thermal and electronic properties of thermally decomposed nickel oxide*, RSC Advances, 8 (2018) 5882-5890.

[174] N.K. Kotsev, L.I. Ilieva, *Determination of non-stoichiometric oxygen in NiO by temperature-programmed reduction*, Catalysis Letters, 18 (1993) 173-176.

[175] B. Polteau, F. Tessier, F. Cheviré, L. Cario, F. Odobel, S. Jobic, *Synthesis of Ni-poor NiO nanoparticles for p-DSSC applications*, Solid State Sciences, 54 (2016) 37-42.

Chapter 2

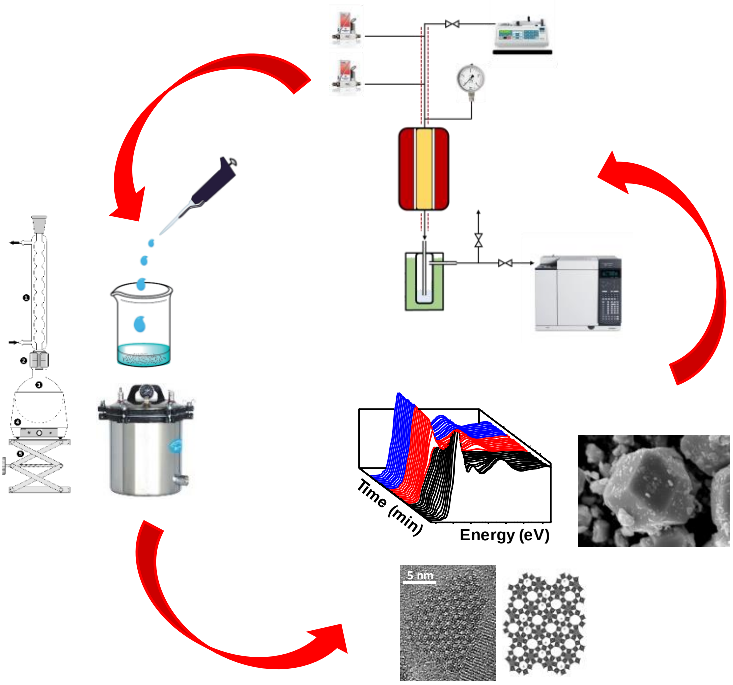
Time (min)
Energy (eV)
5 nm

Experimental procedure

2.1. Catalyst synthesis

The preparation of the catalysts reported in this doctoral thesis has been carried out by several synthetic approaches. In the case of W-based oxides, hydrothermal and reflux methods were mainly undertaken. On the other hand, regarding the preparation of NiO-based catalysts for the ODH of ethane, evaporation (for promoted NiO materials) and wet-impregnation (for supported-NiO catalysts) were the selected methods. The different synthetic procedures are commented in more detail below.

2.1.1. Materials

In the case of W-based catalysts, the following precursors were used in the synthesis: **ammonium metatungstate hydrate** (Sigma-Aldrich; ≥ 85 wt% WO_3 basis); **tungstic acid** (Sigma-Aldrich; 99 %), **vanadium (IV) oxide sulfate hydrate** (Sigma–Aldrich; ≥97%); **vanadyl acetylacetonate** (Sigma–Aldrich, 99.98%); **niobium oxalate** (ABCR); **ammonium chloride** (Sigma–Aldrich, 99.998%, Sigma–Aldrich); **ammonium sulfate** (Sigma–Aldrich, 99.0 %); **ammonium acetate** (Sigma–Aldrich, 98%); and **aqueous ammonia** (Panreac, 25 %).

In the case of Ni-based catalysts, the following precursors were considered: **Ni (II) nitrate hexahydrate** (Sigma-Aldrich, 99.999 % trace metal basis), **oxalic acid** (Sigma Aldrich); **lanthanum (III) oxalate** (Sigma Aldrich), **tin (II) oxalate** (Sigma-Aldrich) and **ammonium niobate (V) oxalate** (Sigma Aldrich).

2.1.2. Hydrothermal synthesis of W-Nb-O and W-V-O mixed oxides

The hydrothermal method refers to chemical reactions that take place in an aqueous media at relatively high temperature and pressures, at supercritical or near-supercritical conditions. It is highly extended in materials science, since it allows the synthesis of a high number of metastable phases that are not accessible under conventional preparation methods, like solid-state reactions. In addition, it allows the preparation of well-ordered crystalline phases with small particle size and high surface areas, what constitutes an interesting fact for catalytic applications. Indeed, hydrothermal conditions can substantially increase the solubility of metal precursors that, under ordinary conditions would be insoluble. This favors chemical transport and dissolution-recrystallization processes that otherwise would not be achieved [1].

In our case, the method consists in the preparation of an aqueous gel containing the selected transition metal salts (mono or bi-component mixtures) (**Figure 2.1 A**). The gel is transferred into a Teflon-lined stainless steel autoclave equipped with a set of valves to introduce a selected atmosphere if necessary (mainly air, or N_2 in the case that an inert atmosphere is required) (**Figure 2.1 B**). Then the autoclave is heated-up to the desired temperature during a selected time. When the reaction is completed, the autoclave is cooled down to room temperature and outgassed, and the resulting solid is filtered, washed with deionized water and dried overnight. Finally, the dried solid is activated at high temperature in air and/or N_2 flow. In this doctoral thesis, materials from the ternary systems $W_{1-x}V_xO_{3-\delta}$ (x = 0.2) and $W_{1-x}Nb_xO_{3-\delta}$ (x = [0-1]), have been synthesized by this hydrothermal method.

Considering $W_{1-x}V_xO_{3-\delta}$ (x = 0.2) system, oxides with a ReO_3-type (i.e. the monoclinic phase of tungsten trioxide, *m*-WO_3) and hexagonal tungsten bronze-type structures (HTB or *h*-WO_3) were obtained (**see Chapter 3**). By selecting the appropriate W- and V-containing precursors, mixtures with a different proportion of the abovementioned structural types have been prepared, what will have important catalytic implications. In a typical formulation, an aqueous solution containing a tungsten (ammonium metatungstate or tungstic acid), vanadium (vanadium (IV) oxide sulfate or vanadyl acetylacetonate) and/or an ammonium precursor (selected from ammonium chloride, ammonium sulfate; ammonium acetate; or aqueous ammonia) was kept at 80 ºC for 10 min under magnetic stirring.

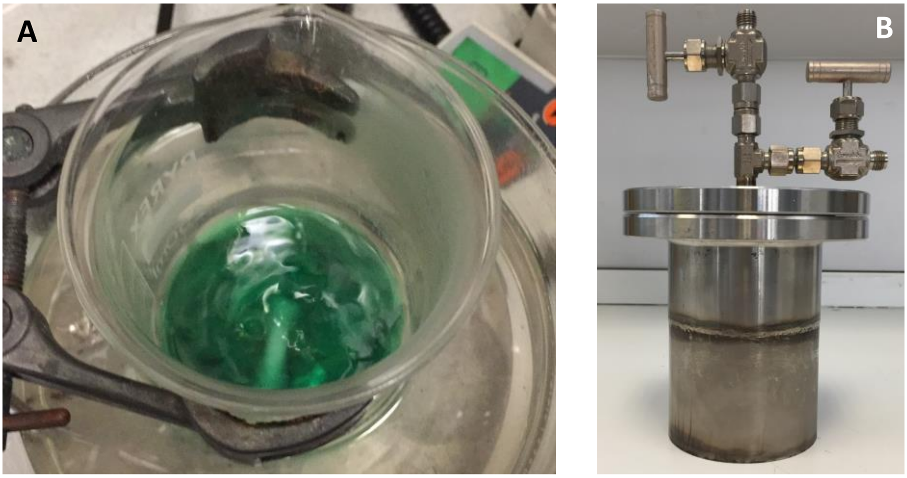

Figure 2.1. A) Synthesis gel of W-V-O oxide prepared by hydrothermal method. B) Stainless steel autoclave for selected atmosphere hydrothermal synthesis.

The synthesis mixture was introduced in a Teflon-lined stainless steel autoclave, which was purged with N_2 for 5 min (P_{N2} = 1 bar). Then, the autoclave was heat-treated at 175 ºC for 48 h, and the resulting solid was filtered, washed with deionized water, and then dried at 100 ºC for 16 h. Finally, the dried solid was firstly heat-treated at 200 ºC in static air for 2h, and further heat-treated 2h at 600 ºC in N_2 flow (15 mL min^{-1} g_{cat}^{-1}).

In the case of $W_{1-x}Nb_xO_{3-\delta}$ (x = 0 - 1) series, HTB´s and pseudocrystalline (i.e. ordered just along [001] crystallographic direction) oxides were mainly obtained by this hydrothermal method (see **Chapter 4**). In an analogous preparation procedure, a Niobium oxalate solution was heated-up to 80 ºC during 10 min. This solution was added dropwise to an ammonium metatungstate aqueous solution, and the mixture was kept 10 min at 80 ºC. Then the mixture was introduced in a Teflon-lined stainless steel autoclave, which was purged and filled with N_2 (P_{N2} = 1 bar); and then heat-treated at 175 ºC for 48 h. Finally, the autoclave was cooled down to room temperature, degassed, and the resulting solid was filtered, washed with deionized water and dried at 100 ºC for 16 h. The dried solids were then heat-treated 2h at 550 ºC under N_2 flow (15 mL min^{-1} g_{cat}^{-1}).

2.1.3. Reflux synthesis of W-Nb-O and W-V-O mixed oxides. Preparation of supported catalysts.

A reflux method for the synthesis of Nb- and V-containing tungsten bronzes (W-Nb-O and W-V-O) has been developed (see **Chapter 5**). In a general way, an aqueous solution containing stoichiometric amounts of the corresponding metal salts, i.e. ammonium metatungstate hydrate, niobium monooxalate adduct and vanadium (IV) oxide sulfate hydrate, was kept under reflux at 150 ºC for 48 h (**Figure 2.2**).

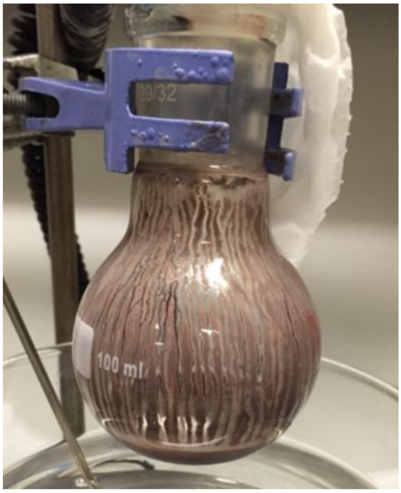

Figure 2.2. W-V-O oxide prepared by reflux synthesis.

In the case of W-Nb oxide, the gel formed was directly rotary evaporated at 60 ºC and subsequently heat-treated for 2h at 400 ºC in N_2 flow (15 mL min^{-1} g_{cat}^{-1}).

For W-V-O oxide, the gel was filtered and washed with deionized water in order to eliminate remaining vanadium species in solution. The resulting solid was then dried at 100 ºC overnight and subsequently heat-treated at 500 ºC for 2 h in N_2 (15 mL min^{-1} g_{cat}^{-1}).

In addition, this synthetic approach has allowed us to prepare supported tungsten bronze catalysts. The oxides were supported on KIT-6 mesoporous silica, which has been synthesized following the procedure reported by Ryoo *et al.* [2]. For supported W-Nb-O catalyst, KIT-6 support was directly added to the synthesis gel after reflux treatment, and kept 2 h under magnetic stirring at ambient temperature. Then the solvent was eliminated in a rotary evaporator and the solid was heat-treated at 400 ºC in N_2 flow (15 mL min^{-1} g_{cat}^{-1}). Regarding KIT-6-supported W-V-O catalyst, as-filtered and washed solid was suspended in 50 mL of deionized water under stirring. Then KIT-6 mesoporous silica was added, and the suspension was kept under magnetic stirring for 2 hours at 25 ºC.

Finally, the solvent was rotary evaporated, and the resulting solids were heat-treated at 500 ºC for 2h in N_2 flow (15 mL min^{-1} g_{cat}^{-1}).

2.1.4. Synthesis of promoted and supported NiO-based catalysts

Promoted and supported NiO-based catalysts have been synthesized by evaporation and wet impregnation methods respectively.

Unpromoted and Metal-promoted NiO oxides (Metal= La, Sn, Nb) were prepared by the evaporation (T= 60 ºC) of a solution of Ni (II) nitrate hexahydrate; oxalic acid; and the corresponding salts of the promoters: lanthanum (III) oxalate, tin (II) oxalate and ammonium niobate (V) oxalate. The oxalic acid/Ni molar ratio was remained constant to 3, whereas the amount of promoter added to the mixture was ca. 8 at. % (i.e. Ni (Ni/(Ni+Metal) molar ratio of 0.08), which is close to the optimal value reported to get the highest selectivity to ethylene in the ODH of ethane [3, 4]. The fresh materials were the dried overnight at 100 ºC and subsequently heat-treated 2h at 500 ºC under static air.

Supported NiO catalysts were prepared by the wet impregnation method, i.e. different supports were added to the abovementioned ethanolic Ni(II) nitrate/oxalic acid solution. The mixture was then evaporated at 60 ºC and the solids were dried at 120 ºC overnight. Finally, the solids were calcined at 500 ºC for 2 h in static air.

Some specific supports were used in the study: a commercial silica (SiO_2), a Porous Clay Heterostructure with SiO_2-TiO_2 pillars (PCH-Ti, which its synthesis is reported in ref. [5]), pure anatase TiO_2 (Sigma-Aldrich) and a high surface area TiO_2 (Degussa P25). The characteristics of these supports are included in **Table 2.1**.

Table 2.1. Characteristics of metal oxide supports.

Support	Commercial	Crystalline phase [a]	Surface area [b] ($m^2\ g^{-1}$)
SiO_2	Sigma-Aldrich	Amorphous	200
PCH-Ti	Home-made	Amorphous	562
TiO_2-ana	Sigma-Aldrich	Anatase	10
TiO_2	Degussa P25	Anatase, rutile	55

[a] Determined by X-ray diffraction. [b] Obtained by BET method from N_2 adsorption isotherms.

2.2. Catalyst characterization

The materials reported all along this work have been characterized by several physicochemical techniques. In this section we will briefly underline the main physical principles behind each method. For further insights in the physics related to these techniques, the reader is referred to the references cited along the section.

2.2.1. Powder X-Ray Diffraction

Powder X-Ray diffraction (XRD) analyses were carried out to identify the crystalline phases present in the catalysts, and also to estimate their average particle size. XRD experiments were carried out in a Panalytical X´pert PRO diffractometer equipped with an X´Celerator detector in a Bragg-Brentano geometry, and using Cu $K_{\alpha 1}$ radiation ($\lambda = 1.5406$ Å).

X-ray diffraction is a non-destructive method based on the elastic scattering of X-ray photons by atoms disposed in a periodic lattice [6, 7]. Diffraction can be considered as an interference phenomenon, in which a constructive interference occurs between the incident (i.e. transmitted) beam and the scattered beam. This is observed when the path difference between both waves is an integer of the wavelength of the radiation, i.e. when Bragg´s law is satisfied (Equation 2.1) (**Fig. 2.3**):

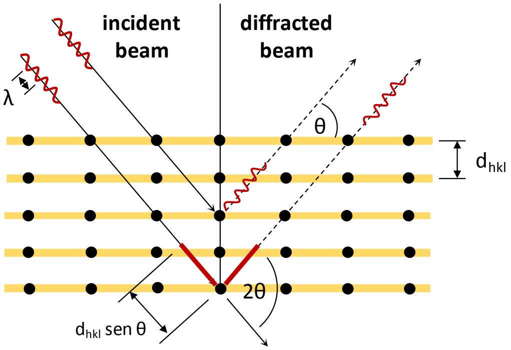

Figure 2.3. Graphical scheme of diffraction phenomena dictated by Bragg´s Law **:** ($n\,\lambda = 2d_{hkl}\,sen\,\theta$).

$$n\,\lambda = 2d_{hkl}\,sen\,\theta$$

Equation 2.1. Bragg´s Law.

where n is the integer, λ is the wavelength of the radiation, d_{hkl} is the interplanar distance of planes with *h*, *k* and *l* Miller indices, and θ is the diffraction angle. Any material will present its own diffraction pattern, which can be used to analyze their crystal structure and atom distribution all along the crystal lattice. In addition, not only structural information can be extracted, but also information about morphology and microstructure. In this sense, it is possible to determine the average particle size by analyzing the line broadening of diffraction peaks for a particular polycrystalline sample, by using Scherrer´s equation:

$$D = \frac{\lambda}{\beta\cos\theta}$$

Equation 2.2. Scherrer´s equation.

where D is the average size of the crystallites, λ is the wavelength of the radiation, θ is the diffraction angle of a specific diffraction line, and β is the line broadening at half maximum intensity after extracting the instrumental broadening.

2.2.2. Scanning electron microscopy (SEM)

SEM images were collected in a field-emission ZEISS Ultra-55 electron microscope at an accelerating voltage of 2 kV. The microscope was equipped with an Oxford LINK ISIS X-rays detector for energy-dispersive X-ray spectroscopy (XEDS) measurements. Counting time for XEDS spectra was 100 s.

Electron microscopy in general is a very versatile technique in which a primary beam of electron interacts with a sample, giving rise to a multitude of signals that can be analyze to extract a great amount of information (**Fig. 2.4**) [8, 9]. In particular, scanning electron microscopy (SEM) is performed by probing an electron beam all over a surface, detecting secondary or backscattered electrons. Images are formed by contrast, which has it origin in the orientation of the particles, i.e. surface zones that face directly the detector will appear brighter than zones pointing away from the detector. Regarding imaging, secondary electrons give better results, since they are mainly originated from the surface of the samples, while backscattered electrons come from deeper in the sample, giving visual information about the composition. In this sense heavier elements will look brighter in the images than lighter ones, when dealing with backscattered electrons.

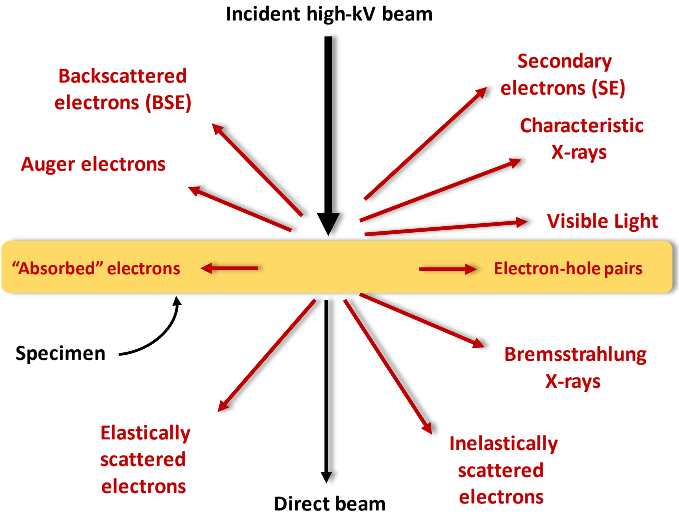
Incident high-kV beam
Backscattered electrons (BSE)
Secondary electrons (SE)
Characteristic X-rays
Auger electrons
Visible Light
"Absorbed" electrons
Electron-hole pairs
Specimen
Bremsstrahlung X-rays
Elastically scattered electrons
Inelastically scattered electrons
Direct beam

Figure 2.4. Types of signals generated when an electron beam interacts with a specimen (adapted from ref. [9]).

2.2.3. Transmission electron microscopy (TEM)

Transmission electron microscopy (TEM) images were obtained in different high-resolution electron microscopes. Images of catalysts $W_{1-x}Nb_{1-x}O_3$ series (see **Chapter 4**) were obtained in a JEOL JEM300F electron microscope operating at 300 kV, with a point resolution of 0.17 nm. The microscope was equipped with an X-ray microanalysis system (ISIS 300, Oxford Instruments, with a LINK "Pentafet" detector) to perform crystal by crystal compositional analysis by energy-dispersive X-ray spectroscopy (XEDS). Analysis by selected area electron diffraction (SAED) on $W_{1-x}Nb_{1-x}O_3$ were also performed in this microscope.

The rest of TEM images presented in this doctoral thesis were collected in a JEOL JEM-2100F microscope working at an accelerating voltage of 200 kV, which was equipped with a high-angle annular dark-field (HAADF) detector, and a X-Max 80 detector (Oxford Instruments) for XEDS analysis. STEM images in both bright and dark-field modes were also collected. The samples were ultrasonically dispersed in n-butanol and subsequently deposited on a polymer coated copper grid, which was placed into the sample holder.

When a high energy electron beam goes through a thin sample, a great part of those electrons are transmitted and dispersed by the material [8, 9]. A transmission electron microscope (TEM) uses diffracted and transmitted electrons to form an image, which can be focalized in a charge-couple device (CCD) screen or a fluorescent film. Its operation can be compared with an optical microscope that makes use of electrons instead of visible light as light source, what implies a higher resolution due to the lower wavelength of electrons. However, it is not able to reach the maximum resolution that theory predicts, as in the case of optical microscopes, since TEM uses magnetic lenses to guide electrons. Aberrations that this type of magnetic lenses produce make the use of aberration-corrected microscopes mandatory to achieve atomic resolution (less than 1 Å). It is also possible to perform selected area electron diffraction experiments (SAED). Electrons, considered as waves, can interact with a crystalline material as if it were a diffraction grating, thus diffracting, and generating a diffraction pattern (in the reciprocal space) of the selected crystallographic orientation. The pattern is composed by spots that represent a family of planes in the crystal structure. By analyzing angles, distribution and distances in the reciprocal space it is possible to extract a lot of structural information about the space group, lattice parameters or presence of defects.

Scanning-transmission mode (STEM) allows the illumination of higher areas of the sample (by rastering electron beam along the sample), what is optimal for Z-contrast analysis (high angle annular dark field mode, HAADF) and XEDS compositional mapping. In HAADF mode, the image is formed by scattered electrons at high angles, that are larger than those where Bragg diffraction takes place. This way the image contrast is directly related to the weight of the elements in the sample, thus generating a brighter contrast for heavier elements. Scanning-transmission mode is the best configuration to elucidate the phase distribution in the catalysts.

2.2.4. Energy-Dispersive X-ray spectroscopy (XEDS)

As stated above, all the microscopes used during this doctoral thesis had X-ray detectors attached to perform XEDS measurements. This technique has been applied to determine catalyst compositions, either the average (by performing 10-20 analyses at low magnification), or crystal by crystal composition (by performing point by point analyses on selected crystals at high magnification). In addition, some XEDS maps has been carried out to elucidate the phase distribution of specific catalysts.

XEDS microanalysis exploits the information that derives from the inelastic interaction of electrons with matter, in which energy exchange takes place [9]. This way, the electron beam interacts with core-level electrons, and transfers a specific amount of energy, which promotes a core-electron to an unoccupied state over the Fermi-level (i.e. the atom is in an excited state). The atom can decay back to the ground state by transferring an electron from the outer shell to the hole that the promoted electron left.

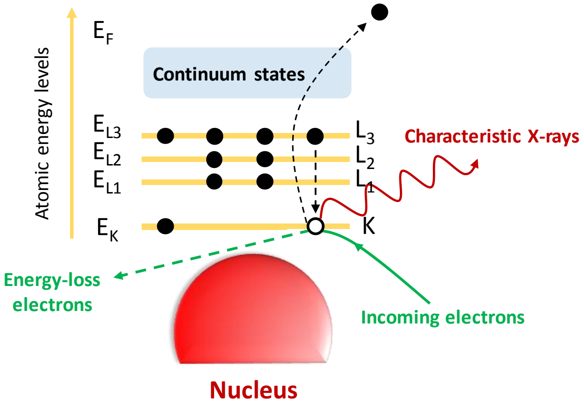

Figure 2.5. Ionization process which leads to K_α X-ray emission (adapted from ref. [9]).

This phenomenon can be accompanied by the emission of either X-rays (**Fig. 2.5**) or Auger electrons, that can be detected. Since the energy of those emitted X-rays are element-specific, we can use them to detect and quantify the concentration of metal species in the catalysts.

2.2.5. X-ray photoelectron spectroscopy (XPS)

X-ray photoelectron spectroscopy (XPS) measurements were performed to study the chemical nature of the surface of the catalysts. XPS analyses were carried out in a SPECS spectrometer which was equipped with a Phoibos 150 MCD-9 detector. In general, the measurements were carried out using a non-monochromatic Al K_α (1486.6 eV) X-ray source. However, in the case of V-containing samples, a monochromatic Al K_α X-ray source was used, in order to avoid the overlapping with O1*s* satellite peak. Spectra were recorded at high-vacuum (10^{-9} mbar) at an analyzer pass energy of 50 eV and an X-ray power of 200 W. Data-treatment was performed with CasaXPS software, referencing the binding energy (BE) values of all the acquired spectra to C1*s* (284.5 eV).

X-ray photoelectron spectroscopy (XPS) is based on photoelectric effect, i.e. a sample irradiated with X-rays emits photoelectrons [6, 8, 10, 11]. It has attracted wide interest in catalysis science due to its high selectivity to the analysis of the top few layers of materials. The method consists in the irradiation a sample with X-rays (generally Al K_α, 1486.6 eV; or Mg K_α radiation, 1253.6 eV), which promote core-level electrons over the Fermi level (E_F). The energy necessary to promote an electron from an inner orbital to E_F is called binding energy (E_b), which is characteristic of each element in the periodic table. It is possible to calculate this Eb by monitoring the kinetic energy of the emitted photoelectrons according to the equation:

$$E_b = h\nu - E_k - \phi$$

Equation 2.3. Binding energy (E_b).

where E_b is the binding energy of emitted electrons, $h\nu$ is the energy of incident X-ray photons, E_k is the kinetic energy of emitted photoelectrons, and ϕ is the work function of the instrument.

Photoelectron peaks are named considering the specific orbital from which the electron is ejected. This way, an electron presenting an orbital angular momentum l (0, 1, 2, 3… for *s, p, d, f* … orbitals respectively) and a spin angular momentum s will present a total momentum j = l + s. For orbital momentum l ≥ 0 there exists multiplicity of states (j = l + s, for s values $\pm\frac{1}{2}$), what gives rise to doublets in XPS spectra of *p*, *d* and *f* core-levels. For example, XPS spectrum of W 4*f* core-level spectrum will show a doublet corresponding to W $4f_{7/2}$ and W$4f_{5/2}$. Both peaks present the same full half width at half maximum (FWHM) and shape, but different area, due to degeneracy of final states (2j+1; ($A_{f5/2}/A_{f7/2}$) = 0.75). The binding energies and doublet separations are well reported in bibliography and collected in several databases like the National Institute of Standards and Technology (NIST) [12] or La Surface [13].

An XPS spectrum can be interpreted in terms of initial and final state effects. Initial state effects comprise mainly the charge on the atom subject of study, in which electron binding energies can substantially vary due to: i) oxidation state of the element, or ii) chemical environment. Thus, the metal species in a different chemical environment will give rise to different chemical shifts. In general, higher oxidation states display higher binding energy values, i.e. the electrons are more attracted by the nucleus. In the same way, bonded electron attractor species will promote shifts to higher binding energies, while electron donors will follow the opposite trend, shifting the signals to lower binding energies. However, the most intricate part of XPS is related with the interpretation of final state effects, which occur after photoemission process, and are factors that affect the atom once the core-electron has left, or that affect the photoelectron while leaving the atom. These effects comprise relaxation processes, hole screening, shake-up or shake-off processes, etc. In addition, important differential charging effects are observed when working with insulators or semiconductors, due to inhomogeneities in the electrical conductivity along the sample. This charge can be partially or totally neutralized by using a low energy electron flood-gun on the sample, but this can lead to misinterpretations when dealing with species that are susceptible to reduction. Internal charging corrections are also performed, taking generally the C1*s* signal as reference.

2.2.6. X-Ray Absorption Spectroscopy (XAS)

X-ray Absorption Spectroscopy (XAS) experiments on NiO-based catalysts (Ni K-edge) were carried out at CLAESS beamline in ALBA synchrotron light-source (Barcelona, Spain), and at Spanish Line (BM25-Spline) at the European Synchrotron Research Facility (ESRF, Grenoble, France). All the measurements were performed in transmission mode, using in-house cells which allow to work under selected atmosphere and temperature (up to 700 ºC) (**Fig. 2.6**).

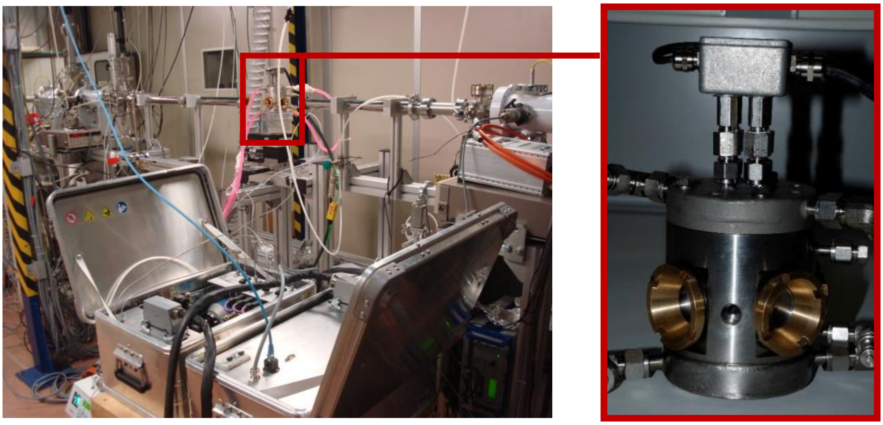

Figure 2.6. In-house cell for *in situ* XAS experiments developed at ITQ

Gas flow controllers were used to introduce gases into the cell. Samples were diluted with boron nitride and pressed into pellets, which were placed into the cell. The optimum mass amount of sample was weighted, in order to maximize the signal to noise ratio ($\mathrm{Ln}(I_0/I_1) \approx 1$). *In situ* time-resolved XANES spectra were collected in the 8100-8490 eV range (3 min/spectrum), meanwhile spectra for EXAFS analysis were collected in the 8100-9175 eV range. All the data were normalized using the software Athena, which was also used for linear combination fitting (LCF) calculations. Metallic Ni and fresh catalysts were used as references for LCF. EXAFS fitting was performed with the software Artemis. Additional measurements in the W L_{III}-edge (10150-10300 eV) were also conducted on Nb-doped and undoped hexagonal tungsten oxide at ALBA synchrotron (Barcelona, Spain).

X-ray absorption spectroscopy (XAS) deals with the study of the oscillations that appear on the high energy zone after the X-ray absorption edge of elements in liquids or solids [6, 14, 15]. Generally, these oscillations are extended from the core-level absorption edge itself up to 1000 eV over the edge, and they can reach ca. 10 % of the total absorption. The origin of those oscillations is the constructive-destructive interference phenomena that occur between the primary electron wave and the backscattered waves generated on the next neighbors of the absorbing atom. Hence, the hypothetical XAS spectrum of an isolated atom, would not present those oscillations. Two main zones in the XAS spectra are typically considered: i) XANES region (X-ray Absorption Near-Edge Structure), which includes the “pre-edge” zone, to approximately 50 eV over the absorption edge; and ii) EXAFS region (Extended X-ray Absorption Fine Structure), from 50 eV over the edge up to 1000 eV over it (**Fig. 2.7**). XANES region gives information about electronic properties and local geometry of the absorbing atoms (oxidation state, coordination geometry, etc.), while EXAFS zone contains information from its short-range chemical environment (for example, number of neighbors on each coordination shell).

In a typical XAS experiment measured in transmission mode, transmitted intensity $I(E)$ is related with original X-ray beam intensity $I_0(E)$ by Lambert-Beer´s law (Equation 2.4):

$$I(E) = I_0 e^{-\mu(E)x}$$

Equation 2.4. Lambert-Beer´s law.

where $\mu(E)$ is the cross-section of the absorbing atom as a function of energy, and x is the sample thickness. The graphical representation of a XAS spectrum is usually performed by plotting this cross-section as a function of energy, using the following expression derived from Lambert-Beer´s law (Equation 2.5):

$$\mu(E)x = Ln\left(\frac{I_0}{I_t}\right)$$

Equation 2.5. Expression for the cross-section of the absorbing atom.

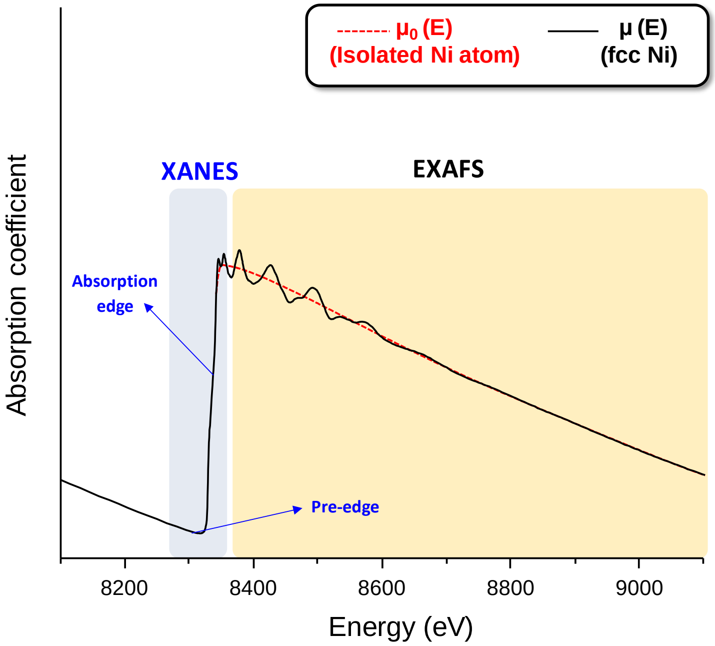

Figure 2.7. XAS spectrum of fcc metallic Ni with main regions marked. Red-dotted line represents the hypothetical absorption of an isolated Ni atom $\mu_0(E)$.

XANES region shape gives information about unoccupied states near Fermi level of the absorbing atom. For example, when measuring in the L_{III}-edge (i.e. a 2*p* orbital), the intensity of the absorption edge is proportional to the number of unoccupied *d* states near Fermi level, i.e. the oxidation state of the absorbing atom. In addition, over the absorption edge, it is possible to obtain information about local symmetry or bond angles. However, a mathematical interpretation of XANES region is quite difficult, since multi-scattering phenomena of low-energy photoelectrons are predominant in this zone. Thus, a qualitative interpretation of the spectra is usually performed. Nevertheless, it is possible to carry out a semi-quantitative interpretation by performing linear combination fitting using reference spectra, which can be very useful when dealing with *in situ* measurements, tracking the reduction degree and specific oxidation states.

At approximately 50 eV over the edge, the oscillations start to be dominated by single-scattering effects, what makes it possible to extract information about the chemical environment of the absorbing atom. This region is what we call EXAFS. These oscillations can be mathematically interpreted. In fact, EXAFS analysis is based on the mathematical treatment of the oscillations of the absorption coefficient $\mu(E)$. If we consider $\mu_0(E)$ as the hypothetical absorption coefficient of an isolated atom (see **Fig. 2.5**), $\mu(E)$ can be expressed as the variation of $\mu_0(E)$ due to a perturbation $\chi(E)$ promoted by backscattering phenomena (Equation 2.6):

$$\mu(E) = \mu_0[1 + \chi(E)]$$

Equation 2.6. Absorption coefficient of the absorbing atom expressed as a perturbation $\chi(E)$ on the hypothetical absorption of an isolated atom.

Consequently, the oscillations of the absorption coefficient can be expressed in the following way (Equation 2.7):

$$\chi(E) = \frac{\mu(E) - \mu_0(E)}{\mu_0(E)}$$

Equation 2.7. Mathematical expression for oscillations in the absorption coefficient

which is then expressed as a function of the photoelectron wavenumber *k* (Equation 2.8):

$$k = \sqrt{\frac{2m(E - E_0)}{h^2}}$$

Equation 2.8. Photoelectron wavenumber.

where E_0 the energy of the absorption edge, *m* is the mass of the electron and *h* is Planck´s constant. Hence, considering that $\chi(k)$ oscillations arise from short-range single scattering processes, they can be modeled by using the so called EXAFS equation (Equation 2.9):

$$\chi(k) = \sum_j \frac{N_j\, f_j\,(k)\, S_j(k)\ e^{-2R_j\,/\,\mu_j\,(k)}\ e^{-2k^2\sigma_j^2}}{k\, R_j^2}\ sen\left[2kR_j + \delta_j(k)\right]$$

Equation 2.9. EXAFS equation.

where *j* refers to the jth coordination shell; N_j represents the coordination number of the jth coordination shell; $f_j(k)$ is the scattering amplitude of the neighboring atom; S_j is the reduction factor of the scattering amplitude; δj (k) is the phase shift function; R_j is the distance to the absorbing atom; $e^{-2k^2\sigma_j^2}$ reflects the atomic disorder, where σ^2 is the Debye-Waller factor; and $e^{-2R_j\,/\,\mu_j\,(k)}$ accounts for inelastic energy losses in the scattering process, where $\mu_j(k)$ is the mean free path of the photoelectron. Hence, from $\chi(k)$ function obtained experimentally, it is possible to determine R_j, N_j and σ^2 from EXAFS equation, by estimating $f_j(k)$, $S_j\,(k)$, $\delta_j\,(k)$ and $\mu_j(k)$.

The achievement of the experimental $\chi(k)$ function (see Equation 2.7) makes the estimation of $\mu_0(k)$ mandatory (i.e. the hypothetical absorption of an isolated atom). As this value cannot be obtained experimentally, it is simulated by using a set of low-order polynomials, which are adjusted to the spectrum by least squares method (see **Fig. 2.5**).

Finally, to simplify the analysis of $\chi(k)$ function, we can consider it as the overlapping of sinusoidal functions corresponding to each type of atom in a different coordination shell. This way it is possible to obtain a pseudo radial distribution function $\gamma_n(r)$ (Equation 2.10) by performing a Fourier Transform in the EXAFS region k-range:

$$\gamma n\,(r) = \frac{1}{2\pi}\int_{k_{min}}^{k_{max}} \chi(k)\, k^n e^{2ikr} dk$$

Equation 2.10. Fourier Transform of $\chi(k)$

where k^n term (with n = 1, 2 or 3) is introduced to increase the integral weight at high k values (mainly due to amplitude attenuation). By introducing different n values in the Fourier transform it is possible to distinguish between heavy or light atoms, since the amplitude of the oscillations of atoms with higher Z will increase more drastically as n increases.

Once EXAFS region has been isolated (what includes background subtraction, identification of the absorption edge E_0, the normalization of the absorption step to a value of 1 and the estimation of the hypothetical $\mu_0(E)$ of the isolated atom) it is possible to estimate the coordination number of the absorbing atom on each shell, the corresponding atomic distances, the edge energy and Debye-Waller factor using the software Artemis.

2.2.7. Fourier-transform infrared spectroscopy (FTIR)

FTIR spectroscopy was applied to study the characteristic vibrational modes of specific metal-oxygen species and other specific groups (like -OH and NH_4^+) in the materials. FTIR spectra were collected at room temperature in transmission mode, in the 400-4000 cm^{-1} frequency range with a Nicolet 205xB spectrophotometer at a spectral resolution of 1 cm^{-1}

(128 accumulations/spectrum). Samples were previously diluted with KBr before the measurement.

FTIR spectroscopy is based on the absorption of photons by molecules, which occurs in transitions between vibrational or rotational levels in which the dipolar moment varies. The intensity of a FTIR band is directly related to the change in the dipolar moment of the molecule. This explain why CO, NO, or OH groups display strong infrared bands, and symmetric molecules like H_2 or N_2 does not show any band in the infrared spectrum. In this thesis the use of FTIR has been limited to the study of FTIR regions: 4000-3000 cm^{-1} (O-H and N-H stretching vibrations), 1700-1300 cm^{-1} (O-H and N-H bending vibrations) and 1200-400 cm^{-1} (M=O, M-O-M modes, and vibrations related to supports). In addition, some FTIR experiments with probe molecules were performed, mainly FTIR of adsorbed pyridine and carbon monoxide (see parts **2.2.11** and **2.2.12** in Experimental section) [8].

2.2.8. Raman spectroscopy

Raman spectroscopy was used to study the characteristic vibrational modes of metal-oxygen species in metal oxides (mainly M=O and M-O-M). Spectra were recorded in a Renishaw inVia spectrometer equipped with an Olympus microscope and a Renishaw HPNIR laser. Exciting wavelength used was 514 nm, which corresponds to the green zone of the electromagnetic spectrum, with a power on the samples of approximately 15 mW.

Raman spectroscopy is based on the analysis of the inelastic radiation scattered by molecules or solids. In contrast to FTIR spectroscopy, in which the samples absorb photons with the same energy of a specific vibrational mode, the mechanism in this case is different. In Raman spectroscopy, the sample is irradiated with a monochromatic radiation in the visible light range (514 nm in our case). Most of the photons will undergo elastic scattering, i.e., the molecules or metal oxide species will be vibrationally excited over their ground state, and will decay back to the ground state, with no energy exchange occurring (this is known as Rayleigh scattering). However, when the excited species decay to the first vibrational level (i.e. decay into an excited state), there is an effective energy transfer, in which the photon loses an amount of energy equal to the one of that excited level, leaving the sample with a lower energy, and giving rise to the "Stokes band". There exists also the "anti-Stokes band", in which the photon leaves the sample with a higher energy, as a result of the interaction with a vibrationally excited molecule, which is in addition excited to an unstable energy level. The decay to the ground state gives rise to this energy gain. Nevertheless, anti-Stokes band has much lower intensity than Stokes band, since the number of excited species is very low. By using a monochromator, the Rayleigh scattering component is filtered out, and just the inelastic scattered radiation is collected.

Not all the vibrational modes can be observed, only modes in which there exists a change in the polarizability of the molecule are detected by Raman, i.e. vibrations in which the molecules change their shape. This makes this technique complementary to infrared spectroscopy (specially for highly symmetric molecules, that do not show any signals in the infrared). However, Raman in much less sensible technique than FTIR, due to the high intensity of Rayleigh scattering component with respect to inelastically scattered photons, but also due to the presence of fluorescence phenomena, that increase the contribution of background, and makes it difficult to distinguish weak signals. Nevertheless, Raman spectra usually show a lower number of bands than FTIR, leading to less complicated spectra, what it makes their interpretation easier [19].

2.2.9. N_2-physisorption

Textural properties of synthesized catalysts were elucidated by means of N_2-physisorption. N_2-adsorption isotherms were collected in a Micromeritics ASAP 2000 instrument. About 200 mg of sample were outgassed under vacuum at 250ºC prior to adsorption. The experiments were carried out in the relative pressure (p/p_0) 0-1 range at 77 K.

Surface areas of all the samples were calculated by Brunauer-Emmet-Teller (BET) method. First, adsorption isotherm is transformed into the BET plot (Equation 2.12):

$$\frac{1}{n[\left(\frac{p}{p_0}\right)-1]}=\frac{1}{n_m C}+\frac{p}{p_0}\frac{C-1}{n_m C}$$

Equation 2.12. BET equation

where n is the amount of adsorbate, n_m is the monolayer capacity, p/p_0 is the relative pressure and C is a constant that accounts for adsorbate-adsorbent interactions. Then, we can obtain the monolayer capacity n_m (moles of adsorbate in the monolayer) by a simple linear regression calculation in the range of relative pressures p/p_0 = 0.05-0.25. Finally, the surface area of catalysts was calculated using Equation 2.13:

$$S_{BET}=n_m\, N_A\, \sigma$$

Equation 2.13

where n_m are the moles of N_2 in the monolayer, N_A is the Avogadro constant and σ is the cross-sectional area of the adsorbate (0.162 nm^2 for nitrogen molecule).

Mesopore volumes and pore size distributions were estimated by Barrett-Joyner-Halenda (BJH) method, which is based on Kelvin equation [16]. Broadly speaking, BJH method is the first derivative of the cumulative adsorbed volume. The procedure consists in the calculation of pore radius (r) derived from Kelvin equation, and the representation of dV/dr as a function of r (or pore diameter), i.e. the slope of the variation of adsorbed volume for each calculated pore size. This gives an estimation of the pore size distribution, and accumulative volumes in a selected pore size. For instance, cumulative volumes in the mesopore size region gives the mesopore volume. In this thesis BJH method has been applied to adsorption branch of the isotherms, in order to avoid the artifacts derived from the tensile strength effect observed in the desorption branch, which produces a fast release of N_2 (i.e. forced closure of the isotherm) and gives a false narrow pore size distribution centered at ca. 3.8 nm. [17].

2.2.10. Pulse chemisorption and temperature programmed desorption of ammonia (TPD-NH_3)

Pulse chemisorption and subsequent TPD-NH_3 were applied to study the acid properties of the materials. Experiments were conducted in a Micromeritics TPD/2900 instrument. The catalysts (0.2 g) were pretreated at 350 °C under argon stream for 1h. Then NH_3 was chemisorbed by pulses at 100 °C until equilibrium was achieved. Prior to increase the temperature, the sample was kept under helium stream at 100 °C for 15 min in order to eliminate physisorbed ammonia. Finally, temperature was increased up to 500 °C at a heating rate of 10 °C min^{-1}. Desorbed NH_3 was monitored by using mass spectrometry and a thermal conductivity detector (TCD).

TPD-NH_3 is a wide extended technique to study the acid characteristics of catalysts. It allows the quantification of surface acid sites by measuring the amount of chemisorbed ammonia (i.e. mol_{NH3} g^{-1}). In fact, ammonia is a hard base that can interact with Lewis acid sites (via electron lone pairs on nitrogen atom) and with Brönsted acid sites (by accepting a surface proton). In addition, it is possible to assess the relative strength of those surface acid sites by monitoring NH_3 desorption. In this respect, ammonia will be desorbed at higher temperatures as the acid strength of the site to which it is chemisorbed increases, i.e. the higher the strength of the acid site, the higher the stability of NH_3 in the chemisorbed state. Although it is a very useful technique, it is quite time-consuming and it does not allow to distinguish between Lewis and Brönsted-type acid sites. To be able to differentiate between both types of sites, spectroscopic techniques with probe molecules are needed.

2.2.11. Fourier-transform infrared (FTIR) spectroscopy of adsorbed pyridine

FTIR spectroscopy using pyridine as probe molecule was used to quantify the number of Lewis and Brönsted acid sites on the catalysts. The experiments were carried out in a Nicolet 710 spectrophotometer, where self-supported pellets (ca. 10 mg) were outgassed under vacuum (10^{-2} Pa) at 200 ºC for 12 h. Pyridine was then introduced into the cell ($6.5\ 10^{2}$ Pa) and, when equilibrium was achieved, the cell was degassed at 150 ºC and cooled down to room temperature. At this point, FTIR spectra of adsorbed pyridine were recorded. In all cases, a spectrum collected in vacuum prior to pyridine adsorption was used as background. The background was subtracted from each spectrum, and the absorbance was normalized to weight (10 mg) before calculations. The concentration of Lewis and Brönsted acid sites was calculated from integrated absorbance of the signals at ca. 1450 and 1545 cm^{-1} following the methodology proposed by Emeis (Equation 2.14) [18]. These signals correspond to the ring bending vibrational modes of: i) pyridine coordinatively bonded to Lewis sites (band at 1450 cm^{-1}); and ii) pyridine in the form of pyridinium ion (PyH^{+}) due to its interaction with Brönsted acid sites (band at 1545 cm^{-1}) (**Fig. 2.8**) [18-20].

$$C\ (L) = 1.42\, A(L)\, R^{2}\, W^{-1}$$

$$C\ (B) = 1.88\, A(B)\, R^{2}\, W^{-1}$$

Equation 2.14. Expressions to calculate the concentration of Lewis (C(L), in mmol g^{-1}) and Brönsted acid sites (C(B), in mmol g^{-1}); where A(L) and A(B) are the integrated absorbance of FTIR signals of pyridine coordinated to Lewis or Brönsted sites; R is the pellet radius; and W is its weight.

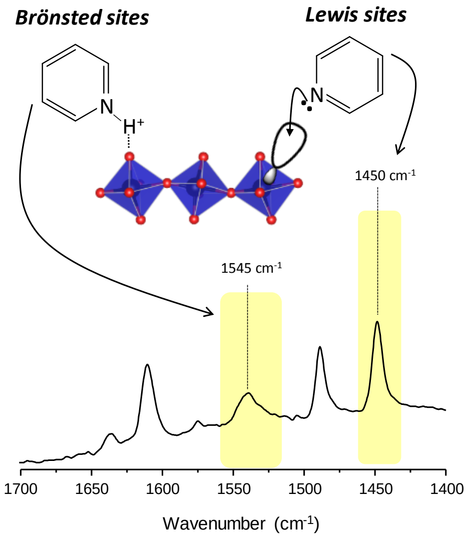

Figure 2.8. Example of a FTIR spectra of adsorbed pyridine of a solid acid catalyst presenting both Brönsted and Lewis acid sites.

2.2.12. Fourier-transform infrared (FTIR) spectroscopy of adsorbed CO at low temperature

FTIR spectroscopy of adsorbed CO was performed in transmission mode at 77 K in a Perkin–Elmer PE 100 spectrometer, in the Department of Inorganic Chemistry in the Fritz Haber Institute of the Max Planck Society (Berlin, Germany). Spectra were collected at a resolution of 0.5 cm^{-1} (256 accumulations per scan). Catalysts were pressed into wafers (2.5 T) of approximately 20 g cm^{-2}, and introduced into the IR cell connected to a vacuum system. Prior to CO adsorption, catalysts were activated under O_2 atmosphere (200 mbar) at 300 ºC for 2 h and cooled-down to room temperature. Then the cell was evacuated (P ≈ 5.10^{-6} mbar) and subsequently cooled-down to 77 K in a 2.0 mbar He atmosphere to promote heat-transfer. Once a temperature of 77 K was reached, a spectrum of activated sample was recorded. Then increasing amounts of CO were added, and spectra at different equilibrium pressures were recorded (P_{eq} = 0.001 - 6.400 mbar). Finally, the cell was evacuated at 77

K, and CO desorption was monitored at decreasing equilibrium pressures (P_{eq} = 0.100 – 5. 10^{-6} mbar). In some cases, data are presented as difference spectra, where the spectrum of the activated sample (recorded at 77 K) is subtracted from each measurement.

Carbon monoxide is a soft base, i.e. presents high polarizability (despite its small size). Due to this, it shows low interaction with solid surfaces, what makes the use of low temperatures necessary (usually 77 K), since it presents a low heat of adsorption [20-22]. CO molecule is very sensitive to the interaction with protic (mainly H^+) and aprotic acid sites (Lewis or coordinatively unsaturated metal sites, CUS) but also to the strength of both types of acid sites on the same material. It can directly interact with surface -OH groups, leading to negative shifts of O-H stretching modes. In addition, carbonyl stretching frequency can vary significantly with respect to its gas-phase frequency (2143 cm^{-1}) depending on the specific interaction with a surface site (especially with CUS sites). CO firstly forms donor bonds of σ-character (via its 5σ orbital) with surface metal centers. Then Metal-carbon bond can be stabilized via π-backdonation from *d* orbitals from the metal to antibonding π* orbital of CO, what will shift carbonyl frequencies to lower values (always comparing with gas-phase frequency of carbonyl, 2143 cm^{-1}). If no π-backdonation mechanism is present and σ-bond is prevalent, C-O frequency shifts to higher frequencies. Consequently, σ-bond will dominate when metal sites present low electron density on d orbitals (as in the case of d^0 cations like W^{6+} or Nb^{5+}).

2.2.13. Temperature-programmed reduction (TPR)

Temperature-programmed reduction was applied to study the reducibility of prepared catalysts. H_2-TPR experiments were carried out in a Micromeritics Autochem 2910 instrument, equipped with a thermal conductivity detector (TCD). About 20 mg of sample were exposed to a reducing stream consisting of a mixture of 10 % H_2 in Ar (flow rate of 50 mL min^{-1}). Then the temperature was increased up to 800 ºC at a heating rate of 10 ºC min^{-1}.

TPR experiments can be very useful when dealing with partial oxidation catalysts. In this sense, it is possible to probe cationic species, which can be detected, since they will present hydrogen uptakes at specific temperatures. For example, hardly reducible cationic species like W^{6+} will present hydrogen uptakes at higher temperatures than $V^{4+/5+}$ or Ni^{2+}, since the latter present a considerable redox activity (i.e. high reducibility). In addition, it is also a very useful technique to titrate the amount of metal oxide in supported catalysts, since it is directly related to the total amount of hydrogen uptake observed (i.e. when the total reduction of the metal oxide takes place).

2.2.14. Thermogravimetric analysis (TG-DTA)

TG-DTA analyses were performed in a Mettler-Toledo thermobalance (TGA/SDTA 851). About 10 mg of sample were introduced in the device, and were heated up to 600 ºC under synthetic air flow (50 mL min^{-1}). Heating rate used was 10 ºC min^{-1}.

Thermogravimetric analysis is used to study weight changes in solid samples as a function of temperature in a selected atmosphere. For this reason, it is mainly performed on as-prepared catalysts, since it can be very useful to study the weight losses during the activation treatment. Nevertheless, it is also useful to study activated materials, since we can probe weight gains, which can be associated to specific oxidation states of constituent elements. The technique can be also applied to the study of used catalysts, for example, in order to quantify coke or carbon deposits.

2.3. Catalytic tests

The materials prepared in this doctoral thesis have been tested as catalysts for several chemical transformations. The specific equipment and procedure to determine the catalytic properties of the materials will be briefly outlined in this section.

2.3.1. Gas phase aerobic transformation of glycerol

Gas phase aerobic transformation of glycerol was carried out in the temperature range 280–350 °C in a fixed-bed reactor at atmospheric pressure. In general, reaction mixture consisted of glycerol-water-oxygen-nitrogen-helium with a molar ratio of 2/40/4/15/39 or 6/37/12/45/0, using contact times, W/F, from 81 to 150 g_{cat} h $mol_{glycerol,})^{-1}$. The effluent stream was bubbled through a condenser device at 0–3 °C, while the remaining gaseous stream containing mainly carbon oxides and oxygen was analyzed by on-line gas chromatography.

The remaining gaseous stream was analyzed with a HP-G1540A gas chromatograph, with a TCD detector, and equipped with: i) molecular sieve 5 Å (3 m length); and ii) Porapak Q (3 m) (**Fig. 2.9**). The condensed mixture containing all the reaction products and the unconverted glycerol was analyzed by gas chromatography, using a Varian 3900 chromatograph, equipped with a 100% dimethylpolysiloxane capillary column (100 m× 0.25 mm× 0.5 μm) and a FID detector.

As stated above, both liquid and gaseous streams are obtained during the catalytic tests. Liquids were recovered every 1.5 h of time on stream and were analyzed by gas chromatography using pentanoic acid as standard. Relative molar response factors were previously obtained by analyzing standard solutions of glycerol and products of known concentration. The main reaction products in all cases were acrylic acid, acrolein, acetic acid and acetaldehyde. Other products were detected in chromatograms, which always represented less than 1% yield. Total moles present in the mixture were obtained from weighted amounts of pentanoic acid added to mixture aliquots, while molar compositions were calculated from molar fractions obtained from areas and relative response factors of the reactants and products (**Fig. 2.10**).

Regarding the analysis of the gaseous stream, N_2 was used as internal standard to calculate the total number of moles in the gas effluent. Response factors were obtained from standard gas bottles with known composition. The composition of the mixture was calculated with molar fractions obtained from areas and relative response factors of reactants and products (CO_2, CO, acrolein, acrylic acid, acetic acid and acetaldehyde).

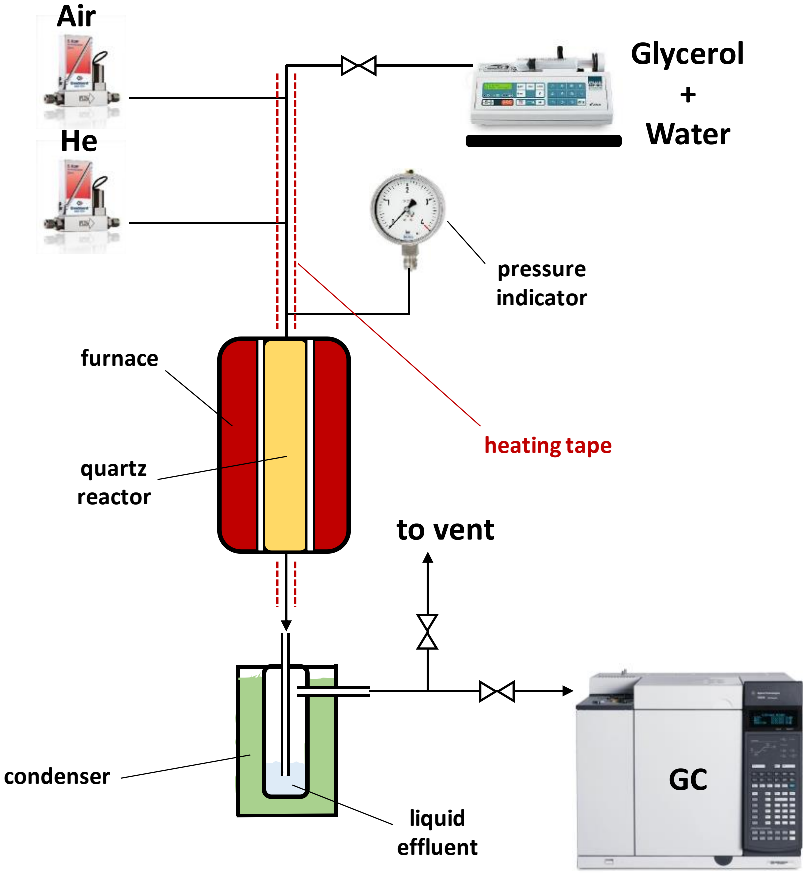
Air
He
Glycerol
+
Water
pressure
indicator
furnace
heating tape
quartz
reactor
to vent
condenser
liquid
effluent
GC

Figure 2.9. Scheme of the reaction system for the gas-phase aerobic transformation of glycerol.

Once molar compositions of the gases and liquids are elucidated, yields were calculated from the number of carbon moles in initial glycerol, and in products (liquids + gases). In the same way, carbon balance was calculated from the total number of carbon moles in analyzed products and in the initial feed. Glycerol conversion was calculated from initial and final glycerol moles in the stream. Then selectivity to each product was obtained from glycerol conversion and yield values. Carbon balances were in the range 70-100%. The lower carbon balance values obtained in some reactions were due to the formation of high molecular weight compounds that are not eluted in the gas chromatograph, that are also, in some cases, deposited in the reactor system´s tubing. Hence, the yield to these heavy by-products is calculated by the percentage needed to close the carbon balance. These calculations are summarized in (**Fig. 2.10**).

Gas fraction

$$\chi_i = \frac{\frac{A_i}{F_{R\,i}}}{\sum_{TOTAL}\frac{A_n}{F_{R\,n}}}$$

$$n_{total\ gas} = \frac{n_{N_2}}{\chi_{N_2}}$$

$$n_i = \chi_i \cdot n_{total\ gas}$$

$$nC_i(gas) = n_i \cdot \varphi_i$$

Liquid fraction

$$\chi_i = \frac{\frac{A_i}{F_{R\,i}}}{\sum_{TOTAL}\frac{A_n}{F_{R\,n}}}$$

$$n_{total\ liquids} = \frac{n_{valeric\ acid}}{\chi_{valeric\ acid}} \cdot \frac{m_{total\ liquids}}{m_{aliquot}}$$

$$n_i = \chi_i \cdot n_{total\ liquids}$$

$$nC_i(liq.) = n_i \cdot \varphi_i$$

χ_i: *molar fraction of compund i*

A_i: *Area of the chromatographic peak of compound i*

$F_{R\,i}$: *Relative response factor of compound i*

n_i: *moles of compond i*

nC_i*(gas) or (liq.): moles of carbon from compound i*

φ_i: *number of carbon atoms in compound i*

$$Glycerol\ conversion\ (\%) = \left(1 - \frac{moles\ of\ glycerol\ out}{Initial\ moles\ of\ glycerol}\right).100$$

$$Yield_i\ (\%) = \left(\frac{nC_i\ (gas) + nC_i\ (liq.)}{Initial\ nC_{glycerol}}\right).100$$

$$Selectivity_i(\%) = \left(\frac{Yield_i}{Glycerol\ conversion}\right).100$$

$$Carbon\ balance\ (\%) = \left(\frac{nC_{TOTAL}\ (gas) + nC_{TOTAL}\ (liq.)}{Initial\ nCglycerol}\right).100$$

Figure 2.10. Summarized calculations for the determination of the catalytic properties on the gas phase transformation of glycerol.

2.3.2. Gas phase aerobic transformation of methanol and ethanol

The gas phase aerobic transformation of methanol and ethanol was carried out in a fixed bed reactor at atmospheric pressure. Catalysts were tested in the 180-380 ºC temperature range and contact time, W/F, from 6.8 to 13.6 g_{cat} h mol_{CH3OH}^{-1}. Feed composition consisted of an alcohol-oxygen-nitrogen mixture with a molar ratio of 6/13/81.

Reactant and products were analyzed on-line by gas chromatography, using an Agilent 7890A gas chromatograph, with both thermal conductivity detector (TCD) and flame ionization detector (FID), equipped with two different chromatographic columns: i) molecular sieve 5 Å (3m length); and RT-U bond (30 m, 0.53 mm).

The procedure for the analysis of reactants and products was the same that the one performed in the gas-phase aerobic transformation of glycerol. In this case, there is just a gaseous stream to analyze, then, the calculations are only performed with the results obtained with the gas chromatograph connected on-line. Carbon balances were always in the range 95-100 %.

2.3.3. Oxidative dehydrogenation of ethane (ODH)

The catalytic tests for the oxidative dehydrogenation of ethane to ethylene were performed in a fixed bed quartz tubular flow reactor at 450 °C. Catalysts were diluted in CSi (silicon carbide, 0.59 mm particle size) to keep a constant catalytic bed volume. In a typical experiment, 100 mg of catalyst (0.42-0.59 mm, particle size) were used, at a total flow of 50 mL min^{-1}. Total flow and catalysts weight were varied in order to attain different ethane conversion values at a given temperature. The feed consisted of a mixture of C_2H_6/O_2/He with molar ratios of 5/5/90. In oxygen-free experiments, the feed consisted of a mixture of C_2H_6/He with molar ratios of 5/95.

Reactants and products were analyzed by means of on-line gas chromatography with a system of two packed columns: i) molecular sieve 5 Å (3 m length); and ii) Porapak Q (3 m). The main reaction products obtained were ethylene and CO_2. In all cases negligible amounts of CO were detected (selectivity to CO lower than 1 %). Blank runs with neither catalyst nor silicon carbide showed no conversion of ethane. The analysis of reactants and products was the same to that presented above for the gas-phase aerobic transformation of glycerol or methanol/ethanol (see section 2.3.1 and section 2.3.1, as well as in **Fig. 2.10**).

2.3.4. Aqueous phase catalytic transformation of biomass-derived short-chain oxygenates

Catalytic tests were carried out into PEEK-lined stainless steel autoclaves equipped with pressure control, a magnetic stirrer and a sampling valve. Autoclaves were covered with a steel jacket equipped with a temperature control system. Feed consisted of an aqueous model mixture of acetic acid-propanal-acetol-ethanol-water (wt.% ratio of 30/25/5/10/30), which resembles that of a waste effluent derived from the aqueous phase separation of a pyrolytic bio-oil.

The experiments were performed with 150 mg of catalyst and 3 g of aqueous mixture, at a N_2 pressure of 15 bar and at 180 and 200 ºC. Small volumes of reaction mixture (50-100 μL) were collected at different time on stream (i.e. from 1h to 7 h).

Reaction mixtures were analyzed by gas chromatography in a Bruker 430 GC with a capillary column (TRB-624, 60 m length) and a FID detector. Reactants and intermediate products were quantified using FID response factors obtained by calibration using chlorobenzene as internal standard.

On the other hand, longer chain oxygenates were grouped as C_5-C_8 and C_9-C_{10}, and analyzed in intervals. Identification of products was carried out by GC-MS, in an Agilent 6890 N GC, which was coupled with an Agilent 5973 N mass selective detector and equipped with a HP-5ms capillary column. In this case, response factors were estimated by group contributions technique.

A maximum theoretical total organic yield can be calculated considering that: i) 100 % of conversion of each reactant, ii) acetic acid can be equally converted into ethyl acetate and acetone and, iii) all the feed is converted into C_9 products, i.e. neither intermediate nor higher carbon chain products are obtained. This assumption leads to a product mixture containing 51.3 wt.% water, 19.1 wt.% ethyl acetate, and 29.6 wt.% of C_9 products. Hence, yield and selectivity to products were calculated assuming a theoretical maximum total organic yield of 29.6 wt.%, and referred to this absolute maximum yield.

For instance, taking into consideration this maximum total organic yield (29.6 wt.%), the results in a catalytic test leading to a 15.0 wt.% of absolute total organic yield will be presented as follows:

$$Total\ Organic\ Yield\ (wt.\%) = \frac{15.0}{29.6}.100 = 55.7\ \%$$

2.4. References

[1] K. Byrappa, *Handbook of Hydrothermal Technology* (Second Edition), William Andrew Publishing, Oxford (2013) pp. 1-52.

[2] F. Kleitz, S. Hei Choi, R. Ryoo, *Cubic Ia3d large mesoporous silica: synthesis and replication to platinum nanowires, carbon nanorods and carbon nanotubes*, Chemical Communications, (2003) 2136-2137.

[3] E. Heracleous, A.A. Lemonidou, *Ni–Nb–O mixed oxides as highly active and selective catalysts for ethene production via ethane oxidative dehydrogenation. Part I: Characterization and catalytic performance*, Journal of Catalysis, 237 (2006) 162-174.

[4] B. Solsona, P. Concepción, B. Demicol, S. Hernández, J.J. Delgado, J.J. Calvino, J.M. López Nieto, *Selective oxidative dehydrogenation of ethane over* SnO_2*-promoted NiO catalysts*, Journal of Catalysis, 295 (2012) 104-114.

[5] B. Solsona, P. Concepcion, J.M. Lopez Nieto, A. Dejoz, J.A. Cecilia, S. Agouram, M.D. Soriano, V. Torres, J. Jimenez-Jimenez, E. Rodriguez Castellon, *Nickel oxide supported on porous clay heterostructures as selective catalysts for the oxidative dehydrogenation of ethane*, Catalysis Science & Technology, 6 (2016) 3419-3429.

[6] J.W. Niemantsverdriet, *Spectroscopy in Catalysis*, John Wiley & Sons Ltd. (2007).

[7] Y. Waseda, E. Matsubara, K. Shinoda, *X-Ray Diffraction Crystallography: Introduction, examples and solved problems*, Springer, Berlin Heidelberg (2011).

[8] B. Imelik, J.C. Vedrine, *Catalyst Characterization - Physical Techniques for Solid Materials*, New York, NY, Plenum Press (1994).

[9] D.B. Williams, C.B. Carter, *Transmission Electron Microscopy: A Textbook for Materials Science*, Springer (1996).

[10] G.C. Smith, *Surface analysis by Electron Spectroscopy: Measurement and interpretation*, Springer (2013).

[11] J. F.Watts, J. Wolstenholme, *An introduction to surface analysis by XPS and AES*, John Wiley & Sons Ltd. (2003).

[12] National Institute of Standards and Technology, https://www.nist.gov/.

[13] La Surface, http://www.lasurface.com.

[14] G. Bunker, Introduction to XAFS: *A practical guide to X-ray Absorption Fine Structure Spectroscopy*, Cambridge University Press, Cambridge, (2010).

[15] J.A. van Bokhoven, C. Lamberti, *X-Ray Absorption and X-Ray Emission Spectroscopy: Theory and applications*, John Wiley & Sons Ltd. (2016).

[16] J. Rouquerol, F. Rouquerol, P. Llewellyn, G. Maurin, K.S.W. Sing, *Adsorption by powders and porous solids: Principles, methodology and applications*, Elsevier Science (2013).

[17] J.C. Groen, L.A.A. Peffer, J. Pérez-Ramírez, *Pore size determination in modified micro- and mesoporous materials. Pitfalls and limitations in gas adsorption data analysis*, Microporous and Mesoporous Materials, 60 (2003) 1-17.

[18] C.A. Emeis, *Determination of integrated molar extinction coefficients for infrared absorption bands of pyridine adsorbed on solid acid catalysts*, Journal of Catalysis, 141 (1993) 347-354.

[19] I.E. Wachs, *Infrared spectroscopy of supported metal oxide catalysts*, Colloids and Surfaces A: Physicochemical and Engineering Aspects, 105 (1995) 143-149.

[20] A. Davydov, *Molecular Spectroscopy of oxide catalyst surfaces*, John Wiley & Sons Ltd. (2003).

[21] G. Ertl, H. Knözinger, J. Weitkamp, *Handbook of Heterogeneous Catalysis*, VCH (1997).

[22] K.I. Hadjiivanov, G.N. Vayssilov, *Characterization of oxide surfaces and zeolites by carbon monoxide as an IR probe molecule*, Advances in Catalysis, Academic Press (2002), pp. 307-511.

Chapter 3

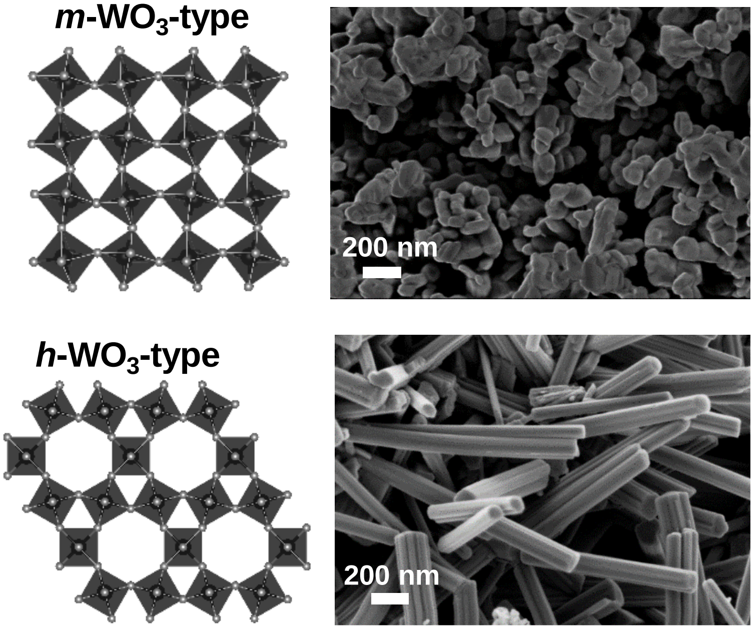
m-WO_3-type
200 nm
h-WO_3-type
200 nm

W-V-O catalysts: Influence of phase composition on their multifunctional acid-redox properties

3.1. Previous considerations

Tungsten oxide-based materials are one of the most versatile systems regarding their multiple applications in materials science, which cover a wide variety of fields, such as superconductivity, gas sensing, electrochromics or catalysis [1-4]. Considering catalytic applications, tungsten oxides have been used as supports and electrocatalysts for fuel cells [5-8]. Focusing on partially reduced tungsten oxides, also known as tungsten oxide bronzes, they have been proposed as efficient catalysts for the hydrogenation of linear and cyclic alkenes, organosulfur compounds and nitroarenes [9]. Moreover, they have also been applied as electrocatalysts for oxygen reduction [10] and photocatalysts [11]. Their extraordinary structural and compositional versatility makes these materials good candidates for the incorporation of different catalytic functionalities. In fact, materials based on tungsten bronzes have already been proposed as catalysts for the partial oxidation of olefins [12] and as acid-redox multifunctional materials for the direct transformation of glycerol into acrylic acid in a one-pot system [13-15]. From the synthetic point of view, it has been demonstrated that synthesis conditions (i.e. pH, organic additives or type of precursors in the synthesis) can have an important effect on the physicochemical properties of the oxides and, subsequently, on the catalytic properties of the final materials [16-19].

In the following chapter, the influence of the phase composition of W-V-O materials (mainly the concentration of *m*-WO_3 and *h*-WO_3-type structures) on their multifunctional acid and redox properties has been studied. For this purpose, a series of W-V-O catalysts, which present a similar chemical composition (i.e. vanadium content), were prepared by a hydrothermal method (see point 2.1.1 in Experimental Section), by using different tungsten, vanadium and ammonium precursors (**Table 3.1**).

The catalysts have been characterized by X-Ray diffraction (XRD), N_2-adsorption, Raman and FTIR spectroscopies, temperature-programmed desorption of ammonia (TPD-NH_3), temperature-programmed reduction with H_2 (H_2-TPR) and X-ray photoelectron spectroscopy (XPS).

Table 3.1. Precursors used in the hydrothermal synthesis of W-V-O catalysts.

Sample	Precursors		
	W-precursors [a]	**V-precursors** [b]	**NH_4^+-salt**
MT-1	$(NH_4)_6H_2W_{12}O_{40}$	$VOSO_4$	-
MT-2	$(NH_4)_6H_2W_{12}O_{40}$	$VO(acac)_2$	-
T-1	H_2WO_4	$VOSO_4$	$NH_3(aq)/NH_4Cl$
T-2	H_2WO_4	$VOSO_4$	NH_4SO_4
T-3	H_2WO_4	$VOSO_4$	NH_4Cl
T-4	H_2WO_4	$VOSO_4$	$NH_4CH_3CO_2$
T-5	H_2WO_4	$VO(acac)_2$	$NH_4CH_3CO_2$

[a] Ammonium metatungstate, $(NH_4)_6H_2W_{12}O_{40}$ or tungstic acid, H_2WO_4.

[b] Vanadyl sulfate, $VOSO_4$ or vanadyl acetyl acetonate, $VO(acac)_2$.

The aerobic transformation of methanol was used as a model reaction in order to estimate the acid-redox multifunctional properties of the catalysts. Finally, these multifunctional properties have been correlated with their catalytic behavior in the one-pot aerobic transformation of glycerol into acrylic acid, evidencing the importance of the crystal structure to obtain selective catalysts.

3.2. Physicochemical characterization of W-V-O oxides

The main physicochemical features of W-V-O catalysts are shown in **Table 3.2**, whereas the precursors used in the synthesis of each catalyst are presented in **Table 3.1**. All the materials display a V/(V+W) ratio in the range 0.12 - 0.18, which is below the maximum theoretical V-content in a hexagonal tungsten bronze-type phase (HTB or h-WO_3) considering a $V/(V+W)_{max}$ of 0.3.

Table 3.2. Physicochemical characteristics of W-V-O catalysts.

Sample	**V/(W+V) atomic ratio**		**h-WO_3 phase content (%)** [c]		**S_{BET}** (m^2/g)	**Weight loss at 350 ºC** (%)[d]	**TPD-NH_3** (µmol/g) [e]
	bulk [a]	surface [b]	as-prepared	heat-treated			
MT-1	0.17	0.05	100	100	20.5	5.42	n.d.
MT-2	0.17	0.16	n.d.[f]	n.d.[f]	16.1	5.37	127
T-1	0.16	0.07	100	100	32.8	5.65	241
T-2	0.12	n.d.	42	31	13.5	2.58	n.d.
T-3	0.12	0.08	46	26	7.2	1.77	50
T-4	0.17	0.15	41	0	7.9	2.91	86
T-5	0.18	0.19	60	54	26.6	4.82	88

[a] Composition obtained by X-Ray energy-dispersive spectroscopy (XEDS). [b] Obtained by X-Ray Photoelectron Spectroscopy (XPS). [c] Estimated from (100) and (022) Bragg reflections using the following equation: HTB (%) = 100 x I_{100}(HTB)/[I_{022}(m-WO_3)+I_{100}(HTB)]. [d] Calculated by thermogravimetric analysis. [e] Temperature-programed desorption of ammonia. [f] A pseudocrystalline phase is only observed (no Bragg signals from HTB phase).

This limitation in the incorporation of vanadium atoms into the structure comes from the maximum number of M^{5+} species in octahedral sites that can be incorporated within HTB phase. This fact is in addition related with the occupancy limit of the hexagonal channels within the framework (*h*-$A_{0.3}W^{6+}_{0.7}W^{5+}_{0.3}O_3$) [20-22]. However, other systems, like W-Nb-O, allow the introduction of dopant concentrations that exceed this hypothetical limit, with the subsequent structural implications (see Chapter 4).

XRD patterns of as-prepared materials are shown in **Figure 3.1 A**, whereas the XRD of the corresponding heat-treated catalysts are presented in **Figure 3.1 B**. Regarding as-prepared materials, two different pure bronze-type phases have been obtained when ammonium metatungstate and/or ammonia/ammonium chloride are added as ammonium precursors in the synthesis: i) a hexagonal tungsten bronze type structure (*h*-WO_3, JCPDS:

33-1387) (**Fig. 3.1 A**, patterns *a* and *c*) [13, 20]; and ii) an oxide with a pseudocrystalline structure, which presents long range order just along [001] direction (i.e. *c*-axis) (**Fig. 3.1 A,** pattern *b*) [23]. This loss of periodicity along *a*-*b* plane makes it difficult to ascribe this pattern to a specific crystal structure. Therefore, it just can be attributed to a perovskite-related ReO_3-type crystal structure, in which long range order is only maintained along [001] direction, in which 2θ values of Bragg signals observed correspond to the interplanar distances of vertex-sharing octahedra (≈ 3.8 Å).

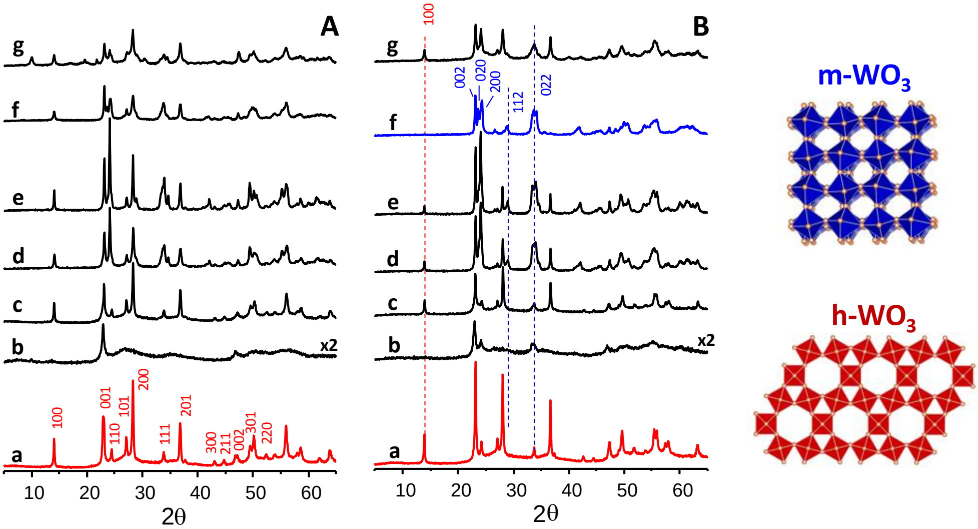

Figure 3.1. XRD patterns of as-prepared (A) and heat-treated W-V-O catalysts. a) MT-1; b) MT-2; c) T-1; d) T-2; e) T-3; f) T-4; g) T-5. Crystal structures of *m*-WO_3 (blue) and *h*-WO_3 (red) type phases are also included.

On the contrary, when tungstic acid was used as tungsten source, a monophasic *h*-WO_3 was only obtained by using a mixture NH_3/NH_4Cl as ammonium precursor (**Fig. 3.1 A**, pattern *c*). The use of other ammonium sources in the synthesis gave rise to mixtures of *h*-WO_3 and a perovskite-related ReO_3-type monoclinic phase of tungsten trioxide (*m*-WO_3, JCPSD: 43-1035) (**Fig. 3.1 A**, patterns *d*-*g)*.

An additional unknown crystalline phase was found when tungstic acid, vanadyl acetylacetonate and ammonium acetate were employed as precursors (**Fig. 3.1 A**, pattern *g*). Nevertheless, this unidentified phase decomposes after the heat-treatment (**Fig. 3.1 B**, pattern *g*). All these observations suggest that the presence of metatungstate ion, or the possible *in situ* formation of polytungstate species during the hydrothermal treatment could have a high influence in the formation of pure bronze phases [12, 24, 25].

XRD profiles of heat-treated materials are presented in **Figure 3.1 B**. Interestingly, only pure *h*-WO_3 samples retain their original crystalline structures (**Fig. 3.1 B,** patterns *a* and *c*). In the rest of materials, *h*-WO_3 phases partially decompose into *m*-WO_3. The hexagonal phase content in both as-prepared and heat-treated materials was estimated from the intensity of (002) and (100) reflections of *m*-WO_3 and *h*-WO_3 respectively (**Table 3.2**). In this regard, as-prepared oxides display a *h*-WO_3 phase content in the range 41-100 %, meanwhile in heat-treated samples the hexagonal tungsten bronze phase content is in the range 0-100 %. It is worth mentioning that, in general, bronze phases (pseudocrystalline and *h*-WO_3) present higher surface areas than those presenting *m*-WO_3 (**Table 3.2**).

Figure 3.2 shows scanning electron microscopy (SEM) images of as-synthesized oxides. It is noteworthy that pure-bronze phases (either *h*-WO_3 or the pseudocrystalline oxide) display 1D morphologies, i.e. rod-like or needle-like nanostructures (**Fig. 3.2**, *a-c*). On the other hand, the rest of materials tend to show also a high concentration of block-shaped morphologies (**Fig. 3.2**, *d-g*). In this sense, these block-type morphologies could favor the decomposition of the hexagonal phase of the tungsten oxide. Block-shaped materials expose a higher proportion of (001) crystallographic faces, what would promote an easier elimination of NH_4^+ ions from the hexagonal channels in the *h*-WO_3 structure, thus facilitating the phase transition to *m*-WO_3 [26, 27].

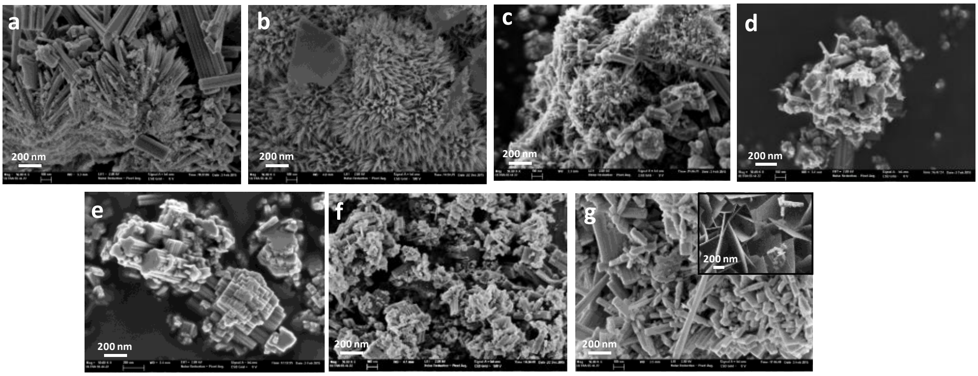
a
200 nm
b
200 nm
c
200 nm
d
200 nm
e
200 nm
f
200 nm
g
200 nm
200 nm

Figure 3.2. SEM micrographs of as-prepared W-V-O materials. a) MT-1; b) MT-2; c) T-1; d) T-2; e) T-3; f) T-4; g) T-5.

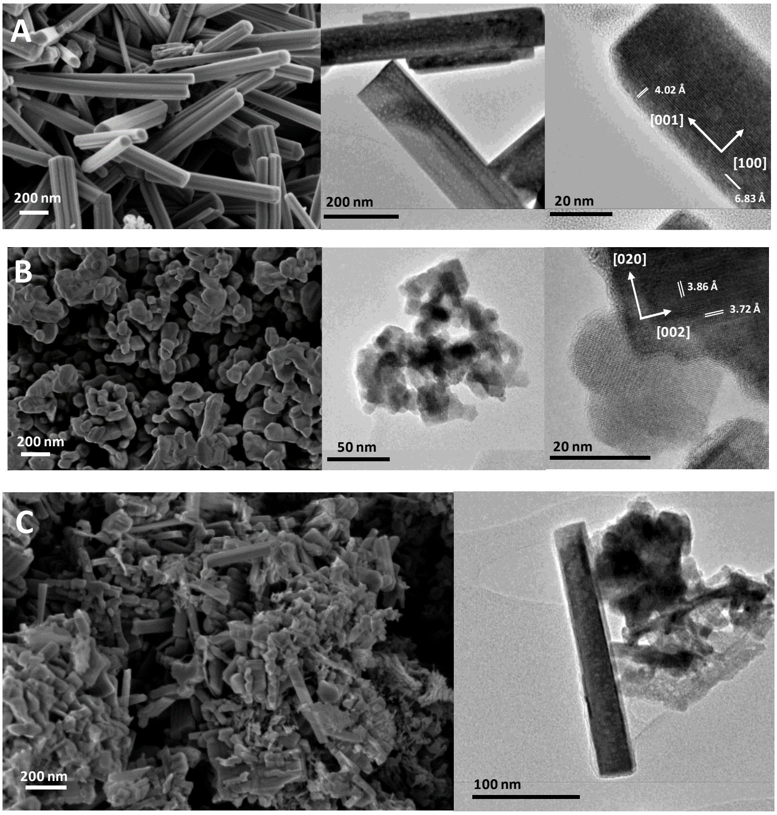
A
200 nm
200 nm
4.02 Å
[001]
[100]
6.83 Å
20 nm
B
200 nm
50 nm
[020]
3.86 Å
3.72 Å
[002]
20 nm
C
200 nm
100 nm

Figure 3.3. SEM and TEM images of heat-treated W-V-O materials. A) MT-1 (*h*-WO_3); B) T-4 (*m*-WO_3); C) T-5 (*h*-WO_3 + *m*-WO_3).

Interestingly, needle and rod-shaped materials maintain their crystal shape after the heat-treatment (**Fig. 3.3 A)**, while block-shaped crystals are no longer observed, and are transformed into platelet-like particles, which have been identified with *m*-WO_3-type phase (**Fig. 3.3 B**). In fact, those unidimensional crystal morphologies can be attributed to bronze-type materials [28-30]. Therefore, materials presenting a mixture of *h*-WO_3 and *m*-WO_3 phases show both platelet and 1D morphologies (**Fig. 3.3 C)**.

Raman spectra of heat-treated materials are shown in **Figure 3.4**. All the catalysts show three bands around 700, 800 and 900 cm^{-1}, which can be assigned to W-O-V, W-O-W and M=O (M: W, V) bridge and stretching vibrations, respectively [31-33]. The absence of Raman bands over 1000 cm^{-1} suggests that no V_2O_5 is formed after heat-treatment [34].

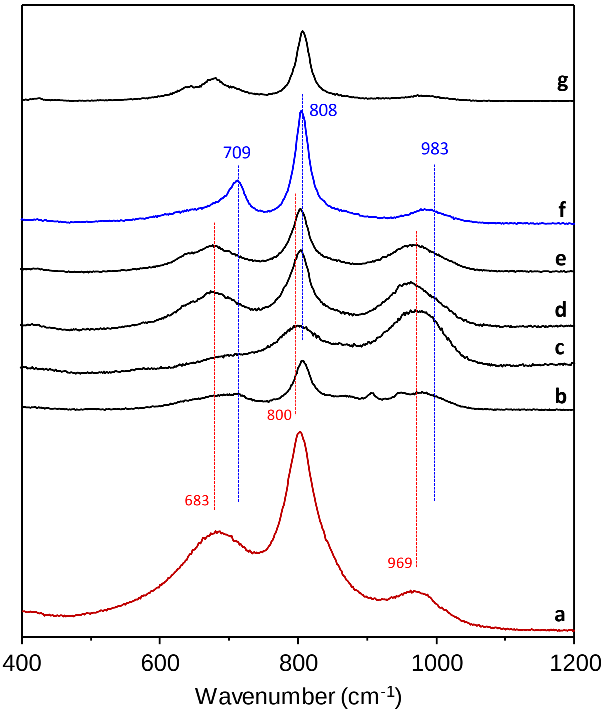

Figure 3.4. Raman profiles of heat-treated W-V-O materials. a) MT-1; b) MT-2; c) T-1; d) T-2; e) T-3; f) T-4; g) T-5.

Monophasic *m*-WO_3 catalyst display Raman signals at 709, 808 and 983 cm^{-1} (**Fig. 3.4**, spectrum *f*). This signals are slighty shifted to lower frequencies for pure *h*-WO_3 phase catalyst (683, 800 and 969 cm^{-1}) (**Fig. 3.4**, spectrum *a*). Hence, for catalysts in which both crystal phases are present, the coexistence of the corresponding Raman bands of each structural type is observed (**Fig. 3.4**, spectra *d*, *e* and *g*).

Differential thermogravimetric analyses (DTG) were performed on as-prepared materials (**Fig. 3.5)**. DTG profiles display two main weight losses: i) below 200 ºC, which can be assigned to the elimination of physisorbed water; and ii) in the range 250-450 ºC, which can be ascribed to the elimination of NH_4^+ cations from the channels [35, 36].

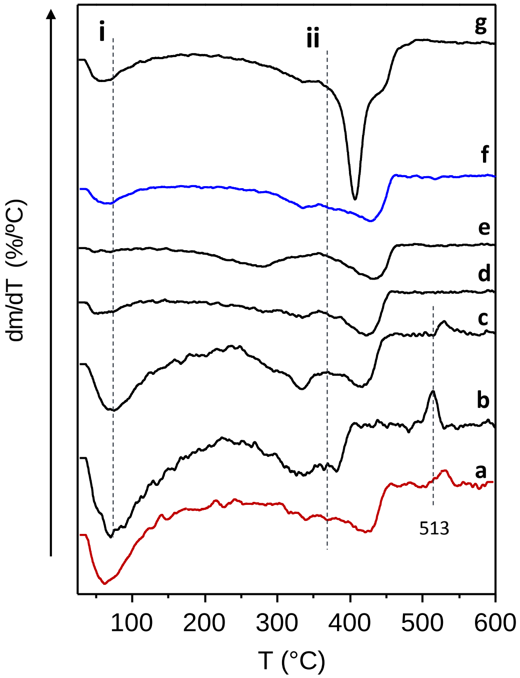

Figure 3.5. DTG profiles of as-prepared oxides: a) MT-1; b) MT-2; c) T-1; d) T-2; e) T-3; f) T-4; g) T-5.

Materials with high amounts of *h*-WO_3 or pseudocrystalline phase present higher weight losses (**Table 3.2**). In addition, samples with higher concentration of bronze phases also show a weight gain around 500 ºC, which can be assigned to the oxidation of V^{4+} or W^{5+} species into V^{5+} or W^{6+} respectively (**Fig. 3.5**).

The activation process of W-V-O materials was studied by analyzing the characteristic stretching vibrational modes of O-H and N-H in as-prepared and heat-treated materials by FTIR spectroscopy (**Fig. 3.6**). All as-prepared catalysts show three bands in the 3000-3700 cm^{-1} region (**Fig. 3.6 A**). The signal at 3430 cm^{-1} can be assigned to O-H stretching vibrations, while bands at 3215 and 3144 cm^{-1} correspond to N-H stretching vibrations of the ammonium groups inside the channels [35, 37, 38].

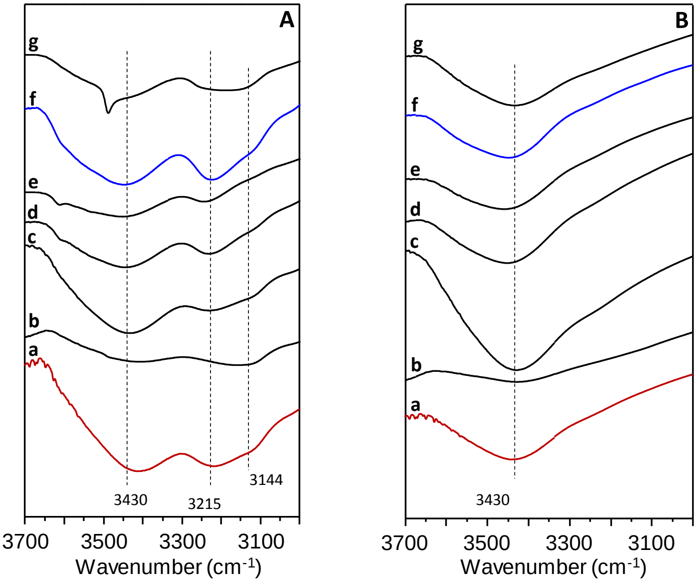

Figure 3.6. FTIR spectra of as-synthesized (A) and heat-treated (B) W-V-O materials: a) MT-1; b) MT-2; c) T-1; d) T-2; e) T-3; f) T-4; g) T-5.

After heat treatments the spectra show the presence of the band corresponding to OH groups (i.e. 3430 cm^{-1}), while the bands ascribed to NH_4^+ groups are not observed anymore (**Fig. 3.6 B**). The elimination of ammonium ions (in the form of NH_3) leaving a H^+ cation in their corresponding position (for example, into the hexagonal channels in the *h*-

WO_3 phase) has been suggested to be the cause of the formation of Brönsted acid sites in bronze-type oxides [39].

The acid characteristics of W-V-O catalysts were determined by means of NH_3 chemisorption and subsequent temperature-programmed desorption (TPD-NH_3) (**Table 3.2** and **Fig. 3.7**). It is observed that higher contents of *h*-WO_3 give rise to a higher concentration of surface acid sites (**Fig. 3.7**, A and B).

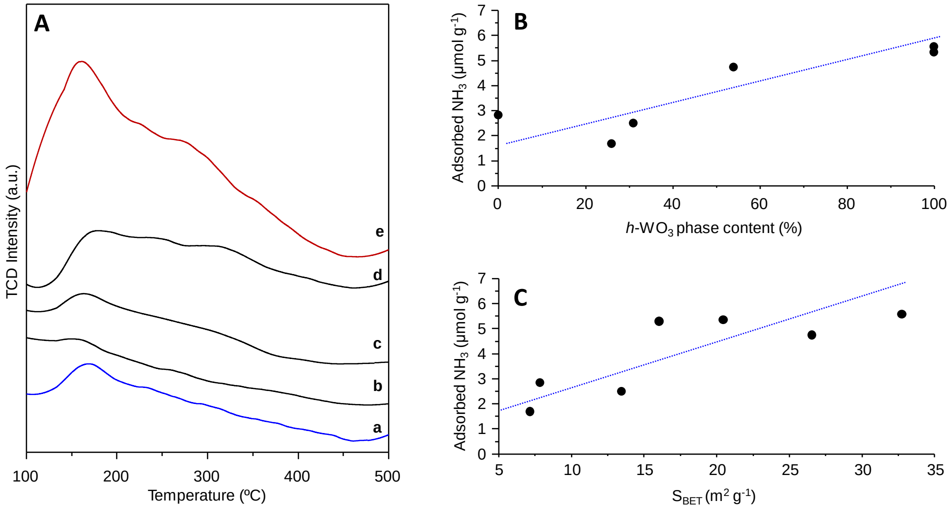

Figure 3.7. TPD-NH_3 profiles of W-V-O catalysts (A) and the variation of adsorbed ammonia as a function of *h*-WO_3 content (B) and surface area (C): a) T-4 (*m*-WO_3 type catalyst); b) T-3; c) T-5; d) MT-2; e) T-1 (*h*-WO_3 type catalyst).

These results suggest that the presence of the hexagonal channels in the *h*-WO_3 phase could promote the formation of Brönsted acid sites, by the elimination of ammonium cations located at those channels by high temperature heat-treatments [39]. For this reason, the amount of surface acid sites is much lower in *m*-WO_3 type phase (**Table 3.2**). Despite this, the effect of the higher surface areas observed in samples with a higher *h*-WO_3-type phase contents cannot be ruled out. In fact, the concentration of surface acid sites also increases linearly with the specific surface area of the catalysts. In this sense, *m*-WO_3, which presents a more compact crystal structure, favors the formation of larger crystals after heat treatments, giving rise to lower surface areas (**Fig. 3.7, C**).

The surface chemical nature of W-V-O catalysts was investigated by XPS spectroscopy. Surface V/(W+V) atomic ratios are summarized in **Table 3.2;** whereas the XPS spectra (V 2$p_{3/2}$ and W 4*f* core levels) are shown in **Figure 3.8**. V 2$p_{3/2}$ core level XPS spectra of the catalysts are presented in **Figure 3.8 A**. The spectra show a single peak at 517.1-517.6 eV, assigned to the presence of surface V^{5+} species [15]. Only in the case of sample MT-1, an additional contribution at lower binding energy is observed (ca. 515.7, 14 at. %) which can be ascribed to V^{4+} species [15].

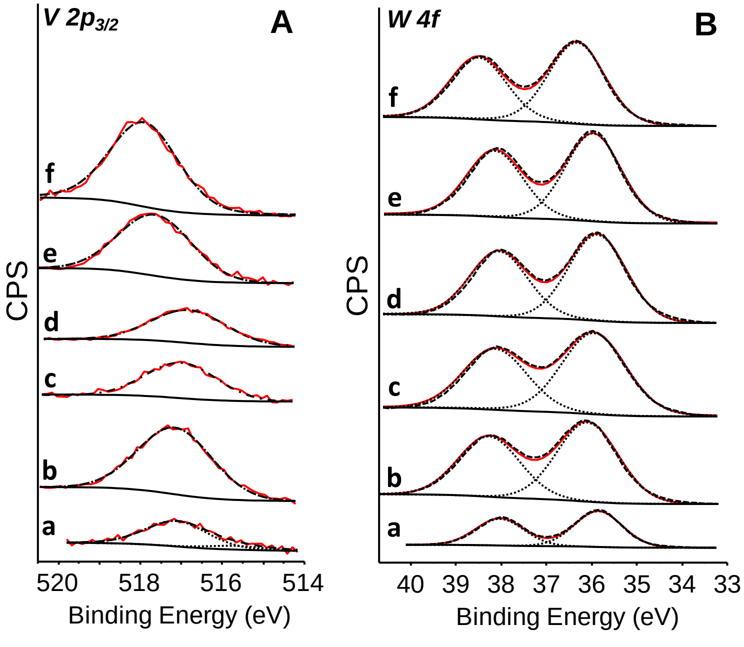

Figure 3.8. V 2$p_{3/2}$ (A) and W 4*f* (B) core level XPS spectra of W-V-O catalysts. a) MT-1; b) MT-2; c) T-1; d) T-3; e) T-4; f) T-5.

Considering the W 4*f* XPS core level spectra (**Fig. 3.8 B**), all the catalysts present similar features, showing a W 4$f_{7/2}$ peak centered at approximately 35.9-36.3 eV, which can be attributed to W^{6+} species [40]. The absence of peaks-shoulders around 33-35 eV indicates the absence of W^{5+} species on the surface of the catalysts [27].

Finally, the reducibility of W-V-O catalysts has been studied by means of temperature-programmed reduction with H_2. The TPR-H_2 patterns of W-V-O catalysts presenting pure *m*-WO_3 or pure *h*-WO_3 are shown in **Figure 3.9**. In both cases, the H_2-TPR profiles display two main reduction peaks.

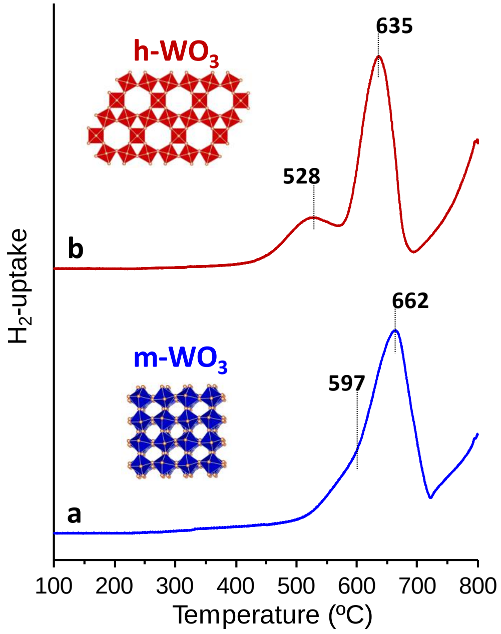

Figure 3.9. H_2-TPR profiles of phase pure *m*-WO_3 and *h*-WO_3-type W-V-O catalysts. a) T-4 (*m*-WO_3-type phase); b) MT-1 (*h*-WO_3-type phase).

The peak appearing at lower temperature (i.e. at 528 and 597 ºC for *h*-WO_3 and *m*-WO_3-type phases respectively) can be ascribed to the reduction of V^{5+} species, while the high temperature peak (i.e. 635 and 662 ºC *h*-WO_3 and *m*-WO_3-type phases respectively) can be attributed to the reduction of W^{6+} cations. Both W-V-O catalysts show differences in the reducibility of the corresponding metal species, being V^{5+} and W^{6+} more reducible in the case of *h*-WO_3 type-phase (MT-1 catalyst).

3.3. Catalytic properties in the gas phase aerobic transformation of methanol and glycerol

3.3.1. Gas phase aerobic transformation of methanol

The aerobic transformation of methanol has been widely used as a test reaction to elucidate the acid-redox surface properties of metal oxide catalysts, but also to probe the structure-reactivity relationships of bulk metal oxides [14, 15, 41-43]. Indeed, the reaction of methanol on acid sites leads to the exclusive formation of dimethyl ether (DME), via a dehydration mechanism. On the other hand, when methanol reacts on redox sites (like V^{4+}/V^{5+} species) it is transformed into formaldehyde and/or carbon oxides (if only redox sites are available), or into other partial oxidation products such as methyl formate or dimethoxymethane (when both acid and redox sites act in a cooperative way, especially at low methanol conversion) [42].

Figure 3.10 displays the catalytic activity (i.e. activity per gram of catalyst) and specific activity (i.e. catalytic activity per unit area) as a function of reaction temperature for W-V-O catalysts. Considering the catalytic activity (**Fig. 3.10**, **A**), it is not possible to find clear correlations between physicochemical features of the materials (i.e. phase composition, surface vanadium content, surface areas) and the activity, mainly due to the heterogeneous chemical characteristics found all along the series (**Table 3.2**).

Despite this, W-V-O catalysts with high contents of *m*-WO_3 type display the lowest catalytic activity (especially T4 and T3 samples). On the other hand, if we normalize the catalytic activity to the specific BET surface area of the materials (**Fig. 3.10**, **B**), the surface activity increases more drastically with the reaction temperature in the case of the catalysts presenting higher contents of *m*-WO_3 type phase, i.e. phase pure *h*-WO_3 catalysts present the lowest activity per unit area.

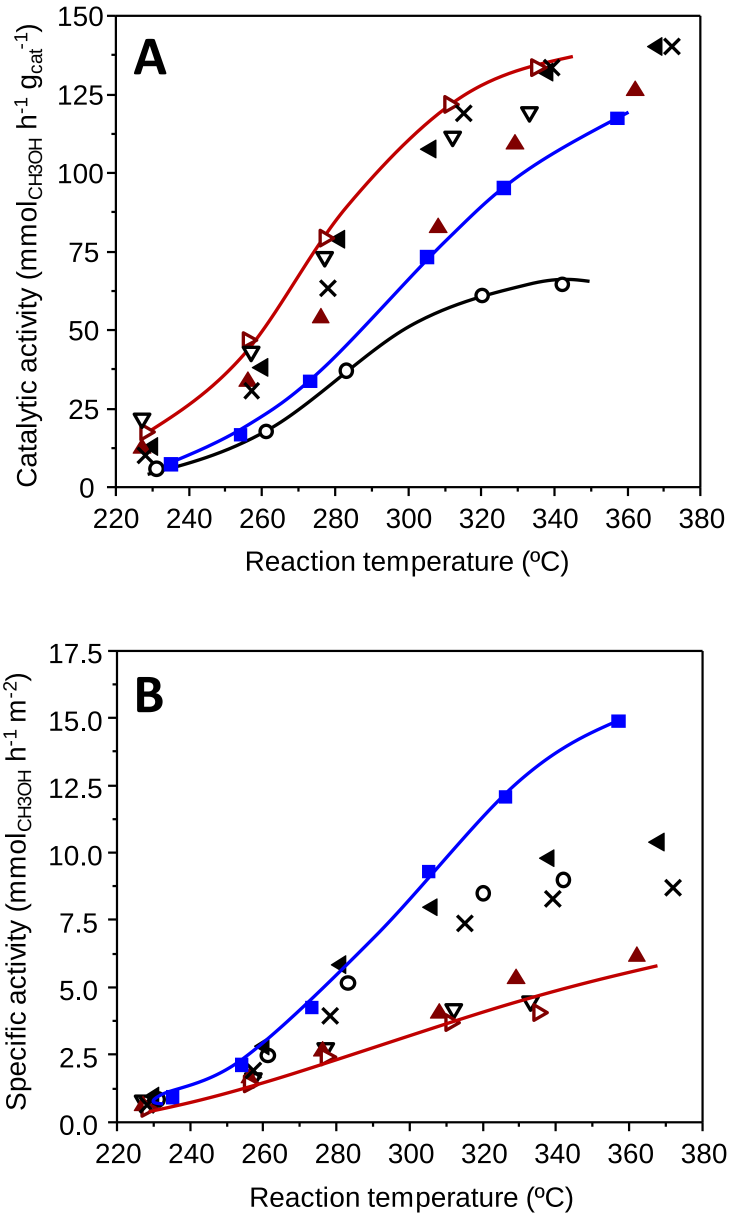

Figure 3.10. Catalytic activity (A) and specific activity (B) as a function of reaction temperature for W-V-O catalysts. MT-1 (▲); MT-2 (**X**); T-1 (▷); T-2 (◀); T-3 (O); T-4 (■); T-5 (▽).

The variation of the selectivity to DME and partial oxidation products, (POPs, mainly formaldehyde and minor amounts of methyl formate and dimethoxymethane), as a function of methanol conversion, during the selective aerobic transformation of methanol on W-V-O catalysts is shown in **Figure 3.11** and **Table 3.3**. The acid-redox properties of the catalysts can then be estimated from selectivity to the abovementioned POPs and DME at low methanol conversion (ca. 10 %) (**Fig. 3.12**). Indeed, there exists a correlation between the phase composition of the catalysts and their acid-redox features. On the one hand, the highest selectivity to POPs is achieved in the absence of *h*-WO_3 (i.e. T4 sample). Therefore, the acid function of the catalysts is progressively lost as the amount of *m*-WO_3-type phase in the catalysts increases.

Table 3.3. Catalytic properties of W-V-O catalysts in the aerobic transformation of methanol.

Sample	***h*-WO_3 phase content (%) [b]**	**Specific activity [c] (at 280 ºC)**	**Initial selectivity [d]**	
			DME (%)	**POPs (%)**
HTB [a]	100	0.95	98.4	1.6
MT-1	100	2.63	37.3	62.7
MT-2	n.d.[b]	3.95	28.0	72.0
T-1	100	2.42	40.8	59.2
T-2	31	5.86	10.3	89.7
T-3	26	5.18	9.5	90.5
T-4	0	5.10	4.5	95.5
T-5	54	2.76	19.2	80.8

[a] V-free hexagonal tungsten bronze material with a *h*-WO_3-type structure. [b] *h*-WO_3 phase content in heat-treated samples. [c] Catalytic activity per unit area at 280 ºC, in $mmol_{MeOH}$ h^{-1} m^{-2}. [d] Initial selectivity determined at 10 % of methanol conversion. Feed composition: $MeOH/O_2/N_2$ molar ratio, 6/13/81.

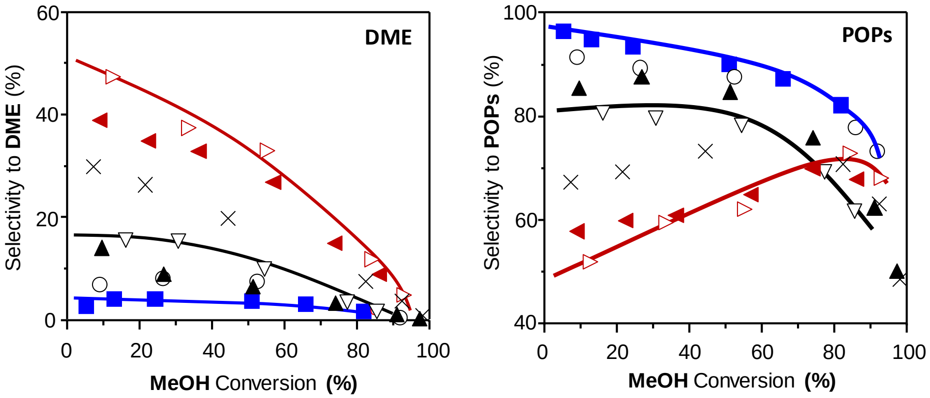

Figure 3.11. Selectivity to DME and POPs as a function of methanol conversion for W-V-O catalysts. MT-1 (▲); MT-2 (**X**); T-1 (▷); T-2 (◀); T-3 (**O**); T-4 (■); T-5 (▽).

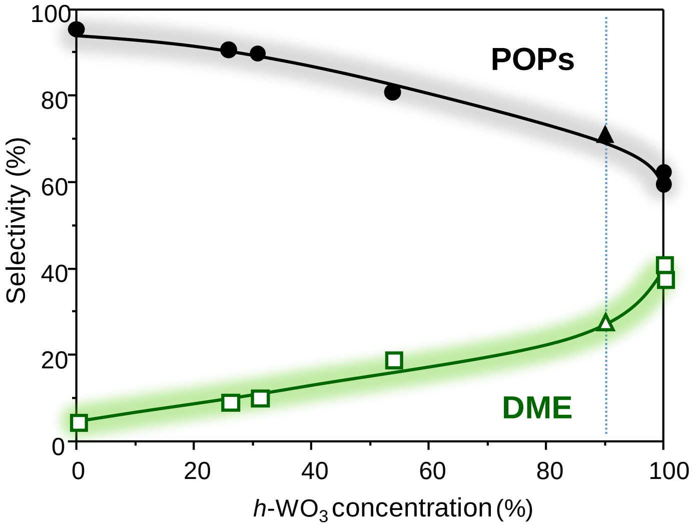

Figure 3.12. Selectivity to DME (green empty symbols) and to partial oxidation products (POPs, black full symbols) during the gas phase aerobic transformation of methanol as a function of the amount of *h*-WO_3 phase (see Table 3.2) in W-V-O catalysts (MeOH conversion = 10 %). The amount of bronze-type phase present in MT-2 pseudocrystalline sample (ca. 85 %) (green and black triangles) has been estimated from the corresponding DME and POPs selectivity during the catalytic test.

For comparative purposes, the catalytic properties in the aerobic transformation of methanol of an undoped hexagonal tungsten bronze (HTB) are also included in **Table 3.3**. This catalyst presents an initial selectivity to DME of 98.4 %, pointing out its mostly pure acid character. The incorporation of vanadium within the *h*-WO_3 type phase leads to the generation of the redox function, as it can be inferred from the increase in the selectivity to POPs. Moreover, the incorporation of vanadium also leads to a higher specific activity of the catalysts, especially at high reaction temperatures (**Table 3.3**) (**Fig. 3.10**, **B**). This increase in the activity can be explained in terms of the corresponding activation energies of the acid and redox processes. In this regard, the redox pathway would present a higher activation energy than the acid one, what would explain the higher increase in the specific activity with the reaction temperature observed in the case of the catalysts with the highest selectivity to POPs (**Table 3.3**) [42]. In fact, catalysts showing a higher selectivity to POPs present also a higher catalytic activity per unit area (**Fig. 3.13**).

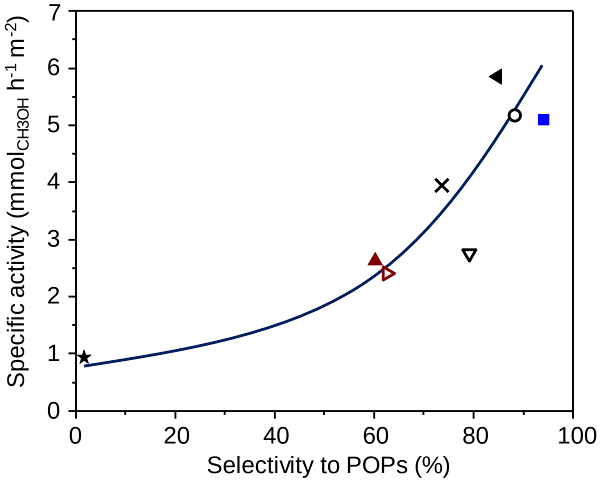

Figure 3.13. Variation of the specific activity with the selectivity to partial oxidation products (POPs) at 280 °C in the aerobic transformation of methanol for the catalysts in Table 3.3. HTB (★); MT-1 (▲); MT-2 (**X**); T-1 (▷); T-2 (◀); T-3 (○); T-4 (■); T-5 (▽).

Interestingly, the presence of *h*-WO_3 phase in W-V-O catalysts leads to a multifunctional acid-redox catalytic behavior, in which the acid character of the materials depends on the concentration of the hexagonal tungsten bronze phase. A maximum DME selectivity of ca. 50 % can be achieved with monophasic *h*-WO_3-type catalysts (**Fig. 3.12**). Therefore, the bronze-type phase content in sample MT-2 (which presents a pseudocrystalline crystal structure, see **Fig. 3.1,** pattern *b*) can be estimated from selectivity values to DME and POPs. The extrapolated value (see triangles in **Fig. 3.12**) gives a bronze phase content equivalent to a *h*-WO_3 concentration of 88%. In fact, a slight decomposition into *m*-WO_3 of the pseudocrystalline phase is observed by XRD after heat treatment (**Fig. 3.1 B**, pattern *b*).

3.3.2. Gas phase aerobic transformation of glycerol

The multifunctional acid-redox properties seem to be crucial to develop selective catalysts for glycerol oxidative dehydration into acrylic acid [13-15, 23]. The reaction undergoes via two consecutive reaction steps that take place on the catalytic surface [13]. Firstly, glycerol undergoes a double dehydration process on acid sites (mainly Brönsted-type) leading to acrolein [44], which is then transformed into acrylic acid on redox sites (i.e. V^{4+} and V^{5+} species, likely via structural O^{2-} sites by a Mars-van Krevelen mechanism) [45]. For this purpose, it is necessary that both redox and acid sites work in a cooperative way at the same reaction conditions, in order to couple both consecutive acid and redox steps in a one-pot system.

Table 3.4 compares glycerol conversion and the selectivity to the main reaction products obtained during the aerobic transformation of glycerol, by using three selected W-V-O catalysts, which present different percentage of *h*-WO_3-type phase. Moreover, the results obtained over a V-free hexagonal tungsten bronze catalyst (HTB, with an *h*-WO_3 type structure) are also included in the table. All the materials show total conversion of glycerol under the reaction conditions used. It can be noted that V-free HTB catalyst shows a selectivity to acrolein of 77 %, what underlines its pure acid character (**Table 3.4**). When vanadium is incorporated in the materials, a decrease in acrolein production is observed, together with a concomitant increase in acrylic acid and carbon oxides formation, due to the consecutive transformation of acrolein on redox sites [46]. It is worth noting that W-V-O catalyst with a phase composition of 100 % *h*-WO_3 displays the highest acrylic acid selectivity and the lowest formation of carbon oxides (**Table 3.4**).

Table 3.4. Catalytic properties of W-V-O catalysts in the aerobic transformation of glycerol.

Sample	h-WO_3 phase content (%) [b]	Glycerol conversion (%) [c]	Selectivity (%) [c]		
			Acrolein	Acrylic acid	CO_x
HTB [a]	100	100	77.8	0.14	10.9
MT-1	100	100	34.1	15.1	32.9
T-5	54	100	18.0	7.8	50.4
T-4	0	100	12.4	4.5	55.2

[a] V-free hexagonal tungsten bronze material with an *h*-WO_3-type structure. [b] h-WO_3 phase content in heat-treated samples. [c] Reaction conditions: 320 ºC, glycerol/oxygen molar ratio, 4/2.

The variation of the selectivity to the main reaction products (acrylic acid and acrolein, AA + AC; and carbon oxides, CO_x), and acrylic acid/acrolein selectivity ratio (AA/AC) as a function of *h*-WO_3 phase content in W-V-O is presented in **Figure 3.14**. It can be observed that the presence of V-containing *h*-WO_3-type phase crystals promotes the formation of both acrolein (AC) and acrylic acid (AA). On the other hand, lower amounts of the hexagonal phase (i.e. higher amounts of *m*-WO_3 phase) lead to a lower formation of oxygenated products (AA and AC), and a concomitant increase of the selectivity to carbon oxides. Also, a higher concentration of *h*-WO_3 favors the selective transformation of acrolein into acrylic acid in the consecutive reaction, leading to higher AA/AC ratios at the same reaction conditions (**Fig. 3.14**, red stars).

These results are in agreement with the reducibility of V^{5+} species observed in H_2-TPR profiles for phase pure *m*-WO_3 and *h*-WO_3 catalysts (**Fig. 3.9**). In this regard, vanadium species in *h*-WO_3 show a higher reducibility, what would favor the oxidation via O^{2-} structural species, leading to the partial oxidation of AC to AA. On the contrary, the lower reducibility observed for V sites in phase pure *m*-WO_3 would favor an oxidation mechanism via O^- and/or O^{2-} adsorbed species, what would lead to total oxidation to CO_x rather than partial oxidation [46].

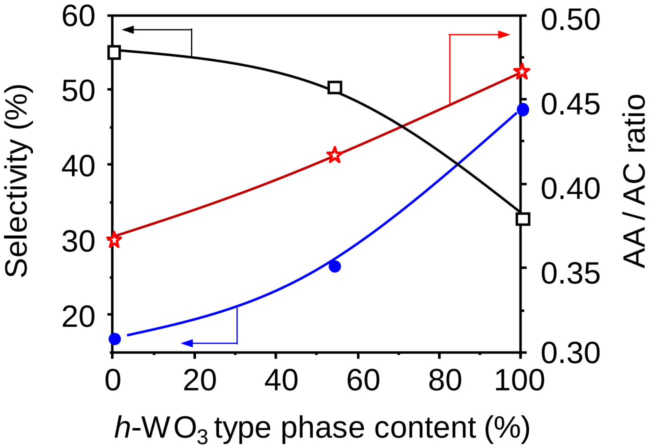

Figure 3.14. Variation of the selectivity to acrolein + acrylic acid (AC+AA, blue circles), the selectivity to carbon oxides (CO_x, black squares) and the AA/AC ratio (red stars) as a function of *h*-WO_3 type phase content in W-V-O catalysts in the gas phase aerobic transformation of glycerol. Reaction conditions: T = 320 °C; Gly/H_2O/O_2/N_2/He molar ratio of 2/40/4/15/39; contact time, W/F, of 81 g_{cat} h mol_{gly}^{-1}.

Moreover, not only vanadium sites in *m*-WO_3 show a lower capacity for partial oxidation than those in *h*-WO_3 type phase. A low acid character of *m*-WO_3-containing W-V-O catalyst (T-4 sample) can be concluded, as deduced from TPD-NH_3 results (**Fig. 3.7**, A) as well as from its catalytic performance in the aerobic transformation of methanol (i.e. very low selectivity to dimethyl ether) (**Figs. 3.11**, **3.12** and **3.13**) (**Table 3.3**). All these results suggest an important drawback in the first reaction step in glycerol transformation (i.e. the double dehydration of glycerol to acrolein), at high concentrations of *m*-WO_3 phase.

Accordingly, these weak acid characteristics must give rise to a low selectivity to acrolein, favoring the selectivity to heavy by-products in the first reaction step [13]. This low initial selectivity to acrolein also penalizes the final acrylic acid selectivity, which is formed in the consecutive step.

3.4. General Remarks

In this chapter, the influence of the phase composition (*m*-WO_3 and *h*-WO_3) on the multifunctional acid-redox properties of W-V-O catalysts has been underlined. By selecting different W-, V-, and NH_4^+-precursors, several W-V-O catalysts with similar composition but different *m*-WO_3 and *h*-WO_3 phase contents were obtained by hydrothermal synthesis. In addition, the materials display also different morphologies and thermal stabilities.

It has been observed that block-shaped particles undergo higher thermal decomposition of the initial *h*-WO_3-type phase to *m*-WO_3-type polymorph, while oxides with 1D morphologies (ascribed to bronze-type phases, mainly with rod and needle-shaped crystals), display a higher stability to thermal treatments, maintaining their *h*-WO_3 crystal structure in a higher extent.

The aerobic transformation of methanol on W-V-O oxides gave us important information about the multifunctional acid-redox properties of the materials. Phase pure *m*-WO_3 W-V-O catalyst presents a high selectivity to partial oxidation products (S_{POPs} = 98 %) and a very low selectivity to dimethyl ether (DME), what indicates a very low concentration of acid sites (as it was demonstrated by TPD-NH_3). At higher concentrations of *h*-WO_3 phase in the catalysts, the initial selectivity to DME progressively increases, reaching a selectivity to both DME and POPs of ca. 50 % for the catalysts containing a 100 % of *h*-WO_3. This means that the acid functionality is progressively generated as the amount of *h*-WO_3 in the catalysts increases.

This has important consequences in the catalytic performance in the aerobic transformation of glycerol, in which the modulation of the acid and redox functionality is a key point to maximize the selectivity to acrylic acid in a one-pot process. The catalytic tests show that the absence of acid sites in *m*-WO_3-type phase W-V-O catalyst has a negative effect on the selectivity to acrolein (which goes through the reaction of glycerol on surface Brönsted acid sites) and, consequently, also on the selectivity to acrylic acid (which is obtained by acrolein oxidation in the consecutive reaction step). Then, the presence of a hexagonal tungsten bronze type (*h*-WO_3) phase in W-V-O catalysts, in which acid and redox functions coexist and act in a cooperative way, increases the selectivity to acrolein in the first reaction step and to acrylic acid in the consecutive step. In fact, the AA/AC ratio also increases with the concentration of *h*-WO_3 type phase in the catalysts, what means that the redox sites on *h*-WO_3 are more selective towards partial oxidation of acrolein into acrylic acid. On the other hand, redox sites in *m*-WO_3 type W-V-O tend to produce essentially carbon oxides, being less selective in the partial oxidation step.

3.5. References

[1] Z.-F. Huang, J. Song, L. Pan, X. Zhang, L. Wang, J.-J. Zou, *Tungsten oxides for photocatalysis*, Electrochemistry, and Phototherapy, Advanced Materials, 27 (2015) 5309-5327.

[2] N. Haldolaarachchige, Q. Gibson, J. Krizan, R.J. Cava, *Superconducting properties of the K_xWO_3 tetragonal tungsten bronze and the superconducting phase diagram of the tungsten bronze family*, Physical Review B, 89 (2014) 104520/104521-104520/104526.

[3] H. Long, W. Zeng, H. Zhang, *Synthesis of WO_3 and its gas sensing: a review*, Journal of Materials Science: Materials in Electronics, 26 (2015) 4698-4707.

[4] J.D. Guo, M.S. Whittingham, *Tungsten oxides and bronzes: synthesis, diffusion and reactivity*, International Journal of Modern Physics B, 7 (1993) 4145-4164.

[5] Z. Zhang, J. Liu, J. Gu, L. Su, L. Cheng, *An overview of metal oxide materials as electrocatalysts and supports for polymer electrolyte fuel cells*, Energy & Environmental Science, 7 (2014) 2535-2558.

[6] M.F. Weber, A.J. Bevolo, H.R. Shanks, G.C. Danielson, *Electrocatalytic activity of cubic sodium tungsten bronze. I. Effects of platinum doping, anodization, and platinum pre-electrolysis of the electrolyte*, Journal of the Electrochemical Society, 128 (1981) 996-1003.

[7] B. Wickman, M. Wesselmark, C. Lagergren, G. Lindbergh, *Tungsten oxide in polymer electrolyte fuel cell electrodes-A thin-film model electrode study*, Electrochimica Acta, 56 (2011) 9496-9503.

[8] T. Maiyalagan, B. Viswanathan, *Catalytic activity of platinum/tungsten oxide nanorod electrodes towards electro-oxidation of methanol*, Journal of Power Sources, 175 (2008) 789-793.

[9] J. Song, Z.-F. Huang, L. Pan, J.-J. Zou, X. Zhang, L. Wang, *Oxygen-deficient tungsten oxide as versatile and efficient hydrogenation catalyst*, ACS Catalysis, 5 (2015) 6594-6599.

[10] Y. Liu, S. Shrestha, W.E. Mustain, *Synthesis of nanosize tungsten oxide and its evaluation as an electrocatalyst support for oxygen reduction in acid media*, ACS Catalysis, 2 (2012) 456-463.

[11] G. Li, C. Guo, M. Yan, S. Liu, *Cs*$_x$*WO*$_3$ *nanorods: Realization of full-spectrum-responsive photocatalytic activities from UV, visible to near-infrared region*, Applied Catalysis B: Environmental, 183 (2016) 142-148.

[12] P. Botella, B. Solsona, E. Garcia-Gonzalez, J.M. Gonzalez-Calbet, J.M. Lopez Nieto, *The hydrothermal synthesis of tetragonal tungsten bronze-based catalysts for the selective oxidation of hydrocarbons*, Chemical Communications (2007) 5040-5042.

[13] M.D. Soriano, P. Concepcion, J.M. Lopez Nieto, F. Cavani, S. Guidetti, C. Trevisanut, *Tungsten-Vanadium mixed oxides for the oxidehydration of glycerol into acrylic acid*, Green Chemistry, 13 (2011) 2954-2962.

[14] M.D. Soriano, A. Chieregato, S. Zamora, F. Basile, F. Cavani, J.M. Lopez Nieto, *Promoted hexagonal tungsten bronzes as selective catalysts in the aerobic transformation of alcohols: glycerol and methanol*, Topics in Catalysis, 59 (2016) 178-185.

[15] A. Chieregato, M.D. Soriano, F. Basile, G. Liosi, S. Zamora, P. Concepcion, F. Cavani, J.M. Lopez Nieto, *One-pot glycerol oxydehydration to acrylic acid on multifunctional catalysts: Focus on the influence of the reaction parameters in respect to the catalytic performance*, Applied Catalysis B: Environmental, 150-151 (2014) 37-46.

[16] D. Nagy, D. Nagy, I.M. Szilagyi, X. Fan, *Effect of the morphology and phases of* WO_3 *nanocrystals on their photocatalytic efficiency*, RSC Advances, 6 (2016) 33743-33754.

[17] S. Lin, Y. Guo, X. Li, Y. Liu, *Glycine acid-assisted green hydrothermal synthesis and controlled growth of* WO_3 *nanowires*, Materials Letters, 152 (2015) 102-104.

[18] B. Miao, W. Zeng, S. Hussain, Q. Mei, S. Xu, H. Zhang, Y. Li, T. Li, *Large scale hydrothermal synthesis of monodisperse hexagonal* WO_3 *nanowire and the growth mechanism*, Materials Letters, 147 (2015) 12-15.

[19] A.C. Marques, L. Santos, M.N. Costa, J.M. Dantas, P. Duarte, A. Gonçalves, R. Martins, C.A. Salgueiro, E. Fortunato, *Office paper platform for bioelectrochromic detection of electrochemically active bacteria using tungsten trioxide nanoprobes*, Scientific Reports, 5 (2015) 9910.

[20] A. Magnéli, *Studies on the Hexagonal Tungsten Bronzes of Potassium, Rubidium and Cesium*, Acta Chemica Scandinavica, 7 (1953) 315-324.

[21] A. Magnéli, B. Blomberg, *Contribution to the knowledge of the alkali tungsten bronzes*, Acta Chemica Scandinavica, 5 (1951) 372-378.

[22] P.G. Dickens, A.C. Halliwell, D.J. Murphy, M.S. Whittingham, *Preparation and characterization of a hexagonal ammonium tungsten bronze phase* $(NH_4)WO_3$, Transactions of the Faraday Society, 67 (1971) 794-800.

[23] A. Chieregato, M.D. Soriano, E. García-González, G. Puglia, F. Basile, P. Concepción, C. Bandinelli, J.M. López Nieto, F. Cavani, *Multielement crystalline and pseudocrystalline oxides as efficient catalysts for the direct transformation of glycerol into acrylic acid*, ChemSusChem, 8 (2015) 398-406.

[24] M. Sanchez Sanchez, F. Girgsdies, M. Jastak, P. Kube, R. Schlögl, A. Trunschke, *Aiding the self-assembly of supramolecular polyoxometalates under hydrothermal conditions to give precursors of complex functional oxides*, Angewandte Chemie International Edition, 51 (2012) 7194-7197.

[25] C.D. Vanderpool, M.B. MacInnis, J.C. Patton, Patent, US3936362A, 1976.

[26] E. Garcia-Gonzalez, M.D. Soriano, E. Urones-Garrote, J.M. Lopez Nieto, *On the origin of the spontaneous formation of nanocavities in hexagonal bronzes (W,V)O_3*, Dalton Transactions, 43 (2014) 14644-14652.

[27] I.M. Szilágyi, J. Madarász, G. Pokol, P. Király, G. Tárkányi, S. Saukko, J. Mizsei, A.L. Tóth, A. Szabó, K. Varga-Josepovits, *Stability and controlled composition of hexagonal WO_3*, *Chemistry of Materials*, 20 (2008) 4116-4125.

[28] C. Guo, S. Yin, P. Zhang, M. Yan, K. Adachi, T. Chonan, T. Sato, *Novel synthesis of homogenous Cs_xWO_3 nanorods with excellent NIR shielding properties by a water controlled-release solvothermal process*, Journal of Materials Chemistry, 20 (2010) 8227-8229.

[29] P. Botella, E. García-González, J.M. López Nieto, J.M. González-Calbet, *MoVTeNbO multifunctional catalysts: Correlation between constituent crystalline phases and catalytic performance*, Solid State Sciences, 7 (2005) 507-519.

[30] Y. Kong, H. Sun, X. Zhao, B. Gao, W. Fan, *Fabrication of hexagonal/cubic tungsten oxide homojunction with improved photocatalytic activity*, Applied Catalysis A: General, 505 (2015) 447-455.

[31] P. Botella, B. Solsona, J.M. Lopez Nieto, P. Concepcion, J.L. Jorda, M.T. Domenech-Carbo, *Mo-W-containing tetragonal tungsten bronzes through isomorphic substitution of molybdenum by tungsten*, Catalysis Today, 158 (2010) 162-169.

[32] W.P. Griffith, P.J.B. Lesniak, *Raman studies on species in aqueous solutions. Part III. Vanadates, molybdates, and tungstates*, Journal of the Chemical Society A: Inorganic, Physical, Theoretical, (1969) 1066-1071.

[33] Z. Zheng, B. Yan, J. Zhang, Y. You, C.T. Lim, Z. Shen, T. Yu, *Potassium tungsten bronze nanowires: polarized micro-Raman*

scattering of individual nanowires and electron field emission from nanowire films, Advanced Materials, 20 (2008) 352-356.

[34] C. Sanchez, J. Livage, G. Lucazeau, *Infrared and Raman study of amorphous* V_2O_5, Journal of Raman Spectroscopy, 12 (1982) 68-72.

[35] I.M. Szilagyi, J. Madarasz, G. Pokol, F. Hange, G. Szalontai, K. Varga-Josepovits, A.L. Toth, *The effect of* K^+ *ion exchange on the structure and thermal reduction of hexagonal ammonium tungsten bronze,* Journal of Thermal Analysis Calorimetry, 97 (2009) 11-18.

[36] N.E. Fouad, A.K.H. Nohman, M.A. Mohamed, M.I. Zaki, *Characterization of ammonium tungsten bronze* $[(NH_4)_{0.33}WO_3]$ *in the thermal decomposition course of ammonium paratungstate,* Journal of Analytical and Applied Pyrolysis, 56 (2000) 23-31.

[37] L. Huo, H. Zhao, F. Mauvy, S. Fourcade, C. Labrugere, M. Pouchard, J.-C. Grenier, *Synthesis and mixed conductivity of ammonium tungsten bronze with tunneling structures,* Solid State Sciences, 6 (2004) 679-688.

[38] D. Perra, N. Drenchev, K. Chakarova, M.G. Cutrufello, K. Hadjiivanov, *Remarkable acid strength of ammonium ions in zeolites: FTIR study of low-temperature CO adsorption on* NH_4FER, RSC Advances, 4 (2014) 56183-56187.

[39] K. Oshihara, T. Hisano, W. Ueda, *Catalytic oxidative activation of light alkanes over Mo-V-based oxides having controlled surface*, Topics in Catalysis, 15 (2001) 153-160.

[40] J.R. Sohn, M.Y. Park, *Characterization of zirconia-supported tungsten oxide catalyst*, Langmuir, 14 (1998) 6140-6145.

[41] I.E. Wachs, K. Routray, *Catalysis science of bulk mixed oxides*, ACS Catalysis, 2 (2012) 1235-1246.

[42] J.M. Tatiboueet, *Methanol oxidation as a catalytic surface probe*, Applied Catalysis A: General, 148 (1997) 213-252.

[43] M. Badlani, I. Wachs, *Methanol: A "smart" chemical probe molecule*, Catalysis Letters, 75 (2001) 137-149.

[44] B. Katryniok, S. Paul, V. Belliere-Baca, P. Rey, F. Dumeignil, *Glycerol dehydration to acrolein in the context of new uses of glycerol*, Green Chemistry, 12 (2010) 2079-2098

[45] G. Centi, F. Cavani, F. Trifirò, *New aspects of the mechanisms of selective oxidation and structure/activity relationships*, in: *Selective oxidation by heterogeneous catalysis*, Springer Science 2001, New York, pp. 363-495.

[46] B. Katryniok, T. Bonnotte, F. Dumeignil, S. Paul, *Production of bioacrylic acid*, in: *Chemicals and fuels from bio-based building blocks,* Volume I, Wiley-VCH Verlag GmbH & Co 2016, pp. 207-244.

Chapter 4

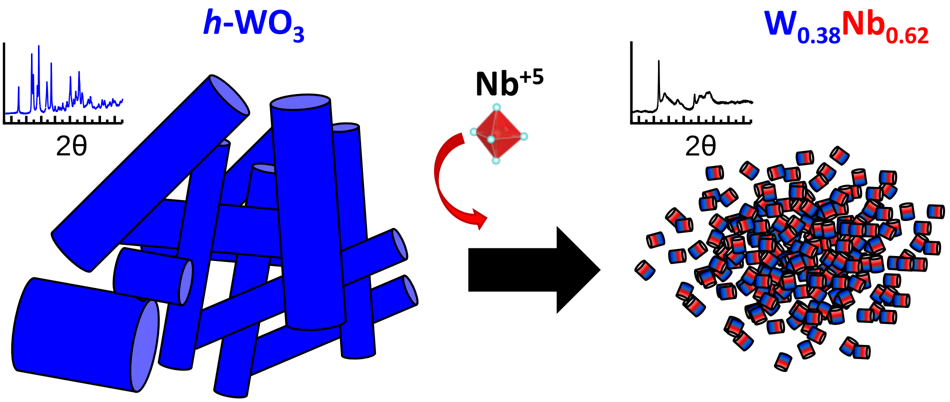
h-WO3
2θ
Nb+5
2θ
W0.38Nb0.62

W-Nb-O bronzes as catalysts for the valorization of biomass-derived feedstocks

4.1. Previous considerations

Biomass is considered one of the main renewable and sustainable alternatives to the use of fossil sources for the production of chemicals and fuels [1, 2]. Among all the possibilities that this feedstock offers, the transesterification of animal fats and vegetable oils is the more extended strategy for biomass valorization, leading to the so-called bio-diesel [3]. In fact, this bio-diesel is nowadays used as automotive fuel. However, the production of these fatty acid methyl esters (FAMEs) by transesterification is accompanied by the generation of high amounts of glycerol as a by-product. This crude glycerol comprises the 10 wt.% of the global bio-diesel production, which is expected to reach 36.9 million tons in 2020 (i.e. 3.69 million tons of glycerol) [4].

Another alternative for the valorization of biomass feedstocks is based on the fast pyrolysis of lignocellulosic biomass [5, 6]. Unlike bio-diesel obtained via transesterification, fast pyrolysis bio-oils are not suitable for combustion engines, due to their undesired physicochemical properties, like high water and oxygen content, high viscosity and acidity. These unfavorable features also prevent their storage for long-term uses, and limit their applicability to fuel in power and heat generation plants. For other purposes, upgrading strategies are necessary [7, 8]. The most extended upgrading approach is hydrotreating, using CoMo, NiMo and/or NiW based catalysts [9]. Unfortunately, these methodologies imply high H_2 and energy consumptions, and shows a low fuel yield.

Recently, an alternative upgrading strategy for pyrolysis-derived bio-oils has been proposed, which comprises co-processing, water addition and a liquid-liquid separation stage, which leads to two separated phases [10]. The organic phase can be upgraded for its direct use as liquid fuel; while the aqueous fraction, composed mainly by short chain oxygenates, would remain as a residue, in a similar way that glycerol does in the case of transesterification processes.

The valorization of both waste streams would be of great interest, in order to improve the sustainability and atom economy of both methods.

As it was commented in the introduction, tungsten bronze-based materials offer a vast variety of possibilities, in terms of composition and structural versatility [11]. Nonetheless, these systems were also very useful from the fundamental point of view. In this regard, the deep understanding of their defect chemistry paved the way to extend the knowledge on transition metal oxides. Particularly, they were very useful in the development of electron microscopy techniques during the second half of the past century [12-15].

In the following chapter the attention has been focused on W-Nb-O system (WO_3-Nb_2O_5), in which the Nb concentration has been varied systematically (Nb/(W+Nb)= 0-1). The structural implications of the isomorphic substitution of W by Nb have been studied, as well as its effect on the textural and acid properties of the materials. The mixed oxides were prepared hydrothermally and heat-treated at 550 ºC under N_2 flow (see point 2.1.1 in Experimental section). In the case of Nb-free *h*-WO_3, i.e. Nb/(W+Nb)= 0, the catalyst was heat-treated at 450 ºC in order to avoid the phase transition to monoclinic *m*-WO_3-type phase, which displays a low surface area and low acid features [16, 17]. The samples are named as W-Nb-*x*, being “*x*” the specific Nb/(W+Nb) ratio in each catalyst (determined by XEDS of large areas of the solids).

The main physicochemical features of the catalysts are summarized in **Table 4.1**. The whole series has been tested in the transformation of two biomass-based raw materials: a) the aerobic transformation of glycerol and; b) the transformation of short chain oxygenates in aqueous phase by C-C bond formation reactions. Both feedstocks can be considered as waste effluents in bio-based processes, hence the interest in their transformation into added-value chemicals.

4.2. Physicochemical characterization of W-Nb-O oxides

An in-depth study of the physicochemical characteristics of W-Nb-O mixed oxides has been undertaken. The effect of the incorporation of Nb into the hexagonal tungsten bronze framework on the structural, textural and acid properties of the materials is discussed in the following sections.

Table 4.1. Main characteristics of W-Nb-O mixed oxides.

Sample	Nb/(W+Nb) atomic ratio[a]	Specific surface area (m^2 g^{-1}) [b]	Average pore size (nm) [c]	Mesopore volume (cm^3 g^{-1}) [c]
W-Nb-0	0.00	28	17.2	0.045
W-Nb-0.29	0.29	38	11.1	0.050
W-Nb-0.40	0.40	67	13.6	0.095
W-Nb-0.53	0.53	102	14.6	0.176
W-Nb-0.62	0.62	124	5.9	0.216
W-Nb-0.80	0.80	129	5.4	0.192
W-Nb-0.95	0.95	129	3.7	0.130
W-Nb-1	1.00	70	3.5	0.061

[a] Obtained by XEDS. [b] Calculated by Brunauer-Emmet-Teller method from N_2-adsorption isotherms. [c] Obtained by BJH method from N_2-adsorption isotherms.

4.2.1. Structural features of W-Nb-O materials

Powder X-ray diffraction profiles of W-Nb-O catalysts are displayed in **Figure 4.1 A**. Diffraction lines of undoped sample (i.e. W-Nb-0) are characteristic of the hexagonal tungsten bronze h-WO_3 phase of tungsten oxide (JCPSD: 01-85-2459) (**Fig. 4.1 A**, pattern *a*). This is a well-ordered material, characterized by: i) vertex sharing WO_6 octahedra ordered along the three crystallographic directions; and ii) the presence of hexagonal and trigonal channels along *c*-axis (i.e. displayed along [001] direction) [16, 18]. It can be observed that the isomorphic substitution of Nb for W causes some changes in the diffraction profiles, what indicates some structural modifications (**Fig. 4.1 A**, patterns *b*-*h*). Particularly, the intensity of diffraction lines with Miller indexes h and/or $k \neq 0$ decreases as Nb content in the oxides increases.

At low Nb/(W+Nb) concentration, the materials preserve the hexagonal tungsten bronze structure, but with a notably decrease in the intensity of those abovementioned Bragg signals (i.e. with h and/or $k \neq 0$) (**Fig. 4.1 A**, patterns *b* and *c*). For higher Nb contents (Nb/(W+Nb) > 0.53), only two well defined diffraction maxima can be observed, which are assigned to (002) and (004) peaks of the h-WO_3 phase (**Fig. 4.1 A**, patterns *d*-*h*). As indicated previously (see Chapter 3), both diffraction maxima (at 2θ ca. 23° and 46 °) are present in all bronze-type structure and every ReO_3-type related structural type, due to the presence of vertex sharing octahedra along one direction. In addition, broad maxima are also present, around 2θ values of 27°, 35°, 50° and 55° (**Fig. 4.1 A**, patterns *d*-*h*).

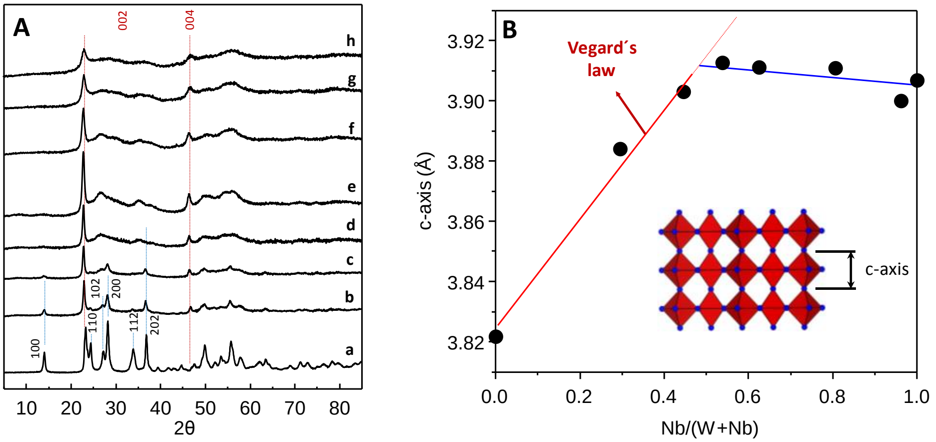

Figure 4.1. A) XRD patterns of W-Nb-O oxides. B) Variation of c-axis (considered as the distance between two vertex sharing octahedra) as a function of Nb in W-Nb-O oxides. a) W-Nb-0; b) W-Nb-0.29; c) W-Nb-0.40; d) W-Nb-0.53; e) W-Nb-0.62; f) W-Nb-0.80; g) W-Nb-0.95; h) W-Nb-1.

All these features observed by XRD can be ascribed to a loss of periodicity along *ab* plane of the crystal structure, due to the incorporation of Nb within the framework. Despite this loss of long-range order in the materials, the connectivity between octahedra is preserved. This way, the isomorphic substitution of Nb for W in the hexagonal tungsten bronze structure promotes the formation of a pseudo-crystalline mixed oxide, ordered just along c-axis, which has already been observed in other systems based on Mo, Nb and V [19-21]. The magnitude of c-axis, considering it as the distance between vertex sharing octahedra, was estimated from (002) maximum in powder XRD diffraction patterns (**Fig. 4.1 B**). Until Nb/(W+Nb)= 0.53, c-axis increases linearly with Nb-content, following Vegard´s law. This is the expected variation considering the crystal radius of W^{6+}, W^{5+} and Nb^{5+} (0.74, 0.76 and 0.78 Å respectively). On the other hand, for higher Nb-contents (i.e. Nb/(W+Nb) > 0.53), which include all pseudocrystalline oxides, c-axis remains constant, and no longer increases (**Fig. 4.1 B**).

Raman spectra of W-Nb-O mixed oxides are shown in **Figure 4.2**. Undoped W-Nb-O sample presents three high intensity Raman bands at approximately 648, 691 and 780 cm^{-1} which can be assigned to O-W-O stretching vibrations of the hexagonal phase of tungsten oxide (**Fig. 4.2**, spectrum *a*) [22]. Low intensity bands at low frequencies (331, 291 and 261 cm^{-1}) are also observed, which have been attributed to deformation O-W-O lattice modes (**Fig. 4.2**, spectrum *a*) [22]. After doping with niobium, a new broad band in the range 900-1000 cm^{-1} appears, assigned to M=O stretching vibrations (M: W, Nb) (**Fig. 4.2**, spectra *b* to *h*) [23].

The intensity of the signal at 780 cm^{-1} decreases also when increasing Nb content, and a new band appears at 750 cm^{-1}, which progressively shifts to lower frequencies, until 709 cm^{-1}. This band can be ascribed to the symmetric stretching mode of distorted NbO_6 octahedra in niobium oxides, and its shift is in line with niobium enrichment along the series. Additionally, the bands below 400 cm^{-1}, assigned to bending modes, become broader at increasing Nb/(W+Nb) contents, likely due to an increase in the structural disorder. In addition, a shift of the signal at 258 cm^{-1} is observed, until 234 cm^{-1} for W-Nb-1 sample. This band at 234 cm^{-1} can be attributed to Nb-O-Nb bending modes [24].

All these observations suggest the isomorphic substitution of W by Nb within the oxide bronze framework. Since Nb-free hexagonal bronze is a partially reduced phase, it should contain tungsten in not fully oxidized state, (i.e. W^{5+} or W^{4+} species). Then, an initial substitution of W^{5+} by Nb^{5+} species could be expected for two main reasons: i) they present the same oxidation state (i.e. 5+); and ii) they show similar crystal radius (0.78 and 0.76 Å for Nb^{5+} and W^{5+} respectively).

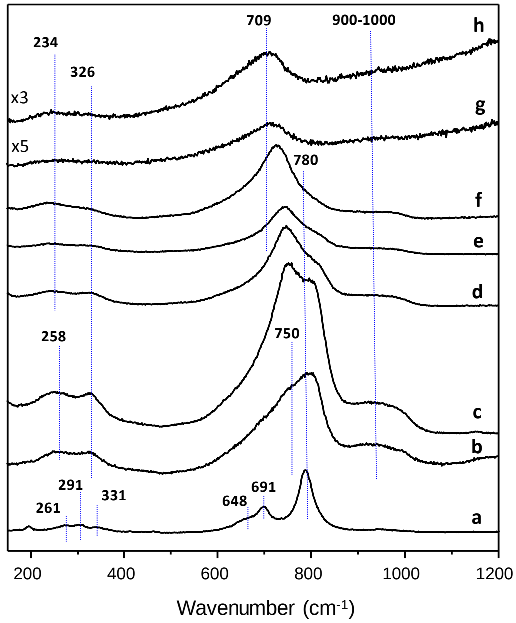

Figure 4.2. Raman profiles of W-Nb-O oxides: a) W-Nb-0; b) W-Nb-0.29; c) W-Nb-0.40; d) W-Nb-0.53; e) W-Nb-0.62; f) W-Nb-0.80; g) W-Nb-0.95; h) W-Nb-1.

In order to confirm the presence of W^{5+}/W^{6+} species, W 4*f* core level XPS spectra of undoped W-Nb-0 and doped W-Nb-0.29 oxides are presented in **Figure 4.3 A**. Two signals, corresponding to W^{6+} (B.E. W $4f_{7/2}$ = 35.9 eV) and W^{5+} (B.E. W $4f_{7/2}$ = 35.1 eV) in an octahedral coordination can be observed in the case of Nb-free sample (**Fig. 4.3 A**, spectrum *a*) [22, 25]. When Nb is incorporated, the band assigned to W^{5+} is no longer present, likely due to the isomorphic substitution by Nb^{5+} (**Fig. 4.3 A**, spectrum *b*).

To confirm XPS results, both Nb-free and Nb-containing catalysts (i.e. samples W-Nb-0 and W-Nb-0.29), were analyzed by X-ray absorption spectroscopy (XAS). Both materials show differences in the XANES W L_{III}-edge region of the spectrum, which are directly related to the electronic properties of the absorbing atom (**Figure 4.3 B**).

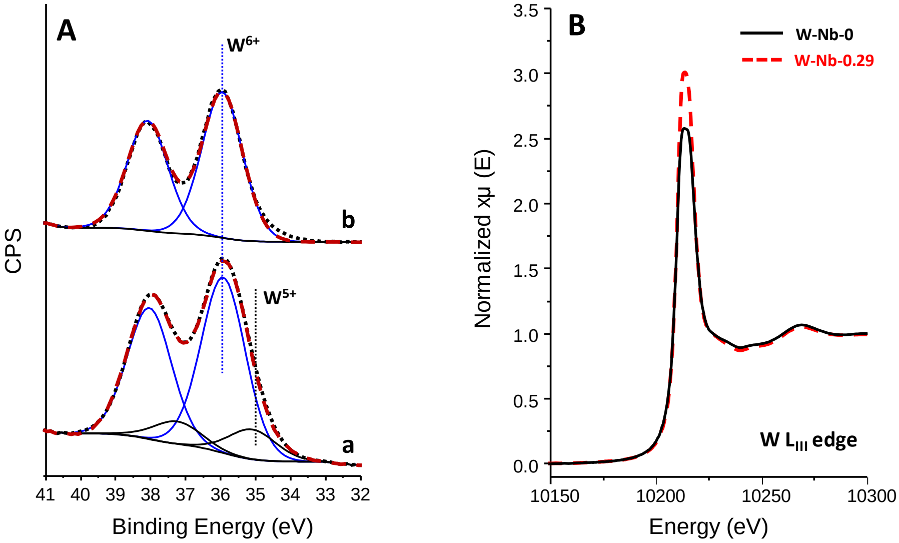

Figure 4.3. A) W 4f core-level XPS spectra of Nb-free (W-Nb-0, a) and Nb-substituted (W-Nb-0.29, b) materials. B) W L_{III}-edge XAS spectra in the XANES region of Nb-free (W-Nb-0, black line) and Nb-substituted (W-Nb-0.29, red dotted line) materials.

Specifically, Nb-free sample shows a lower white line intensity than doped W-Nb-0.29 oxide. This white line at L_{III} edge appears due to electronic transitions from $2p_{3/2}$ core level to vacant *d* states in the valence band [26]. Consequently, a higher intensity white line indicates a higher probability of absorption, i.e. a higher number of empty *d* states. In fact, the intensity of the white line is very sensitive to small variations in the electronic properties and oxidation states. The increase in the intensity of the white line in the doped material (**Fig. 4.3 B**, spectrum *b*) is in line with XPS results, suggesting the substitution of Nb^{5+} for W^{5+}: W^{5+} is a d^1 metal, and the probability of the $p \rightarrow d$ transition is lower than in the case of W^{6+}, which is a d^0 metal. This fact would also explain the higher thermal stability of Nb-containing tungsten bronze in comparison with undoped *h*-WO_3 [17]. The oxidation of W^{5+} to W^{6+} in *h*-WO_3 would promote also the phase transition *m*-WO_3 phase. Then, the isomorphic substitution of those W^{5+} species in the hexagonal tungsten bronze structure by metal species which its maximum oxidation state is lower than 6+ would preserve the partially reduced nature of the hexagonal phase, increasing the temperature range in which *h*-WO_3 structure is stable.

To confirm this hypothesis, undoped *h*-WO_3 (i.e. W-Nb-0 catalyst) was heat-treated at 550 ºC, in order to promote the phase transition to *m*-WO_3 The XRD patterns of undoped tungsten trioxide and Nb-containing W-Nb-0.29 sample (both heat-treated at 550ºC in N_2 flow) are shown in **Figure 4.4**. It can be clearly observed that undoped sample presents *m*-WO_3 (JCPSD: 43-1035) as the main crystalline phase, while Nb-doped sample retains *h*-WO_3 crystal phase after the heat-treatment.

W-Nb-O samples were further investigated by high resolution electron microscopy (HRTEM) and selected area electron diffraction (SAED) (**Figs. 4.5** and **4.6**). At low Nb content, i.e. W-Nb-0.29, the sample is composed by crystals with an average size of 50 nm, which present a hexagonal tungsten bronze structure (as it can be confirmed by the ring diffraction pattern) (**Figure 4.5 A**). The corresponding HRTEM image of this catalyst displays interplanar distances corresponding to the *h*-WO_3 phase (**Figure 4.5 B)**, and certain heterogeneity in composition, which varies from crystal to crystal in the ranges W: 82-70 at%; Nb: 18-30 at%.

Two main features can be observed when increasing Nb content up to Nb/(W+Nb) = 0.53 (**Fig. 4.5**, pictures **C** and **D**). On the one hand, an increase in the degree of disorder along *ab* plane can be noted, suggested by the disappearance of the diffraction ring corresponding to the (100) reflection of the *h*-WO_3-type structure (**Fig. 4.5**, picture **C**).

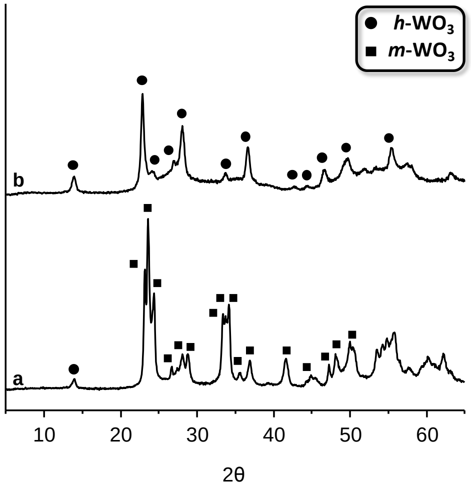

Figure 4.4. XRD patterns of undoped (a) and Nb-containing tungsten oxide (b) heat-treated at 550 ºC in N_2 flow; a) W-Nb-0; b) W-Nb-0.29.

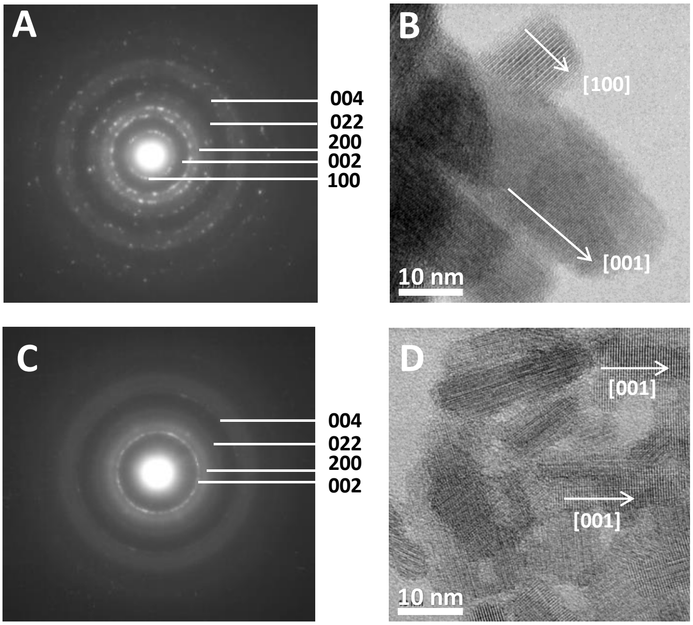
A
004
022
200
002
100
B
[100]
[001]
10 nm
C
004
022
200
002
D
[001]
[001]
10 nm

Figure 4.5. SAED patterns (A and C) and HRTEM images (B and D) of W-Nb-0.29 (A-B) and W-Nb-0.53 (C-D) mixed oxides. Miller indexes have been assigned on the basis of *h*-WO_3-type phase (JCPSD: 01-85-2459).

On the other hand, a decrease in the average particle size down to ca. 10 nm is also detected, together with some heterogeneity in chemical composition (W: 65-50 at%; Nb: 35-50 at%) (**Fig. 4.5**, picture **D**). It is worth noting that samples W-Nb-0.53 and W-Nb-0.62, showed small crystals (ca. 5 nm) in which $Cs_{0.5}Nb_{2.5}W_{2.5}O_{14}$-type structure (isostructural with the well-known orthorhombic M1-type phase catalyst for ODH and partial oxidation of short chain alkanes [27]) can be clearly recognized (**Fig. 4.6**, pictures **A** and **B)**. According to these results, it can be concluded that the use of Nb:W ratios close to 1 seems to favor the formation of the abovementioned orthorhombic bronze (M1-type phase).

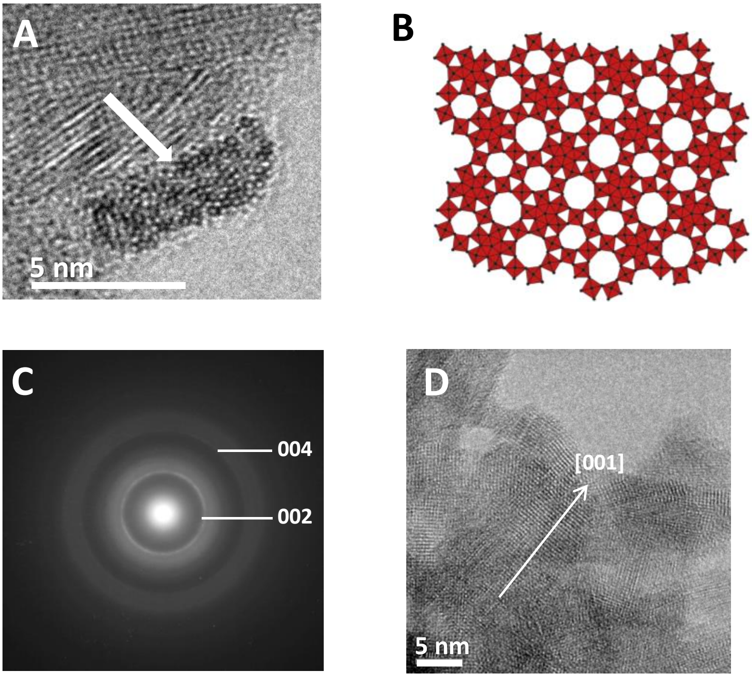

Figure 4.6. A) HRTEM image of a crystal (white arrow) in W-Nb-0.62, showing the structure along [001] direction of $Cs_{0.5}Nb_{2.5}W_{2.5}O_{14}$-type phase, also known as M1-phase. B) Representation of the *ab* plane ([001] crystallographic direction) of $Cs_{0.5}Nb_{2.5}W_{2.5}O_{14}$-type phase [27]. C) SAED ring pattern of W-Nb-0.80 sample. D) HRTEM image of W-Nb-0.80 sample. Miller indexes have been assigned based on *h*-WO_3-type phase (JCPSD: 01-85-2459).

All these features are compatible with those observed in XRD patterns, in which the presence of $Cs_{0.5}Nb_{2.5}W_{2.5}O_{14}$ -type phase can be deduced from the broad diffraction lines appearing at approximately 8º (marked with an asterisk in **Fig. 4.7**).

For higher Nb-contents (Nb/(W+Nb) ≥ 0.8), no evidences of the presence of $Cs_{0.5}Nb_{2.5}W_{2.5}O_{14}$ -type crystal phase have been found. In fact, SAED patterns of W-Nb-0.8 and W-Nb-1 oxides only display rings at the corresponding interplanar distances of (002) and (004) planes, being the rest of signals in the form of diffuse halos (**Fig. 4.6**, picture **C**).

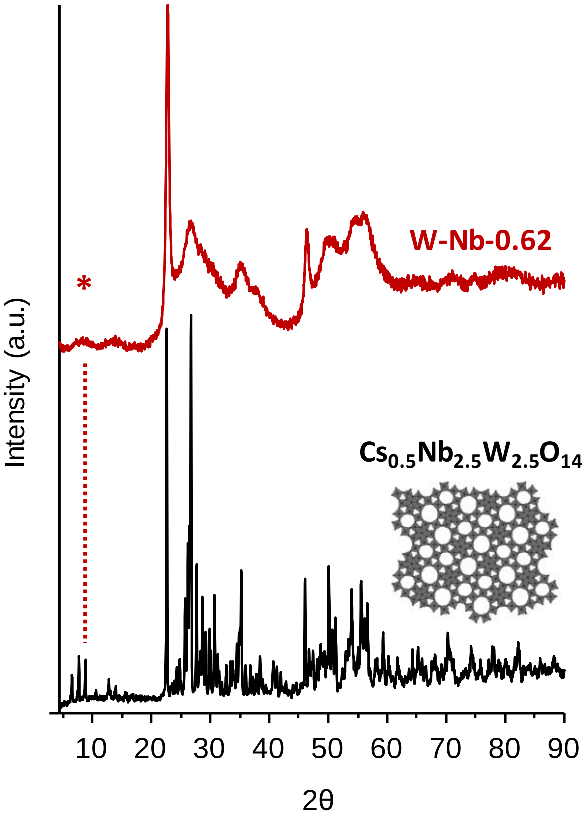

Figure 4.7. XRD patterns of hydrothermally synthesized $Cs_{0.5}Nb_{2.5}W_{2.5}O_{14}$ and W-Nb mixed oxide with Nb content of 62 at% (W-Nb-0.62 sample).

In addition, average crystal size continues its decreasing trend, being in the range of 5-10 nm size for Nb/(W+Nb) ≥ 0.8 (**Fig. 4.6**, picture **D**).

4.2.2. Textural features of W-Nb-O mixed oxides. N_2-adsorption study

Textural properties of all W-Nb oxide series have been studied by means of N_2 physisorption. **Figure 4.8** presents N_2 adsorption-desorption isotherms of W-Nb oxides, whereas the surface areas of catalysts are shown in **Table 4.1**. Samples with low Nb-contents (i.e. Nb/(W+Nb) ≤ 0.53) display type II isotherms (**Fig. 4.8**, isotherms *a* to *d*). At higher Nb-content (i.e. Nb/(W+Nb) > 0.53), a transition from type II to type IV isotherms is observed, which are typical of mesoporous materials (**Fig. 4.8**, isotherms *e* to *h*). In fact, these results can be correlated with the subsequent variation of mesopore volumes, average pore size and pore size distributions (**Table 4.1** and **Fig. 4.9**). In this way, a decrease in the average pore size can be noticed when the Nb-content in the materials increases (from 17.2 nm for W-Nb-0 sample to 3.5 nm for W-Nb-1 sample). In parallel, an increase in mesopore volumes can be observed when the Nb-content in the materials increases (**Table 4.1**). Interestingly, materials with Nb/(W+Nb) contents higher than 0.53 (i.e. those displaying type IV isotherms), present narrow pore size distributions in the range 5.3-3.5 nm (**Fig. 4.9**, *e*-*h*). However, this is no longer observed for samples with lower Nb/(W+Nb) contents, in which pore size distributions present a flat profile (**Fig. 4.9**, *a*-*d*).

A drastic decrease in the average pore size occurs when the Nb content exceeds ca. 50 %, decreasing from 14.6 to 5.9 nm, which matches with the transition between type II and type IV isotherms (**Table 4.1**). Indeed, a connection between textural properties (mainly mesoporous nature) and microstructural modifications observed by HRTEM (i.e. a decrease in the average particle size at increasing Nb concentrations in the materials) can be proposed, in which the narrow pore size distributions found at higher Nb contents could be related with the voids generated by the packed agglomeration of nanoparticles.

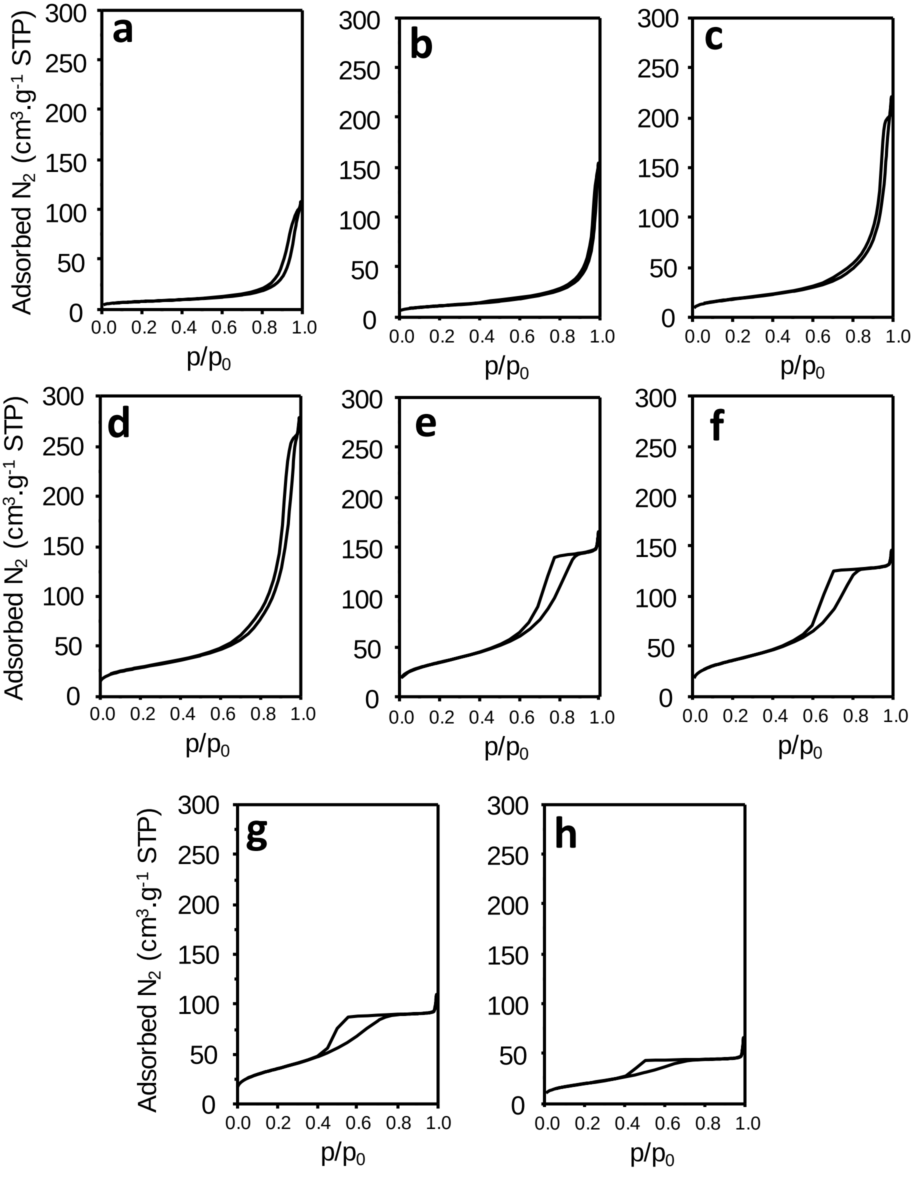

Figure 4.8. Nitrogen adsorption-desorption isotherms of W-Nb oxides. a) W-Nb-0; b) W-Nb-0.29; c) W-Nb-0.40; d) W-Nb-0.53; e) W-Nb-0.62; f) W-Nb-0.80; g) W-Nb-0.95; h) W-Nb-1.

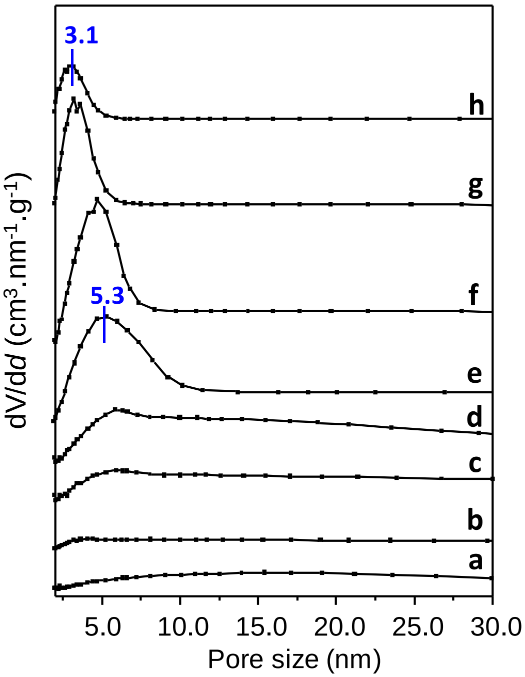

Figure 4.9. BJH pore size distributions of W-Nb oxides, calculated from the adsorption branch of N_2-adsorption-desorption isotherms. a) W-Nb-0; b) W-Nb-0.29; c) W-Nb-0.40; d) W-Nb-0.53; e) W-Nb-0.62; f) W-Nb-0.80; g) W-Nb-0.95; h) W-Nb-1.

4.2.3. Acid properties of W-Nb-O oxides. Temperature-programmed desorption and FTIR spectroscopy studies

Acid characteristics of the whole W-Nb-O series were determined by means of temperature-programmed desorption of NH_3 (TPD-NH_3) and FTIR of adsorbed pyridine. Their corresponding results are shown in **Figures 4.10 A** and **4.10 B**, respectively. In addition, the main acid characteristics are summarized in **Table 4.2**.

All the catalysts show the characteristic FTIR bands related to ring bending modes of pyridinium ion, i.e. formed by the interaction of pyridine with Brönsted acid sites (PyH^+ in **Figure 4.10 A**); and ring modes of pyridine coordinatively bonded to Lewis acid centers (PyL in **Figure 4.10 A**) [28].

It can be seen that the intensity of the band assigned to Lewis sites (PyL, appearing at ca. 1450 cm^{-1}) increases when increasing Nb-content (**Fig. 4.10**, **A**). In the same way, the intensity of the signal ascribed to Brönsted-type sites (band at ca.1538 cm^{-1}) also increases, but in a lesser extent (**Fig. 4.10**, **A**).

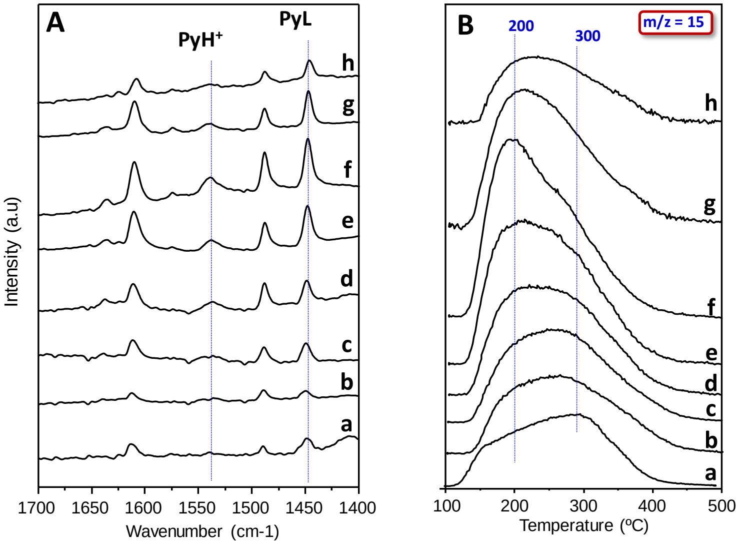

Figure 4.10. FTIR spectra of adsorbed pyridine (A) and TPD-NH_3 profiles (B) of W-Nb oxides. a) W-Nb-0; b) W-Nb-0.29; c) W-Nb-0.40; d) W-Nb-0.53; e) W-Nb-0.62; f) W-Nb-0.80; g) W-Nb-0.95; h) W-Nb-1.

TPD-NH_3 profiles of the catalysts**,** following the characteristic mass of ammonia (i.e. m/z = 15), are presented in **Figure 4.10 B**. Two main contributions to the desorption are found, at 200 and 300 ºC; which can be assigned to the desorption of NH_3 from acid sites with low and medium-high acid strength, respectively. The incorporation of Nb into the framework increases the relative intensity of the low-temperature signal, i.e. it increases the proportion of low strength acid sites, likely Lewis-type sites.

On the other hand, **Figure 4.11** shows the variation of the concentration of acid sites (**Fig. 4.11**, **A**), the density of the surface acid sites (**Fig. 4.11**, **B**) and the Brönsted/Lewis acid sites ratio (BAS/LAS) with the Nb/(Nb+W) content in the catalyst (**Fig. 4.11**, **C)**. When considering the concentration of surface acid sites per gram of catalyst (**Fig. 4.11 A**, and **Table 4.2**), it can be suggested that concentration of acid sites on the catalyst surface increases with Nb-content in the materials, reaching a maximum at a Nb/(W+Nb) ratio of 0.8.

Table 4.2 Acid characteristics of W-Nb-O mixed oxides catalysts.

Sample	**Concentration of acid sites (μmol_{py} g^{-1})** [a]	**Surface density of acid sites (μmol_{py} m^{-2})** [a]	**BAS/LAS** [a,b]
W-Nb-0	27.4	0.98	0.3
W-Nb-0.29	29.7	0.78	1.8
W-Nb-0.40	56.2	0.84	1.1
W-Nb-0.53	73.2	0.71	1.2
W-Nb-0.62	89.2	0.70	0.5
W-Nb-0.80	122.3	0.95	0.7
W-Nb-0.95	62.2	0.48	0.4
W-Nb-1	36.4	0.54	0.8

[a] From FTIR of adsorbed pyridine. [b] Brönsted/Lewis acids sites ratio.

On the contrary, the surface density of acid sites (i.e. the number of acid sites per unit area) follows the opposite trend; the number of acid sites per unit area decreases when the Nb-content increases (**Fig. 4.11 B**). This fact indicates a more pronounce effect on the surface area than in the concentration of acid sites. In this sense, surface area would increase in a higher extent than the number of acid sites. In fact, the presence of oxalate ions in the synthesis could also favor a lower particle size of the final materials. Moreover, a correlation between Nb concentration and Brönsted/Lewis acid sites ratio (BAS/LAS) has been detected (**Fig. 4.11**, **C**). It can be seen BAS/LAS progressively decreases as Nb is introduced within the oxide framework.

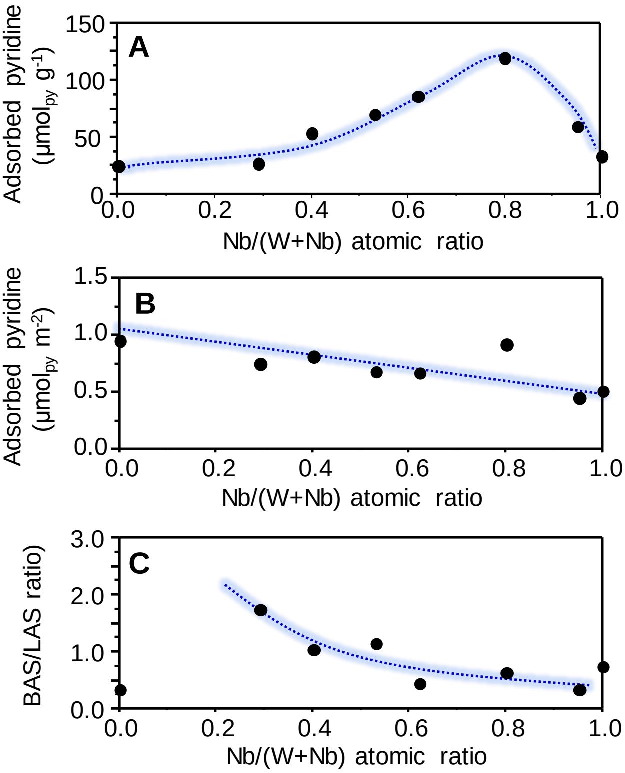

Figure 4.11. Acid characteristics of W-Nb oxides as function of Nb content. A) Concentration of acid sites. B) Surface density of acid sites. C) Brönsted/Lewis acid sites ratio (BAS/LAS).

However, undoped W-Nb-0 displays the lowest BAS/LAS ratio, which could be explained by the presence of ammonium cations into the hexagonal channels of *h*-WO_3 (/i.e. blocking Brönsted acid sites) due to the lower heat-treatment temperature applied for this sample. Indeed, the elimination of those ammonium species (mainly by heat treatments) can have two different effects: i) the generation of Brönsted acid sites [29] and, ii) the phase transition towards the monoclinic *m*-WO_3 phase of tungsten oxide [22].

In a parallel way, the acid features of selected catalysts from the series were also studied by means of low temperature (77 K) FTIR spectroscopy, using CO as basic probe molecule. At low temperatures CO molecule undergoes interactions with both Brönsted (via H-bond) and Lewis (coordinatively unsaturated sites, CUS) acid sites. This leads to frequency shifts of the characteristic υ(CO) gas phase stretching mode (2143 cm^{-1}) (see point 2.2.12 in Experimental section). In addition, CO interaction with acidic O-H surface groups leads to shifts in the original O-H stretching modes (3800-3200 cm^{-1}) to lower frequencies, what allows to study the nature of Brönsted acid sites [30].

Figure 4.12 displays the low-temperature (77 K) FTIR spectra of adsorbed CO at increasing CO equilibrium pressures (P_{COeq}) (0-5.5 mbar) in the C-O (**Fig. 4.12**, pictures **A-D**) and O-H (**Fig. 4.12**, pictures **E-H**) stretching regions for selected catalyst of W-Nb-O series. Differences in the FTIR profiles are observed between two groups of samples: i) catalysts with low Nb concentrations (W-Nb-0 and W-Nb-029) and; ii) catalysts with higher Nb contents (W-Nb-0.62 and W-Nb-1). Focusing on C-O stretching region (**Fig. 4.12**, pictures **A-D**), it can be noted that at relatively low P_{COeq} (ca. 0.020 mbar, green lines in **Fig. 4.12**), catalysts with high Nb contents display a higher amount of adsorbed CO (i.e. higher CO coverages). Considering O-H stretching region, catalysts also present different degree of O-H…CO interaction at a fixed P_{COeq}, as deduced from the different band intensities observed at an equilibrium, pressure of 0.020 mbar (green lines in **Fig. 4.12**, pictures **E-H**). Some extra features in the O-H region are found for W-Nb-0 catalysts, in the range 3400-3300 cm^{-1} (**Fig. 4.12**, **E**). These contributions could be related with the presence of NH_4^+ cations, chemisorbed water or crystallized H_2O inside the cell. The experiments were repeated and they gave essentially the same FTIR profiles for this sample.

According to the heterogeneous physicochemical features observed along W-Nb-O system (in terms of crystal structure, particle size, textural properties, etc.), it makes more sense to compare the catalysts at fixed CO-coverages, rather than in terms of fixed equilibrium pressures.

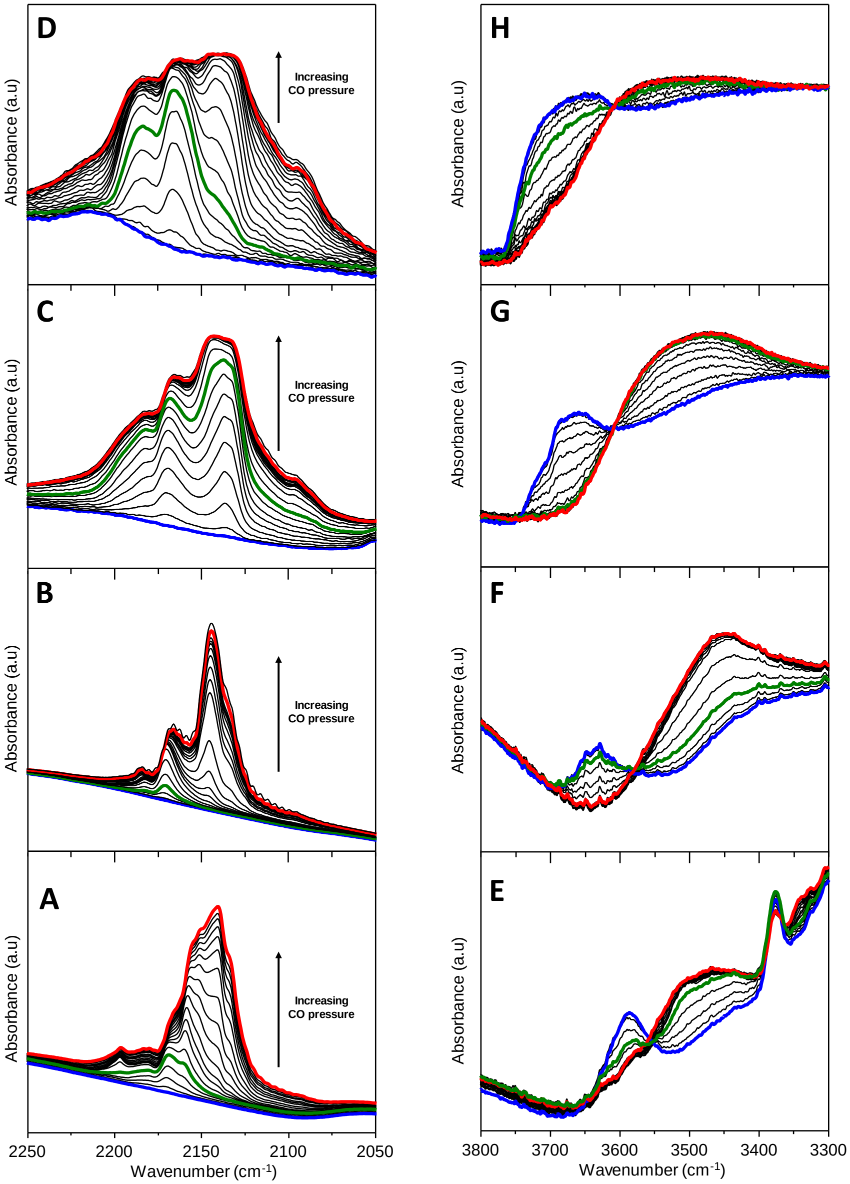

Figure 4.12. Low-temperature (77 K) FTIR spectra of adsorbed CO at increasing CO equilibrium pressures of selected W-Nb-O catalysts. C-O stretching region (A-D). O-H stretching region (E-H). Blue, green and red spectra were obtained at $P_{COeq.}$ of 0, 0.02 and 2.00 mmbar. W-Nb-0 (A and E); W-Nb-0.29 (B and F); W-Nb-0.62 (C and G); W-Nb-1 (D and H).

In fact, coverages are easily calculated from the difference spectra (i.e. background subtracted spectra) in the C-O stretching region. **Figure 4.13** shows the variation of CO coverage as a function of equilibrium pressures for some selected samples from W-Nb-O system (i.e. CO adsorption isotherms).

Coverages were calculated from the integrated peak areas of the signals in the C-O stretching region at each equilibrium pressure achieved, considering that a coverage θ = 1 is reached when the total area of the signal does not vary significantly at increasing CO pressures (i.e. when the rotational modes of gas-phase CO appear in the spectra). It can be observed that the samples with higher Nb contents show a more drastic increase in the coverage at low CO pressures (especially W-Nb-0.62), than W-Nb-0 or W-Nb-0.29 catalysts (**Fig. 4.13**).

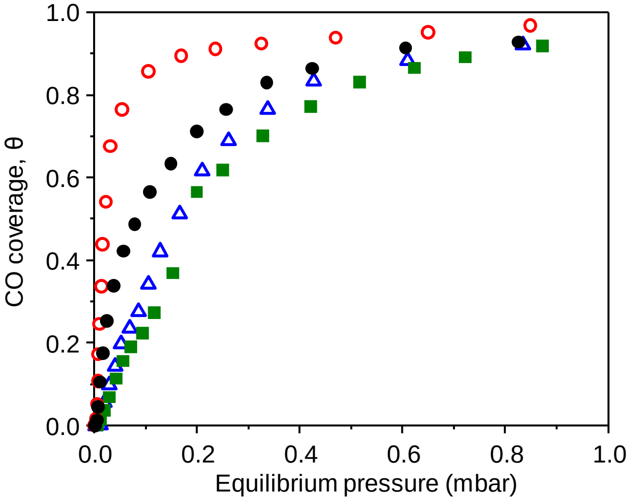

Figure 4.13. Coverage as a function of CO equilibrium pressure for W-Nb-0 (**△**), W-Nb-0.29 (■), W-Nb-0.62 (**○**) and W-Nb-1 (●).

Figure 4.14 displays background-subtracted (i.e. difference spectra, see point 2.2.12 in Experimental section) FTIR spectra of CO stretching region recorded at 77 K and a fixed surface coverage of θ = 0.25. All the catalysts show three different frequency regimes at ca. 2135-2145, 2150-2170, 2175-2200 cm^{-1}, which are typically ascribed to physisorbed CO, and CO bonded to Bronsted and Lewis acid sites, respectively [30-34]. Nb-containing catalysts present similar FTIR υ(CO) signals, with three bands located at ca. 2181, 2166 and 2145-2137 cm^{-1}, displaying different relative intensities depending on Nb concentration (**Fig. 4.14**, spectra *b* to *c*). Specifically, the intensity of band at 2181 cm^{-1}, assigned to CUS sites (likely W^{6+} and/or Nb^{5+} Lewis acid sites) increases with Nb content. This fact goes in line with acid features observed by FTIR of adsorbed pyridine, which suggested an increase of surface Lewis acid character as Nb concentration in the materials increase (**Fig. 4.11**).

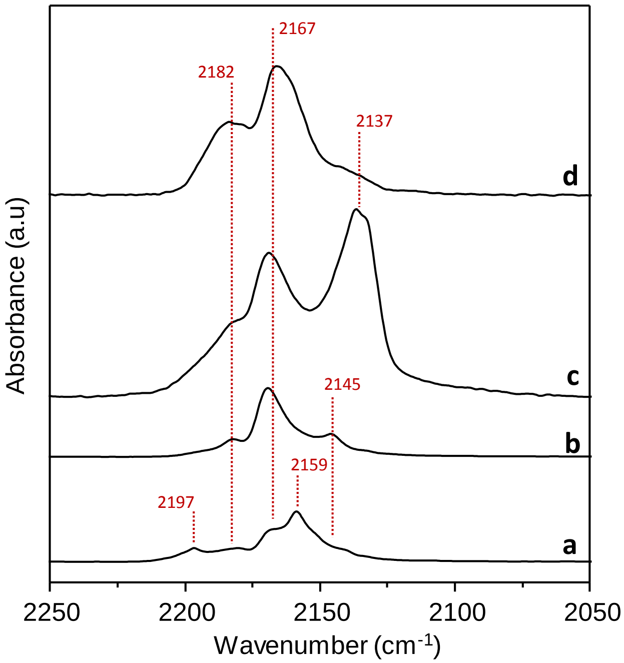

Figure 4.14. Background subtracted low-temperature (77 K) FTIR spectra of adsorbed CO of selected W-Nb-O catalysts at a CO coverage θ = 0.25: a) W-Nb-0; b) W-Nb-0.29; c) W-Nb-0.62; d) W-Nb-1.

Interestingly, W-Nb-0.62 sample displays the highest contribution to physisorbed CO (band at 2137 cm^{-1}) along the series of catalysts analyzed (**Fig. 4.14**, spectrum *c*). These relatively high amounts of physisorbed gas could be explained considering the specific structural characteristics of this sample. We must recall that W-Nb-0.62 presents high concentration of small crystals with an M1-type structure (as observed by HRTEM and XRD, **Figs. 4.6** and **4.7**, respectively). Ueda et al. reported that metal oxides with an M1-type phase structure present a certain degree of microporosity, associated with the presence of unoccupied heptagonal channels in the framework [35-38]. The presence of such micropores in W-Nb-0.62 could explain both the high amount of physically adsorbed CO (**Fig. 4.13**, spectrum *c*), and also the drastic increase in the CO-coverage at low equilibrium pressures observed for this catalyst (see also **Fig. 4.14**).

On the other hand, Nb-free hexagonal tungsten bronze catalyst, presents two additional signals at 2197 and 2159 cm^{-1}, which can be assigned to the presence of additional Lewis and Brönsted-type acid sites respectively (**Fig. 4.14**, spectrum *a*). Regarding the high frequency band at 2197 cm^{-1}, Knözinger et. al. assigned this signal to CO bonded to W^{5+} and/or W^{6+} CUS [39]. In our case, this band is exclusively observed in the undoped sample W-Nb-0, being absent in the rest of the catalysts. According to XPS and XAS analysis performed (**Fig. 4.3**), which suggested the isomorphic substitution of Nb^{+5} for reduced $W^{4+/5+}$ species, we can tentatively assign this high frequency signal observed in W-Nb-0 sample to CO interacting with coordinatively unsaturated W^{5+} sites.

According to the other additional band observed in undoped W-Nb-0 catalyst, appearing at 2159 cm^{-1}, it could be ascribed to other types of CO interactions via H-bond (**Fig. 4.14**, spectrum *a*). It could be associated either with the presence of NH_4^+ ions in the hexagonal channels in h-WO_3 framework, or the presence of chemisorbed H_2O. In fact, CO could undergo H-bond with hydrogen atoms in both ammonium ions and chemisorbed water on the surface [40].

Figure 4.15 shows the corresponding O-H region of the difference spectra presented in **Figure 4.14** at a CO coverage θ = 0.25 (**Figure 4.15 A**), and the background-subtracted FTIR spectra of the catalysts after CO desorption at high vacuum (ca. 10^{-6} mbar) and low temperature (77 K) (**Figure 4.15 B**). All the catalysts show a group of two broads bands in the range 3700-3450 cm^{-1} (**Fig. 4.15 A**).

The negative band at 3700-3600 cm^{-1} in the difference spectra appears due to the H-bond interaction occurring between CO molecule and surface O-H groups. This way, the strength of O-H bonds of those groups interacting with the basic probe decreases, giving rise to a frequency shift to lower wavenumbers. Since the number of "unaltered" O-H groups decreases, a negative band appears in the difference spectra (3700-3600 cm^{-1}).

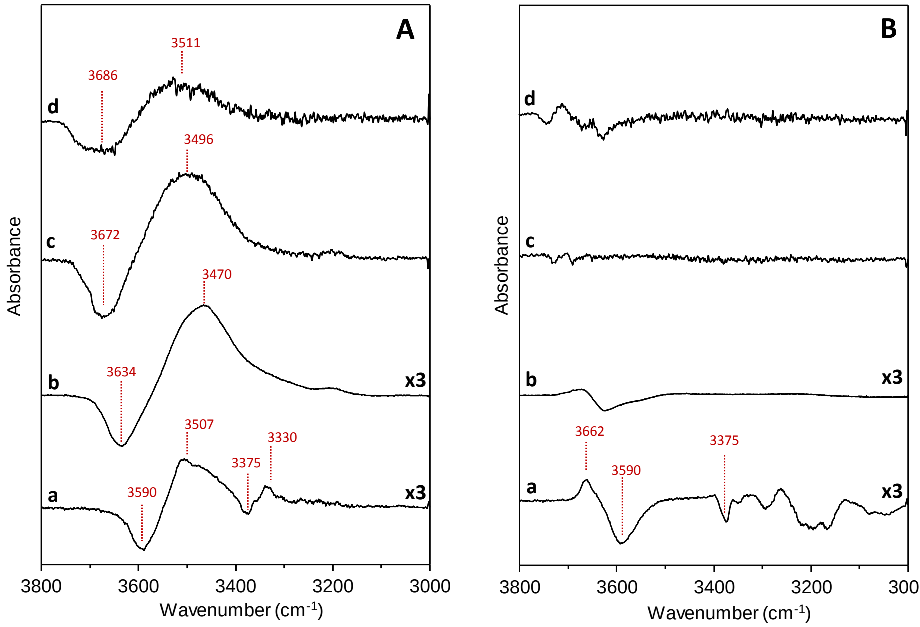

Figure 4.15. Background-subtracted low-temperature (77 K) FTIR spectra in the O-H stretching region after CO-adsorption (coverage θ = 0.25) (A), and after CO-desorption at high vacuum (ca. 10^{-6} mbar) (B), of selected W-Nb-O catalysts: a) W-Nb-0; b) W-Nb-0.29; c) W-Nb-0.62; d) W-Nb-1.

Concomitantly, a positive band at ca. 3500 cm^{-1} appears, related to those OH interacting with CO, which present a lower O-H bond strength. These broad signals suggest the presence of several types of Brönsted acid sites, that likely could be associated with: i) surface bridging hydroxyls; ii) with hydroxyl groups located at the mouth or inside the hexagonal or heptagonal channels; iii) with hydroxyl species bonded to W^{n+} and/or Nb^{5+}; iv) with O-H bonds due to chemisorbed water.

Nb-free W-Nb-0 catalyst displays some additional features in its FTIR profile (**Fig. 4.15 A**, spectrum *a*). A negative signal at 3375 cm^{-1} is observed, which can be ascribed to N-H stretching vibrations of ammonium cations located in the hexagonal channels of the h-WO_3 structure [40]. Subsequently, additional positive bands appear at lower frequencies, as a result of the lower N-H bond strength of those ammonium cations interacting with CO.

Interestingly, the spectra recorded after CO-desorption in high vacuum show important differences depending on Nb content in the materials (**Fig. 4.15 B**), especially in the case of Nb-free catalyst (**Fig. 4.15 B,** spectrum a). The spectra of the undoped sample presents negative bands in the whole region analyzed, what suggests changes in the original state of the catalyst, i.e. prior to CO-adsorption. The presence of these negative bands could be ascribed to the elimination of H_2O molecules (likely chemisorbed, or by the generation of oxygen vacancies), and ammonium cations. The generation of oxygen vacancies (i.e. CUS or Lewis sites) by the formation of water during vacuum pretreatments cannot be ruled out, since it could also explain the lower BAS/LAS ratio observed for W-Nb-0 (**Table 4.2**). In addition, a positive band at 3662 cm^{-1} is also generated after desorption, which suggests either water readsorption-chemisorption, or the generation of new O-H groups by the elimination of ammonium species in the hexagonal channels. All these effects are more pronounce at low Nb-contents (**Fig. 4.15 B**; spectra *a* and *b*), suggesting that the presence of water or vaccumm treatments could modify the acid properties of these specific materials (especially under reaction conditions). In fact, it has been reported that Lewis acid sites can be transformed into Brönsted sites via water dissociation in oxygen vacancies, creating two new O-H groups [41] (see additional pyridine experiments performed in the next section).

4.3. Catalytic behavior in the transformation of biomass derived-feedstocks

Considering the tailored acid features observed in W-Nb-O system, which fundamentally depend on Nb content in the catalysts, the materials have been tested as catalysts in the conversion of biomass-derived feedstocks: the aerobic transformation of glycerol to acrolein, and the aqueous phase transformation of short chain oxygenates (derived from the aqueous extraction of pyrolytic bio-oils). Both streams could be considered residues at bio-refineries.

4.3.1. Gas-phase aerobic transformation of glycerol

Table 4.3 shows representative results obtained during the gas-phase aerobic transformation of glycerol performed on W-Nb-O catalysts.

Table 4.3. Catalytic properties of W-Nb-O oxides in the aerobic transformation of glycerol.

Catalyst	Glycerol conversion (%)	Yield (%)			
		Acrolein	CO_x	Heavy compounds [a]	Others [b]
W-Nb-0	100.0	82.2	8.9	4.4	4.1
W-Nb-0.29	99.9	83.5	7.8	6.1	2.8
W-Nb-0.53	99.7	67.6	11.2	15.8	5.5
W-Nb-0.80	99.7	62.6	11.0	22.4	4.0
W-Nb-1	100.0	45.3	15.7	35.8	3.2

[a] Considered as compounds that are not eluted into the gas chromatograph. [b] Small amounts of acetaldehyde, acetic acid and acrylic acid. Reaction conditions: 295 ºC, glycerol/oxygen molar ratio, 4/2, Contact time W/F of 81 g_{cat} h $(mol_{gly})^{-1}$

We must indicate that, under the reaction conditions used here, total conversion of glycerol is observed all along the series, regardless of Nb-content. The main reaction product in all cases was acrolein, which is obtained via a double dehydration mechanism [42]. The two steps would consist in: i) removal of the internal OH- group; and ii) a tautomerization-dehydration of the terminal OH- group of glycerol. Although acrolein is observed in all the cases, the selectivity to the different products is highly dependent on the Nb-content in the materials. However, and in addition to acrolein, other reactions products have been also detected. Thus, heavy compounds (products that are not eluted into the gas chromatograph due to their high molecular weight) and carbon oxides, together with small amounts of acetaldehyde, acetic acid and acrylic acid (grouped as “others”, in **Table 4.3**) are obtained.

The selectivity to acrolein decreases when the Nb-content in the catalysts increases (**Fig. 4.16**), together with a concomitant increase of by-products; i.e. carbon oxides and heavy compounds. In this sense, acid characteristics of catalysts seem to control the selectivity profiles in the aerobic transformation of glycerol; the increase in the yield to heavy compounds and carbon oxides related with the increment in the Lewis acid nature of the surface.

Although both the decrease of acid strength and surface density of acid sites with Nb content (see **Figs. 4.11 B** and **4.10 B**, respectively) should favor the desorption of acrolein, the higher concentration of Lewis sites could have a dramatic effect in the selectivity profiles (**Fig. 4.16**). In particular, Lewis sites (mainly related to the presence of Nb^{5+} species) could coordinate acrolein [43], hindering its desorption, and promoting the formation of heavy compounds and CO_x. Therefore, the most selective catalysts in this case are those with low Nb/(W+Nb) ratios, presenting a high proportion of Brönsted acid sites.

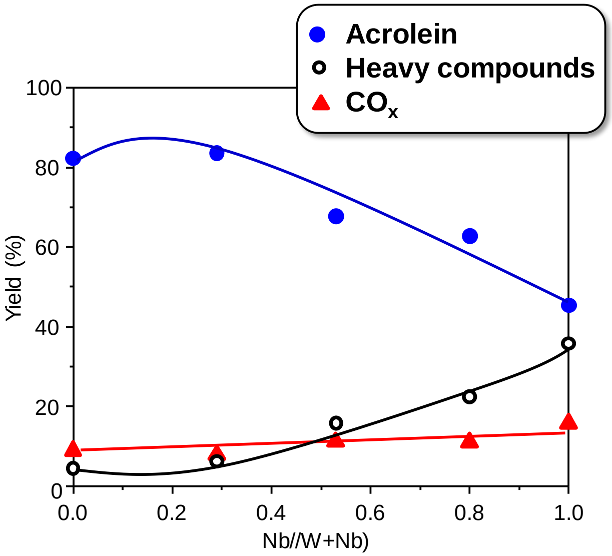

Figure 4.16. Variation of the selectivity to acrolein, carbon oxides and heavy compounds as a function of Nb content in the catalysts. Symbols: Acrolein (●), heavy compounds (○) and CO_x (▲). Reaction conditions: gly/O_2/ molar ratio of 2/4, T = 295 ºC, Contact time W/F of 81 g_{cat} h $(mol_{gly})^{-1}$

It is worth recalling the results obtained by FTIR of adsorbed CO (**Figs. 4.12** to **4.15**) and adsorbed pyridine (**Figs. 4.10** and **4.11) (Table 4.2**), considering the acid features of W-Nb-0 catalyst. Regarding FTIR of adsorbed pyridine, Nb-free sample gave the lowest BAS/LAS ratio of W-Nb-O series (**Table 4.2)**. In addition, CO-adsorption experiments suggested the possible desorption-readsorption of water on coordinatively CUS sites, but also the elimination of NH_4^+ cations, leading to new O-H groups. According to catalytic results obtained in the gas-phase aerobic transformation of glycerol, in which Brönsted acid sites favor the double dehydration into acrolein, changes in the acid features of W-Nb-0 catalysts under reaction conditions could be taking place (i.e. mainly variations in the Brönsted-Lewis acid nature of the surface). To shed some light on this fact, additional FTIR experiments of adsorbed pyridine have been carried out on Nb-free catalyst **(Fig. 4.17** and **Table 4.4).**

Prior to pyridine adsorption, fresh W-Nb-0 catalyst was pretreated at 200 ºC in vacuum for 12 and 2h, and then the experiments were carried out as it is detailed in point 2.2.11 in the Experimental section (**Figure 4.17**, spectra *a* and *b*, respectively). It can be observed that shorter vacuum pretreatments increase the BAS/LAS ratio measured by FTIR of adsorbed pyridine from 0.3 to 0.7 (**Table 4.4**). This higher proportion of Lewis sites at longer vacuum treatments can be explain in terms of the generation of oxygen vacancies, which can be formed in tungsten oxide systems in vacuum at moderate temperatures, with the subsequent changes in sample color (i.e. chromogenic effect) [44]. In fact, a color change from pale blue to dark blue was observed after the experiment.

Table 4.4. BAS/LAS ratio of W-Nb-0 catalyst measured by FTIR of adsorbed pyridine after different sample pretreatment.

Sample	Pretreatment	BAS/LAS ratio
Fresh	12 h at high vacuum	0.3
Fresh	2 h at high vacuum	0.7
Used [a]	2 h at high vacuum	0.9

[a] Measured after the gas-phase aerobic transformation of glycerol. Reaction conditions: 295 ºC, glycerol/oxygen ratio, 4/2, Contact time W/F of 81 g_{cat} h $(mol_{gly})^{-1}$

Additionally, in order to study the possible effect of water on the acid properties of this sample during the gas-phase aerobic transformation of glycerol, the used catalyst was also pretreated at 200 ºC for 2h prior to pyridine adsorption. The spectrum was recorded in the same conditions detailed in the Experimental section (**Figure 4.17**, spectrum *c*).

Again BAS/LAS ratio increases from 0.7 to 0.9 (**Table 4.4**). Assuming the presence of oxygen vacancies in the fresh catalyst (i.e. CUS sites) prior to pyridine adsorption, these results suggest that the dissociation of water on Lewis sites under reaction conditions could be taking place. This would give rise to new Brönsted-type sites, and would also give an explanation to: i) the increase in the BAS/LAS ratio in the used catalysts and; ii) the high selectivity to acrolein observed for W-Nb-0 catalyst in the gas-phase aerobic transformation of glycerol.

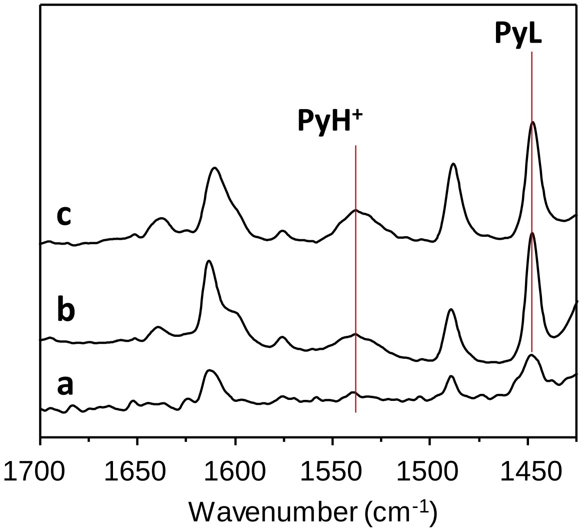

Figure 4.17. FTIR spectra of adsorbed pyridine of fresh and used W-Nb-0 sample: a) Fresh catalyst pretreated in high vacuum for 12h. b) Fresh catalyst pretreated in high vacuum for 2h. c) Used catalyst pretreated in high vacuum for 2h.

4.3.2. Catalytic properties in the valorization of aqueous effluents via C-C bond formation reactions

The whole series of W-Nb-O materials were also tested in the transformation of short-chain oxygenates in aqueous media. The mixture used as feed resembles that of a waste effluent at a bio-refinery, specifically an effluent derived from the aqueous phase separation of a pyrolysis bio-oil. The model mixture presents an acetic acid/ propanal/acetol/ethanol/water wt.% ratio of 30/25/5/10/30. According to reaction scheme depicted in **Figure 4.18** (picture **A**), short chain molecules can undergo chain growth via ketonization and/or aldol condensation reactions to give C_5-C_8 intermediate products, which can further react to form C_9-C_{10} products, useful for blending with automotive fuels [45].

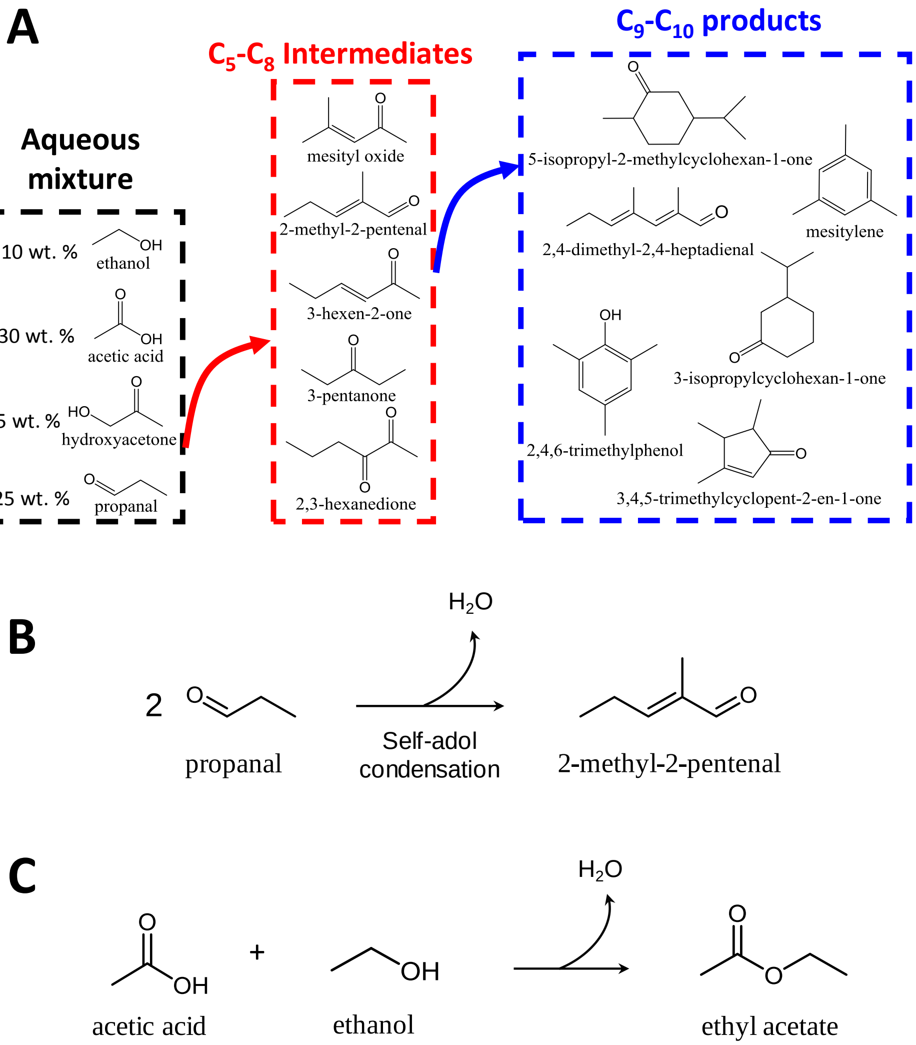
A
Aqueous mixture
10 wt. %
OH
ethanol
30 wt. %
O
OH
acetic acid
5 wt. %
HO
O
hydroxyacetone
25 wt. %
O
propanal
C5-C8 Intermediates
O
mesityl oxide
O
2-methyl-2-pentenal
O
3-hexen-2-one
O
3-pentanone
O
O
2,3-hexanedione
C9-C10 products
O
5-isopropyl-2-methylcyclohexan-1-one
O
2,4-dimethyl-2,4-heptadienal
mesitylene
O
3-isopropylcyclohexan-1-one
OH
2,4,6-trimethylphenol
O
3,4,5-trimethylcyclopent-2-en-1-one
B
H2O
2
O
propanal
Self-adol condensation
O
2-methyl-2-pentenal
C
H2O
O
OH
acetic acid
+
OH
ethanol
O
O
ethyl acetate

Figure 4.18. A) Summarized reaction network of the aqueous-phase valorization of short chain oxygenates by aldol condensation-ketonization reactions. B) Self-aldol condensation of propanal to 2-methyl-2pentenal. C) Esterification of acetic acid and ethanol to ethyl acetate.

For example, in the first reaction step propanal can react via self-aldol condensation to form 2-methyl-2-pentenal (**Figure 4.18**, picture **B**), which can then continue reacting with another propanal molecule to form 2,4-dimethyl-2,4-heptadienal. The combination of ketonization-aldol condensation-cyclation reactions can explain all the compounds detected in the mixture after reaction (some examples are presented in **Figure 4.18**, picture **A**) [45]. The total organic yield (TOY) presented in this section includes all intermediates and C_9-C_{10} products (C_5-C_{10}) formed during the reaction. This TOY is calculated assuming a maximum formation of 30 wt.% C_9 products, considering the initial mixture composition (for more details see point 2.3.4 in Experimental section). In addition, esterification reactions can take place between ethanol and acetic acid, with the formation of ethyl acetate, which is always observed in all the catalytic tests (**Figure 4.18**, picture **C**).

Considering C-C bond formation reactions, it has been reported that Lewis acid/base pairs can assist the formation of intermediates of aldol condensation and ketonization, while Brönsted acid/base pairs favor the formation of esterification products [46, 47]. The tests were carried out at 180 and 200 ºC at an N_2 pressure of 13 bar, in Teflon-lined stainless steel autoclaves. The results have been explained bearing in mind the specific acid properties of the catalysts, and discussed in terms of conversion of the reactants and selectivity to the main condensation and/or ketonization products (2-methyl-2-pentenal, C_5-C_8 and C_9-C_{10} products), and to ethyl acetate (as the main by-product) (**Table 4.5** and **Table 4.6**).

The variation of the conversion of each oxygenate, at 180 ºC at 7 h of time on stream, as a function of Nb-content in the catalysts is comparatively shown in **Figure 4.19 A**. The main difference was observed for propanal conversion, which increases with Nb-content, reaching a maximum at $Nb/(W+Nb) \approx 0.62$ (90 % propanal conversion). The rest of reactants show similar conversion degrees, regardless of Nb content in the catalysts (conversion of 100 %, 37-47 % and 13-19 % for acetol, ethanol and acetic acid, respectively) (**Fig. 4.19 A** and **Table 4.5**). Accordingly, the selectivity to 2-methyl-2-pentenal (2M2P) increases with Nb-content, with 2-methyl-2-pentenal formed by self-aldol condensation of propanal.

Table 4.5. Catalytic performance in the valorization of short-chain oxygenates in aqueous phase at 180 °C.[a]

Sample	Conversion (wt. %)[b]				Selectivity (wt. %)[c]			
	Acetol	C_3HO	EtOH	AA	C_5-C_8	C_9-C_{10}	2M2P	Ethyl acetate
W-Nb-0	100	61.2	40.4	17.2	19.5	8.6	38.1	33.8
W-Nb-0.29	100	77.8	38.0	15.2	21.2	8.8	38.7	31.3
W-Nb-0.53	100	84.5	43.4	13.3	18.5	13.3	40.2	28.0
W-Nb-0.62	100	90.1	47.2	17.8	17.6	14.3	42.3	25.8
W-Nb-0.80	100	84.0	36.7	19.9	13.3	15.7	45.2	25.7
W-Nb-0.95	100	89.7	43.3	13.7	11.4	13.9	46.3	28.4
W-Nb-1	100	80.3	40.9	18.1	16.3	14.2	41.8	27.7

[a] Reaction conditions: 3 g of aqueous model mixture and 150 mg of catalyst under stirring for 7h at 180 °C; P_{N2}= 13 bar; [b] C_3HO= propanal; AA=Acetic acid; [c] 2M2P= 2-methyl-2-pentenal.

Table 4.6. Total organic yield as a function of reaction temperature for W-Nb-O catalysts.

Sample	Total organic yield (%)[a]	
	180 °C	200°C
W-Nb-0	49.2	52.9
W-Nb-0.29	51.5	56.6
W-Nb-0.53	62.2	59.3
W-Nb-0.62	68.4	64.2
W-Nb-0.80	65.2	64.5
W-Nb-0.95	64.6	63.9
W-Nb-1	61.2	65.2

[a] Total organic yield measured at 7h of reaction.

In the same way, the selectivity to C_9-C_{10} oxygenated products also increases with Nb/(W+Nb) ratio. In this case, they are formed via condensation of C_5-C_8 with smaller molecules. Accordingly, the selectivity to C_5-C_8 oxygenates follows the opposite trend, i.e. decreasing at higher Nb contents in the catalyst (**Figure 4.19**).

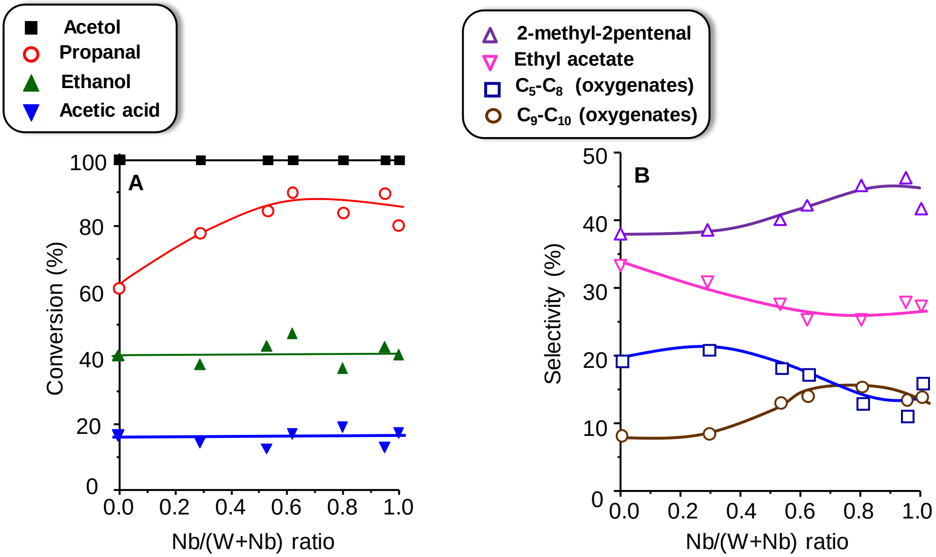

Figure 4.19. Conversion of each short-chain oxygenate (A) and selectivity to the main reaction products (B) as a function of Nb-content in the catalysts. Reaction conditions: 3 g of aqueous model mixture and 150 mg of catalyst under stirring for 7h at 180 ºC; P_{N2}= 13 bar;

Ethyl acetate was the main by-product obtained, derived from the esterification reaction that takes place between acetic acid and ethanol. It can be observed that the selectivity to ethyl acetate also decreases when Nb content increases. All these facts are in agreement with the specific acid features of the materials, considering that Lewis-type acid characteristics would favor the reaction towards condensation products, meanwhile, Brönsted acid sites would increase the reactivity via esterification [46, 47].

According to these results, the catalytic performance of W-Nb mixed oxide could be interpreted in terms of the concentration and nature of their surface acid sites (**Fig. 4.20**).

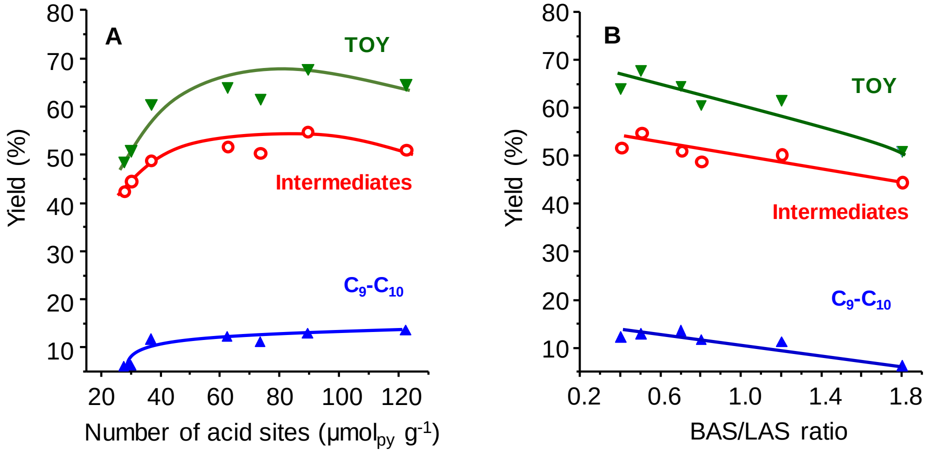

Figure 4.20. Total organic yield (TOY) and yield to intermediates (sum of 2-methyl-2-pentenal and C_5-C_8 fraction) and to C_9-C_{10} oxygenates as a function of the concentration of acid sites (A) and as a function of Brönsted/Lewis acid sites ratio (B).

Figure 4.20 (picture **A**) presents the total organic yield (TOY, sum of 2M2P, C_5-C_8 and C_9-C_{10} fractions, Table 4.5), yield to intermediates (sum of 2M2P and C_5-C_8 oxygenates) and the yield to C_9-C_{10} oxygenates as a function of the concentration of surface acid sites. It can be noted that, as the concentration of acid sites increases, the yield to both intermediates and C_9-C_{10} fractions also increases, thus increasing the total organic yield (**Fig. 4.20 A**).

In addition, Brönsted/Lewis acid sites ratio play an important role on the catalytic performance (**Fig. 4.20 B**). Since W-Nb-0 catalysts seems to increase its BAS/LAS ratio in aqueous conditions (as observed in the previous sections), the results are not included in **Figure 4.20**. On the one hand, a high concentration of Brönsted acid sites (i.e. high BAS/LAS ratios) does not favor condensation reactions to intermediates and C_9-C_{10}.

On the contrary, a higher concentration of Lewis acid sites (i.e. lower BAS/LAS ratio) directs the reactivity via condensation reactions, i.e. towards C_5-C_8 and C_9-C_{10} products formation, thus maximizing the total organic yield (**Fig. 4.20 B**).

Catalysts were also tested at higher reaction temperature (200 ºC). **Figure 4.21** displays the yields to intermediates and C_9-C_{10} products as a function of Nb content at 7 h of time of stream at 180 and 200 ºC. Some differences can be noted depending on the reaction temperature. When increasing from 180 to 200 ºC, the yield to second condensation products increases (i.e. C_9-C_{10}) (**Fig. 4.21 A**), with the concomitant decrease in the yield to intermediates (**Fig. 4.21 B**).

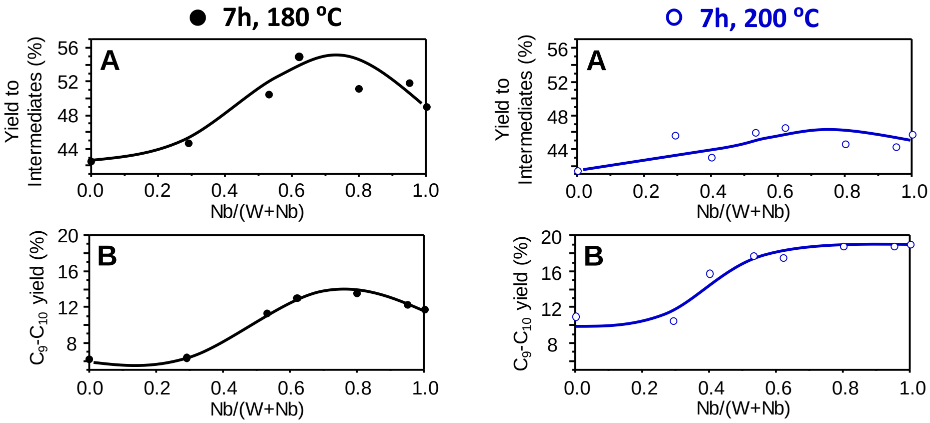

Figure 4.21. Yield to intermediates (sum of 2-methyl-2-pentenal and C_5-C_8 fraction) (A) and to C_9-C_{10} oxygenates (B) as a function of Nb content in the catalysts. Reaction conditions: 7h at 180 °C (left); 7h at 200 °C (right).

Finally, to evaluate the hydrothermal stability of the catalysts, they were tested after 3 consecutive uses at 200 ºC during 7 h of reaction (**Fig. 4.22**). It can be seen that catalyst retain their catalytic performance, with just a slight decrease in the selectivity to 2M2P and C_5-C_8 products in the case of W-Nb-0.62 sample. Interestingly, both catalysts showed no leaching of the active components after each use (as determined by ICP-AES).

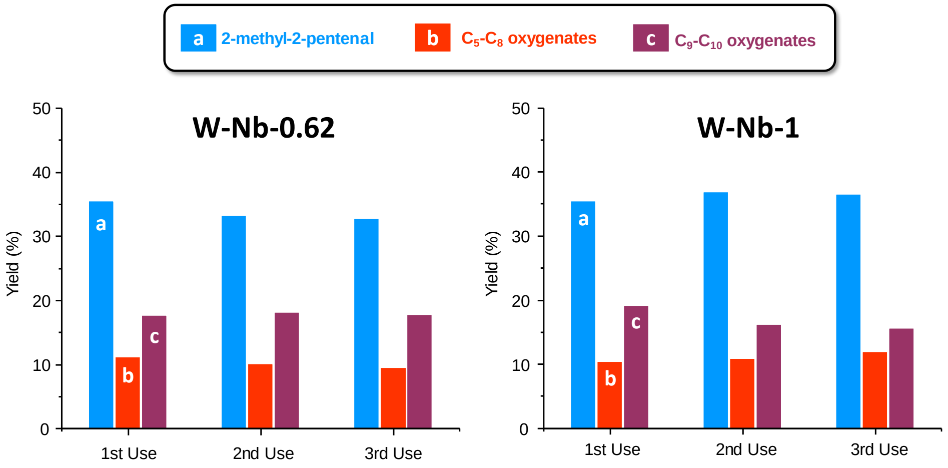

Figure 4.22. Yield to 2M2P (a), to C_5-C_8 (b) and C_9-C_{10} (c) after three consecutive uses for W-Nb-0.62 and W-Nb-1. Reaction conditions: T= 200 ºC; time on stream 7h.

4.4. General Remarks

A series of W-Nb mixed oxides have been prepared by hydrothermal synthesis, in which Nb content has been varied systematically. Characterization results show that the isomorphic substitution of Nb for W has an important influence on the structural, acid and textural properties of the materials. The incorporation of Nb within *h*-WO_3 promotes a loss of periodicity along *ab* plane of the crystal structure, giving rise to pseudocrystalline oxides just ordered along [001] direction when Nb/(W+Nb) ≥ 0.53. Nevertheless, as it can be inferred from HRTEM studies, for Nb/(W+Nb) ratios in the range 0.53-0.62, the formation of small crystals of a $Cs_{0.5}Nb_{2.5}W_{2.5}O_{14}$-type structure (isostructural with M1-type MoVTeNb phase) seems to be favored. In addition, acid and textural properties of the materials can be tuned by controlling Nb content. This way, the progressive insertion of Nb increases the surface area and mesopore volumes; and decreases the average pore size. Moreover; for Nb/(Nb+W) > 0.53, apart from their high mesopore volumes, narrow pore size distributions are observed. Considering acid properties, there exists a substantial increase in the total concentration of acid sites (i.e. acid sites per gram of catalyst) as Nb/(W+Nb) ratio increases, reaching a maximum at ca. 0.62-0.80. However, the surface density of acid sites (i.e. acid sites per unit area) decreases as Nb content increases. In addition, the presence of Nb increases the Lewis acid nature of the surface (i.e. decreasing BAS/LAS ratio at higher Nb/(W+Nb) ratios).

The whole series of W-Nb oxides were tested as catalyst in the transformation of biomass-derived feedstocks, which can be considered waste streams in bio-processes: i) the aerobic transformation of glycerol; and ii) the valorization of short chain oxygenates derived from the aqueous phase separation of pyrolytic bio-oils. In both processes, the acid characteristics of the catalysts are the key factor that dictates the catalytic behavior. In the case of the aerobic transformation of glycerol, all the catalysts displayed high activity (conversion of glycerol of 100 % in all the cases) and high selectivity to acrolein (S_{AC} = 83.5 - 45.3 %) (double dehydration product). The selectivity to acrolein progressively decreases with Nb ratio in the materials, with the subsequent increase of the selectivity to heavy by-products and carbon oxides. The drop in acrolein selectivity has been attributed to the increase of the Lewis nature of the surface, by which the desorption of the product (i.e. acrolein) is hindered and consecutive reactions towards carbon oxides and high molecular weight compounds are promoted. On the other hand, the valorization of short chain oxygenates in the aqueous phase (acetic acid / propanal / acetol / ethanol / water wt. ratio of 30/25/5/10/30) can be carried out by the use of catalysts that direct the reactivity through C-C bond formation routes (especially aldol condensation reactions). In this sense, unlike the aerobic transformation of glycerol, the increase of the Lewis acid nature of the surface has a beneficial effect on the catalytic performance, favoring the conversion of small oxygenates (mainly propanal), and the selectivity to 2-methyl-2-pentenal, to C_5-C_8 and C_9-C_{10} fractions, thus also maximizing the total organic yield of the process (TOY_{max} = 68 %, Nb/(W+Nb) = 0.62). Despite the highly demanding reaction conditions (acidic media, 30 wt.% acetic acid) the catalysts maintain their catalytic performance after 3 consecutive uses, presenting no leaching of the active species.

4.5. References

[1] P. R. Gruber, B. Kamm, K. Michael, *Biorefineries - Industrial processes and products : Status quo and future directions*, Wiley-VCH, 2006.

[2] J. Moncada, J.A. Tamayo, C.A. Cardona, *Integrating first, second, and third generation biorefineries: Incorporating microalgae into the sugarcane biorefinery*, Chemical Engineering Science, 118 (2014) 126-140.

[3] L.C. Meher, D. Vidya Sagar, S.N. Naik, *Technical aspects of biodiesel production by transesterification—a review*, Renewable and Sustainable Energy Reviews, 10 (2006) 248-268.

[4] D. Sun, Y. Yamada, S. Sato, W. Ueda, *Glycerol as a potential renewable raw material for acrylic acid production*, Green Chemistry, 19 (2017) 3186-3213.

[5] R.H. Venderbosch, W. Prins, Fast pyrolysis technology development, Biofuels, Bioproducts and Biorefining, 4 (2010) 178-208.

[6] M. Balat, *An overview of the properties and applications of biomass pyrolysis oils*, Energy Sources, Part A: Recovery, Utilization, and Environmental Effects, 33 (2011) 674-689.

[7] M. Asadieraghi, W.M.A. Wan Daud, H.F. Abbas, *Model compound approach to design process and select catalysts for in-situ bio-oil upgrading*, Renewable Sustainable Energy Rev., 36 (2014) 286-303.

[8] I. Graca, J.M. Lopes, H.S. Cerqueira, M.F. Ribeiro, *Bio-oils upgrading for second generation biofuels*, Industrial & Engineering Chemistry Research, 52 (2013) 275-287.

[9] D. C. Elliot, *Historical developments in hydroprocessing bio-oils*, Energy & Fuels, 21 (2007) 1792-1815.

[10] D. Radlein, A. Quignard, US Patent, 2014/028833, 2014.

[11] D.J.M. Bevan, P. Hagenmuller, *Non-stoichiometric compounds: Tungsten Bronzes, vanadium bronzes and related compounds*, Elsevier Science 2013.

[12] A. Magneli, *Non-stoichiometry and structural disorder in some families of inorganic compounds*, Pure and Applied Chemistry, 50 (1975) 1261-1271.

[13] S. Iijima, J.G. Allpress, *Structural studies by high-resolution electron microscopy: tetragonal tungsten bronze-type structures in the system* Nb_2O_5-WO_3, Acta Crystallographica Section A, 30 (1974) 22-29.

[14] S. Iijima, J.G. Allpress, *Structural studies by electron microscopy: coherent intergrowth of the* ReO_3 *and tetragonal tungsten bronze structure types in the system* Nb_2O_5-WO_3, Acta Crystallographica Section A, 30 (1974) 29-36.

[15] S. Andersson, J. Galy, *Wadsley defects and crystallographic shear in hexagonally close-packed structures*, Journal of Solid State Chemistry, 1 (1970) 576-582.

[16] M.D. Soriano, P. Concepcion, J.M. Lopez Nieto, F. Cavani, S. Guidetti, C. Trevisanut, *Tungsten-Vanadium mixed oxides for the oxidehydration of glycerol into acrylic acid*, Green Chemistry, 13 (2011) 2954-2962.

[17] M.D. Soriano, A. Chieregato, S. Zamora, F. Basile, F. Cavani, J.M. Lopez Nieto, *Promoted hexagonal tungsten bronzes as selective catalysts in the aerobic transformation of alcohols: Glycerol and methanol*, Topics in Catalysis, 59 (2016) 178-185.

[18] R.H. Mitchell, *Perovskites: Modern and Ancient*, Almaz Press 2002.

[19] H. Hibst, F. Rosowski, G. Cox, *New Cs-containing* Mo-V^{4+} *based oxides with the structure of the M1 phase-Base for new catalysts for the direct alkane activation*, Catalysis Today, 117 (2006) 234-241.

[20] T. Murayama, N. Kuramata, S. Takatama, K. Nakatani, S. Izumi, X. Yi, W. Ueda, *Synthesis of porous and acidic complex metal oxide catalyst based on group 5 and 6 elements*, Catalysis Today, 185 (2012) 224-229.

[21] A. Chieregato, M.D. Soriano, E. García-González, G. Puglia, F. Basile, P. Concepción, C. Bandinelli, J.M. López Nieto, F. Cavani, Multielement crystalline and pseudocrystalline oxides as efficient catalysts for the direct transformation of glycerol into acrylic acid, ChemSusChem, 8 (2015) 398-406.

[22] I.M. Szilágyi, J. Madarász, G. Pokol, P. Király, G. Tárkányi, S. Saukko, J. Mizsei, A.L. Tóth, A. Szabó, K. Varga-Josepovits, *Stability and controlled composition of hexagonal* WO_3, Chemistry of Materials, 20 (2008) 4116-4125.

[23] A.A. McConnell, J.S. Anderson, C.N.R. Rao, *Raman spectra of niobium oxides*, Spectrochimica Acta, Part A, 32A (1976) 1067-1076.

[24] J.M. Jehng, I.E. Wachs, *Niobium oxalate: new precursor for preparation of supported niobium oxide catalysts*, ACS Symposium Series, 437 (1990) 232-242.

[25] J.R. Sohn, M.Y. Park, *Characterization of zirconia-supported tungsten oxide catalyst*, Langmuir, 14 (1998) 6140-6145.

[26] S. Yamazoe, Y. Hitomi, T. Shishido, T. Tanaka, *XAFS Study of Tungsten L1- and L3-Edges: Structural analysis of* WO_3 *species loaded on* TiO_2 *as a catalyst for photo-oxidation of* NH_3, The Journal of Physical Chemistry C, 112 (2008) 6869-6879.

[27] M.D. Soriano, E. García-González, P. Concepción, C.B. Rodella, J.M. López Nieto, *Self-organized transformation from hexagonal to orthorhombic bronze of Cs–Nb–W–O mixed oxides prepared hydrothermally*, Crystal Growth & Design, 17 (2017) 6320-6331.

[28] I.E. Wachs, *Infrared spectroscopy of supported metal oxide catalysts*, Colloids and Surfaces A: Physicochemical and Engineering Aspects, 105 (1995) 143-149.

[29] K. Oshihara, T. Hisano, W. Ueda, *Catalytic oxidative activation of light alkanes over Mo–V-based oxides having controlled surface*, Topics in Catalysis, 15 (2001) 153-160.

[30] K.I. Hadjiivanov, G.N. Vayssilov, *Characterization of oxide surfaces and zeolites by carbon monoxide as an IR probe molecule*, Advances in Catalysis, Academic Press 2002, pp. 307-511.

[31] M.I. Zaki, H. Knözinger, *Carbon monoxide — A low temperature infrared probe for the characterization of hydroxyl group properties on metal oxide surfaces*, Materials Chemistry and Physics, 17 (1987) 201-215.

[32] M. Scheithauer, T.K. Cheung, R.E. Jentoft, R.K. Grasselli, B.C. Gates, H. Knözinger, *Characterization of* WO_x/ZrO_2 *by vibrational spectroscopy and n-pentane isomerization catalysis*, Journal of Catalysis, 180 (1998) 1-13.

[33] A.S. Rocha, A.C. Faro, L. Oliviero, J. Van Gestel, F. Maugé, *Alumina-, niobia-, and niobia/alumina-supported NiMoS catalysts: Surface properties and activities in the hydrodesulfurization of*

thiophene and hydrodenitrogenation of 2,6-dimethylaniline, Journal of Catalysis, 252 (2007) 321-334.

[34] F.C. Lange, H. Schmelz, H. Knözinger, *Infrared-spectroscopic investigations of selective catalytic reduction catalysts poisoned with arsenic oxide*, Applied Catalysis B: Environmental, 8 (1996) 245-265.

[35] S. Ishikawa, W. Ueda, *Microporous crystalline Mo–V mixed oxides for selective oxidations*, Catalysis Science & Technology, 6 (2016) 617-629.

[36] Y. Goto, K.-i. Shimizu, T. Murayama, W. Ueda, *Hydrothermal synthesis of microporous W–V–O as an efficient catalyst for ammoxidation of 3-picoline*, Applied Catalysis A: General, 509 (2016) 118-122.

[37] M. Sadakane, K. Kodato, T. Kuranishi, Y. Nodasaka, K. Sugawara, N. Sakaguchi, T. Nagai, Y. Matsui, W. Ueda, *Molybdenum-vanadium-based molecular sieves with microchannels of seven-membered rings of corner-sharing metal oxide octahedra*, Angewandte Chemie, International Edition, 47 (2008) 2493-2496.

[38] T. Murayama, N. Kuramata, W. Ueda, *Hydrothermal synthesis of W–Ta–O complex metal oxides by assembling MO_6 (M=W or Ta) octahedra and creation of solid acid*, Journal of Catalysis, 339 (2016) 143-152.

[39] F. Hilbrig, H. Schmelz, H. Knözinger, *Acidity of WO_x/TiO_2 catalysts for selective catalytic reduction (SCR)*, in: L. Guczi, F. Solymosi, P. Tétényi (Eds.) Studies in Surface Science and Catalysis, Elsevier 1993, pp. 1351-1362.

[40] D. Perra, N. Drenchev, K. Chakarova, M.G. Cutrufello, K. Hadjiivanov, *Remarkable acid strength of ammonium ions in zeolites: FTIR study of low-temperature CO adsorption on NH_4FER*, RSC Advances, 4 (2014) 56183-56187.

[41] R. Schaub, P. Thostrup, N. Lopez, E. Lægsgaard, I. Stensgaard, J.K. Nørskov, F. Besenbacher, *Oxygen vacancies as active sites for water dissociation on rutile TiO_2 (110)*, Physical Review Letters, 87 (2001) 266104.

[42] B. Katryniok, S. Paul, V. Belliere-Baca, P. Rey, F. Dumeignil, *Glycerol dehydration to acrolein in the context of new uses of glycerol*, Green Chemistry, 12 (2010) 2079-2098.

[43] A. Chieregato, C. Bandinelli, P. Concepción, M.D. Soriano, F. Puzzo, F. Basile, F. Cavani, M.L. Nieto José, *Structure–reactivity correlations in vanadium-containing catalysts for one-pot glycerol oxidehydration to acrylic acid*, ChemSusChem, 10 (2016) 234-244.

[44] M.R. Goulding, C.B. Thomas, R.J. Hurditch, *A comparison of thermo- and photo-chromic behaviour in films of amorphous* WO_3, Solid State Communications, 46 (1983) 451-453.

[45] A. Fernández-Arroyo, D. Delgado, M.E. Domine, J.M. López-Nieto, *Upgrading of oxygenated compounds present in aqueous biomass-derived feedstocks over* NbO_x*-based catalysts*, Catalysis Science & Technology, 7 (2017) 5495-5499.

[46] A. Gangadharan, M. Shen, T. Sooknoi, D.E. Resasco, R.G. Mallinson, *Condensation reactions of propanal over* $Ce_xZr_{1-x}O_2$ *mixed oxide catalysts*, Applied Catalysis A: General, 385 (2010) 80-91.

[47] K. Suwannakarn, E. Lotero, J.G. Goodwin, *Solid Brønsted acid catalysis in the gas-phase esterification of acetic ac*id, Industrial & Engineering Chemistry Research, 46 (2007) 7050-7056.

Chapter 5

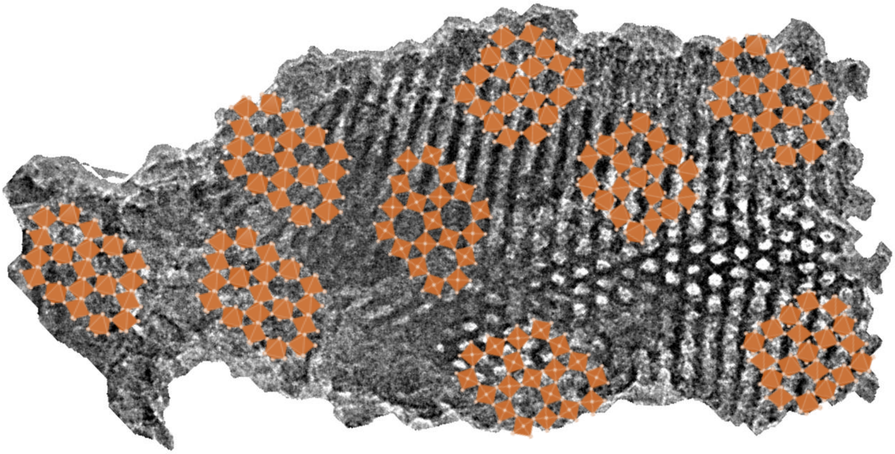

Reflux-synthesized bulk and supported W-Nb-O and W-V-O oxide bronzes: Aerobic transformation of alcohols

5.1. Previous considerations

As it was commented in the previous chapters, by the selection of the proper catalytic system, it is possible to perform the transformation of glycerol into acrolein (by using monofunctional Brönsted-type acid catalysts) or to acrylic acid (by selecting a bifunctional acid-redox catalyst) [1-8]. Studies on the mechanism of the one-pot oxidehydration of glycerol over V-based catalysts have shown the role of both acid and redox function in the consecutive stages of the reaction [9]. Interestingly, they show the capital importance of tuning the acid properties of the materials to prevent total oxidation of intermediates and products, and the formation of heavy by-products (ketals and oligomers) [8, 9]. Specifically, the reaction requires catalysts with optimum acid characteristics, i.e. they must present acid sites with enough strength and density in order to perform the dehydration of glycerol to acrolein in the first reaction step, but no too strong or too close together that they hinder the desorption of intermediates and products, hence favoring undesired reactions such as overoxidation or oligomerization.

In the following chapter the attention has been focused on the preparation of tungsten bronze-based materials (i.e. W-V-O and W-Nb-O) by an alternative reflux method (see point 2.1.3 in Experimental section) (**Table 5.1**).

Table 5.1. Synthesis method and composition of bulk and supported tungsten bronze catalysts

Catalyst	Synthesis method	Atomic Composition[a]			
		Si	W	Nb	V
KIT-6	Hydrothermal	100	---	---	---
WNb-H	Hydrothermal	---	0.71	0.29	---
R-WNb	Reflux	---	0.74	0.26	---
R-WNb/KIT	Reflux (Supported)	0.46	0.39	0.15	
WV-H	Hydrothermal	---	0.82	---	0.18
R-WV	Reflux	---	0.78	---	0.22
R-WV/KIT	Reflux (Supported)	0.85	0.12	---	0.03

[a] Obtained by X-ray Energy Dispersive Spectroscopy (XEDS).

In addition, this synthesis procedure has led to the successful preparation of supported W-Nb-O and W-V-O catalysts. In this study, the materials have been supported on a mesoporous KIT-6 silica.

The catalysts have been characterized by using several physico-chemical techniques. Their catalytic performance in the gas phase aerobic transformation of ethanol and glycerol has been compared with that obtained with the corresponding bulk materials obtained hydrothermally, which present a hexagonal tungsten bronze structure. The effect of the support on the acid properties of the materials is discussed.

5.2. Physicochemical characterization bulk and supported materials

The main physicochemical features of the catalysts are summarized in **Table 5.2**. Considering Nb-containing catalysts, reflux-synthesized sample (R-WNb) shows a considerable higher surface area than the material obtained hydrothermally (WNb-H) (82 and 38 m^2 g^{-1} respectively, **Table 5.2**).

Table 5.2. Textural and acid properties of bulk and supported catalysts

Catalyst	**Surface area (m^2 g^{-1})^a**	**Mesopore Volume (cm^3 g^{-1})^b**	**TPD-NH_3 ^{c}**	
			μmol_{NH3} g^{-1}	**μmol_{NH3} m^{-2}**
KIT-6	971	1.44	10	0.01
WNb-H	38	n.d.	139	3.6
R-WNb	82	0.08	308	3.7
R-WNb/KIT	179	0.32	332	1.8
WV-H	31	n.d.	102	3.3
R-WV	25	0.02	151	6.0
R-WV/KIT	358	0.20	107	0.3

^{a} Brunnauer-Emmet-Teller surface area; ^{b} Calculated by BJH method;
^{c} Temperature programmed desorption of ammonia.

In the case of V-containing catalysts, reflux (R-WV) and hydrothermal (WV-H) methods give rise to materials with similar surface areas (25 and 31 $m^2\ g^{-1}$, respectively) (**Table 5.2**). However, when reflux-synthesized materials are supported on mesoporous KIT-6 silica, the surface area of the catalysts substantially increases, especially for V-containing (R-WV/KIT catalysts, with a surface area of 358 $m^2\ g^{-1}$) (**Table 5.2**), although this is mainly due to the characteristics of the mesoporous support rather than to features related to bronze-type materials.

In fact, a decrease in pore volumes and surface area with respect to pure support is observed for supported metal oxides (**Table 5.2**), together with the loss of the narrow pore size distribution of KIT-6 (**Fig. 5.1 A**). It is worth noting that the crystalline nature of the mesoporous KIT-6 is also lost in supported catalysts (**Figure 5.1 B**).

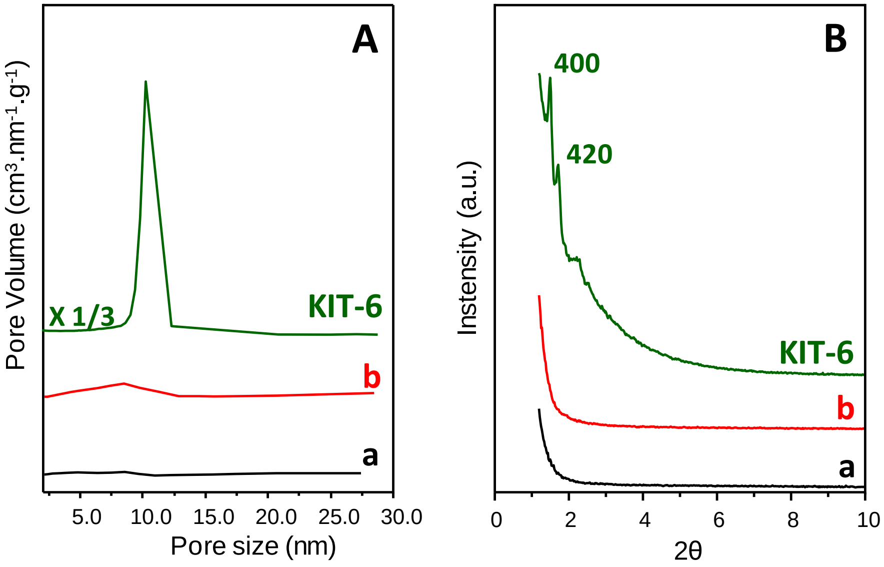

Figure 5.1. Pore size distribution (A) and low-angle XRD patterns (B) of: a) R-WNb/KIT (black); b) R-WV/KIT (red); and KIT-6 support (green)

XRD patterns of bulk and supported catalysts are displayed in **Figure 5.2**. Niobium-containing samples (reflux, hydrothermal and supported catalysts) show Bragg peaks corresponding to *h*-WO_3-type phase (JCPDS: 85-2460) [10] (**Fig. 5.2**, patterns *a* to *c*). On the other hand, vanadium-containing catalysts show differences in the crystal structure depending on the synthesis method used (**Fig. 5.2,** patterns *d* to *f*). Hydrothermally synthesized material (WV-H) displays diffraction signals of a *h*-WO_3-type phase (**Fig. 5.2**, pattern *f*), while reflux and supported catalysts show only two clear peaks at ca. 23 and 46 ° (**Fig. 5.2**, patterns *d* and *e*). They also show broad signals around 27, 35, 50 and 56 °. All these features can be attributed to the presence of a pseudocrystalline oxide ordered along c-axis [8, 11, 12].

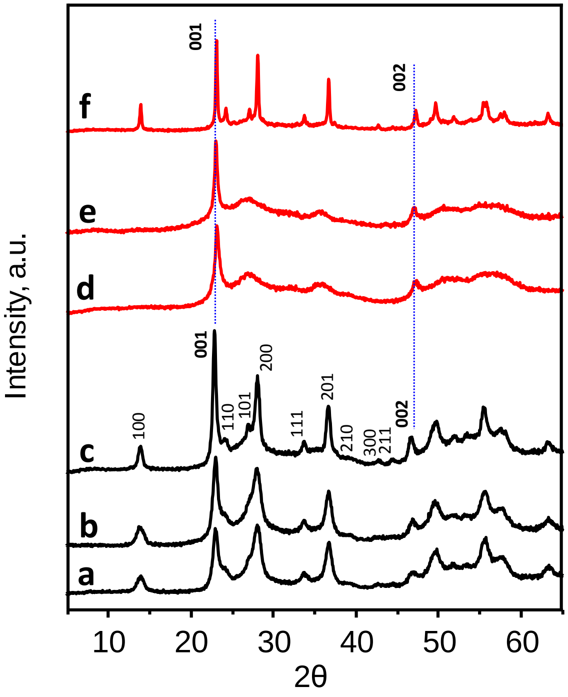

Figure 5.2. XRD patterns of bulk and supported W-Nb and W-V mixed oxides: a) R-WNb; b) R-WNb/KIT; c) WNb-H; d) R-WV; e) R-WV/KIT; f) WV-H.

In this sense, reflux synthesis inhibits the ordered growth along *ab* crystallographic plane. This loss of order could be the consequence of the synthesis procedure, in which the continuous stirring could hinder the crystal growth on those directions.

Samples with vanadium or niobium were further investigated by scanning electron microscopy (SEM). Niobium-containing catalysts show always platelet-shaped particle aggregates, regardless of the synthesis method used (**Fig. 5.3**, pictures *a* to *c*).

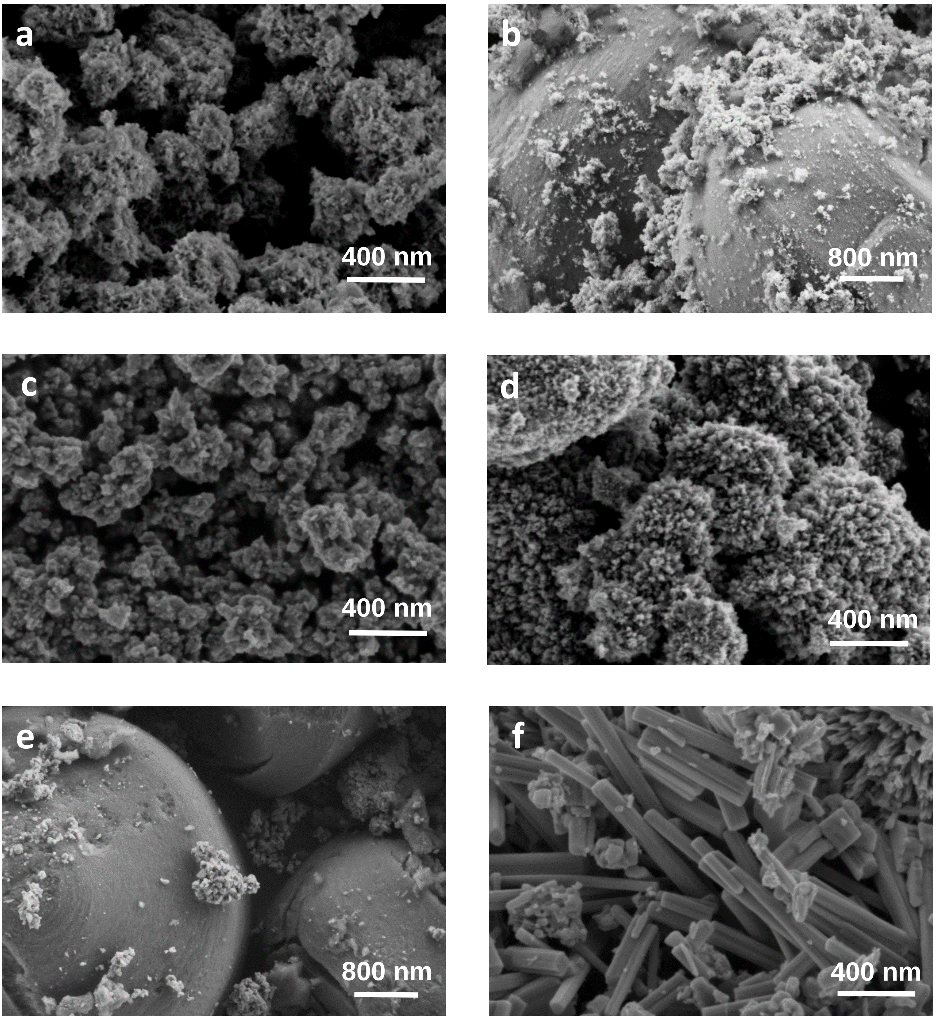

Figure 5.3. SEM micrographs of bulk and supported mixed oxides. a) R-WNb; b) R-WNb/KIT; c) WNb-H; d) R-WV; e) R-WV/KIT; f) WV-H.

However, the corresponding supported materials show smaller particle size than that of WNb-H catalyst. In addition, KIT-6 spheres are also recognized in R-WNb/KIT sample (**Fig. 5.3**, picture *b*).

In the case of V-containing catalysts, some differences in particle morphology have been observed depending on the synthesis procedure (**Fig. 5.3**, pictures *d* to *f*). Thus, unsupported and supported materials obtained by reflux method show cauliflower-like aggregates (i.e. R-WV and R-WV/KIT) (**Fig. 5.3**, pictures *d* and *e* respectively), while the sample prepared hydrothermally (i.e. WV-H) displays rod-shaped crystals (**Fig. 5.3**, spectrum *f*). These observations suggest that reflux synthesis could inhibit the growth of one-dimensional crystals, leading to a lower crystallization degree and giving rise to pseudocrystalline structures observed by X-ray diffraction, mainly in vanadium containing catalysts.

In order to elucidate the nature of metal-oxygen bonds, the catalysts were also studied by Raman and FTIR spectroscopy. **Figure 5.4 A** shows Raman spectra of bulk and supported catalysts. In the case of Nb-containing materials, two main Raman bands at 705 and 790 cm^{-1} are observed, which can be attributed to O-M-O (M= W and Nb) and O-W-O stretching vibrations of MO_6 octahedra in the hexagonal tungsten bronze lattice. In addition, a low intensity band centered at 950 cm^{-1} is found, which can be ascribed to M=O stretching vibrations (M= W, Nb) [10, 13].

For V-containing catalysts, bands related to O-M-O and O-W-O appear at 695 and 801 cm^{-1}, respectively (**Fig. 5.4 A**, spectra *d* to *f*), which are slightly shifted with respect to the ones observed in W-Nb oxides. Interestingly, a substantial increase of the relative intensity of the band located at ca. 900-1000 cm^{-1} is observed, comparing with W-Nb series. This band can be assigned to V=O stretching vibrations [7], and its relative intensity is higher for unsupported and supported samples prepared by reflux (R-WV and R-WV/KIT catalysts) (**Fig. 5.4 A**, spectra *d* and *e*, respectively). This observation suggests a higher proportion of V=O species in reflux-synthesized W-V-O mixed oxides, which are in fact those amorphous in the *ab* plane of the tungsten bronze structure (see **Figure**

5.2). Indeed, a lower crystalline nature of the *ab* plane could favor the presence of higher number of V=O due to a higher number of disconnected VO$_6$ octahedra.

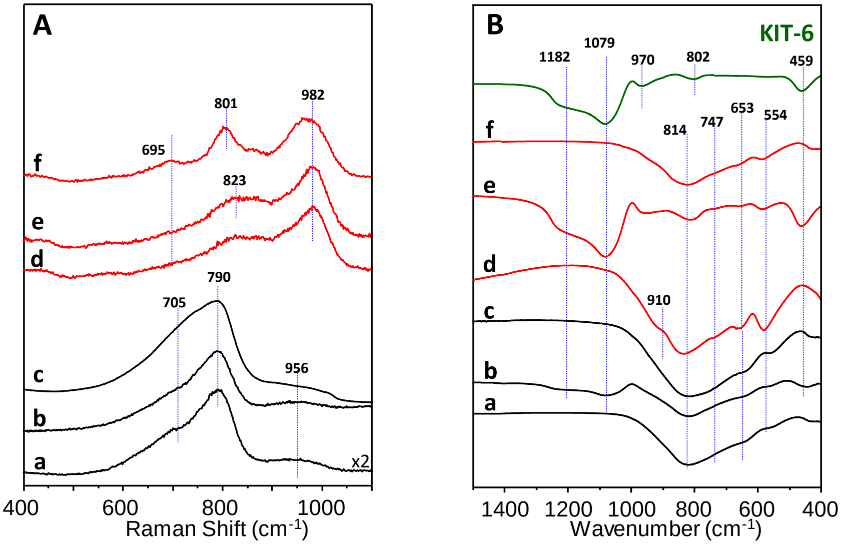

Figure 5.4. Raman (A) and FTIR (B) spectra of bulk and supported materials: a) R-WNb; b) R-WNb/KIT; c) WNb-H; d) R-WV; e) R-WV/KIT; f) WV-H.

Figure 5.4 B displays also FTIR spectra of bulk and supported materials. All the spectra show IR bands at 814, 747, 653 and 553 cm^{-1}, related to tungsten bronze materials (**Fig. 5.4. B**, *a-f*) [5, 7, 14]. Again, R-WV and R-WV/KIT sample shows a band at 910 cm^{-1} which can be ascribed to those V=O stretching type vibrations (**Fig. 5.4. B**, *d* and *e*). In addition, supported materials display extra signals at 1182, 1079, 970, 802, and 459 cm^{-1}, which are ascribed to Si-O vibrational modes of the siliceous support [15].

The acid characteristics of bulk and supported materials were elucidated by means of temperature-programmed desorption of ammonia (TPD-NH$_3$). The TPD-NH$_3$ patterns are presented in **Figure 5.5**, whereas the acid characteristics are summarized in **Table 5.2**. TPD-NH$_3$ analysis of KIT-6 silica shows very low acid features (**Table 5.2**): accordingly, it can be considered as an inert support.

Considering W-Nb-O based catalysts, R-WNb and R-WNb/KIT display a higher concentration of surface acid sites (i.e. acid sites per gram of catalyst) than that prepared hydrothermally (WNb-H catalyst) (**Table 5.2**). However, if we take into account the surface density of acid sites (i.e. number of acid sites per unit area), R-WNb and WNb-H present similar characteristics. On the other hand, supported R-WNb/KIT shows a lower density of acid sites, mainly due to the characteristics of the support (**Table 5.2**).

On the other hand, TPD-NH_3 profiles display three main desorption signals at low (ca. 200 ºC), medium (ca. 300 ºC) and high (ca. 400 ºC) temperature, which can be attributed to NH_3 desorbed from acid sites with low, medium and high acid strength, respectively. The contribution to medium-high acid strength sites decreases when reflux-synthesized W-Nb-O is supported on KIT-6 silica (R-WNb/KIT) (**Fig. 5.5**, *a* and *b* respectively). However, WNb-H shows the lowest contribution to medium-high temperature signals in the TPD-NH_3 profile, what implies a lower acid strength (**Fig. 5.5**, *c*).

In the case of W-V-O catalysts, a similar trend in TPD-NH_3 profiles than those observed for Nb-containing catalysts is observed (**Fig. 5.5**, *d*-*f*). This way, the intensity of desorption signals at medium and high temperatures decreases when R-WV (**Fig. 5.5**, *d*) is supported on KIT-6 (R-WV/KIT) (**Fig. 5.5**, *e*). Interestingly, for W-V materials, hydrothermally-synthesized WV-H catalysts displays an acid strength in between reflux-synthesized and supported catalysts, as it can be inferred from desorption signals in the TPD profiles, which show: i) a contribution to medium strength acid sites higher than R-WV/KIT (i.e. signal at 280 ºC; **Fig. 5.5**, *d*-*f*); and ii) a lower contribution to that signal than R-WV catalyst (**Fig. 5.5**, *d*-*f*). Then, R-WV displays the highest concentration and density of acid sites in V-containing series (**Table 5.2**).

Both concentration and density of acid sites in reflux-synthesized W-V-O catalyst decreases when it is supported on KIT-6 mesoporous silica, likely due to the elimination of the abovementioned medium and high strength acid sites (**Fig. 5.5**, *e-d*). As in the case of niobium containing catalysts, the surface density of acid sites is much lower in supported R-WV/KIT with respect to those prepared by reflux (R-WV) or hydrothermally (WV-H), due to the textural properties of the support (**Table 5.2**).

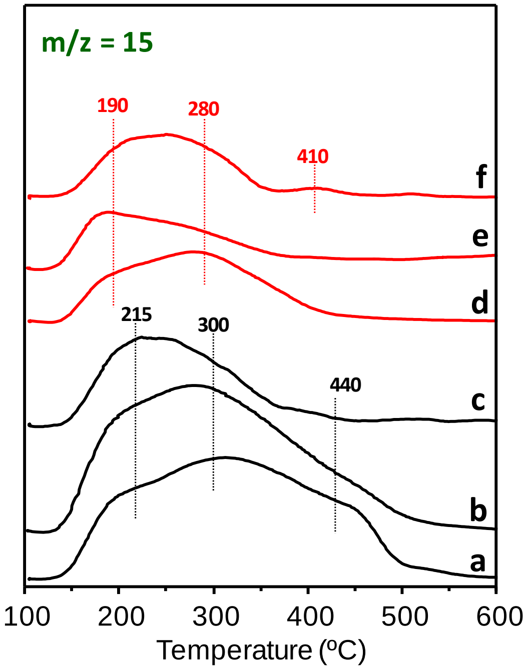

Figure 5.5. TPD-NH_3 profiles of bulk and supported WNb and WV oxides. a) R-WNb; b) R-WNb/KIT; c) WNb-H; d) R-WV; e) R-WV/KIT; f) WV-H.

Summarizing, materials synthesized by reflux method (R-WNb and R-WV) display a higher proportion of medium and high strength acid sites than hydrothermally synthesized materials (WNb-H and WV-H). The relative proportion of those medium-high strength acid sites can substantially be reduced by dispersing R-WNb and R-WV on an inert support, like KIT-6. Both supported and unsupported catalysts present a lower proportion of high acid strength acid centers than an undoped hexagonal tungsten bronze *h*-WO_3 [5, 7].

5.3. Gas-phase aerobic transformation of ethanol

The catalytic performance of bulk and supported W-Nb-O catalysts during the gas-phase aerobic transformation of ethanol is summarized in **Figure 5.6**. No differences, neither in ethanol conversion (**Fig. 5.6**, A), nor in selectivity to reaction products (**Fig. 5.6**, B and C) are observed among Nb-containing catalysts.

In general, diethyl ether (**Fig. 5.6**, B) and ethylene (**Fig. 5.6**, C) were the main reaction products, with the presence of minor amounts of carbon oxides and acetaldehyde (selectivity to both CO_x and acetaldehyde lower than 6 %). However, if we consider that supported R-WNb/KIT catalyst presents ca. 50 % of tungsten and niobium atoms with respect to bulk materials (see **Table 5.1**), it can be concluded that supported catalyst shows an efficiency for ethanol transformation higher than unsupported catalysts. Probably, a lower crystal size and/or a better dispersion of Nb-doped hexagonal tungsten bronze on the mesoporous silica could explain this behavior.

On the other hand, **Figure 5.7** compares the selectivity profiles of W-Nb-O catalysts at low (30 %) and high (80 %) ethanol conversion. The results show differences in ethylene/diethyl ether ratio depending on conversion degree, in which ethylene is already observed at low ethanol conversion. As the conversion of ethanol increases, the selectivity to diethyl ether decreases, for the benefit of ethylene formation. This suggests that ethylene is formed by both parallel and consecutive reactions. In fact, dehydration of ethanol has been reported to give diethyl ether, via intermolecular dehydration; and ethylene, via intramolecular dehydration, being the latter favored at higher reaction temperatures [16-20]. Despite this, catalysts display similar selectivity profiles regardless of the synthesis method used.

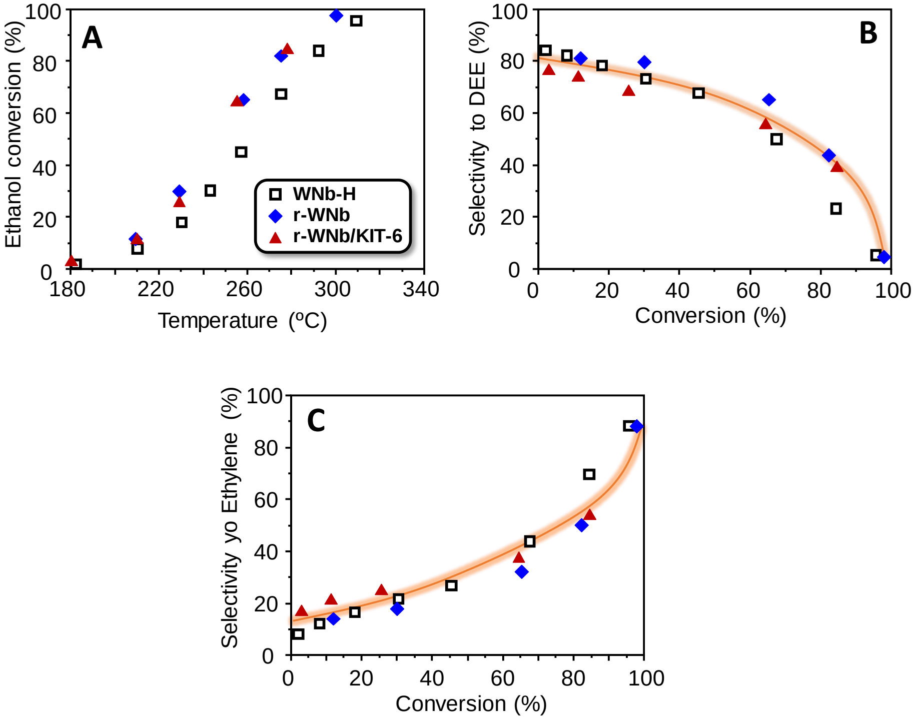

Figure 5.6. Catalytic performance of W-Nb-O catalysts. A) Ethanol conversion as a function of reaction temperature. B) Selectivity to diethyl ether as a function of ethanol conversion. C) Selectivity to ethylene as a function of ethanol conversion. Symbols: R-WNb (◆), R-WNb/KIT (▲), WNb-H (☐). Reaction conditions: EtOH/O_2/N_2 molar ratio of 6/13/81, Contact time W/F = 6.8 g_{cat} h mol_{EtOH}^{-1}.

The catalytic properties in ethanol aerobic transformation of bulk and supported W-V-O catalysts are summarized in **Figure 5.8**. The conversion of ethanol strongly depends on the catalyst preparation procedure. In this way, it can be observed that supported R-WV/KIT shows a lower catalytic activity than bulk materials (**Fig. 5.8**, A).

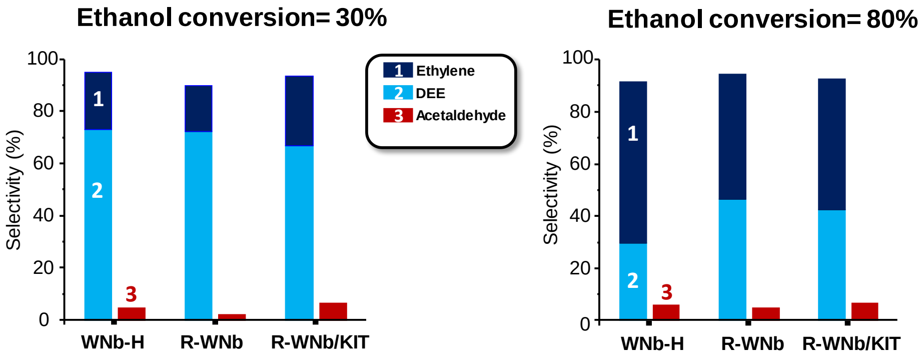

Figure 5.7. Selectivity profiles of bulk and supported W-Nb-O catalysts at low (20 %, left) and high (80 %, right) conversion of ethanol. DEE: diethyl ether. Reaction conditions: EtOH/O_2/N_2 molar ratio of 6/13/81, Contact time W/F = 6.8 g_{cat} h mol_{EtOH}^{-1}.

On the other hand, these catalysts show a considerable formation of acetaldehyde (**Fig. 5.8**, B), due to the presence of redox sites (i.e. V^{4+}/V^{5+}). Also, the formation of diethyl ether, DEE (**Fig. 5.8**, C), and ethylene (**Fig. 5.8**, D) is observed, due to dehydration reactions on acid sites. In addition, small amounts of acetic acid and ethyl acetate were also observed (especially over R-WV catalyst).

Along the series, the selectivity to carbon oxides was negligible, being lower than 3 %, under these reaction conditions. We must inform that, at low ethanol conversion, acetaldehyde and diethyl ether were the main products observed in all cases, with minor amounts of ethylene. However, as ethanol conversion increases the selectivity to acetaldehyde and diethyl ether decreases, with a concomitant increase in the selectivity to ethylene, ethyl acetate and acetic acid (**Fig. 5.8**).

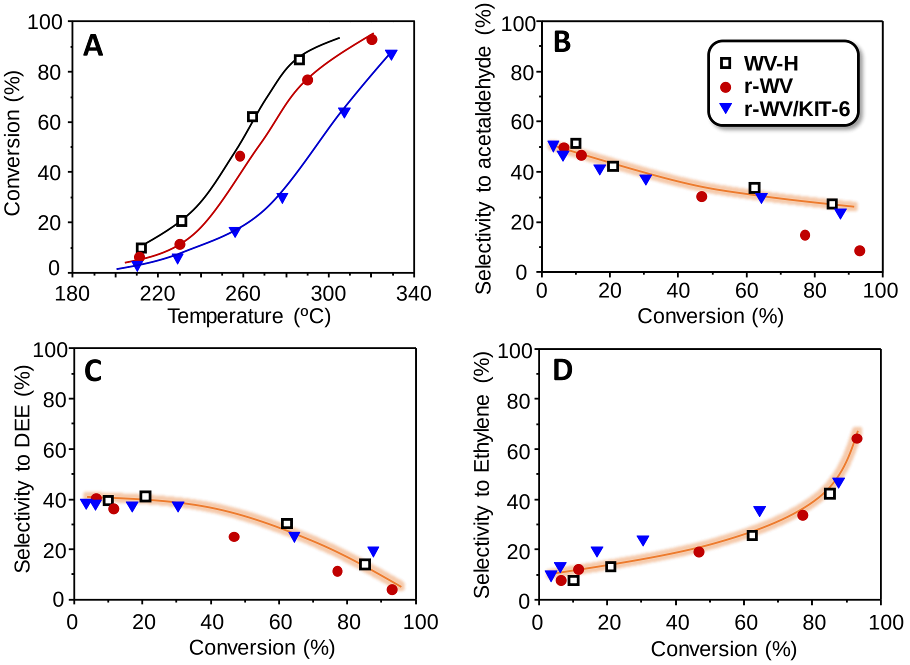

Figure 5.8. Catalytic performance of W-V-O catalysts. A) Ethanol conversion as a function of reaction temperature. B) Selectivity to acetaldehyde as a function of ethanol conversion. C) Selectivity to diethyl ether as a function of ethanol conversion. D) Selectivity to ethylene as a function of ethanol conversion. Symbols: R-WV (●), R-WV/KIT (▼), WV-H (□). Reaction conditions: EtOH/O_2/N_2 molar ratio of 6/13/81, Contact time W/F = 6.8 g_{cat} h mol_{EtOH}^{-1}.

Figure 5.9 displays the selectivity to the main reaction products achieved at low (30 %) or high (80 %) conversion of ethanol for bulk and supported W-V-O materials. The main difference along the series is observed in the selectivity to acetaldehyde, ethyl acetate and acetic acid; being the selectivity to ethylene and diethyl ether (products of dehydration on surface acid sites) similar all along the series. In this sense the selectivity to acetaldehyde, ethyl acetate and acetic acid decreases in the following trend: R-WV > WV-H > R-WV/KIT.

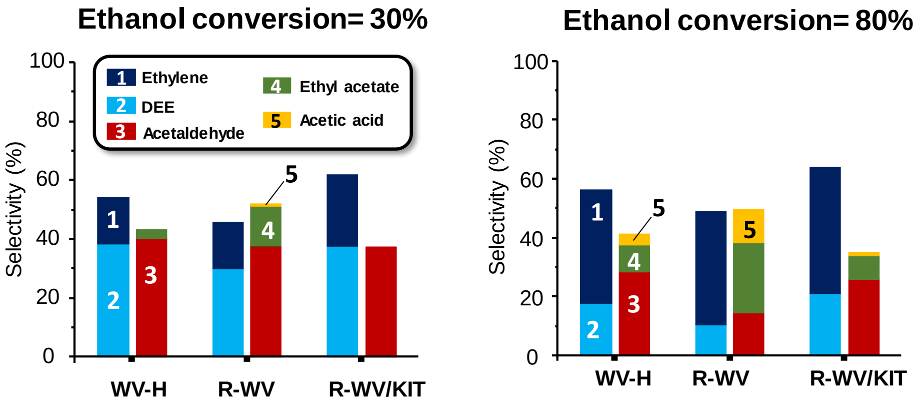

Figure 5.9. Selectivity profiles of bulk and supported W-V catalysts at low (20 %, left) and high (80 %, right) conversion of ethanol. DEE: diethyl ether. Reaction conditions: $EtOH/O_2/N_2$ molar ratio of 6/13/81, Contact time W/F = 6.8 g_{cat} h mol_{EtOH}^{-1}.

Interestingly, the higher selectivity to ethyl acetate and acetic acid seems to be related to the acid characteristics of the catalysts. As it was observed by TPD-NH_3, R-WV sample shows the highest acid strength among W-V-O catalysts. If we focus our attention on the selectivity to products in which redox sites are involved, (i.e. acetaldehyde, ethyl acetate and acetic acid), it can be noted that the sum of acetaldehyde, ethyl acetate and acetic acid is kept constant at low and high conversion degrees (**Figure 5.9**). This fact suggests that both ethyl acetate and acetic acid are formed via consecutive transformation of acetaldehyde. Regarding acetic acid formation, several routes can be suggested, likely the oxidation of ethanol, acetaldehyde and/or ethyl acetate on surface redox sites. On the other hand, ethyl acetate could be formed by esterification of acetic acid with ethanol on high strength acid sites. Hence R-WV displays both the higher proportion of strong surface acid sites and the highest selectivity to ethyl acetate.

5.4. Gas-phase aerobic transformation of glycerol

Both series (Nb- and V-containing catalysts) of bulk and supported tungsten bronze-based catalysts were also tested in the aerobic transformation of glycerol. The catalytic results for Nb-containing catalysts are shown in **Figure 5.10**, whereas those obtained for V-containing catalysts are presented in **Figure 5.11**.

Considering niobium-containing series, all the catalysts show yields to acrolein higher than 70 % at 298 ºC (**Fig. 5.10**; A, C and E). At higher reaction temperatures the selectivity to acrolein decreases, and the reaction is directed to the formation of carbon oxides (**Fig. 5.10**; B, D and F). It is worth noting that total conversion of glycerol was always attained. This is an important fact in order to prevent oligomerization and uncontrolled consecutive reactions towards the formation of heavy by-products [5, 9].

In general, all the catalysts display comparable catalytic performance, in terms of the nature of the main reaction products and by-products, however they show some differences in selectivity depending on the synthesis method. Reflux-synthesized R-WNb sample presents the highest yield to carbon oxides and heavy compounds, what is traduced in a lower selectivity to acrolein (ca. 70 % at 298 ºC) (**Fig. 5.10**, A and B). On the other hand, supported R-WNb/KIT catalyst shows a lower selectivity to both by-products (i.e. carbon oxides and heavy compounds), with a subsequent increase in the selectivity to acrolein (ca. 75 % at 298 ºC) (**Fig. 5.10**, C and D). The better catalytic performance has been achieved with hydrothermally-synthesized WNb-H catalyst, which shows the lowest selectivity to carbon oxides and heavy by-products and, consequently, the highest yield to acrolein (ca. 83 % at 298 ºC) (**Fig. 5.10**, E and F).

All these catalytic features can be explained considering the specific acid characteristics of the catalysts. As it was commented above (see Section 5.3), the acid strength of acid sites in R-WNb decreases when the mixed oxides are supported on mesoporous KIT-6 (i.e. R-WNb/KIT catalyst).

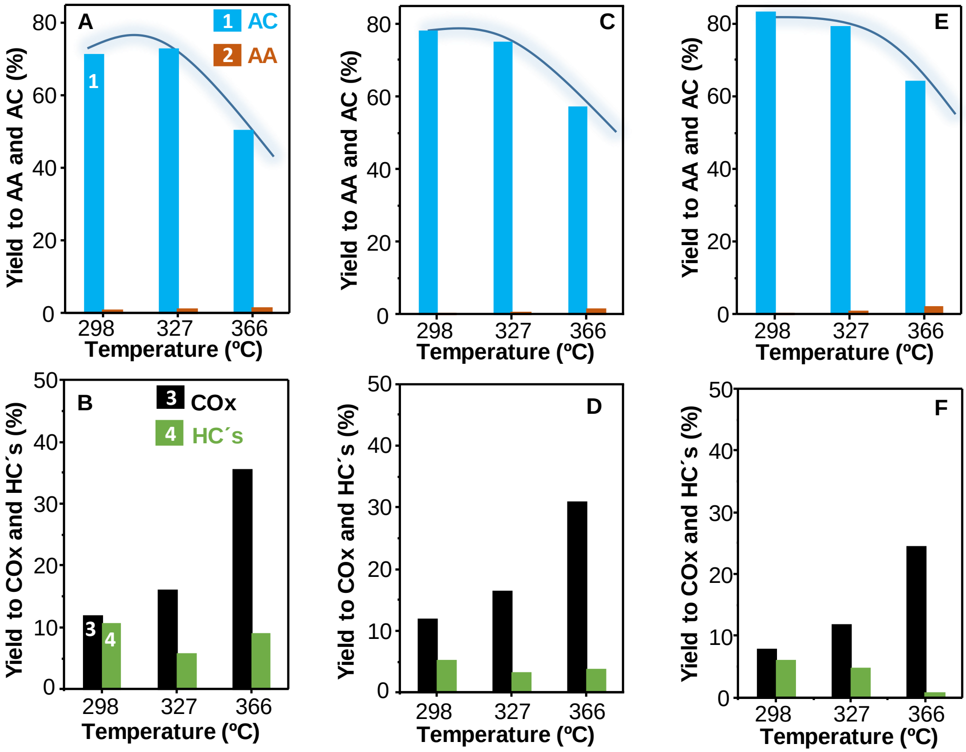

Figure 5.10. Yields to acrolein (AC, blue), acrylic acid (AA, brown), carbon oxides (CO_x, black) and heavy compounds (HC´s, green) at different reaction temperatures. A-B) R-WNb; C-D) R-WNb/KIT; E-F) WNb-H. Reaction conditions: Gly/H_2O/O_2/N_2/He molar ratio of 2/40/4/15/39, contact time W/F = 81 g_{cat} h mol_{gly}^{-1}.

This would explain the increase in the selectivity to acrolein over R-WNb/KIT catalyst, since lower acid strength acid sites would promote the desorption of acrolein, avoiding side reactions to CO_x and heavy compounds [9]. Accordingly, WNb-H sample shows both the lowest acid strength and the highest selectivity to acrolein in the aerobic transformation of glycerol in the gas phase, due to a lower formation of by-products.

Figure 5.11 presents the catalytic performance of V-containing bulk and supported materials in the gas phase aerobic transformation of glycerol. Again all the catalysts showed total conversion of glycerol under the reaction conditions used. In this case, the catalysts display different product distribution with respect to Nb-doped tungsten bronzes, showing a lower selectivity to acrolein and a substantial increase in the yield to acrylic acid (**Fig. 5.11**). This indicates the multifunctional acid-redox character of V-based series, by which glycerol transformation takes place via two consecutive steps: i) dehydration of glycerol to acrolein on acid sites and; ii) partial oxidation of acrolein into acrylic acid on $V^{5+/}V^{4+}$ redox pairs. Although specific functionalities are associated with each reaction step, it is important to take into account that acid sites play an important role on both consecutive stages. In this sense the strength and distribution of surface acid sites govern the adsorption-desorption steps of reaction intermediates and products during catalytic cycles [9]. Particularly, they should present sufficient strength and density to perform the glycerol dehydration to acrolein, but not too high that it could hinder the desorption of intermediates and products, what would favor consecutive reactions to undesired products (mainly carbon oxides and oligomers).

Reflux synthesized samples (i.e. R-WV and supported R-WV/KIT catalysts) display their highest selectivity to acrylic acid at higher temperature, ca. 327 ºC (**Fig. 5.11**, A and C), than that observed over WV-H catalyst, ca. 300 ºC (**Fig. 5.11**, E). This behavior suggests a higher catalytic activity of the latter material. In fact, WV-H shows the maximum total yield to acrolein and acrylic acid (Y_{AC+AA} = 44 % at 300 ºC) along the series (**Fig. 5.11**, E). In all cases, the yield to carbon oxides increases when increasing reaction temperature, while the yield to heavy by-products observed was ca. 5-20 % in all the range examined (**Fig. 5.11**; B, D and F). The highest selectivity to acrylic acid was achieved on supported R-WV/KIT (S_{AA} = 31%), even higher than that obtained with WV-H catalyst (S_{AA} = 26 %) and much higher than reflux-synthesized unsupported r-WV catalyst (S_{AA} = 19 %) (**Fig. 5.11**; A, C and E).

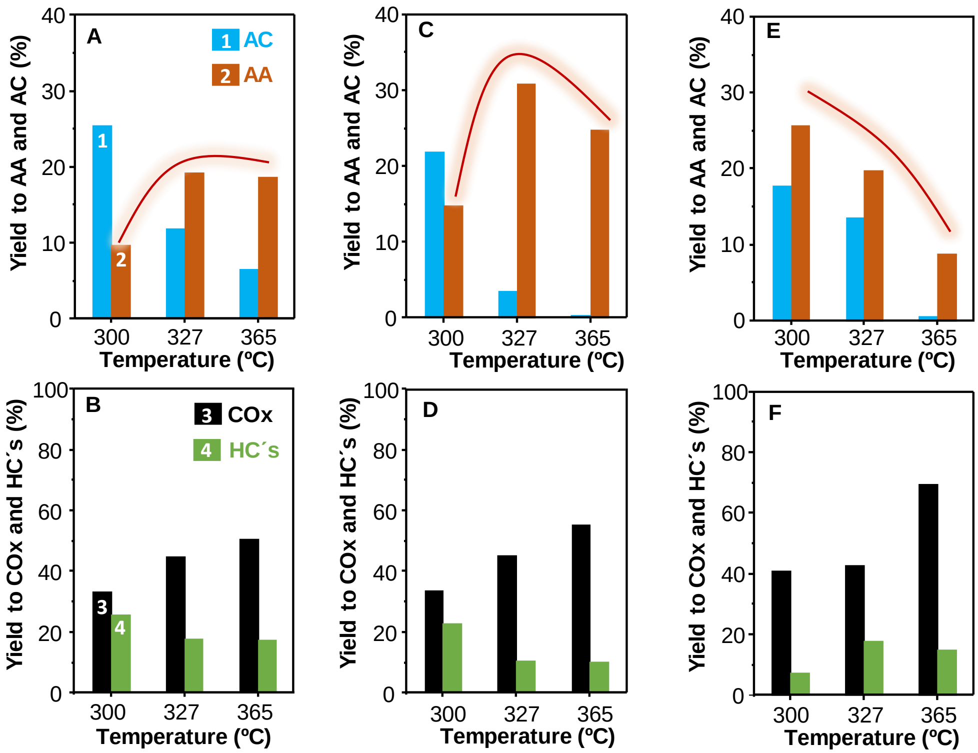

Figure 5.11. Yields to acrolein (**AC**, blue), acrylic acid (**AA**, brown), carbon oxides (**CO$_x$**, black) and heavy compounds (**HC´s**, green) at different reaction temperatures over V-containing catalysts: R-WV (A and B); R-WV/KIT (C and D); WV-H (E and F). Reaction conditions: Gly/H_2O/O_2/N_2/He molar ratio of 2/40/4/15/39, contact time W/F = 81 g_{cat} h mol_{gly}^{-1}.

As occurred in W-Nb-O based catalysts, the specific acid features, particularly that related to acid strength, could explain these differences in selectivity profiles. In the same way, the catalytic results observed over unsupported R-WV catalyst are substantially improved (in terms of yield to acrylic acid) when W-V-O is supported on mesoporous KIT-6 silica (**Fig. 5.11**, A and C). This is due to a decrease in the proportion of high and medium strength surface acid sites; which would enhance acrylic acid and acrolein desorption, avoiding total oxidation and oligomerization (**Fig. 5.11**, *d* and *e*). In spite of these observations, the effect of V=O in the pseudocrytalline oxide cannot be ruled out.

According to Raman and FTIR results, the number of V=O species in both supported and unsupported reflux-synthesized samples (i.e. pseudocrystalline phases) is higher than in the case of the catalyst prepared hydrothermally. This could also facilitate an improvement of the partial oxidation of acrolein to acrylic acid in the consecutive step [8, 9].

5.5. General Remarks

Summarizing, the effect of the synthesis method on the physicochemical characteristics and catalytic performance in the gas phase aerobic transformation of ethanol and glycerol of V- and Nb- containing tungsten oxide bronzes has been studied. Characterization results demonstrate that it is possible to prepare W-Nb and W-V oxide bronzes by an alternative reflux method, in which V- and Nb- have been incorporated into the tungsten bronze structure. In addition, materials prepared by reflux have been successfully supported on a mesoporous silica (KIT-6). Both reflux and hydrothermal method gave rise to a well ordered *h*-WO_3 in the case of W-Nb-O series. On the other hand, V-containing tungsten bronze catalysts prepared by reflux method present a pseudocrystalline structure in which the long-range order is lost along *a* and *b* directions; meanwhile hydrothermal conditions favor the crystallization of a *h*-WO_3-type structure.

Catalytic performance in both ethanol and glycerol aerobic transformation show a similar catalytic behavior (in terms of the chemical nature of the products) for reflux, supported and hydrothermally-synthesized catalysts of each series. Nb-containing materials present a high selectivity to dehydration products in both ethanol (formation of diethyl ether and ethylene) and glycerol (high selectivity to acrolein) gas-phase transformations, indicating their main acid character. On the other hand, V-containing materials led to the formation of both dehydration and oxidation products in the gas phase transformation of the alcohols, what points out their bifunctional acid-redox character. In ethanol transformation, both redox and acid sites work in a parallel way, leading to the formation of diethyl ether and ethylene on acid sites, and acetaldehyde on redox sites. In the case of the gas phase transformation of glycerol, the reaction mechanisms follow a different path, in which acrolein is formed on a first reaction step by dehydration on Brönsted acid sites; and acrylic acid is formed in a consecutive step by partial oxidation of acrolein on redox sites. In addition, a considerable amount of carbon oxides are formed, especially at high reaction temperatures, together with variable amounts of heavy by-products (5-20 % yield).

The effect of the support on the acid properties of reflux-synthesized catalysts has been outlined. When catalysts prepared by reflux method are supported on a mesoporous KIT-6 silica, the proportion of medium and high acid strength surface acid sites decreases. As a result, the catalytic performance improves for supported W-Nb-O and W-V-O catalysts, especially in the aerobic transformation of glycerol. Particularly, the elimination of medium-high strength acid centers would favor the desorption of the products, avoiding the overoxidation to carbon oxides and the formation of heavy by-products, thus increasing the selectivity to acrolein (in the case of W-Nb-O catalysts) and to acrylic acid (in the case on W-V-O catalysts).

5.5. References

[1] D. Cespi, F. Passarini, G. Mastragostino, I. Vassura, S. Larocca, A. Iaconi, A. Chieregato, J.L. Dubois, F. Cavani, *Glycerol as feedstock in the synthesis of chemicals: a life cycle analysis for acrolein production*, Green Chemistry, 17 (2015) 343-355.

[2] M. Dalil, D. Carnevali, J.-L. Dubois, G.S. Patience, *Transient acrolein selectivity and carbon deposition study of glycerol dehydration over WO_3/TiO_2 catalyst*, Chemical Engineering Journal, 270 (2015) 557-563.

[3] Y. Magatani, K. Okumura, J.-L. Dubois, J.-F. Devaux, Patent, WO/2011/033689

[4] R. Znaiguia, J.-M. Millet, S. Loridant, P. Rey, US20150239815, 2015.

[5] M.D. Soriano, P. Concepcion, J.M. Lopez Nieto, F. Cavani, S. Guidetti, C. Trevisanut, *Tungsten-Vanadium mixed oxides for the oxidehydration of glycerol into acrylic acid*, Green Chemistry, 13 (2011) 2954-2962.

[6] A. Chieregato, M.D. Soriano, F. Basile, G. Liosi, S. Zamora, P. Concepción, F. Cavani, J.M. López Nieto, *One-pot glycerol oxidehydration to acrylic acid on multifunctional catalysts: Focus on the influence of the reaction parameters in respect to the catalytic performance*, Applied Catalysis B: Environmental, 150-151 (2014) 37-46.

[7] M.D. Soriano, A. Chieregato, S. Zamora, F. Basile, F. Cavani, J.M. López Nieto, *Promoted Hexagonal Tungsten Bronzes as Selective Catalysts in the Aerobic Transformation of Alcohols: Glycerol and Methano*l, Topics in Catalysis, 59 (2016) 178-185.

[8] A. Chieregato, M.D. Soriano, E. García-González, G. Puglia, F. Basile, P. Concepción, C. Bandinelli, J.M. López Nieto, F. Cavani, *Multielement Crystalline and Pseudocrystalline Oxides as Efficient Catalysts for the Direct Transformation of Glycerol into Acrylic Acid*, ChemSusChem, 8 (2015) 398-406.

[9] C. Alessandro, B. Claudia, C. Patricia, S.M. Dolores, P. Francesco, B. Francesco, C. Fabrizio, J.M. López Nieto, *Structure–Reactivity Correlations in Vanadium-Containing Catalysts for One-Pot Glycerol Oxidehydration to Acrylic Acid*, ChemSusChem, 10 (2017) 234-244.

[10] I.M. Szilágyi, J. Madarász, G. Pokol, P. Király, G. Tárkányi, S. Saukko, J. Mizsei, A.L. Tóth, A. Szabó, K. Varga-Josepovits, *Stability and controlled composition of hexagonal* WO_3, Chemistry of Materials, 20 (2008) 4116-4125.

[11] T. Murayama, N. Kuramata, S. Takatama, K. Nakatani, S. Izumi, X. Yi, W. Ueda, *Synthesis of porous and acidic complex metal oxide catalyst based on group 5 and 6 elements*, Catalysis Today, 185 (2012) 224-229.

[12] H. Hibst, F. Rosowski, G. Cox, *New Cs-containing Mo-*V^{4+} *based oxides with the structure of the M1 phase-Base for new catalysts for the direct alkane activation*, Catalysis Today, 117 (2006) 234-241.

[13] J.M. Jehng, I.E. Wachs, *Structural Chemistry and Raman spectra of niobium oxides*, Chemistry of Materials, 3 (1991) 100-107.

[14] K.R. Dey, T. Debnath, C.H. Rüscher, M. Sundberg, A. Hussain, *Synthesis and characterization of niobium doped hexagonal tungsten bronze in the systems,* $Cs_xNb_yW_{1-y}O_3$, Journal of Materials Science, 46 (2011) 1388-1395.

[15] K. Soni, B.S. Rana, A.K. Sinha, A. Bhaumik, M. Nandi, M. Kumar, G.M. Dhar, *3-D ordered mesoporous KIT-6 support for effective hydrodesulfurization catalysts*, Applied Catalysis B: Environmental, 90 (2009) 55-63.

[16] M. Zhang, Y. Yu, *Dehydration of ethanol to ethylene*, Industrial & Engineering Chemistry Research, 52 (2013) 9505-9514.

[17] T.K. Phung, L. Proietti Hernández, G. Busca, *Conversion of ethanol over transition metal oxide catalysts: Effect of tungsta addition on catalytic behaviour of titania and zirconia*, Applied Catalysis A: General, 489 (2015) 180-187.

[18] W. Alharbi, E. Brown, E.F. Kozhevnikova, I.V. Kozhevnikov, *Dehydration of ethanol over heteropoly acid catalysts in the gas phase*, Journal of Catalysis, 319 (2014) 174-181.

[19] T.K. Phung, L. Proietti Hernández, A. Lagazzo, G. Busca, *Dehydration of ethanol over zeolites, silica alumina and alumina: Lewis acidity, Brønsted acidity and confinement effects*, Applied Catalysis A: General, 493 (2015) 77-89.

[20] T.T.N. Nguyen, V. Belliere-Baca, P. Rey, J.M.M. Millet, *Efficient catalysts for simultaneous dehydration of light alcohols in gas phase*, Catalysis Science & Technology~~,~~ 5 (2015) 3576-3584.

Chapter 6

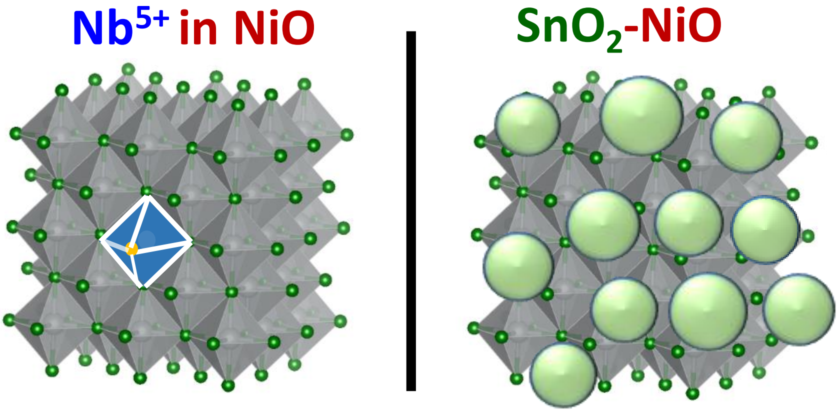
Nb^{5+} in NiO
SnO_2-NiO

Promoted NiO catalysts: Studies on the redox and catalytic properties in the ODH of ethane

6.1. Previous considerations

Olefins (specially ethylene and propene) can be considered the "holy grail" of the petrochemical industry [1]. Among them, ethylene, with a worldwide production of 150 million tons in 2015, stands as its most important building block [2, 3]. In fact, ethylene is directly used in the production of polyethylene (with an annual production of ca. 70 million tons), and as precursor of some of the main commodity chemicals in the chemical industry (like vinyl chloride, ethyl benzene or ethylene oxide) [4]. Nowadays, its production is mainly based on steam cracking, which is a high energy-demanding process. Since steam crackers are on their production limit, and the demand of ethylene steadily grows year by year, the development of new alternative processes for its production becomes necessary [5-10]. With a view to a future application, the oxidative dehydrogenation (ODH) of ethane is probably the most interesting alternative for the production of ethylene [8-10]. However, very few catalytic systems have shown an outstanding catalytic performance for this reaction. Particularly, we can point out two types of catalysts, which present high selectivity to ethylene at medium and/or high ethane conversion levels: i) catalysts based on multicomponent mixed metal oxides, as MoVTeNbO mixed oxides, presenting yields to ethylene up to 75 % [11, 12]; and ii) catalysts based on NiO, showing yields to ethylene of ca. 40 %. [13-15].

Considering NiO-based catalysts, two types of systems have been reported to be higly efficient in the ODH of ethane: i) M-promoted NiO, especially Sn- [15-17] and Nb-promoted [13, 14, 17-22] catalysts; and ii) supported NiO materials, mainly Al_2O_3 [23-25] and TiO_2-supported nickel oxide [26]. In this chapter, the attention has been focused on promoted NiO catalysts.

Despite their high efficiency in the oxidation of ethane, the nature of the active and selective sites still generates some controversy. For instance, it has been proposed that the nature of surface active sites can be modified depending on the acid characteristics of the promoter metal oxide [17].

Also, the morphology of NiO particles has been reported to be important in the catalytic performance of these materials, as it can modify the cubic lattice parameter of NiO [27].

According to this, the aim of this chapter is to shed some light on the redox properties of promoted NiO catalysts and their importance in the catalytic performance in the ODH of ethane. Hence, unpromoted and Me-promoted NiO (Me = La, Nb, Sn) have been prepared by the same evaporation method (see point **2.1.4** in Experimental Section), and studied by means of *in situ* XAS spectroscopy, under oxidative (in the presence of oxygen) and reductive conditions (in the absence of oxygen). The materials have also been characterized by XRD, Raman, XPS, temperature-programmed reduction in H_2, and electron microscopy. The effect of reduction-reoxidation kinetics and the promoter-nickel oxide phase distribution is discussed.

6.2. Catalytic properties of promoted NiO catalysts in the ODH of ethane

The catalytic results in ethane ODH for unpromoted and Me-promoted NiO catalysts (Me= La, Nb, Sn) are summarized in **Table 6.1**. Unpromoted and La-promoted nickel oxide (i.e. NiO and NiO-La) show a selectivity to ethylene relatively low (i.e. 37.1 and 52.4 %, respectively) at an ethane conversion of 7.0 and 8.4%, respectively). However, Nb- and Sn-promoted nickel oxide catalysts (i.e. NiO-Nb and NiO-Sn, respectively) present a high selectivity to ethylene at similar ethane conversion (i.e. 8.6 and 8.8%, respectively). In this way, NiO-Nb and NiO-Sn catalysts show a comparable catalytic behavior in terms of catalytic activity and selectivity in the ODH of ethane (**Table 6.1**).

With the aim of studying the robustness of the catalysts under reductive conditions, catalytic tests in the absence of oxygen were carried out after 2 h on stream. **Figures 6.1** and **6.2** shows the variation of ethane conversion and the selectivity to the main reaction products in the presence of oxygen (ethane/O_2/He molar ratio of 5/5/90) and in the absence of oxygen (ethane/O_2/He = 5/0/95) achieved over NiO-Nb (**Fig. 6.1**) and NiO-Sn samples (**Fig. 6.2**). We must indicate that, after 2 h online, O_2 was replaced by He, what gives rise to significant differences in the selectivity profiles in both cases.

Table 6.1. Catalytic behavior of unpromoted and promoted NiO catalysts.

Catalyst	**Ethane conversion (%)**[a]	**Selectivity to ethylene (%)**[a]
NiO-Nb	8.6	83.4
NiO-Sn	8.8	83.7
NiO-La	8.4[b]	52.4[b]
NiO	7.0	37.1

[a] Reaction conditions: ethane/O_2/He molar ratio of 5/5/90; 450 ºC; contact time W/F = 2 g_{cat} h $(mol_{ethane})^{-1}$. [b] Contact time W/F = 1 g_{cat} h $(mol_{ethane})^{-1}$.

Thus, over NiO-Nb catalyst, the conversion of ethane increases from 9 % to 22 % when oxygen is removed from the feed (**Fig. 6.1,** A). This is accompanied by an initial increase in the selectivity to CO_2 (from 17 % to ca. 40 %), and a drop of ethylene selectivity, which was not detected anymore (**Fig. 6.1**, B). Then, methane was the main reaction product detected in the output stream, with a selectivity of approximately 60 %. After ca. 30 min without oxygen, ethane conversion decreases until ca. 15 % (**Fig. 6.1**, A), mainly due to a decrease in the formation of carbon oxides (**Fig. 6.2**, B). In parallel, methane selectivity increases until 95 % (**Fig. 6.2**, B). Finally, the conversion of ethane increases constantly, whereas the selectivity to carbon dioxide and methane is kept constant at 5 % and 95 % respectively. It is worth noting that: i) hydrogen was always detected once oxygen was substituted by helium in the feed; and ii) the carbon balance decreased until 75 %. This behavior can be explained by: i) the reduction of nickel oxide to metallic nickel, and ii) the formation of large amounts of coke on the catalyst surface, which was corroborated after reaction.

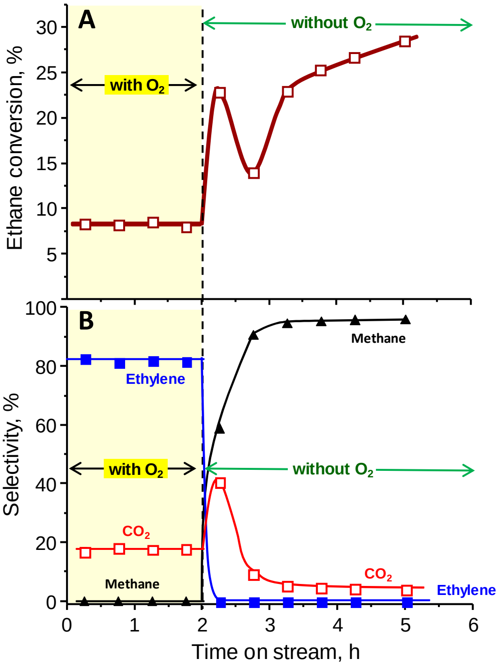

Figure 6.1. Variation of ethane conversion (A) and selectivity to reaction products (B) as a function of time on stream during the ODH of ethane for NiO-Nb catalyst. Catalytic tests were conducted in the presence (molar ratio ethane/O_2/He = 5/5/90) and in the absence (molar ratio ethane/O_2/He = 5/0/95) of oxygen in the feed. Reaction conditions: 450 ºC, contact time W/F = 2 g_{cat} h $(mol_{ethane})^{-1}$.

In the case of NiO-Sn catalyst (**Fig. 6.2**), the catalytic performance in the absence of oxygen was surprisingly different to that observed over NiO-Nb. Thus, the drastic decrease in ethane conversion when oxygen was removed from the feed is followed by an increase in the selectivity to ethylene (from 84 % to 93 %), and a concomitant decrease in the selectivity to carbon dioxide (from 16 % to 7%) (**Fig. 6.2**, B). Finally, the ethane conversion went on decreasing the next 4 hours on stream, keeping its selectivity profile unaltered (**Fig. 6.2**, A).

According to these results, ethane activation in aerobic conditions seems to be similar on both catalytic systems. However, in anaerobic conditions, the reactivity takes two different pathways depending on the catalyst composition.

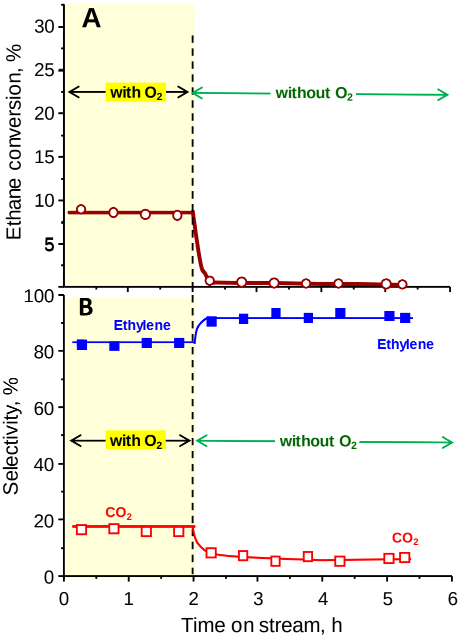

Figure 6.2. Variation of ethane conversion (A) and selectivity to reaction products (B) as a function of time on stream during the ODH of ethane for NiO-Sn catalyst. Catalytic tests were conducted in the presence (molar ratio ethane/O_2/He = 5/5/90) and in the absence (molar ratio ethane/O_2/He = 5/0/95) of oxygen in the feed. Reaction conditions: 450 ºC, contact time W/F = 2 g_{cat} h $(mol_{ethane})^{-1}$.

It appears that Ni sites on NiO-Nb catalyst undergo a fast reduction to metallic nickel in the absence of oxygen (reductive atmosphere), which is very active in hydrocarbon reforming reactions, thus producing hydrogen and methane. On the other hand, Ni species on NiO-Sn must remain in a relatively high oxidation state, even when oxygen is not present in the feed. In this particular case, product distribution does not present significant differences with respect to oxidative conditions, although it shows a very low conversion of ethane (ca. 0.5 %). The low amounts of ethylene and carbon dioxide produced under the absence of oxygen can be explained by means of a Mars-van Krevelen mechanism, by which the remaining lattice oxygen, would be responsible for the oxidation of the alkane.

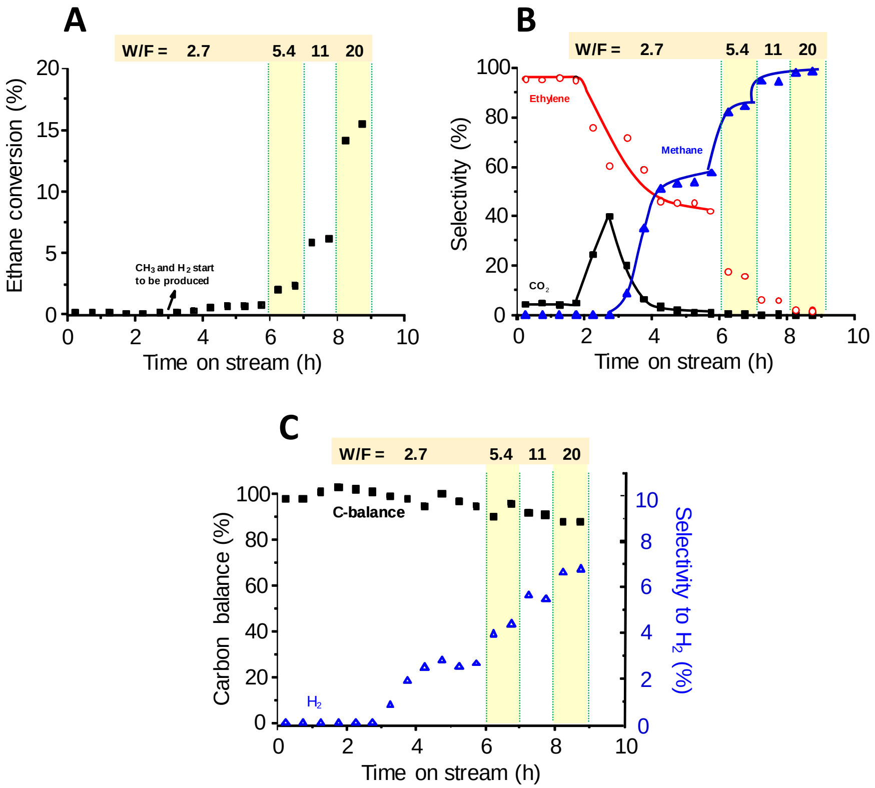

Figure 6.3. Evolution of ethane conversion (A), selectivity to main reaction products (B), carbon balance and selectivity to hydrogen (C) with time on stream for NiO-Sn catalyst. Reaction conditions: ethane/O_2/He molar ratio of 30/0/70; 475 ºC, contact time W/F in the range 2.7-20 g_{cat} h $(mol_{ethane})^{-1}$.

The reduction of Ni^{2+} species in NiO-Sn was only observed after several hours online and using much higher concentration of ethane in the feed. For example, using an ethane/O_2/He molar ratio of 30/0/70, higher contact time (W/F up to 20 g_{cat} h $(mol_{ethane})^{-1}$) and higher reaction temperature (475 ºC) (**Fig. 6.3**). This way, hydrogen and methane start to be produced after ca. 2.5 h online, showing a similar catalytic behavior than NiO-Nb, but with a much lower activity. Hence, all these observations suggest that Ni^{2+}

species in NiO-Nb display a remarkably higher reducibility than those in NiO-Sn when an oxygen-free feed is used (ethane/He).

6.3. Characterization of promoted NiO catalysts

XRD patterns of calcined catalysts are shown in **Figure 6.4**. All the materials show Bragg signals at positions corresponding to the cubic phase of NiO (Fm3m, ICSD No: 184626). Promoted NiO catalysts present much broader diffraction peaks (**Fig. 6.4**, patterns *a*-*c*) than unpromoted NiO (**Fig. 6.4**, pattern *d*), which can be associated with a lower crystallinity and/or a lower particle size of NiO crystals in promoted catalysts. In fact, the average crystallite size, estimated by Scherrer equation, shows a considerable smaller crystal size for NiO-Nb, NiO-Sn and NiO-La catalysts (8, 15 and 10 nm, respectively) than unpromoted nickel oxide sample (ca. 30 nm) (**Table 6.2**).

Table 6.2. Physicochemical features of NiO-based catalysts.

Catalyst	Particle size (nm)[a]	Cubic cell parameter (Å) [b]	H_2-TPR [c]	
			TM (ºC) [d]	H_2-uptake [e]
NiO-Nb	8	4.1759	357	19.57
NiO-Sn	15	4.1767	331	21.54
NiO-La	10	4.1714	308	22.59
NiO	30	4.1760	298	20.61

[a] Estimated by Scherrer equation; [b] Obtained by profile fitting. [c] Temperature-programmed reduction in H_2 (H_2-TPR); [d] TM: temperature for the maximum H_2-uptake; [e] H_2-uptake in $mmol_{H2}\ g_{Ni}^{-1}$.

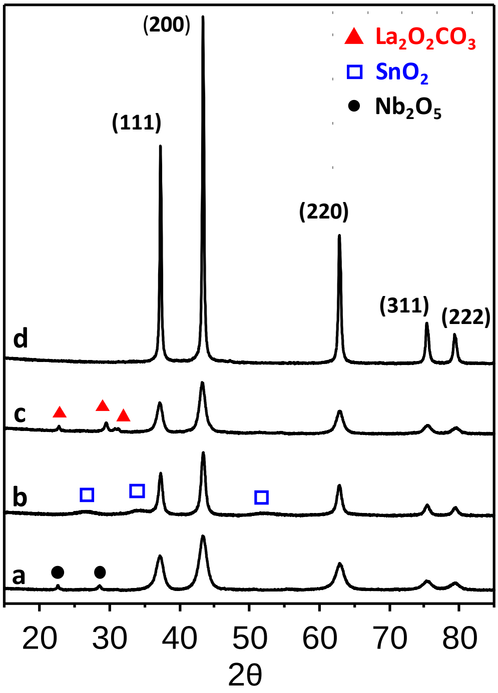

Figure 6.4. XRD patterns of NiO-based catalysts. a) NiO-Nb; b) NiO-Sn; c) NiO-La; d) NiO. Symbols: (●) Nb_2O_5 (JCPDS: 01-071-0336); (□) SnO_2 (JCPDS: 00-046-1088); (▲)$La_2O_2CO_3$ (JCPDS: 00-048-1113).

On the other hand, no significant differences in the cubic cell parameter were found along the series ($a \approx 4.17$ Å) (**Table 6.2**). Apart from diffraction peaks related to NiO, diffraction patterns of promoted catalysts display additional signals, which can be assigned to the presence of minor amounts of Nb_2O_5 (JCPDS: 01-071-0336) (**Figure 6.4**, pattern *a*), SnO_2 (JCPDS: 00-046-1088) (**Fig. 6.4**, pattern *b*) or $La_2O_2CO_3$ (JCPDS: 00-048-1113) (**Fig. 6.4**, pattern *c*). Interestingly, the presence of very broad peaks assigned to SnO_2 in NiO-Sn sample suggest the presence of very small tin oxide nanoparticles (**Fig. 6.4**, pattern *b*). In the case of NiO-Nb and NiO-La this feature is not observed, showing low intensity but well-defined narrow Bragg signals of both Nb_2O_5 and $La_2O_2CO_3$, respectively (**Fig. 6.4**, patterns *a* and *c*).

Average bulk composition of promoted catalysts (estimated by XEDS) shows small differences in promoter concentration (of ca. 5.9 and 8.7 at. % for NiO-Nb and NiO-Sn respectively) (**Table 6.3**).

On the other hand, XEDS line-scans of individual particles in each sample indicate a Nb content in the range 5.4-11 at.% for NiO-Nb (Figure 6.5, A); meanwhile NiO-Sn shows a very low concentration of Sn in isolated NiO particles, being in the range 0.5-1 at.% (**Fig. 6.5,** B). According to this, the fact that *a* lattice parameter of NiO-Nb sample does not vary with respect to unpromoted nickel oxide (**Table 6.2**) at this promoter concentration can be explained either by the presence of Nb_2O_5, that would decrease the Nb content in NiO, and/or by the presence of extra-framework Nb^{5+} species, likely on the surface, that would not modify NiO framework.

Table 6.3. Bulk and surface composition of NiO-based catalysts.

Catalyst	**Composition (at. %)**			
	Bulk [a]		**Surface** [b]	
	Ni	**Promoter**	**Ni**	**Promoter**
Nb-NiO	94.6	5.9	91.7	8.3
Sn-NiO	91.3	8.7	88.9	11.1
La-NiO	95.8	4.2	98.7	1.3
NiO	100	0.0	100	0.0

[a] Obtained by X-ray Energy Dispersive Spectroscopy (XEDS). [b] Determined by X-ray Photoelectron Spectroscopy.

On the contrary, nickel oxide particles in NiO-Sn catalyst display a very low dopant concentration in all cases. Thus, these observations suggest that almost all Sn atoms in the sample must be in the form of SnO_2 nanoparticles.

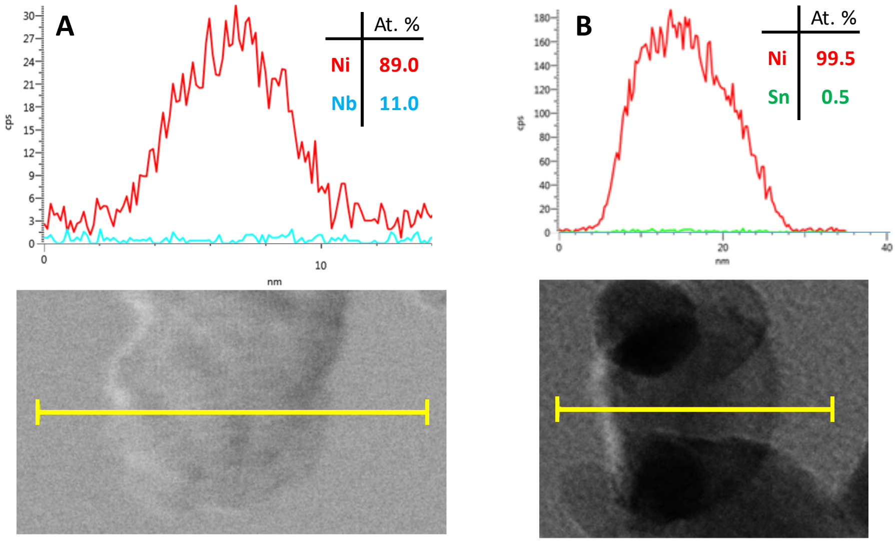

Figure 6.5. Bright-Field STEM images and their corresponding XEDS line-scans of NiO-Nb (A) and NiO-Sn (B) isolated particles.

Considering surface composition, determined by XPS, both NiO-Nb and NiO-Sn present an enrichment of promoter concentration in comparison with bulk-composition (determined by XEDS) (**Table 6.3**). This would suggest the presence of Nb species on the surface, or maybe the formation of a surface Ni-Nb-O mixed phase [21]. The enrichment in the case of Sn-promoted catalysts could be explained considering the presence of SnO_2 nanoparticles on NiO surface.

In this line, Raman spectroscopy supports this different distribution of the promoters (**Fig. 6.6**). A shift in the frequency of vibrational modes of NiO (**Fig. 6.6**, spectrum *a*), from 494 cm^{-1} to 527 cm^{-1}, is observed for NiO-Nb sample (**Fig. 6.6**, spectrum *c*). Hence, this could confirm a higher interaction of Nb with the pristine NiO lattice [28]. On the other hand, vibrational modes of NiO remain unchanged in the case of Sn-promoted catalyst (**Fig. 6.6**, spectrum *b*). Thus, at the bulk level, both promoters act in a different way, in which niobium modifies original NiO framework in a greater extent than tin does. Hence, Sn must me acting mainly as a surface promoter.

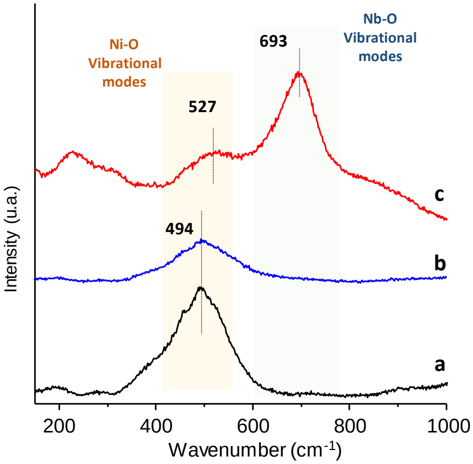

Figure 6.6. Raman spectra of unpromoted (a), Sn- (b) and Nb-promoted (c) NiO catalysts.

In addition, HAADF-STEM micrographs and XEDS analyses of both Sn- and Nb-promoted catalysts (**Figs. 6.7** and **6.8**) show differences in the promoter distribution. A homogeneous distribution of niobium is found for NiO-Nb catalyst (**Figs. 6.7 A** and **6.8 A**). Interestingly, no Nb_2O_5 was detected, likely because it is present in the form of large particles. However, NiO-Sn catalysts presents a heterogeneous distribution of the promoter all along the sample, by which very small SnO_2 particles are covering NiO particles (**Figs. 6.7 B** and **6.8 B**). Attending to the similar catalytic behavior of both catalysts in the ODH of ethane (i.e. reactions performed in the presence of oxygen in the feed), it looks that it is possible to achieve similar promoter-NiO interaction by intimate contact of two separated oxide phases, as in the case of NiO-Sn catalysts, or by a homogeneous distribution of the promoter (either by isomorphic substitution or surface species), like in the case of NiO-Nb, thus modifying Ni species in nickel oxide by both ways.

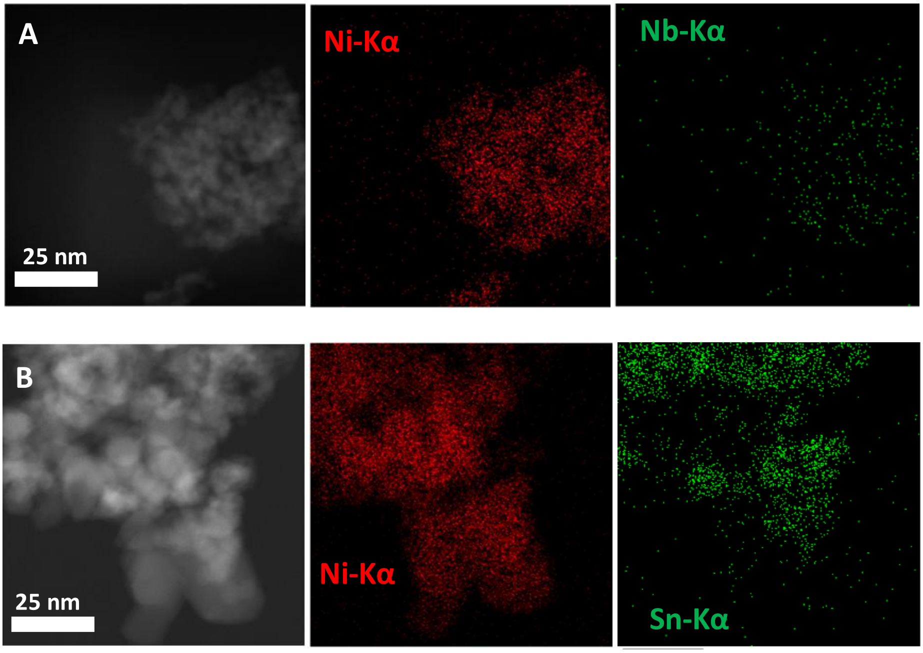
A
Ni-Kα
Nb-Kα
25 nm
B
Ni-Kα
Sn-Kα
25 nm

Figure 6.7. HAADF-STEM images and their corresponding XEDS maps of NiO-Nb (A) and NiO-Sn (B) catalysts

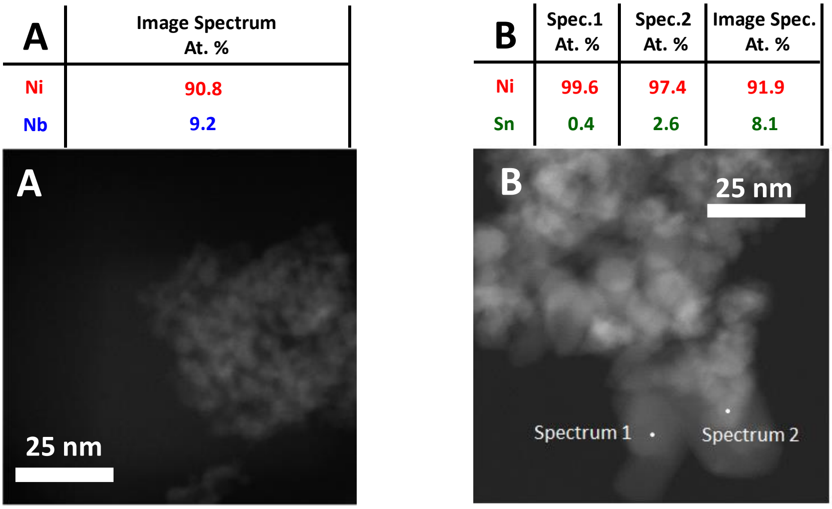

A	Image Spectrum At. %
Ni	90.8
Nb	9.2

B	Spec.1 At. %	Spec.2 At. %	Image Spec. At. %
Ni	99.6	97.4	91.9
Sn	0.4	2.6	8.1

A
25 nm
B
25 nm
Spectrum 1
Spectrum 2

Figure 6.8. HAADF-STEM images and the corresponding atomic composition determined by XEDS (point analysis and full image analysis) of NiO-Nb (A) and NiO-Sn (B).

Reducibility of NiO-based materials was initially studied by means of temperature-programmed reduction in hydrogen (H_2-TPR). H_2-TPR results are comparatively presented in **Figure 6.8** and **Table 6.2**. All the catalysts present two reduction maxima at 357 and 406 ºC (NiO-Nb), 300 and 331 ºC (NiO-Sn), 308 and 333 ºC (NiO-La) or 298 and 321 ºC (NiO). However, the temperature for the maximum H_2-uptake (TM) decreases according to the following trend (**Table 6.2**): NiO-Nb > NiO-Sn > NiO-La > NiO.

The presence of several reduction peaks could be related to the steps proposed for the reduction of NiO, i.e. $NiO \rightarrow Ni^{+\delta} \rightarrow Ni^0$ [29]; but also due to the presence of additional Ni-promoter mixed phases [21]. In fact, high-temperature signals in supported NiO catalysts have been ascribed to the presence of this type of mixed phases due to a high active phase-support interaction [30, 31]. On the contrary, low temperature reduction peaks (at ca. 290 ºC) could be related to the presence of unpromoted or unsupported NiO particles. Also, it has been proposed that non-stoichiometric nickel oxide presents a lower initial activation energy of reduction than stoichiometric NiO, thus giving reduction signals at lower temperatures [32].

Considering all these assumptions, the intensity of the low temperature reduction peak decreases when Nb^{5+} or Sn^{4+} are used as promoters, and in a lesser extent when La^{4+} is used (**Fig. 6.9**). In parallel, the intensity of the second reduction signal (at 357 and 331 ºC, respectively) is higher for NiO-Nb and NiO-Sn catalysts. Then, it seems that highly reducible Ni sites seem to be transformed/eliminated when Nb^{5+} and Sn^{4+} are added as promoters (this change is also observed in the case of La-promoted sample, but with a lower effect) (**Fig. 6.9**).

Additionally, an *in situ* X-ray absorption spectroscopy (XAS) study has been performed in order to shed some light on the redox properties of promoted NiO-based catalysts. Time-resolved XANES measurements were carried out in the Ni K-edge, during the reduction-reoxidation-reduction consecutive treatments under H_2/He, O_2/He and ethane/He mixtures, respectively. During the experiments all the samples underwent progressive transitions between the typical XANES features of NiO (high intensity white line at ca. 8349 eV and a low intensity shoulder at 8334 eV); and those typical of metallic Ni (a low intensity white line at ca. 8349 eV and a broad shoulder at 8334 eV) [33].

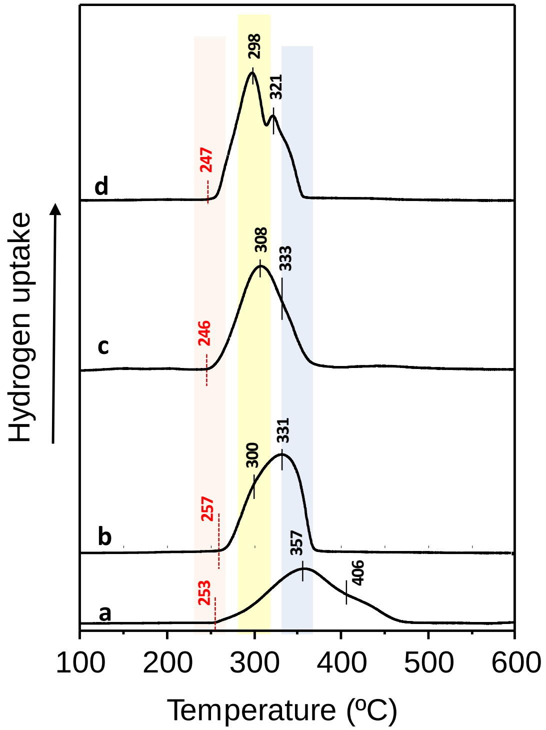

Figure 6.9. H_2-TPR profile of promoted NiO catalysts: a) NiO-Nb; b) NiO-Sn; c) NiO-La; d) NiO.

Figure 6.10 displays *in situ* time-resolved XANES spectra of unpromoted and Me-promoted nickel oxide catalysts, recorded during the abovementioned reduction-reoxidation-reduction sequential treatments at 450 °C. In addition, kinetic curves of reduction, reoxidation and reduction steps (calculated by linear combination fitting, LCF, using the fresh catalysts and Ni (0) as references) are also depicted in **Figure 6.10** (right).

Interestingly, unpromoted and promoted NiO catalysts present different behavior during the redox experiments, especially if we compare NiO-Nb and NiO-Sn (**Fig. 6.10**, profiles *a* and *b*, respectively). However, significant differences can be also noted when comparing NiO-La and unpromoted NiO samples (**Fig. 6.10**, *c* and *d*, respectively).

NiO-Nb and NiO-Sn catalysts present a similar slow reduction kinetic under H_2/He atmosphere, (**Fig. 6.10**, profiles *a* and *b*, step 1). However, during the reoxidation step under O_2/He, Nb- promoted sample undergoes an almost instantaneous total reoxidation to NiO (**Fig. 6.10**, profile *a*, step 2), whereas Sn-promoted catalyst displays a progressive partial reoxidation (reduction degree of 0.21, i.e. 79 % NiO) (**Fig. 6.10**, profile *b*, step 2). These catalysts present also important differences when the reduction was carried out under ethane/He atmosphere, step 3 (**Fig. 6.10**, profiles *a* and *b*). After a short induction period (6-10 min) for step 3, NiO-Nb is reduced into metallic Ni (**Fig. 6.10**, profile *a*). On the contrary, NiO-Sn is not reduced, keeping its reduction degree unaltered during 30 min (**Fig. 6.10**, profile *b*, step 3).

Considering NiO and NiO-La catalysts, which present low selectivity to ethylene during the ethane ODH, both materials present a faster reduction kinetic under H_2/He atmosphere, being the rate of reduction for NiO-La higher than that of NiO catalyst (**Fig. 6.10**, profiles *c* and *d*, step 1). In both cases NiO and NiO-La show faster reduction kinetics than Nb- and Sn-promoted catalysts. It is worth noting that NiO-La catalyst displays a very fast total reoxidation (100 % NiO) under O_2/He atmosphere (**Fig. 6.10**, profile *c*, step 2), meanwhile unpromoted NiO, presents the slowest reoxidation kinetic along the series, not achieving total reoxidation to NiO (≈ 70 % NiO) (**Fig. 6.10**, profile *d*, step 2).

Then the better catalytic performance of NiO-La with respect to NiO could be explained in terms of its better reoxidation capacity. In this regard, a faster reoxidation rate would help to keep Ni species in +2 oxidation state during catalytic cycles.

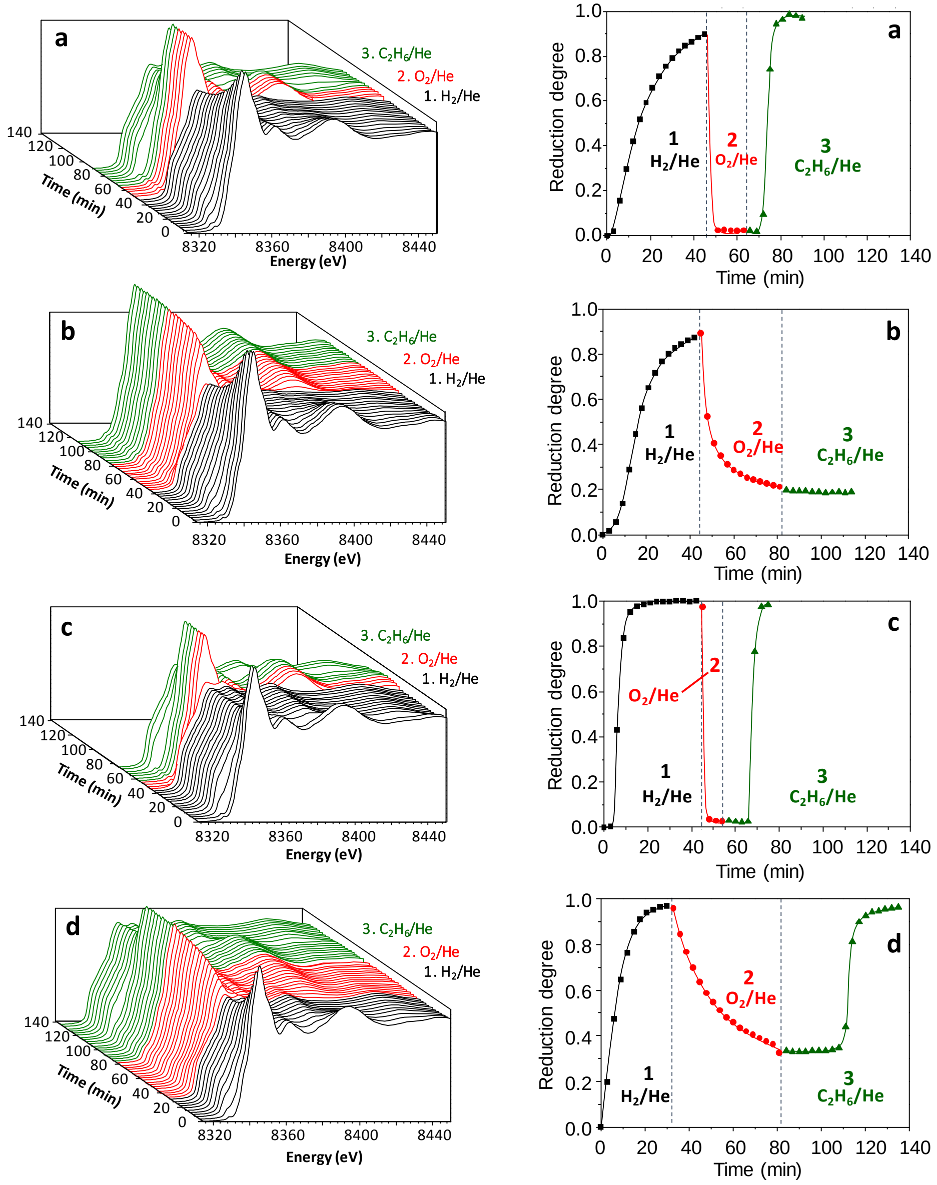

Figure 6.10. *In situ* time-resolved XANES spectra in the Ni K-edge (left) and their corresponding kinetic curves calculated by LCF (right) during reduction-reoxidation-reduction experiments. a) NiO-Nb; b) NiO-Sn; c) NiO-La, d) NiO. Reaction conditions: T = 450ºC; (1, ■) H_2/He, 25/25 (mL min^{-1}); (2, ●) O_2/He, 5/25 (mL min^{-1}); (3, ▲) ethane/He, 5/25 (mL min^{-1}).

Finally, under ethane/He atmosphere (**Fig. 6.10**, profiles *c* and *d*, step 3), NiO shows a reduction kinetic slower than NiO-La catalyst. This higher reduction kinetic of NiO sample could be due to the formation of carbon deposits as a consequence of remaining metallic nickel after the reoxidation step, or caused by its larger particle size. In this way, the effects of particle size and morphology on catalytic performance of these catalysts cannot be completely ruled out.

According to these results, it can be suggested that reduction and reoxidation (in a lesser extent) steps during the catalytic cycles can play an important role in the ODH of ethane. Thus, slow reduction kinetics and fast reoxidation rates would facilitate a more controlled oxygen supply during redox cycles, thus favoring a higher selectivity to ethylene and limiting CO_x formation during ethane ODH. Nonetheless, according to sequential *in situ* experiments (especially under O_2/He and ethane/He), microstructural characteristics such as particle size, phase distribution, or the formation of carbon deposits on catalyst surface can also influence redox kinetics.

In order to clarify these features, *in situ* XAS experiments under reaction conditions, in the absence and presence of oxygen in the feed (reduction-reoxidation sequence), were carried out on NiO and NiO-Sn. The corresponding results are shown in **Figure 6.11** (profiles *a* and *b*, respectively). Again, NiO-Sn catalyst stays in its fully oxidized state after 1h under reductive conditions (ethane /He) (**Fig. 6.11**, profile *a*). In this case, cracking-reforming reactions are less probable, since no metallic Ni is observed in the catalyst. Then, the extremely high resistance to reduction (i.e. its extremely low reducibility) under ethane atmosphere found for NiO-Sn must be due to intrinsic characteristics of the material.

Regarding unpromoted NiO sample (**Fig. 6.11**, profile *b*), it also shows similar behavior than that reported previously in **Figure 6.10** (profile *d*): i) presenting an induction period to the reduction in ethane/He atmosphere (step 1); and ii) the reduced catalyst does not achieve total reoxidation under oxidation conditions (O_2/He atmosphere) (step 2). In this case, the lower reoxidation capacity can be ascribed to the larger particle size, which would prevent oxygen diffusion to catalyst particles. Thus, we can ascribe the anomalous behavior of this sample under reductive and oxidative conditions to their microstructural features or to particle size effects (hindered diffusion of reactants), being the presence of carbon deposits less decisive.

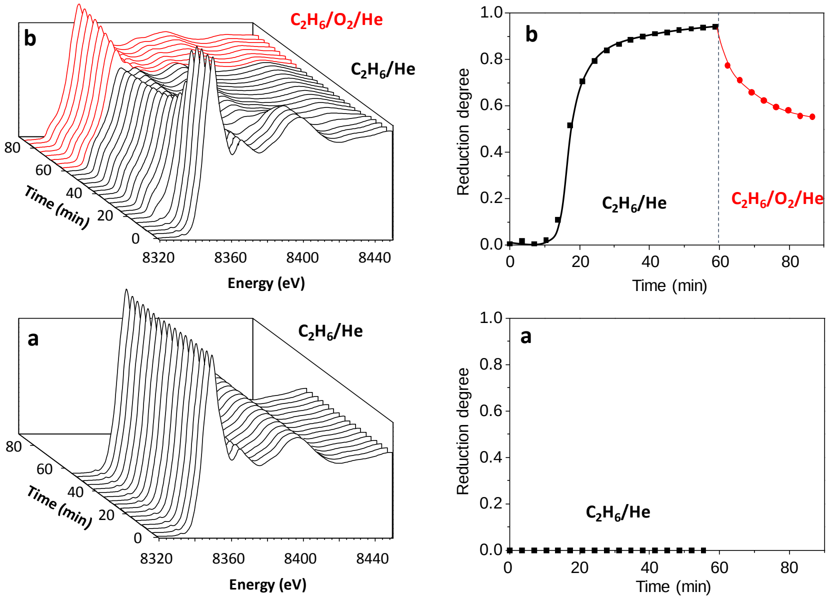

Figure 6.11. *In situ* time-resolved XANES spectra in the Ni K-edge (left) and their corresponding kinetic curves calculated by LCF (right) during reduction-reoxidation treatments. a) NiO-Sn; b) NiO. Reaction conditions: T = 500 ºC; (■) ethane/He, 5/25 (mL min^{-1}); (●) O_2/He, 5/25 (mL min^{-1}).

In situ time-resolved XAS experiment during reduction-reoxidation-reduction sequences (i.e. in H_2/He, O_2/He and ethane/He, respectively) over Nb- and Sn- promoted catalysts were also conducted at different temperatures (400, 450 and 500 ºC). The corresponding results for Nb- and Sn- promoted catalysts are shown in **Figure 6.12** and **Figure 6.13**, respectively.

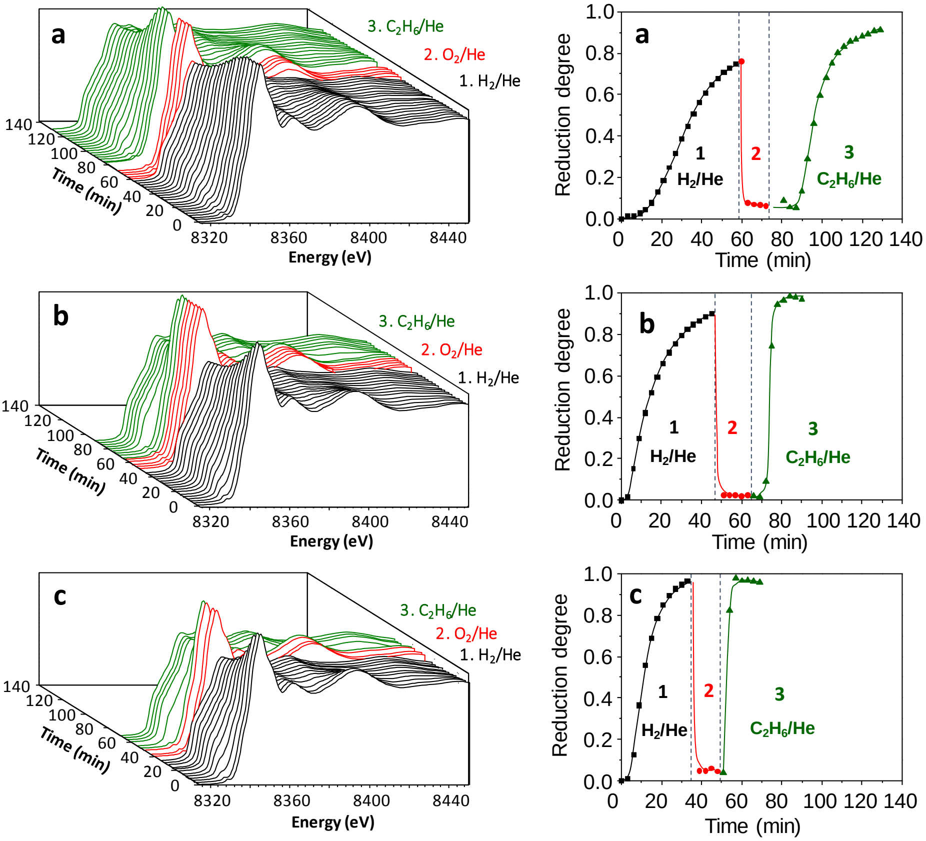

Figure 6.12. *In situ* time-resolved XANES spectra in the Ni K-edge (left) and their corresponding kinetic curves calculated by LCF (right) during reduction-reoxidation-reduction experiments at different temperatures over NiO-Nb catalysts. a) 400 ºC; b) 450 ºC; c) 500 ºC. Reaction conditions: (1, ■) H_2/He, 25/25 (mL min^{-1}); (2, ●) O_2/He, 5/25 (mL min^{-1}); (3, ▲) ethane/He, 5/25 (mL min^{-1}).

NiO-Nb shows an instantaneous reoxidation in O_2/He regardless of the temperature used in the experiments (**Fig. 6.12**, *a*-*c*, step 2). However, temperature has a clear effect on reduction kinetics, displaying higher reduction rates under both H_2/He and ethane/He as temperature increases (**Fig. 6.12**, *a*-*c*, steps 1 and 3).

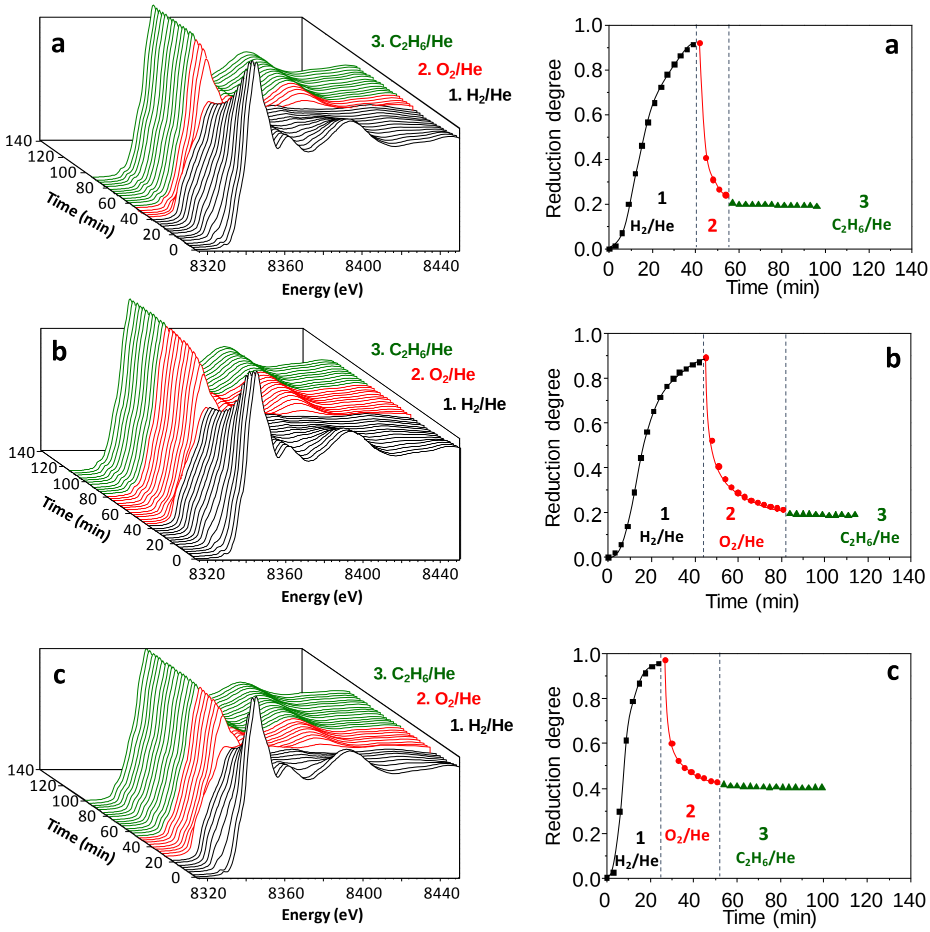

Figure 6.13. *In situ* time-resolved XANES spectra in the Ni K-edge (left) and their corresponding kinetic curves calculated by LCF (right) during reduction-reoxidation-reduction experiments at different temperatures over NiO-Sn catalyst. a) 400 ºC; b) 450 ºC; c) 500 ºC. Reaction conditions: (step 1, ■) H_2/He, 25/25 (mL min^{-1}); (step 2, ●) O_2/He, 5/25 (mL min^{-1}); (step 3, ▲) ethane/He, 5/25 (mL min^{-1}).

However, *in situ* experiments and kinetic curves of NiO-Sn display a very different behavior under reductive and oxidative conditions (**Fig. 6.13**, *a-c*). Under H_2/He, it shows a faster reduction kinetic as reaction temperature increases (**Fig. 6.12**, *a-c*, step 1). However, when the reaction is carried out in ethane/He (**Fig. 6.12**, *a-c*, step 3), the reduction never takes place, irrespective of the reaction temperature used. Surprisingly, an unexpected behavior is observed in the reoxidation treatment in O_2/He flow, under which the catalyst presents different oxidation degrees depending on the reaction temperature (**Fig. 6.12**, *a*-*c*, step 2).

Figure 6.14 displays XANES spectra of NiO-Sn recorded after 12 min under O_2/He at 400, 450 and 500 ºC (**Fig. 6.14**; *a*, *b* and *c*, respectively). It can be seen that the oxidation degree of the catalyst decreases as the reaction temperature increases.

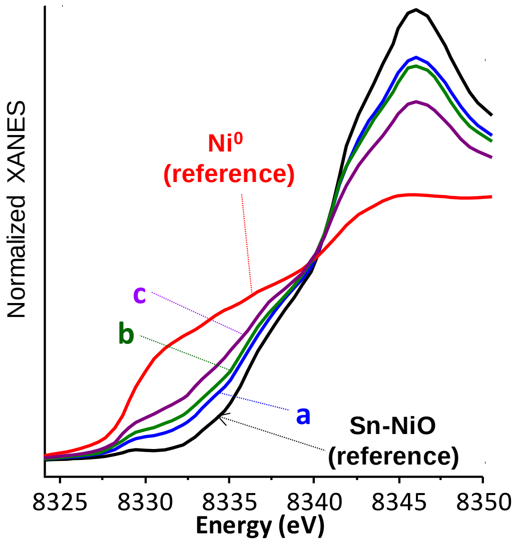

Figure 6.14. XANES spectra in the Ni K-edge NiO-Sn recorded after 12 min of reoxidation treatment in O_2/He (5/25 mL min^{-1}) at different temperatures (spectra of metallic Ni and NiO are also shown). a) 400 ºC; b) 450 ºC; c) 500 ºC.

As far as gas-solid reactions are concerned, an increase in the reaction temperature should promote a faster reoxidation kinetic in an oxygen-rich atmosphere. Considering the specific phase distribution in NiO-Sn catalyst; i.e. the presence of SnO_2 nanoparticles covering NiO; an increase in the reaction temperature would also favor tin oxide sintering all over the surface of NiO particles, thus hindering the diffusion of O_2 to the catalyst, and explaining the opposite trend observed in the reoxidation stage (step 2).

In order to confirm all these findings, catalysts used under ethane/He flow at 450 ºC (both Sn- and Nb-promoted NiO) were characterized by XRD (**Fig. 6.15**), STEM and XEDS (**Fig. 6.16**). X-ray diffraction patterns of fresh and used NiO-Nb and NiO-Sn catalysts are displayed in **Fig. 6.15**. As commented above, fresh Nb-promoted catalyst presents diffraction lines corresponding to the cubic phase of NiO (Fm3m, ICSD No: 184626) and low intensity peaks assigned to Nb_2O_5 (JCPDS: 01-071-0336) (**Fig. 6.15**, pattern *a***)**. After reaction in the absence of oxygen (see **Figs. 6.1** and **6.2**) it can be seen that: i) Nickel oxide is reduced to metallic fcc-Ni (JCPDS: 01-070-1849); and ii) Nb_2O_5, and also probably other Nb^{5+} species in the catalyst, are reduced to NbO_2 (JCPDS: 01-074-2387) (**Fig. 6.15**, pattern *b*).

On the contrary, NiO-Sn presents the same diffraction profiles before (**Fig. 6.15**, pattern *c*) and after the reduction-reoxidation-reduction sequence (**Fig. 6.15**, pattern *d*). This underlines the features observed by *in situ* XAS experiments, suggesting that the presence of SnO_2 nanoparticles covering NiO could inhibit nickel oxide reduction into metallic Ni.

Figure 6.16 shows HAADF-STEM images and the corresponding XEDS maps of used Sn- and Nb-promoted catalysts (**Fig. 6.16**, A and B, respectively). A homogeneous distribution of carbon is detected all over the surface of NiO in the case of used NiO-Sn (**Fig. 6.16**, A).

On the other hand, NiO-Nb presents whire-shaped carbon particles, likely result of its relatively fast reduction process to Ni (0). Thus, although metallic Ni is not present in Sn-promoted catalysts, it could be possible that also carbon deposits help to prevent reduction under ethane/He atmosphere.

The stability tests performed over NiO-Sn catalyst in the absence of oxygen at higher temperature and contact time (as presented in **Fig. 6.3**), suggest that the sample can be reduced under more severe conditions.

Figure 6.17 A shows the XRD pattern of used NiO-Sn catalyst. These results show the formation of metallic hcp-Ni phase (JCPDS: 45-1027) in used catalyst.

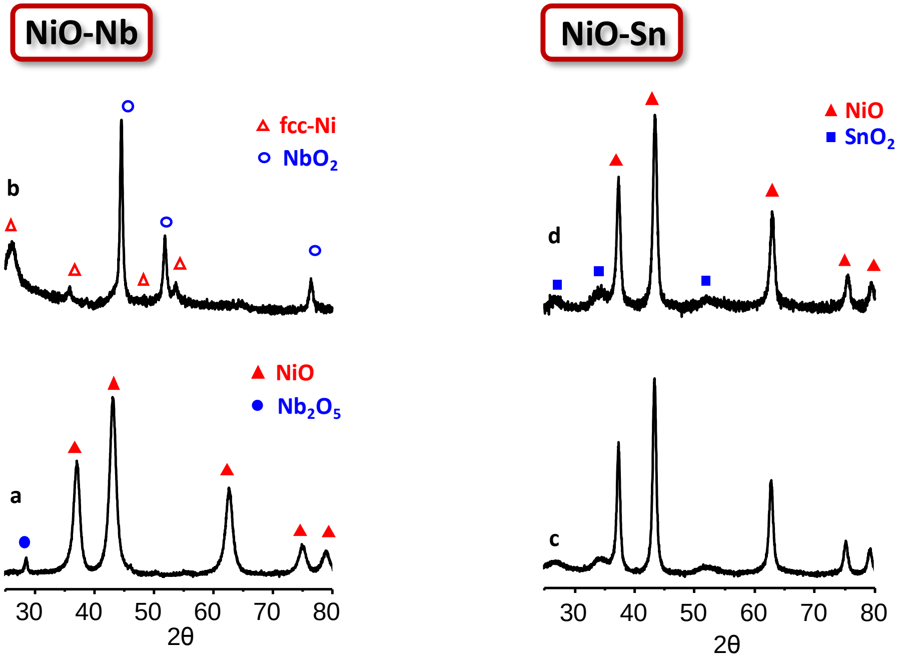

Figure 6.15. XRD profiles of fresh (*a* and **c**) and used (*b* and *d*) under ethane/He flow (5/95 mL min^{-1} at 450 ºC) of NiO-Sn (*a*, b) and NiO-Nb (*c*, *d*) catalysts.

This is not at all the most common Ni (0) crystal structure, and it is reported to be formed just in special conditions, like when NiO is covered by graphite [34]. According to this, BF-STEM and XEDS maps show that reduced NiO-Sn catalyst presents a thick layer of carbon covering all its surface (**Fig. 6.17**, B and C).

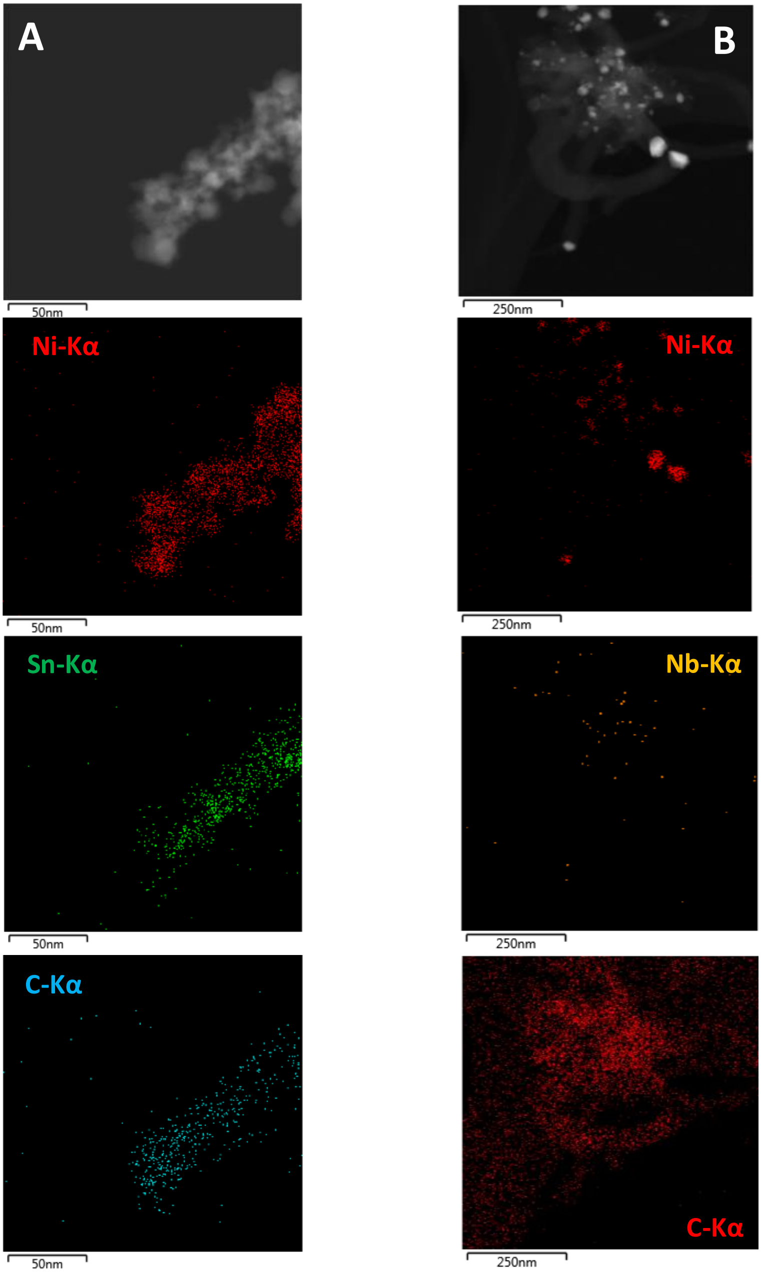
A
B
50nm
250nm
Ni-Kα
Ni-Kα
50nm
250nm
Sn-Kα
Nb-Kα
50nm
250nm
C-Kα
C-Kα
50nm
250nm

Figure 6.16. HAADF-STEM images and XEDS maps of used NiO-Sn (A) and NiO-Nb (B) catalysts.

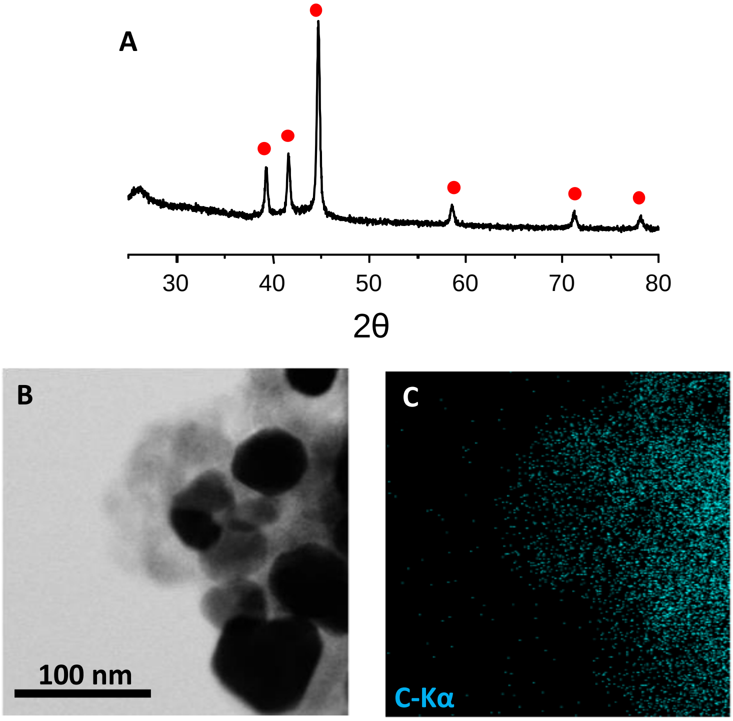

Figure 6.17. XRD profile (A) and BF-STEM image (B) and the corresponding C-K_{α} of reduced NiO-Sn catalyst (reduction conditions in Figure 6.3). Symbols: (●) hpc-Ni (JCPDS: 45-1027).

6.4. General Remarks

During this chapter, the correlation of redox features and the catalytic properties of promoted and unpromoted NiO catalysts in the oxidative and nonoxidative activation of ethane have been underlined. Along the series, Sn- and Nb-promoted NiO show the highest efficiency in the ODH of ethane; presenting a very similar catalytic behavior. Both catalysts are characterized by the presence of NiO particles of small size, although crystal size depends on the chemical nature of the promoter. In addition, for a better comparison, unpromoted and La-promoted NiO catalysts, presenting a relatively low selectivity to ethylene in the ODH of ethane, have also been studied.

The reducibility of Ni^{2+} species in the catalysts seems to play one of the most important roles in the catalytic performance. This way, the most selective materials are those showing the slowest reduction kinetic in H_2/He (NiO-Nb and NiO-Sn), whereas those displaying the fastest reduction rates present the lowest selectivity to ethylene (NiO-La and unpromoted NiO). Reoxidation step seems also to play a role in the catalytic behavior, as it has been observed when comparing unpromoted and La-promoted NiO. In this sense a faster reoxidation rate seems to increase the selectivity to ethylene (NiO-La > NiO). Nevertheless, reoxidation kinetic is very dependant on the morphology, phase distribution and particle size of the catalysts, as it has been shown for Sn- and Nb-promoted NiO materials.

Interestingly, despite Nb- and Sn-promoted catalysts show similar catalytic properties in the ODH of ethane (ethane/O_2/He), they display a completely opposite behavior when oxygen is removed from the feed (ethane/He). According to this, Ni^{2+} species in NiO-Nb are instantaneously reduced to Ni (0), giving rise to the formation of methane, coke and hydrogen as main products. On the contrary, Ni^{2+} sites in NiO-Sn sample remain unreduced, presenting similar catalytic behavior than in the presence of oxygen (but with a lower catalytic activity). The aggregation of SnO_2 nanoparticles covering NiO particles could partially explain its extremely low reducibility under ethane/He observed for this catalyst; fact that is not observed in Nb-promoted catalyst, in which Nb is homogeneously distributed in the catalyst. NiO-Sn sample is only reduced under more severe reductive conditions, i.e. higher concentration of ethane in the feed at higher temperatures and contact time.

All these findings suggest that it is possible to achieve a similar NiO-promoter interaction (with the consequent modification of the pristine NiO phase), by two different promotion mechanisms: i) the homogeneous distribution of the promoter element over the surface or its isomorphic substitution in NiO framework (like in Nb-promoted NiO); or ii) by the intimate contact between two different oxide phases (SnO_2 and NiO in the case of Sn-promoted NiO).

6.5. References

[1] J.T. Grant, J.M. Venegas, W.P. McDermott, I. Hermans, *Aerobic oxidations of light alkanes over solid metal oxide catalysts*, Chemical Reviews, 118 (2018) 2769-2815.

[2] D. Lippe, *Planned maintenance to slow first-half 2016 ethylene production*, Oil & Gas Journal, 114 (2016) 62-70.

[3] M. Ghanta, D. Fahey, B. Subramaniam, *Environmental impacts of ethylene production from diverse feedstocks and energy sources*, Applied Petrochemical Research, 4 (2014) 167-179.

[4] T.J. Farmer, M. Mascal, *Platform Molecules*, in: *Introduction to Chemicals from Biomass*, John Wiley & Sons Ltd. 2015, pp. 89-155.

[5] S.P. Pyl, C.M. Schietekat, M.-F. Reyniers, R. Abhari, G.B. Marin, K.M. Van Geem, *Biomass to olefins: Cracking of renewable naphtha*, Chemical Engineering Journal, 176-177 (2011) 178-187.

[6] T. Dijkmans, S.P. Pyl, M.-F. Reyniers, R. Abhari, K.M. Van Geem, G.B. Marin, *Production of bio-ethene and propene: alternatives for bulk chemicals and polymers*, Green Chemistry, 15 (2013) 3064-3076.

[7] M. Zhang, Y. Yu, *Dehydration of ethanol to ethylene*, Industrial & Engineering Chemistry Research, 52 (2013) 9505-9514.

[8] M.M. Bhasin, J.H. McCain, B.V. Vora, T. Imai, P.R. Pujadó, *Dehydrogenation and oxydehydrogenation of paraffins to olefins*, Applied Catalysis A: General, 221 (2001) 397-419.

[9] F. Cavani, N. Ballarini, A. Cericola, *Oxidative dehydrogenation of ethane and propane: How far from commercial implementation?*, Catalysis Today, 127 (2007) 113-131.

[10] C.A. Gärtner, A.C. van Veen, J.A. Lercher, *Oxidative dehydrogenation of ethane: common principles and mechanistic aspects*, ChemCatChem, 5 (2013) 3196-3217.

[11] J.M.L. Nieto, P. Botella, M.I. Vazquez, A. Dejoz, *The selective oxidative dehydrogenation of ethane over hydrothermally synthesised MoVTeNb catalysts*, Chemical Communications, (2002) 1906-1907.

[12] P. Botella, E. García-González, J.M. López Nieto, J.M. González-Calbet, *MoVTeNbO multifunctional catalysts: Correlation between constituent crystalline phases and catalytic performance*, Solid State Sciences, 7 (2005) 507-519.

[13] E. Heracleous, A.A. Lemonidou, *Ni–Nb–O mixed oxides as highly active and selective catalysts for ethene production via ethane oxidative dehydrogenation. Part I: Characterization and catalytic performance*, Journal of Catalysis, 237 (2006) 162-174.

[14] E. Heracleous, A.A. Lemonidou, *Ni–Nb–O mixed oxides as highly active and selective catalysts for ethene production via ethane oxidative dehydrogenation. Part II: Mechanistic aspects and kinetic modeling*, Journal of Catalysis, 237 (2006) 175-189.

[15] B. Solsona, P. Concepción, B. Demicol, S. Hernández, J.J. Delgado, J.J. Calvino, J.M. López Nieto, *Selective oxidative dehydrogenation of ethane over* SnO_2*-promoted NiO catalysts*, Journal of Catalysis, 295 (2012) 104-114.

[16] B. Solsona, J.M. López Nieto, S. Agouram, M.D. Soriano, A. Dejoz, M.I. Vázquez, P. Concepción, *Optimizing both catalyst preparation and catalytic behaviour for the oxidative dehydrogenation of ethane of Ni–Sn–O catalysts*, Topics in Catalysis, 59 (2016) 1564-1572.

[17] J.M. López Nieto, B. Solsona, R.K. Grasselli, P. Concepción, *Promoted NiO catalysts for the oxidative dehydrogenation of ethane*, Topics in Catalysis, 57 (2014) 1248-1255.

[18] I. Popescu, Z. Skoufa, E. Heracleous, A. Lemonidou, I.-C. Marcu, *A study by electrical conductivity measurements of the semiconductive and redox properties of Nb-doped NiO catalysts in correlation with the oxidative dehydrogenation of ethane*, Physical Chemistry Chemical Physics, 17 (2015) 8138-8147.

[19] Z. Skoufa, E. Heracleous, A.A. Lemonidou, *On ethane ODH mechanism and nature of active sites over NiO-based catalysts via isotopic labeling and methanol sorption studies*, Journal of Catalysis, 322 (2015) 118-129.

[20] X. Sun, B. Li, H. Metiu, *Ethane activation by Nb-doped NiO*, The Journal of Physical Chemistry C, 117 (2013) 23597-23608.

[21] B. Savova, S. Loridant, D. Filkova, J.M.M. Millet, *Ni–Nb–O catalysts for ethane oxidative dehydrogenation*, Applied Catalysis A: General, 390 (2010) 148-157.

[22] S.-B. Ivan, I. Popescu, I. Fechete, F. Garin, V.I. Parvulescu, I.-C. Marcu, *The effect of phosphorus on the catalytic performance of nickel oxide in ethane oxidative dehydrogenation*, Catalysis Science & Technology, 6 (2016) 6953-6964.

[23] E. Heracleous, A.F. Lee, K. Wilson, A.A. Lemonidou, *Investigation of Ni-based alumina-supported catalysts for the oxidative dehydrogenation of ethane to ethylene: structural characterization and reactivity studies*, Journal of Catalysis, 231 (2005) 159-171.

[24] L. Smoláková, M. Kout, E. Koudelková, L. Čapek, *Effect of calcination temperature on the structure and catalytic performance of the Ni/Al_2O_3 and Ni–Ce/Al_2O_3 catalysts in oxidative dehydrogenation of ethane*, Industrial & Engineering Chemistry Research, 54 (2015) 12730-12740.

[25] J.P. Bortolozzi, L.B. Gutierrez, M.A. Ulla, *Synthesis of Ni/Al_2O_3 and Ni–Co/Al_2O_3 coatings onto AISI 314 foams and their catalytic application for the oxidative dehydrogenation of ethane*, Applied Catalysis A: General, 452 (2013) 179-188.

[26] R. Sanchis, D. Delgado, S. Agouram, M.D. Soriano, M.I. Vázquez, E. Rodríguez-Castellón, B. Solsona, J.M. López Nieto, *NiO diluted in high surface area TiO_2 as an efficient catalyst for the oxidative dehydrogenation of ethane*, Applied Catalysis A: General, 536 (2017) 18-26.

[27] B. Solsona, P. Concepcion, J.M. Lopez Nieto, A. Dejoz, J.A. Cecilia, S. Agouram, M.D. Soriano, V. Torres, J. Jimenez-Jimenez, E. Rodriguez Castellon, *Nickel oxide supported on porous clay heterostructures as selective catalysts for the oxidative dehydrogenation of ethane*, Catalysis Science & Technology, 6 (2016) 3419-3429.

[28] R.E. Dietz, G.I. Parisot, A.E. Meixner, *Infrared absorption and raman scattering by two-magnon processes in NiO*, Physical Review B, 4 (1971) 2302-2310.

[29] W. Shan, M. Luo, P. Ying, W. Shen, C. Li, *Reduction property and catalytic activity of $Ce_{1-X}Ni_XO_2$ mixed oxide catalysts for CH_4 oxidation*, Applied Catalysis A: General, 246 (2003) 1-9.

[30] L. Zhang, J. Lin, Y. Chen, *Studies of surface NiO species in NiO/SiO_2 catalysts using temperature-programmed reduction and X-ray diffraction*, Journal of the Chemical Society, Faraday Transactions, 88 (1992) 2075-2078.

[31] A. Fernández, J.P. Espinós, D. Leinen, A.R. González-Elipe, J.M. Sanz, *Charging and mixing effects during the XPS analysis of*

mixtures of oxides, Surface and Interface Analysis, 22 (1994) 111-114.

[32] F. Medina, P. Salagre, J.L.G. Fierro, J.E. Sueiras, *NiO reducibilities: Structural and catalytic properties of their pure and potassium-doped reduced forms*, Journal of Catalysis, 142 (1993) 392-405.

[33] J. Sa, Y. Kayser, C.J. Milne, D.L. Abreu Fernandes, J. Szlachetko, *Temperature-programmed reduction of NiO nanoparticles followed by time-resolved RIXS*, Physical Chemistry Chemical Physics, 16 (2014) 7692-7696.

[34] V.M. Karpan, G. Giovannetti, P.A. Khomyakov, M. Talanana, A.A. Starikov, M. Zwierzycki, J. van den Brink, G. Brocks, P.J. Kelly, *Graphite and Graphene as Perfect Spin Filters*, Physical Review Letters, 99 (2007) 176602.

Chapter 7

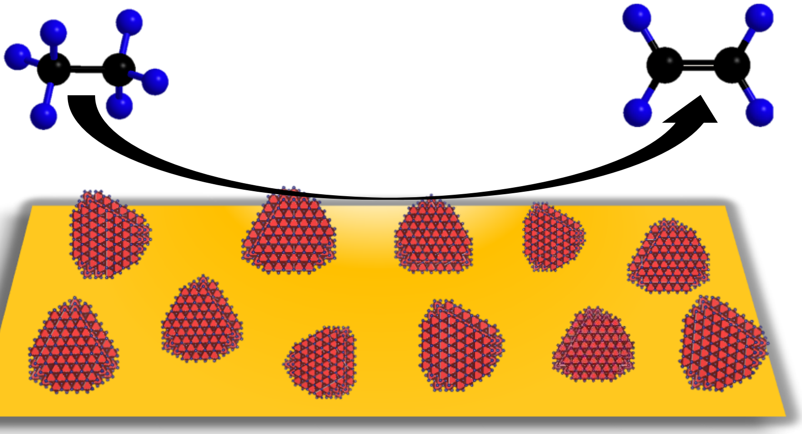

Supported NiO catalysts: Study on the effect of the support on NiO active phase

7.1. Previous considerations

As stated in Chapter 6, besides MoV-based oxides and promoted NiO catalysts, supported nickel oxides also present an outstanding catalytic performance in the ODH of ethane [1-5]. Among all supported NiO phases, those supported on porous clay heterostructures (PCH) [1], TiO_2 [2] and Al_2O_3 [3-5] have shown the best catalytic behavior, reaching ethylene selectivities in the range 80-90 %. Interestingly, they display similar selectivity to ethylene than the best promoted NiO catalysts (Sn- and Nb-promoted catalysts), but presenting a lower active phase content [6-8]. In this context, the chemical nature and surface area of the supports are key aspects to take into account in order to achieve a high selectivity to ethylene in the ODH of ethane.

Despite being one of the best catalysts to perform the ODH of ethane, the causes that transform an apparently unselective catalyst like bulk NiO (selectivity to ethylene of ca. 30 %) into a very selective catalyst when it is supported on specific metal oxides are still unclear. For instance, the optimum NiO loading necessary to achieve the best selectivity to ethylene varies depending on the surface area of the support [2]. This underlines the importance of active phase-support interactions. Also, Lemonidou et al. reported recently that the support can also influence the redox kinetics in NiO oxygen transfer materials (OTM´s), being related with oxide-support interaction strength [9].

The aim of this chapter is to shed some light on these oxide-support interactions, i.e. their effect in the chemical nature of Ni species in a series of supported catalysts, and which is the influence on the catalytic performance in the ODH of ethane. For this purpose, a series of catalysts showing low, medium and high selectivity to ethylene have been synthesized (see point 2.1.4 in Experimental section): unsupported NiO, and NiO supported on SiO_2 (NiO/SiO_2), TiO_2-anatase (NiO/TiO_2-a), TiO_2-P25 (NiO/TiO_2-P25) and on a porous clay heterostructure with SiO_2 and TiO_2 pillars (NiO/PCH-Ti). The study of the redox properties has been carried out by means of temperature-programmed reduction in H_2 (H_2-

TPR) and *in situ* time-resolved X-ray Absorption Spectroscopy (XAS). To elucidate the chemical environment and nature of Ni species, the samples have been analyzed by EXAFS and XPS. The catalytic performance is discussed in terms of the different particle size and the presence of Ni and O defects.

7.2. Catalytic properties of supported NiO catalysts in the ODH of ethane

The catalytic activity at 450 ºC and the selectivity to ethylene achieved at an ethane conversion of 10 % during the ODH of ethane on unsupported and supported NiO catalysts are summarized in **Table 7.1.** Unsupported NiO and NiO/SiO_2 display the lowest selectivity to ethylene (ca. 30 %). However, when NiO is supported on Ti-containing supports, the selectivity to ethylene increases drastically, achieving selectivity values of ca. 89 % for NiO/TiO_2-P25.

Table 7.1. Catalytic performance of unsupported and supported NiO catalysts.

Catalyst	**NiO loading (wt%)**[a]	**Catalytic Activity** (g_{ethane} kg_{NiO}^{-1} h^{-1})[b]	**Selectivity to ethylene (%)**[c]
NiO	100	1117	33
NiO/SiO_2	10	5080	30
NiO/PCH-Ti	17	10941	78
NiO/TiO_2-a	20	5725	64
NiO/TiO_2-P25	20	5400	89

[a] Calculated by XEDS; [b] Catalytic activity at 450 ºC and at ethane conversion of ca. 5 %; [c] Reaction conditions: ethane/O_2/He molar ratio of 3/1/26, ethane conversion of 10 % and 450 ºC.

The variation of the selectivity to ethylene as a function of ethane conversion is depicted in **Figure 7.1**. It is worth noting that in all cases the ethylene formed showed a very low reactivity in the conversion range studied. Specifically, CO_2 was the only by-product observed under these reaction conditions, which seems to be formed directly from ethane combustion. In fact, the selectivity to ethylene remains constant along the conversion range examined, i.e. it does not change with ethane conversion, even for the less selective catalysts (NiO and NiO/SiO_2).

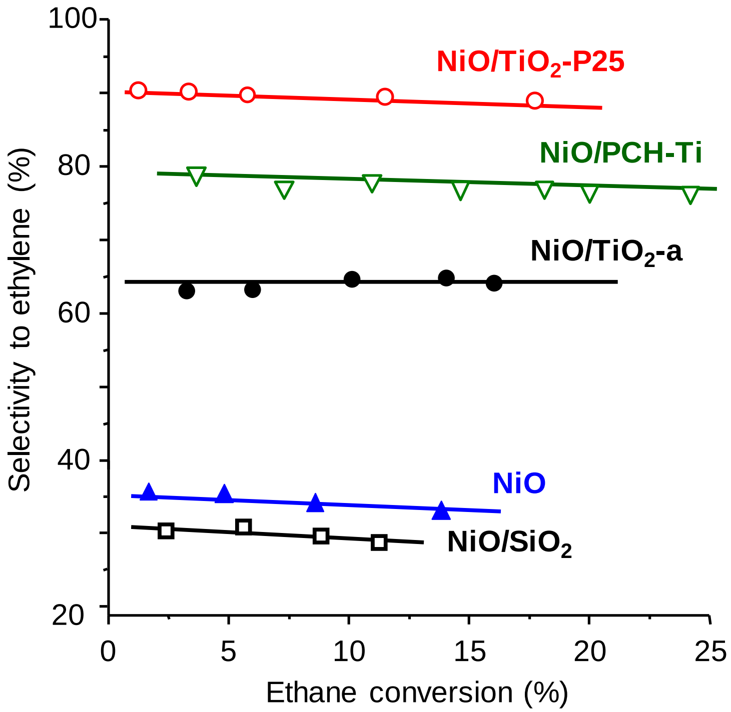

Figure 7.1. Selectivity to ethylene as a function of ethane conversion for NiO-based catalysts. Symbols: NiO (▲); NiO/SiO_2 (◻); NiO/PCH-Ti (▽); NiO/TiO_2-a (●); NiO/TiO_2-P25 (○). Reaction conditions: ethane/O_2/He molar ratio of 3/1/26, T = 450 ºC.

In general, considering supported vanadium oxide catalysts, CO is usually observed as secondary reaction product, as a consequence of deep oxidation of ethylene [10]. On the contrary, CO is not detected in our case. The absence of CO could be explained by a fast total oxidation of CO to CO_2, which in fact takes place on NiO at much lower reaction temperatures that those used in these experiments [11, 12]. Nevertheless, this low reactivity towards total oxidation products is in line with results reported on other NiO-based systems for the ODH of ethane [1, 3, 6-9, 13-16]. Besides NiO-based materials, this catalytic behavior in the ODH of ethane has only been reported for MoV-based mixed oxides presenting an M1-type crystal structure [13, 17, 18]. Interestingly, supported materials displayed a notably higher catalytic activity than unsupported NiO (**Table 7.1**).

7.3. Characterization of promoted NiO catalysts

XRD patterns of bulk NiO and supported catalysts are depicted in **Figure 7.2**. In all cases Bragg peaks corresponding to NiO cubic phase are observed (Fm3m; ICSD No. 184626), which can be distinguished as the only crystalline Ni-containing phase in the samples. For supported NiO catalysts, additional diffraction peaks are found, which can be ascribed to the specific supports used (**Fig. 7.2**, patterns *b* to *e*), except for amorphous SiO_2, which just displays NiO signals (**Fig.7.2**, pattern *b*).

Considering TiO_2 supported catalysts, the main structural-type observed was TiO_2 anatase (JCPDS: 84-1286). However, the sample supported on TiO_2-P25 shows also low intensity peaks corresponding to TiO_2-rutile phase (JCPSD: 82-0514). In addition, no shifts in peak positions are observed along the series, which means that, apparently, no changes in the cubic cell parameter of NiO occur.

Interestingly, unsupported NiO catalyst presents narrower diffraction peaks (**Fig. 7.2**, pattern *a*) than supported NiO materials (**Fig. 7.2**, patterns *b-e*). This is in fact related to a smaller crystallite size in supported catalysts. Hence, NiO crystallite size was estimated by using Scherrer equation, showing a smaller average particle size for supported NiO catalysts (**Table 7.2**).

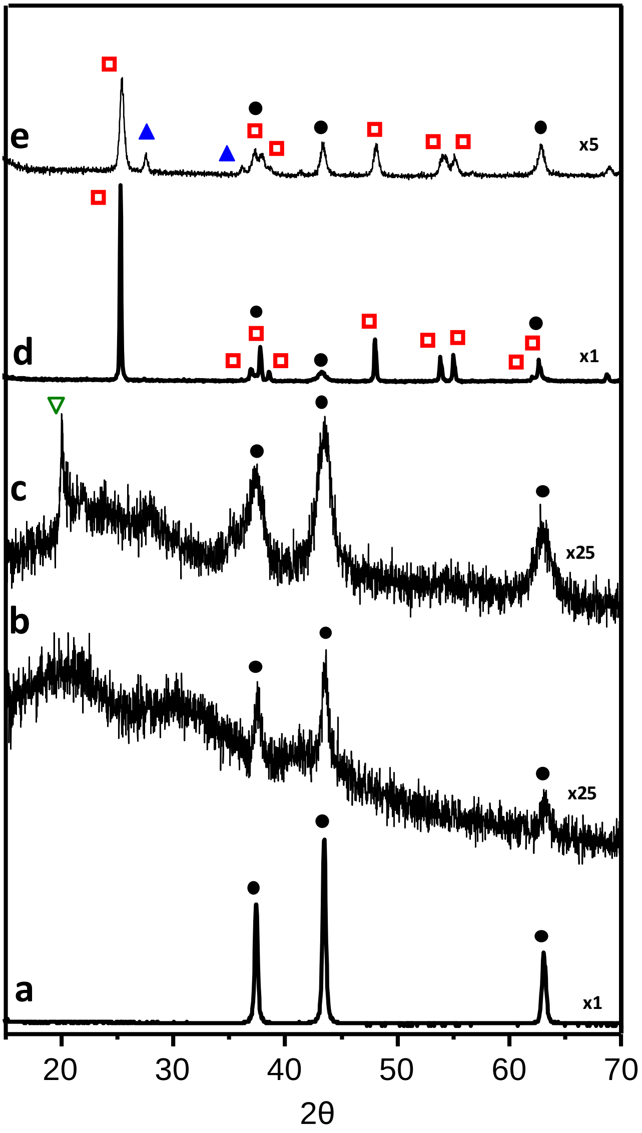

Figure 7.2. XRD profiles of bulk and supported NiO catalysts. a) NiO; b) NiO/SiO_2; c) NiO/PCH-Ti; d) NiO/TiO_2-a; and e) NiO/TiO_2-P25. Symbols: NiO (●); PCH-Ti (▽); TiO_2-anatase (◘); TiO_2-rutile (▲).

Table 7.2. Main physicochemical features of NiO-based catalysts

Catalyst	Average particle size (nm) [a]	BET surface area (m^2 g^{-1}) [b]	XPS [c]	
			Sat.I/Main peak	Sat.II/Main peak
NiO	30.0	15	4.07	3.90
NiO/SiO_2	12.6	168	1.36	1.96
NiO/PCH-Ti	6.2	360	1.46	1.57
NiO/TiO_2-a	13.1	26	1.33	0.84
NiO/TiO_2-P25	19.2	50	1.58	1.99

[a] Calculated by Scherrer equation; [b] Obtained from N_2-adsorption isotherms by Brunauer-Emmett-Teller method; [c] X-ray Photoelectron Spectroscopy.

Figure 7.3 shows the variation of the catalytic activity with NiO average particle size (achieved at 450 ºC at an ethane conversion lower than 5 %). According to characterization results, it can be concluded that the use of supports helps to reduce the average particle size of NiO. In addition, the catalytic activity in the ODH of ethane increases as the particle size of NiO decreases (**Fig. 7.3**).

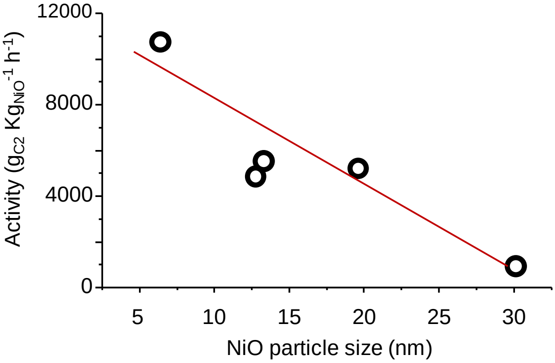

Figure 7.3. Variation of the catalytic activity with NiO average particle size. Reaction conditions: ethane/O_2/He molar ratio of 3/1/26; catalytic activity at 450 ºC at an ethane conversion lower than 5 %.

The reducibility of NiO-based catalysts was studied by means of temperature-programmed reduction in H_2 (H_2-TPR). H_2-TPR profiles are presented in **Figure 7.4**. If the temperature of maximum consumption of H_2 is considered, the reducibility of NiO catalysts decreases according to the following trend: NiO/SiO_2 > NiO ≈ NiO/TiO_2-P25 > NiO/TiO_2-a > NiO/PCH-Ti.

As it was observed in the previous chapter, H_2-TPR profiles show several reduction peaks, which can be associated to Ni species presenting different reducibility. Unsupported NiO displays two reduction signals, assigned to a two-step reduction: $Ni^{2+} \rightarrow Ni^{\delta+} \rightarrow Ni^0$ (**Fig. 7.4**, *a*) [19].

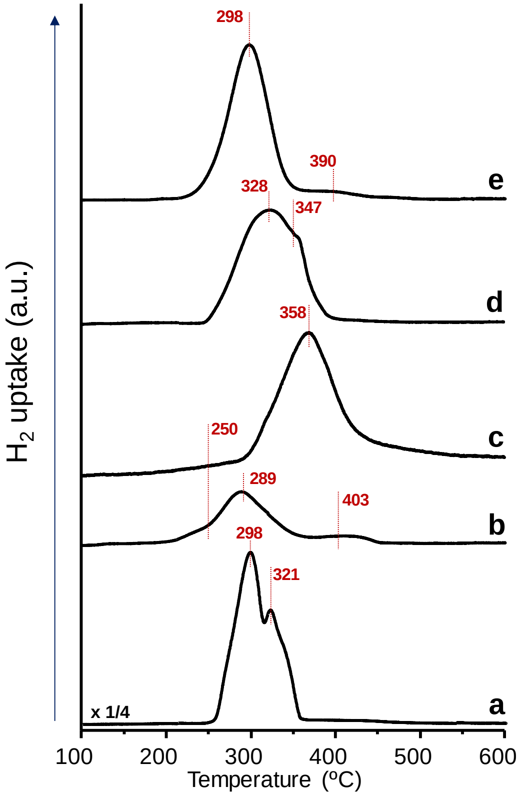

Figure 7.4. H_2-TPR profiles of NiO-based catalysts. a) NiO; b) NiO/SiO_2; c) NiO/PCH-Ti; d) NiO/TiO_2-a; and e) NiO/TiO_2-P25.

This features can be explained considering NiO particle size and diffusion of H_2 into the oxide matrix. Thus, a bigger crystal size would present a higher contribution to the higher temperature signal in the TPR profile, due to diffusional problems of the reductant. This fact again underlines the effect of morphology and microstructural features on the reducibility, as it was previously stated in the case of Sn-promoted NiO (see Chapter 6).

This catalyst presented a very low reducibility in ethane/He flow due to its specific phase distribution, which shows SnO_2 nanoparticles covering NiO, what hinders its reduction by ethane. This could also be the case of NiO/PCH-Ti, which displays the lowest reducibility of the series (**Fig. 7.4**, pattern *c*). Particularly, the reduction of NiO located in the interlayer pores could be hindered with respect to well accessible NiO particles. In addition, low intensity reduction signals at high temperatures (at ca. 400 ºC) are also observed, especially in the case of Ni/SiO_2 and NiO/TiO_2-P25. These high temperature signals can be ascribed to the presence of Ni-support mixed phases (mainly Ni (II) titanates and silicates), which are reported to show much lower reducibility (**Fig. 7.4**, patterns *b* and *c*) [20].

Also, reduction peaks at low temperatures (ca. 200-250 ºC) are found, which are associated with the presence of non-stoichiometric NiO, presenting a lower activation energy for the reduction [21]. Summarizing, some heterogeneity in terms of reducibility is observed along the series of supported-NiO catalysts (i.e. the samples show the presence of Ni sites with different reducibility). Accordingly, it is difficult to directly connect the catalytic performance to the specific reducibility observed in each case, although it seems that a lower reducibility favors the selectivity to ethylene in the ODH of ethane.

Figure 7.5 displays *in situ* time-resolved XANES spectra of NiO-based catalysts (NiO; NiO/SiO_2; NiO/PCH-Ti; NiO/TiO_2-P25), which were recorded during the reduction in H_2/He flow (25/25 mL min^{-1}) at 450 ºC. All the samples show a transition from the characteristic XANES features of NiO to those of metallic Ni. With comparative purposes, representative XANES spectra of pure NiO and Ni (0) are displayed in **Figure 7.6** (**Fig.**

7.6, A). Interestingly, changes in time and reduction velocity, depending on the support, can be observed along the series of supported NiO catalyst.

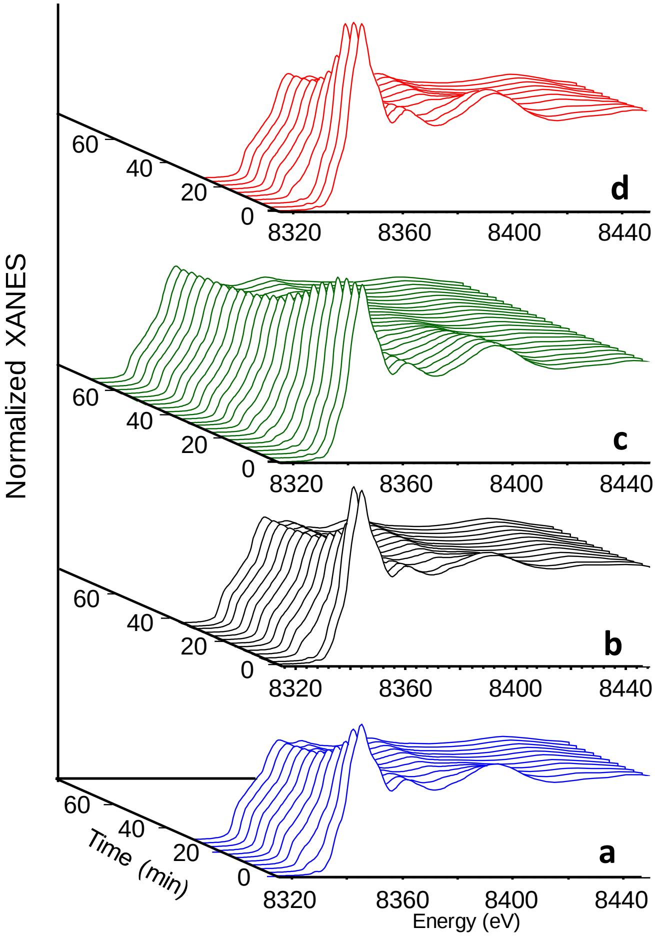

Figure 7.5. *In situ* time-resolved XANES spectra in the Ni K-edge during the reduction in H_2/He of NiO-based catalysts. a) NiO; b) NiO/SiO_2; c) NiO/PCH-Ti; d) NiO/TiO_2-P25. Reduction conditions: H_2/He 25/25 (mL min^{-1}) at 450 ºC.

On the other hand, **Figure 7.6 B** shows the kinetic curves of reduction in H_2 obtained by linear combination fitting of the corresponding spectra in **Figure 7.5**, by using fresh catalysts and metallic Ni spectra as references for the calculations (**Fig. 7.6**, B).

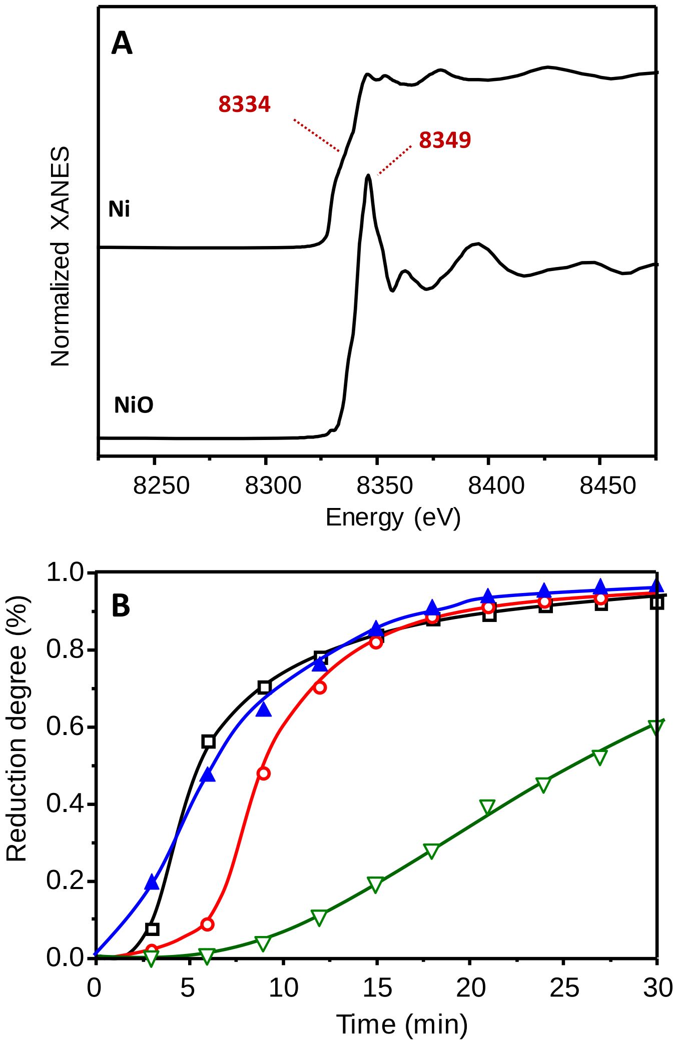

Figure 7.6. A) XANES spectra in the Ni K-edge of NiO and metallic Ni. B) Kinetic curves of reduction in H_2 obtained by linear combination fitting of the corresponding spectra in Figure 7.5. Symbols: NiO (▲); NiO/SiO_2 (□); NiO/PCH-Ti (▽); NiO/TiO_2-P25 (○) . Reduction conditions: H_2/He 25/25 (mL min^{-1}) at 450 °C.

Unsupported NiO and NiO/SiO_2 show the fastest reduction kinetic all along the series (**Figure 7.6**, B), which are in fact the less selective catalysts in the ODH of ethane (see catalytic results in **Table 7.1**). On the contrary, NiO/PCH-Ti displays the slowest reduction kinetic in H_2/He, which is in agreement with H_2-TPR results. In addition, NiO/TiO_2-P25 also shows a slower reduction rate than NiO and NiO/SiO_2 samples. Accordingly, slow reduction kinetics seem to favor a higher selectivity to ethylene, as it was observed in the case of promoted-NiO.

Ni $2p_{3/2}$ core level XPS spectra of NiO-based catalysts are shown in **Figure 7.7**. All the samples display a main peak in the range 853-854 eV, showing a line-broadening which can be considered as an additional peak (ca. 1.5 eV over the main peak). This contribution (also known as Satellite I), has been assigned to the presence of several types of defects, like Ni^{3+} cations [22, 23], Ni^{2+} vacancies or Ni^{2+}-OH species [24], but also to non-local screening effects [25]. The other broad contribution observed in the spectra, and situated at approximately 7 eV over the main peak (known as Satellite peak II, or shake-up satellite), is usually ascribed to ligand-metal charge transfer [24-26].

Additionally, supported-NiO materials show an extra contribution in the XPS spectra, just below the main peak (marked with an asterisk in **Figure 7.7**), due to differential charging. This differential charging is usually caused by heterogeneities in the electrical conductivity of the samples [27, 28].

The relative intensity of satellite peaks on the XPS spectra can be used to extract some information about the nature of Ni surface species in the catalysts [29, 30]. It can be observed that the relative intensity of both satellites is much lower for supported NiO catalysts (**Table 7.2**). Particularly, Sat. I/Main peak ratios are very dependent on NiO particle size and the number of defects [22-26]. Hence, supported NiO catalysts present much higher Sat. I/Main peak ratio than that observed for unsupported NiO (**Fig. 7.7**) (**Table 7.2**).

This has already been observed in other catalytic systems based on NiO, either in supported or in promoted nickel oxides. These effects have been associated to the generation of defects or to particle size changes due to the interaction with the support or the promoter [1, 6]. Taking all these facts into consideration, it appears difficult to separate the contribution of particle size and defects to the satellite peaks.

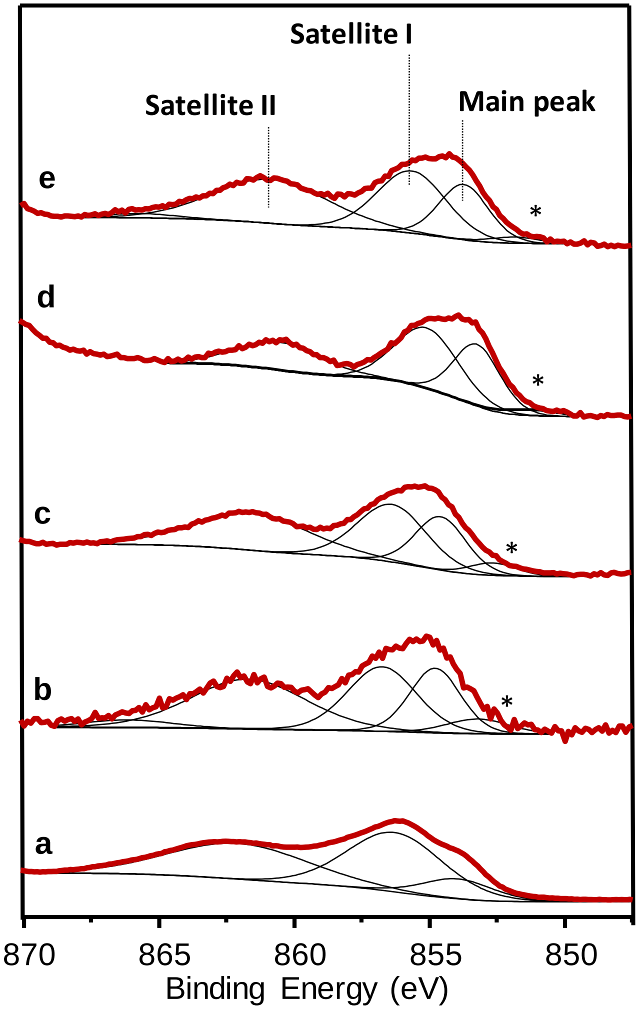

Figure 7.7. Ni 2$p_{3/2}$ core level XPS spectra of NiO-based catalysts. a) NiO; b) NiO/SiO_2; c) NiO/PCH-Ti; d) NiO/TiO_2-a; e) NiO/TiO_2-P25. (*) peak due to differential charging.

Nevertheless, it can be seen that the selectivity to ethylene in the ODH of ethane increases proportionally with Sat. I/Main peak ratio for Ti-containing NiO catalysts, what suggests that maybe defects could be playing a role in the catalytic performance (**Fig. 7.8**).

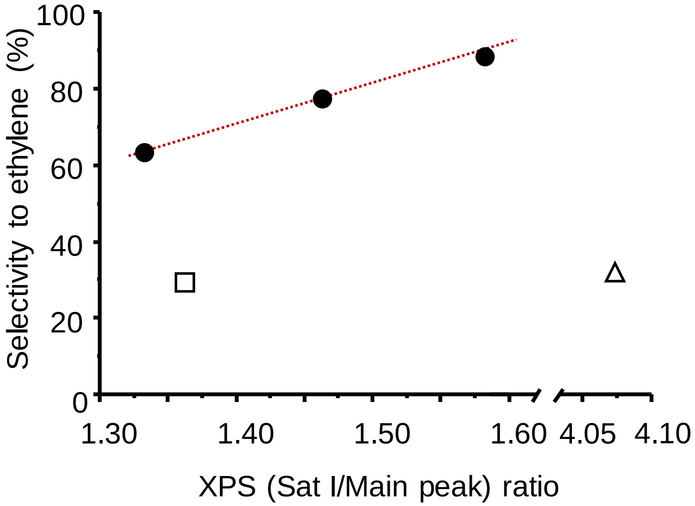

Figure 7.8. Variation of the selectivity to ethylene as a function of Satellite I/Main peak ratio in the Ni 2$p_{3/2}$ core level XPS spectra for unsupported and supported NiO catalysts. Symbols: Ti-containing NiO catalysts (●); unsupported NiO (△); NiO/SiO$_2$ (□).

In order to study the short-range environment of Ni species in the materials, NiO-based catalysts were further investigated by EXAFS analysis in the Ni K-edge region. **Figure 7.9** shows the module of the Fourier Transform (F.T.) of the EXAFS oscillations for each catalyst, whereas **Table 7.3** summarizes the EXAFS analysis results.

No significant differences in Ni-O (1st coordination shell) and Ni-Ni (2nd coordination shell) distances are found along the series, being equal regardless of the support used (**Table 7.3**). This is in line with XRD results, in which no variation of the cubic cell parameter was observed in the series. However, slight differences in the relative intensities of the signals corresponding to the 1st (NiO) and 2nd (Ni-Ni) coordination shells can be noted depending on the support (**Fig. 7.9**). This differences suggest changes in the coordination environment of Ni as a function of the support used, i.e. changes in the coordination numbers of both Ni-O and Ni-Ni shells.

The coordination numbers for the 1st and 2nd coordination shells were calculated from the amplitude reduction factors (S_0^2) extracted from EXAFS fittings, taking unsupported NiO as a reference (i.e. $N_{Ni-O} = 6$; and $N_{Ni-Ni} = 12$ for NiO sample) (**Fig. 7.9** and **Table 7.3**). According to this, both Ni-O and Ni-Ni coordination numbers decrease for supported catalysts.

Table 7.3. EXAFS analysis results for NiO-based catalysts

Catalyst	**EXAFS** [a]			
	1st Shell (Ni-O)		**2nd Shell (Ni-Ni)**	
	N [b]	**d_{Ni-O} (Å)**	**N**	**d_{Ni-O} (Å)**
NiO	6.00	2.08	12.00	2.95
NiO/SiO$_2$	6.00	2.08	11.60	2.95
NiO/PCH-Ti	5.72	2.08	10.68	2.95
NiO/TiO$_2$-a	5.29	2.08	10.92	2.95
NiO/TiO$_2$-P25	5.15	2.08	10.44	2.95

[a] Extended X-Ray Fine Structure; [b] Coordination number of the corresponding shell.

This decrease is even more significant when Ti-containing supports are used. This suggests a higher interaction between TiO_2 and NiO, which would give rise to a higher number of Ni and O defects (likely vacancies). Nevertheless, the differences observed in the first coordination shell can be also due to a distorted octahedral environment, rather than to an actual decrease in the Ni-O coordination number (**Table 7.3**) [31].

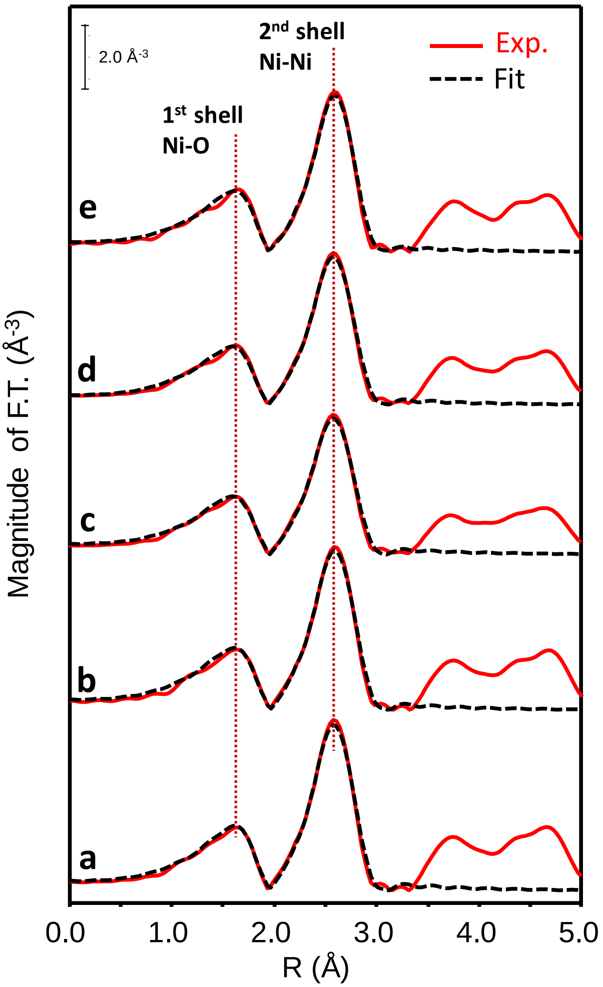

Figure 7.9. Module of the Fourier Transform of EXAFS Ni k-edge zone of NiO catalysts. a) NiO; b) NiO/SiO_2; c) NiO/PCH-Ti; d) NiO/TiO_2-a; e) NiO/TiO_2-P25.

Figure 7.10 shows the variation of the selectivity to ethylene with Ni-O and Ni-Ni coordination numbers (1st and 2nd coordination shell respectively) of unsupported and supported NiO catalysts. A correlation between the selectivity to ethylene in the ODH of ethane and the coordination number for the 1st and 2nd coordination shells can be underlined (**Fig. 7.10**). In this way, the selectivity to ethylene increases as the coordination number for the 1st (Ni-O) (**Fig. 7.10**, A) and 2nd (Ni-Ni) (**Fig. 7.10**, B) shells decreases. Even though the correlation of selectivity and Ni-O coordination number is not as clear (**Fig. 7.10**, A) as in the case of Ni-Ni shell (**Fig. 7.10**, B), 1st and 2nd shell neighbors seem to be lower for the most selective catalysts.

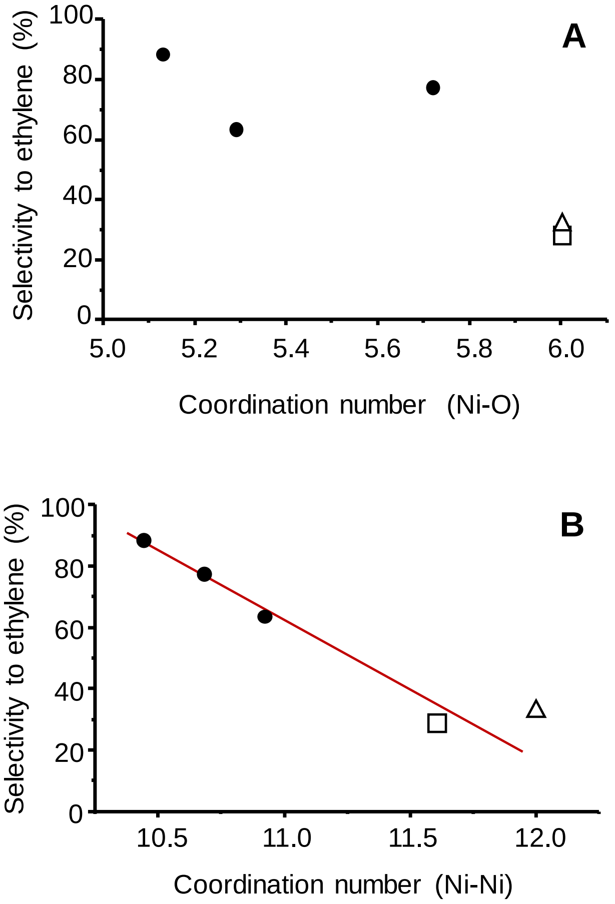

Figure 7.10. Variation of the selectivity to ethylene as a function of the coordination numbers calculated by EXAFS fitting for the 1st (A) and 2nd (B) coordination shells. Symbols: Symbols: Ti-containing NiO catalysts (●); unsupported NiO (△); NiO/SiO_2 (◘).

Finally, the specific features in the XANES region of XAS spectra in the Ni K-edge for the whole series of supported NiO catalysts were analyzed (**Fig. 7.11**). Interestingly, a decrease in the intensity of the white line is also observed for the most selective catalysts (see inset in **Fig. 7.11**). Moreover, the selectivity to ethylene in the ODH of ethane increases linearly as the normalized intensity of the white line decreases (**Fig. 7.12**).

The intensity of the white line (as it was commented in Chapter 4) is very sensitive to changes in the average oxidation state of the absorbing atom. In this case, the decrease of the white line intensity could tentatively be assigned to a decrease in the average oxidation state of Ni, likely due to the elimination of Ni^{3+} sites [32]. In fact, these non-stoichiometric species have been reported to be responsible for the deep oxidation in the ODH of ethane [3, 7, 8].

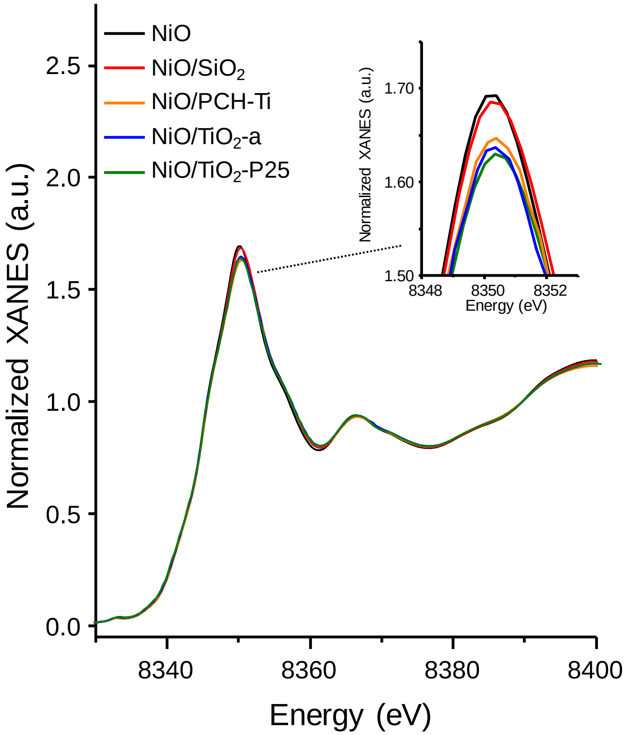

Figure 7.11. XANES spectra in the Ni K-edge of supported NiO catalysts.

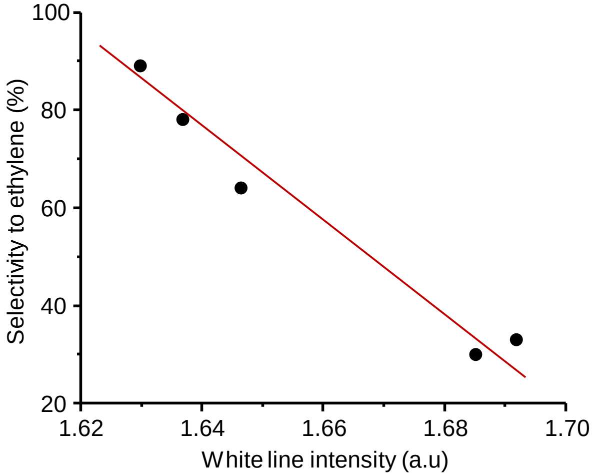

Figure 7.12. Variation of the selectivity to ethylene as a function of the normalized intensity of the XANES white line in the Ni K-edge for supported NiO catalysts.

Thus, according to these observations, a high selectivity to ethylene in the ODH of ethane seems to be connected with the elimination of specific O and/or Ni species, i.e. with the elimination of non-selective sites by the creation of defects, likely vacancies; due to active phase-support interactions.

7.4. General Remarks

During this chapter, the effect of the support on the chemical nature of Ni species in supported NiO catalysts has been studied. Depending on the nature of the support, materials with different catalytic behavior have been prepared.

Unsupported and NiO/SiO_2 present the lowest selectivity to ethylene in the ODH of ethane (33 and 30 % respectively). Interestingly, a substantial increase in the selectivity to ethylene is observed when Ti-containing materials are used as supports: TiO_2 (NiO/TiO_2-a, 64 %; and NiO/TiO_2-P25, 89 %) or a porous clay heterostructure with SiO_2-TiO_2 pillars

(NiO/PCH-Ti, 78 %). Apart from ethylene, carbon dioxide was the other reaction product observed. The appearance of CO_2 as the only deep oxidation product suggests a relatively low reactivity of ethylene over these NiO-based catalysts.

The support can also substantially modify the morphology and chemical nature of NiO, thus affecting the catalytic performance. The catalytic activity appears to be related to NiO crystallite size, being higher as the NiO particle size decreases. On the other hand, the support can also modify the chemical nature of nickel oxide. The reducibility of the catalyst was studied by means of H_2-TPR and *in situ* time-resolved XAS experiments under H_2/He atmosphere. According to this experiments, Ti-containing NiO catalysts present a lower reducibility and slower reduction rates in H_2 than unsupported NiO and NiO/SiO_2. This is an important fact, since a low reducibility seems to improve the selectivity to ethylene in the ODH. Nevertheless, the samples show Ni species with low, medium and high reducibility, as elucidated by H_2-TPR. In addition, the nature of surface Ni sites and Ni chemical environment was investigated by mean of XPS and EXAFS analysis respectively. Both characterization techniques suggest a role played by defects in the catalytic performance, likely the presence of Ni and O vacancies in NiO lattice, and the elimination of non-stoichiometric Ni^{3+} sites. In fact, it appears to exist a correlation between the selectivity to ethylene in the ODH of ethane and the coordination number Ni-O and Ni-Ni for the first and second shells. This way the selectivity to ethylene increases as the number of neighbors decreases, and as the intensity of Ni K-edge white line intensity decreases.

7.5. References

[1] B. Solsona, P. Concepcion, J.M. López Nieto, A. Dejoz, J.A. Cecilia, S. Agouram, M.D. Soriano, V. Torres, J. Jimenez-Jimenez, E. Rodriguez Castellon, *Nickel oxide supported on porous clay heterostructures as selective catalysts for the oxidative dehydrogenation of ethane*, Catalysis Science & Technology, 6 (2016) 3419-3429.

[2] R. Sanchis, D. Delgado, S. Agouram, M.D. Soriano, M.I. Vázquez, E. Rodríguez-Castellón, B. Solsona, J.M. López. Nieto, *NiO diluted in high surface area* TiO_2 *as an efficient catalyst for the oxidative dehydrogenation of ethane*, Applied Catalysis A: General, 536 (2017) 18-26.

[3] E. Heracleous, A.F. Lee, K. Wilson, A.A. Lemonidou, *Investigation of Ni-based alumina-supported catalysts for the oxidative dehydrogenation of ethane to ethylene: structural characterization and reactivity studies*, Journal of Catalysis, 231 (2005) 159-171.

[4] L. Smoláková, M. Kout, E. Koudelková, L. Čapek, *Effect of calcination temperature on the structure and catalytic performance of the* Ni/Al_2O_3 *and* $Ni–Ce/Al_2O_3$ *catalysts in oxidative dehydrogenation of ethane*, Industrial & Engineering Chemistry Research, 54 (2015) 12730-12740.

[5] J.P. Bortolozzi, L.B. Gutierrez, M.A. Ulla, *Synthesis of* Ni/Al_2O_3 *and* $Ni–Co/Al_2O_3$ *coatings onto AISI 314 foams and their catalytic application for the oxidative dehydrogenation of ethane*, Applied Catalysis A: General, 452 (2013) 179-188.

[6] B. Solsona, P. Concepción, B. Demicol, S. Hernández, J.J. Delgado, J.J. Calvino, J.M. López Nieto, *Selective oxidative dehydrogenation of ethane over* SnO_2*-promoted NiO catalysts*, Journal of Catalysis, 295 (2012) 104-114.

[7] E. Heracleous, A.A. Lemonidou, *Ni–Nb–O mixed oxides as highly active and selective catalysts for ethene production via ethane oxidative dehydrogenation. Part I: Characterization and catalytic performance*, Journal of Catalysis, 237 (2006) 162-174.

[8] E. Heracleous, A.A. Lemonidou, *Ni–Nb–O mixed oxides as highly active and selective catalysts for ethene production via ethane oxidative dehydrogenation. Part II: Mechanistic aspects and kinetic modeling*, Journal of Catalysis, 237 (2006) 175-189.

[9] D. Ipsakis, E. Heracleous, L. Silvester, D.B. Bukur, A.A. Lemonidou, *Reduction and oxidation kinetic modeling of NiO-based oxygen transfer materials*, Chemical Engineering Journal, 308 (2017) 840-852.

[10] C.A. Gärtner, A.C. van Veen, J.A. Lercher, Oxidative *dehydrogenation of ethane: Common principles and mechanistic aspects*, ChemCatChem, 5 (2013) 3196-3217.

[11] M.-G. Jeong, I.H. Kim, S.W. Han, D.H. Kim, Y.D. Kim, *Room temperature CO oxidation catalyzed by NiO particles on mesoporous* SiO_2 *prepared via atomic layer deposition: Influence of pre-annealing temperature on catalytic activity*, Journal of Molecular Catalysis A: Chemical, 414 (2016) 87-93.

[12] S.W. Han, D.H. Kim, M.-G. Jeong, K.J. Park, Y.D. Kim, *CO oxidation catalyzed by NiO supported on mesoporous* Al_2O_3 *at room temperature*, Chemical Engineering Journal, 283 (2016) 992-998.

[13] P. Botella, E. García-González, A. Dejoz, J.M. López Nieto, M.I. Vázquez, J. González-Calbet, *Selective oxidative dehydrogenation of ethane on MoVTeNbO mixed metal oxide catalysts*, Journal of Catalysis, 225 (2004) 428-438.

[14] J.M. López Nieto, B. Solsona, R.K. Grasselli, P. Concepción, *Promoted NiO catalysts for the oxidative dehydrogenation of ethane*, Topics in Catalysis, 57 (2014) 1248-1255.

[15] B. Savova, S. Loridant, D. Filkova, J.M.M. Millet, *Ni–Nb–O catalysts for ethane oxidative dehydrogenation*, Applied Catalysis A: General, 390 (2010) 148-157.

[16] B. Solsona, J.M. López Nieto, S. Agouram, M.D. Soriano, A. Dejoz, M.I. Vázquez, P. Concepción, *Optimizing both catalyst preparation and catalytic behaviour for the oxidative dehydrogenation of ethane of Ni–Sn–O catalysts*, Topics in Catalysis, 59 (2016) 1564-1572.

[17] J.M.L. Nieto, P. Botella, M.I. Vazquez, A. Dejoz, *The selective oxidative dehydrogenation of ethane over hydrothermally synthesised MoVTeNb catalysts*, Chemical Communications, (2002) 1906-1907.

[18] P. Botella, A. Dejoz, M.C. Abello, M.I. Vázquez, L. Arrúa, J.M. López Nieto, *Selective oxidation of ethane: Developing an orthorhombic phase in Mo–V–X (X=Nb, Sb, Te) mixed oxides*, Catalysis Today, 142 (2009) 272-277.

[19] W. Shan, M. Luo, P. Ying, W. Shen, C. Li, *Reduction property and catalytic activity of* $Ce_{1-x}Ni_xO_2$ *mixed oxide catalysts for* CH_4 *oxidation*, Applied Catalysis A: General, 246 (2003) 1-9.

[20] L. Zhang, J. Lin, Y. Chen, *Studies of surface NiO species in* NiO/SiO_2 *catalysts using temperature-programmed reduction and X-ray diffraction*, Journal of the Chemical Society, Faraday Transactions, 88 (1992) 2075-2078.

[21] F. Medina, P. Salagre, J.L.G. Fierro, J.E. Sueiras, *NiO Reducibilities: structural and catalytic properties of their pure and potassium-doped reduced forms*, Journal of Catalysis, 142 (1993) 392-405.

[22] P. Salagre, J.L.G. Fierro, F. Medina, J.E. Sueiras, *Characterization of nickel species on several γ-alumina supported nickel samples*, Journal of Molecular Catalysis A: Chemical, 106 (1996) 125-134.

[23] M. Tomellini, *X-ray photoelectron spectra of defective nickel oxide*, Journal of the Chemical Society, Faraday Transactions 1: Physical Chemistry in Condensed Phases, 84 (1988) 3501-3510.

[24] J.C. Vedrine, G. Hollinger, M.D. Tran, *Investigations of antigorite and nickel supported catalysts by x-ray photoelectron spectroscopy*, Journal of Physical Chemistry, 82 (1978) 1515-1520.

[25] V. Biju, M. Abdul Khadar, *Electronic structure of nanostructured nickel oxide using Ni 2p XPS analysis*, Journal of Nanoparticles Research, 4 (2002) 247-253.

[26] V.M.A. van, Sawatzky, *Nonlocal screening effects in 2p x-ray photoemission spectroscopy core-level line shapes of transition metal compounds*, Physical Review Letters, 70 (1993) 2459-2462.

[27] Y.V. Larichev, B.L. Moroz, V.I. Bukhtiyarov, *Electronic state of ruthenium deposited onto oxide supports: An XPS study taking into account the final state effects*, Applied Surface Science, 258 (2011) 1541-1550.

[28] A. Fernandez, J.P. Espinos, D. Leinen, A.R. Gonzalez-Elipe, J.M. Sanz, *Charging and mixing effects during the XPS analysis of mixtures of oxides*, Surface and Interface Analysis, 22 (1994) 111-114.

[29] A.R. Gonzalez-Elipe, J.P. Holgado, R. Alvarez, G. Munuera, *Use of factor analysis and XPS to study defective nickel oxide*, Journal of Physical Chemistry, 96 (1992) 3080-3086.

[30] G.C. Allen, S.J. Harris, J.A. Jutson, J.M. Dyke, *A study of a number of mixed transition metal oxide spinels using x-ray photoelectron spectroscopy*, Applied Surface Science, 37 (1989) 111-134.

[31] D.C. Koningsberger, *Stereo chemistry and electronic structure XAFS spectroscopy: Data-analysis and applications*. in*: Neutron and synchrotron radiation for condensed matter studies*, Volume II, *Applications to solid state physics and chemistry*, Springer-Verlag Berlin Heidelberg 1994, pp. 213-244.

[32] J. Rabeah, J. Radnik, V. Briois, D. Maschmeyer, G. Stochniol, S. Peitz, H. Reeker, C. La Fontaine, A. Brückner, *Tracing active sites in supported Ni catalysts during butene oligomerization by Operando Spectroscopy under pressure*, ACS Catalysis, 6 (2016) 8224-8228.

Chapter 8

Overall conclusions

Catalysis science will be one of the key players in the overcoming energy transition to renewables. The understanding of both the structure and chemical functionality of solid catalysts (which in the end leads to structure-function-reactivity correlations) will be essential for achieving the rational design of new multifunctional catalytic materials for diverse applications. This way, materials chemistry stands out as the main supplier of the necessary tools to face this challenge.

The present doctoral thesis provides some examples of how materials science can contribute to understand the catalytic performance of specific oxide systems for the transformation of biomass and natural gas derived feedstocks. On the one hand, tungsten bronze based materials are stablished as very adaptive systems, in which catalytic functionality can be modulated through several strategies.

In the case of W-V-O oxides (synthesized by a hydrothermal method), the acid-redox properties can be tailored by controlling the phase composition in the catalysts (i.e. h-WO_3/m-WO_3 ratio) at a fixed vanadium content. Then, the acid characteristics of the catalysts increase proportionally with the concentration of h-WO_3-type phase in the materials (as confirmed also from catalytic results of gas-phase methanol transformation, used as a test/characterization reaction). This has important implications in the catalytic performance in the gas-phase oxidative dehydration of glycerol to acrylic acid (a two-step process), since surface acid properties are pivotal in the first reaction step (dehydration step to form acrolein). In addition, the higher reducibility of vanadium sites in h-WO_3-type phase leads to higher yields to acrylic acid (produced by the subsequent partial oxidation of acrolein, formed in the first reaction step).

Considering W-Nb-O materials, prepared by hydrothermal synthesis, the incorporation of Nb within the h-WO_3 leads to modulated acid properties, by which the concentration of Lewis acid sites on the catalyst surface increases with Nb content in the materials. Furthermore, the incorporation of Nb also has structural implications, promoting the loss of long range order in the structure, especially in the *ab* plane. At Nb/(W+Nb) ratios of ca. 0.5, small W-Nb mixed oxide nanoparticles (ca. 5-10 nm) isostructural with the so-called M1 phase ($Cs_{0.5}Nb_{2.5}W_{2.5}O_{14}$-type structure) have been obtained. Accordingly, high Brönsted/Lewis acid site ratios (achieved at low Nb contents) promote high yields to acrolein in the gas phase aerobic transformation of glycerol. On the other hand, high Nb contents (i.e. low Brönsted/Lewis ratios) lead to high yields to CO_x and heavy compounds in this reaction. On the contrary, low Brönsted/Lewis ratios lead to high yields to C_5-C_{10} products in the aqueous phase valorization of short chain oxygenates. This way, a higher proportion of Lewis acid sites directs the reactivity through aldol condensation mechanisms (favoring the formation of longer carbon chain products) rather than esterification. Despite the high demanding reaction conditions (i.e. low pH and high water contents), the catalysts maintain their catalytic behavior after 3 uses.

The versatility of these bronze-type oxides is not only limited to their crystal structure and composition, but also to the synthetic approaches that can be applied to synthesize them. In this sense, W-V-O and W-Nb-O mixed oxides with a pseudocrystalline and a hexagonal tungsten bronze structure have been synthesized by a reflux method. This approximation has allowed us to prepare mesoporous-supported catalysts (i.e. W-V-O and W-Nb-O supported on a mesoporous KIT-6 silica). Supported catalysts show a decrease in the acid strength of their surface acid sites, leading to higher yields to acrolein and acrylic acid during the gas phase aerobic transformation of glycerol.

It is worth noting that catalytic phenomenon is taking place on the surface. Then the use test reactions as an extra characterization tool is a good strategy to study the nature of the specific surface catalytic functionalities. This has been carried out by using methanol and ethanol gas-phase transformations as test reactions to elucidate the acid/redox nature of surface active sites.

Apart from tungsten bronze-based materials, this thesis is also focused on gaining further insights on the effect of NiO-promoter or NiO-support interaction in the oxidative dehydrogenation (ODH) of ethane over nickel oxide-based catalysts. It has been shown that the interaction between promoter and NiO can be undertaken either by a well dispersion/ incorporation of the promoter within NiO framework (like in the case of Nb-promoted NiO catalyst), or by intimate contact of two separated oxide phases (like in the case of Sn-promoted nickel oxide catalyst), leading, in both cases, to similar catalytic performance in the oxidative dehydrogenation of ethane (ca. 90 % selectivity to ethylene). However, this different phase distribution leads to a very different catalytic behavior when oxygen is not present in the feed. In the absence of oxygen Nb-promoted nickel oxide is instantaneously reduced to metallic nickel. In the case of Sn-promoted catalysts, nickel oxide preserves its oxidized state even in the absence of oxygen in the feed, being still selective to ethylene in the ODH of ethane. The general trend is that the lower the reducibility (studied by means of temperature programmed reduction in H_2 and *in situ* time-resolved XAS), the higher the selectivity to ethylene in the ODH of ethane.

The study has been extended to a series of supported NiO catalysts displaying a selectivity to ethylene in the range 30-90 % in the ODH of ethane. The catalytic activity along the series increases as NiO crystallite size decreases. On the other hand, the selectivity to ethylene varies linearly with the number of Ni neighbors in the second coordination shell (i.e. with Ni-Ni coordination number), as determined by the analysis of the EXAFS region in the X-ray absorption spectra in the Ni K-edge of the catalysts. Accordingly, the high selectivity to ethylene obtained in the best supported NiO catalysts could be ascribed to the generation of cationic vacancies, likely due to the elimination of non-selective Ni^{3+} sites and electrophilic oxygen species.

Appendix I

Index of Figures

Page

Chapter 1. Introduction

Figure 1.1. Global energy supply in percentages from 1830 to 2007…………………………………………………... 3

Figure 1.2. Shares of primary energy by feedstock with projection to 2040……………………………………………. 5

Figure 1.3. Proposed pathways for the valorization of natural gas via oxidative processes………………………………. 7

Figure 1.4. Proposed routes for the production of olefins from biomass………………………………………………… 8

Figure 1.5. Reaction scheme of the oxidative dehydrogenation of ethane…………………………………………………... 9

Figure 1.6. a) Supported vanadium oxide; b) NiO with a sodium chloride-type structure viewed along [111] direction; c) Mo-V mixed oxide with an M1-type structure viewed along [001] direction………………………… 9

Figure 1.7. Schematic representation of the Mars-van Krevelen redox mechanism during the oxidative dehydrogenation of alkanes……………………….... 10

Figure 1.8. General scheme of primary treatments of lignocellulosic biomass…………………………… 14

Figure 1.9. General scheme the transformation of triglycerides into chemicals and fuels……………………………... 15

Figure 1.10. Scheme of the transesterification of triglycerides in basic media………………………………………....... 16

Figure 1.11. Different strategies for glycerol transformation into valuable chemicals………………………………… 17

Figure 1.12. Scheme of glycerol dehydration to acrolein on Brönsted acid sites…………………………………… 18

Figure 1.13. Schematic representation of glycerol transformation on acid, redox and on multifunctional acid-redox catalysts……………………………………………… 18

Figure 1.14. The 12 principles of Green Chemistry as listed by Anastas et al…………………………………………….. 21

Figure 1.15. Reaction scheme of partial oxidation of n-butane to maleic anhydride…………………………………….. 22

Figure 1.16. Crystal structure of vanadyl pyrophosphate (VPP) viewed along [010] (A) and [100] (B) directions. Blue tetrahedra and red octahedra correspond to $[PO_4]_{Td}$ and $[VO_6]_{Oh}$ units respectively……………………….. 23

Figure 1.17. Schematic representation of Grasselli´s seven pillars of oxidation catalysis…………………………………… 24

Figure 1.18. a) Representation of the formation of the Magneli phase $W_{20}O_{58}$ through the formation of crystallographic shear planes (ordered Wadsley defects) by loss of oxygen. b) Scheme of the rotational fault generated in ReO_3-type tungsten oxide phase which correlates its structure with the tetragonal tungsten bronze (TTB) polymorph…………………... 26

Figure 1.19. Representation of some of tungsten oxide crystal phases in the system WO_2-WO_3, highlighting their oxygen/tungsten ratio, related with the proportion of W^{4+}, W^{5+} and W^{6+} in the structure……………………. 27

Figure 1.20. Scheme of the formation mechanism of a Mo-V oxide with a M1-type structure under hydrothermal conditions……………………………………………. 28

Figure 1.21. Representation of the hexagonal tungsten bronze structure (also known HTB and h-WO_3) along [010] (A) and [001] (B) directions………………………….. 29

Figure 1.22. Simplified reaction scheme of the gas-phase transformation of glycerol on a multifunctional acid-redox hexagonal tungsten bronze-based catalyst…….. 29

Figure 1.23. Schematized reaction pathway on undoped and Nb-doped NiO catalysts during the ODH of ethane……… 31

Figure 1.24. Selectivity to ethylene in the ODH of ethane at 400 ºC as a function of NiO loading for a series of TiO_2-supported catalysts presenting different support surface areas. Symbols: (■) 11 $m^2 g^{-1}$ TiO_2; (○) 55 $m^2 g^{-1}$ TiO_2; (▲) 85 $m^2 g^{-1}$ TiO_2………………………… 32

Chapter 2. Experimental procedure

Figure 2.1. A) Synthesis gel of W-V-O oxide prepared by hydrothermal method. B) Stainless steel autoclave for selected atmosphere hydrothermal synthesis………… 59

Figure 2.2. W-V-O oxide prepared by reflux synthesis…………... 60

Figure 2.3. Graphical scheme of diffraction phenomena dictated by Bragg´s Law **:** ($n\,\lambda\ =\ 2d_{hkl}\ sen\ \theta$)…………….. 63

Figure 2.4. Types of signals generated when an electron beam interacts with a specimen……………………………. 65

Figure 2.5. Ionization process which leads to K_α X-ray emission... 67

Figure 2.6. In-house cell for *in situ* XAS experiments developed at ITQ…………………………………………………... 70

Figure 2.7. XAS spectrum of fcc metallic Ni with main regions marked. Red-dotted line represents the hypothetical absorption of an isolated Ni atom $\mu_0(E)$……………… 72

Figure 2.8. Example of a FTIR spectra of adsorbed pyridine of a solid acid catalyst presenting both Brönsted and Lewis acid sites……………………………………… 81

Figure 2.9. Scheme of the reaction system for the gas-phase aerobic transformation of glycerol…………………... 85

Figure 2.10. Summarized calculations for the determination of the catalytic properties on the gas phase transformation of glycerol……………………………………………… 86

Chapter 3. W-V-O catalysts: Influence of the phase composition on their multifunctional acid-redox properties.

Figure 3.1. XRD patterns of as-prepared (A) and heat-treated W-V-O catalysts. a) MT-1; b) MT-2; c) T-1; d) T-2; e) T-3; f) T-4; g) T-5. Crystal structures of *m*-WO_3 (blue) and *h*-WO_3 (red) type phases are also included…………………………………………….. 98

Figure 3.2. SEM micrographs of as-prepared W-V-O materials. a) MT-1; b) MT-2; c) T-1; d) T-2; e) T-3; f) T-4; g) T-5……………………………………………… 100

Figure 3.3. SEM and TEM images of heat-treated W-V-O materials. A) MT-1 (*h*-WO_3); B) T-4 (*m*-WO_3); C) T-5 (*h*-WO_3 + *m*-WO_3)……………………………… 100

Figure 3.4. Raman profiles of heat-treated W-V-O materials. a) MT-1; b) MT-2; c) T-1; d) T-2; e) T-3; f) T-4; g) T-5…………………………………………………… 101

Figure 3.5. DTG profiles of as-prepared oxides: a) MT-1; b) MT-2; c) T-1; d) T-2; e) T-3; f) T-4; g) T-5……………… 102

Figure 3.6. FTIR spectra of as-synthesized (A) and heat-treated (B) W-V-O materials: a) MT-1; b) MT-2; c) T-1; d) T-2; e) T-3; f) T-4; g) T-5……………………………. 103

Figure 3.7. TPD-NH_3 profiles of W-V-O catalysts (A) and the variation of adsorbed ammonia as a function of h-WO_3 content (B) and surface area (C): a) T-4 (*m*-WO_3 type catalyst); b) T-3; c) T-5; d) MT-2; e) T-1 (*h*-WO_3 type catalyst)………………………………………… 104

Figure 3.8. V $2p_{3/2}$ (A) and W $4f$ (B) core level XPS spectra of W-V-O catalysts. a) MT-1; b) MT-2; c) T-1; d) T-3; e) T-4; f) T-5……………………………………………….. 105

Figure 3.9. H_2-TPR profiles of phase pure *m*-WO_3 and *h*-WO_3-type W-V-O catalysts. a) T-4 (*m*-WO_3-type phase); b) MT-1 (*h*-WO_3-type phase)…………………………... 106

Figure 3.10. Catalytic activity (A) and specific activity (B) as a function of reaction temperature for W-V-O catalysts. MT-1 (▲); MT-2 (**X**); T-1 (▷); T-2 (◀); T-3 (○); T-4 (■); T-5 (▽)……………………….. 108

Figure 3.11. Selectivity to DME and POPs as a function of methanol conversion for W-V-O catalysts. MT-1 (▲); MT-2 (**X**); T-1 (▷); T-2 (◀); T-3 (○); T-4 (■); T-5 (▽)…………………………………….. 110

Figure 3.12. Selectivity to DME (green empty symbols) and to partial oxidation products (POPs, full black symbols) during the gas phase aerobic transformation of methanol as a function of the amount of h-WO$_3$ phase (see Table 3.2) in W-V-O catalysts (MeOH conversion = 10 %). The amount of bronze-type phase present in MT-2 pseudocrystalline sample (ca. 85 %) (green and black triangles) has been estimated from the corresponding DME and POPs selectivity during the catalytic test……………………………………….. 110

Figure 3.13. Variation of the specific activity with the selectivity to partial oxidation products (POPs) at 280 ºC in the aerobic transformation of methanol for the catalysts in Table 3.3. HTB (★); MT-1 (▲); MT-2 (**X**); T-1 (▷); T-2 (◀); T-3 (○); T-4 (■); T-5 (▽)……………………………………………….. 111

Figure 3.14. Variation of the selectivity to acrolein + acrylic acid (AC+AA, blue circles), the selectivity to carbon oxides (CO$_x$, black squares) and the AA/AC ratio (red stars) as a function of *h*-WO$_3$ type phase content in W-V-O catalysts in the gas phase aerobic transformation of glycerol. Reaction conditions: T = 320 ºC; Gly/H$_2$O/O$_2$/N$_2$/He molar ratio of 2/40/4/15/39; contact time, W/F, of 81 g$_{cat}$ h mol$_{gly}^{-1}$…………………………………………. 114

Chapter 4. W-Nb-O bronzes as catalysts for the valorization of biomass-derived feedstocks.

Figure 4.1. A) XRD patterns of W-Nb-O oxides. B) Variation of c-axis (considered as the distance between two vertex sharing octahedral) as a function of Nb in W-Nb-O oxides. a) W-Nb-0; b) W-Nb-0.29; c) W-Nb-0.40; d)

W-Nb-0.53; e) W-Nb-0.62; f) W-Nb-0.80; g) W-Nb-0.95; h) W-Nb-1... 128

Figure 4.2. Raman profiles of W-Nb-O oxides: a) W-Nb-0; b) W-Nb-0.29; c) W-Nb-0.40; d) W-Nb-0.53; e) W-Nb-0.62; f) W-Nb-0.80; g) W-Nb-0.95; h) W-Nb-1......... 130

Figure 4.3. A) W 4f core-level XPS spectra of Nb-free (W-Nb-0, a) and Nb-substituted (W-Nb-0.29, b) materials. B) W L_{III}-edge XAS spectra in the XANES range of Nb-free (W-Nb-0, black line) and Nb-substituted (W-Nb-0.29, red dotted line) materials................................. 131

Figure 4.4. XRD patterns of undoped (a) and Nb-containing tungsten oxide (b) heat-treated at 550 ºC in N_2 flow; a) W-Nb-0; b) W-Nb-0.29............................... 133

Figure 4.5. SAED patterns (A and C) and HRTEM images (B and D) of W-Nb-0.29 (A-B) and W-Nb-0.53 (C-D) mixed oxides. Miller indexes have been assigned on the basis of *h*-WO_3-type phase (JCPSD: 01-85-2459)...... 133

Figure 4.6. A) HRTEM image of a crystal (white arrow) in W-Nb-0.62, showing the structure along [001] direction of $Cs_{0.5}Nb_{2.5}W_{2.5}O_{14}$-type phase, also known as M1-phase. B) Representation of the *ab* plane ([001] crystallographic direction) of $Cs_{0.5}Nb_{2.5}W_{2.5}O_{14}$-type phase [27]. C) SAED ring pattern of W-Nb-0.80 sample. D) HRTEM image of W-Nb-0.80 sample. Miller indexes have been assigned based on *h*-WO_3-type phase (JCPSD: 01-85-2459)........................ 134

Figure 4.7. XRD patterns of hydrothermally synthesized $Cs_{0.5}Nb_{2.5}W_{2.5}O_{14}$ and W-Nb mixed oxide with Nb content of 62 at% (W-Nb-0.62 sample)................. 135

Figure 4.8. Nitrogen adsorption-desorption isotherms of W-Nb oxides. a) W-Nb-0; b) W-Nb-0.29; c) W-Nb-0.40; d) W-Nb-0.53; e) W-Nb-0.62; f) W-Nb-0.80; g) W-Nb-0.95; h) W-Nb-1…………………………………….. 137

Figure 4.9. BJH pore size distributions of W-Nb oxides, calculated from the adsorption branch of N_2-adsorption-desorption isotherms. a) W-Nb-0; b) W-Nb-0.29; c) W-Nb-0.40; d) W-Nb-0.53; e) W-Nb-0.62; f) W-Nb-0.80; g) W-Nb-0.95; h) W-Nb-1…….... 138

Figure 4.10. FTIR spectra of adsorbed pyridine (A) and TPD-NH_3 profiles (B) of W-Nb oxides. a) W-Nb-0; b) W-Nb-0.29; c) W-Nb-0.40; d) W-Nb-0.53; e) W-Nb-0.62; f) W-Nb-0.80; g) W-Nb-0.95; h) W-Nb-1…………….... 139

Figure 4.11. Acid characteristics of W-Nb oxides as function of Nb content. A) Concentration of acid sites. B) Surface density of acid sites. C) Brönsted/Lewis acid sites ratio (BAS/LAS)…………………………………….. 141

Figure 4.12. Low-temperature (77 K) FTIR spectra of adsorbed CO at increasing CO equilibrium pressures of selected W-Nb-O catalysts. C-O stretching region (A-D). O-H stretching region (E-H). Blue, green and red spectra were obtained at $P_{COeq.}$ of 0, 0.020 and 2.000 mmbar. W-Nb-0 (A and E); W-Nb-0.29 (B and F); W-Nb-0.62 (C and G); W-Nb-1 (D and H)……………… 143

Figure 4.13. Coverage as a function of CO equilibrium pressure for W-Nb-0 (△), W-Nb-0.29 (■), W-Nb-0.62 (○) and W-Nb-1 (●)…………………………………….. 144

Figure 4.14. Background subtracted low-temperature (77 K) FTIR spectra of adsorbed CO of selected W-Nb-O catalysts at a CO coverage θ = 0.25: a) W-Nb-0; b) W-Nb-0.29; c) W-Nb-0.62; d) W-Nb-1…………….. 145

Figure 4.15. Background-subtracted low-temperature (77 K) FTIR spectra in the O-H stretching region after CO-adsorption (coverage θ = 0.25) (A), and after CO-desorption at high vacuum (ca. 10^{-6} mbar) (B), of selected W-Nb-O catalysts: a) W-Nb-0; b) W-Nb-0.29; c) W-Nb-0.62; d) W-Nb-1…………………….. 147

Figure 4.16. Variation of the selectivity to acrolein, carbon oxides and heavy compounds as a function of Nb content in the catalysts. Symbols: Acrolein (●), heavy compounds (○) and CO_x (▲). Reaction conditions: gly/O_2/ molar ratio of 2/4, T = 295 ºC, Contact time W/F of 81 g_{cat} h $(mol_{gly})^{-1}$…………………………… 151

Figure 4.17. FTIR spectra of adsorbed pyridine of fresh and used W-Nb-0 sample: a) Fresh catalyst pretreated in high vacuum for 12h. b) Fresh catalyst pretreated in high vacuum for 2h. c) Used catalyst pretreated in high vacuum for 2h……………………………………….. 153

Figure 4.18. A) Summarized reaction network of the aqueous-phase valorization of short chain oxygenates by aldol condensation-ketonization reactions. B) Self-aldol condensation of propanal to 2-methyl-2pentenal. C) Esterification of acetic acid and ethanol to ethyl acetate……………………………………………….. 154

Figure 4.19. Conversion of each short-chain oxygenate (A) and selectivity to the main reaction products (B) as a function of Nb-content in the catalysts. Reaction conditions: 3 g of aqueous model mixture and 150 mg of catalyst under stirring for 7h at 180 ºC; P_{N2}= 13 bar……………………………………………………… 157

Figure 4.20. Total organic yield (TOY) and yield to intermediates (sum of 2-methyl-2-pentenal and C_5-C_8 fraction) and to C_9-C_{10} oxygenates as a function of the concentration of acid sites (A) and as a function of Brönsted/Lewis acid sites ratio (B)…………………….. 158

Figure 4.21. Yield to intermediates (sum of 2-methyl-2-pentenal and C_5-C_8 fraction) (A) and to C_9-C_{10} oxygenates (B) as a function of Nb content in the catalysts. Reaction conditions: 7h at 180 ºC (left); 7h at 200 ºC (right)…... 159

Figure 4.22. Yield to 2M2P (a), to C_5-C_8 (b) and C_9-C_{10} (c) after three consecutive uses for W-Nb-0.62 and W-Nb-1. Reaction conditions: 7h at 200 ºC…………………… 160

Chapter 5. Reflux-synthesized bulk and supported W-Nb-O and W-V-O oxide bronzes: Aerobic transformation of alcohols.

Figure 5.1. Pore size distribution (A) and low-angle XRD patterns (B) of: a) R-WNb/KIT (black); b) R-WV/KIT (red); and KIT-6 support (green)…………………………..... 171

Figure 5.2. XRD patterns of bulk and supported W-Nb and W-V mixed oxides: a) R-WNb; b) R-WNb/KIT; c) WNb-H; d) R-WV; e) R-WV/KIT; f) WV-H………………. 172

Figure 5.3. SEM micrographs of bulk and supported mixed oxides. a) R-WNb; b) R-WNb/KIT; c) WNb-H; d) R-WV; e) R-WV/KIT; f) WV-H……………………….. 173

Figure 5.4. Raman (A) and FTIR (B) spectra of bulk and supported materials: a) R-WNb; b) R-WNb/KIT; c) WNb-H; d) R-WV; e) R-WV/KIT; f) WV-H……….... 175

Figure 5.5. TPD-NH_3 profiles of bulk and supported WNb and WV oxides. a) R-WNb; b) R-WNb/KIT; c) WNb-H; d) R-WV; e) R-WV/KIT; f) WV-H…………………. 177

Figure 5.6. Catalytic performance of W-Nb-O catalysts. A) Ethanol conversion as a function of reaction temperature. B) Selectivity to diethyl ether as a function of ethanol conversion. C) Selectivity to ethylene as a function of ethanol conversion. Symbols: R-WNb (◆), R-WNb/KIT (▲), WNb-H (□). Reaction conditions: EtOH/O_2/N_2 molar ratio of 6/13/81, Contact time W/F = 6.8 g_{cat} h mol_{EtOH}^{-1}……. 179

Figure 5.7. Selectivity profiles of bulk and supported W-Nb-O catalysts at low (20 %, left) and high (80 %, right) conversion of ethanol. DEE: diethyl ether. Reaction conditions: EtOH/O_2/N_2 molar ratio of 6/13/81, Contact time W/F = 6.8 g_{cat} h mol_{EtOH}^{-1}……………… 180

Figure 5.8. Catalytic performance of W-V-O catalysts. A) Ethanol conversion as a function of reaction temperature. B) Selectivity to acetaldehyde as a function of ethanol conversion. C) Selectivity to diethyl ether as a function of ethanol conversion. D) Selectivity to ethylene as a function of ethanol conversion. Symbols: R-WV (●), R-WV/KIT (▼), WV-H (□). Reaction conditions: EtOH/O_2/N_2 molar ratio 6/13/81, Contact time W/F = 6.8 g_{cat} h mol_{EtOH}^{-1}……………………………………….. 181

Figure 5.9. Selectivity profiles of bulk and supported W-V catalysts at low (20 %, left) and high (80 %, right) conversion of ethanol. DEE: diethyl ether. Reaction conditions: EtOH/O_2/N_2 molar ratio of 6/13/81, Contact time W/F = 6.8 g_{cat} h mol_{EtOH}^{-1}……………… 182

Figure 5.10. Yields to acrolein (AC, blue), acrylic acid (AA, brown), carbon oxides (CO_x, black) and heavy compounds (HC´s, green) at different reaction temperatures. A-B) R-WNb; C-D) R-WNb/KIT; E-F) WNb-H. Reaction conditions: Gly/H_2O/O_2/N_2/He molar ratio of 2/40/4/15/39, contact time W/F = 81 g_{cat} h mol_{gly}^{-1}.. 184

Figure 5.11. Yields to acrolein (**AC**, blue), acrylic acid (**AA**, brown), carbon oxides (**CO_x**, black) and heavy compounds (**HC´s**, green) at different reaction temperatures over V-containing catalysts: R-WV (A and B); R-WV/KIT (C and D); WV-H (E and F). Reaction conditions: Gly/H_2O/O_2/N_2/He molar ratio of 2/40/4/15/39, contact time W/F = 81 g_{cat} h mol_{gly}^{-1}.. 186

Chapter 6. Promoted NiO catalysts: Studies on the redox and catalytic properties in the ODH of ethane

Figure 6.1. Variation of ethane conversion (A) and selectivity to reaction products (B) as a function of time on stream during the ODH of ethane for NiO-Nb catalyst. Catalytic tests were conducted in the presence (molar ratio ethane/O_2/He = 5/5/90) and in the absence (molar ratio ethane/O_2/He = 5/0/95) of oxygen in the feed. Reaction conditions: 450 ºC, contact time W/F = 2 g_{cat} h $(mol_{ethane})^{-1}$.................................... 198

Figure 6.2. Variation of ethane conversion (A) and selectivity to reaction products (B) as a function of time on stream during the ODH of ethane for NiO-Sn catalyst. Catalytic tests were conducted in the presence (molar ratio ethane/O_2/He = 5/5/90) and in the absence (molar ratio ethane/O_2/He = 5/0/95) of oxygen in the feed. Reaction conditions: 450 ºC, contact time W/F = 2 g_{cat} h $(mol_{ethane})^{-1}$………………………………… 199

Figure 6.3. Evolution of ethane conversion (A), selectivity to main reaction products (B), carbon balance and selectivity to hydrogen (C) with the time on stream for NiO-Sn catalyst. Reaction conditions: ethane/O_2/He molar ratio of 30/0/70; 475 ºC, contact time W/F in the range 2.7-20 g_{cat} h $(mol_{ethane})^{-1}$…………………… 200

Figure 6.4. XRD patterns of NiO-based catalysts. a) NiO-Nb; b) NiO-Sn; c) NiO-La; d) NiO. Symbols: (●) Nb_2O_5 (JCPDS: 01-071-0336); (☐) SnO_2 (JCPDS: 00-046-1088); (▲)$La_2O_2CO_3$ (JCPDS: 00-048-1113)……… 202

Figure 6.5. Bright-Field STEM images and their corresponding XEDS line-scans of NiO-Nb (A) and NiO-Sn (B) isolated particles……………………………………….. 204

Figure 6.6. Raman spectra of unpromoted (a), Sn- (b) and Nb-promoted (c) NiO catalysts………………………….. 205

Figure 6.7. HAADF-STEM images and their corresponding XEDS maps of NiO-Nb (A) and NiO-Sn (B) catalysts……………………………………………… 206

Figure 6.8. HAADF-STEM images and the corresponding atomic composition determined by XEDS (point analysis and full image analysis) of NiO-Nb (A) and NiO-Sn (B)… 206

Figure 6.9. H_2-TPR profile of promoted NiO catalysts: a) NiO-Nb; b) NiO-Sn; c) NiO-La; d) NiO………………….... 208

Figure 6.10. *In situ* time-resolved XANES spectra in the Ni K-edge (left) and their corresponding kinetic curves calculated by LCF (right) during reduction-reoxidation-reduction experiments. a) NiO-Nb; b) NiO-Sn; c) NiO-La, d) NiO. Reaction conditions: T = 450ºC; (1, ■) H_2/He, 25/25 (mL min^{-1}); (2, ●) O_2/He, 5/25 (mL min^{-1}); (3, ▲) ethane/He, 5/25 (mL min^{-1})…………………………………………………… 210

Figure 6.11. *In situ* time-resolved XANES spectra in the Ni K-edge (left) and their corresponding kinetic curves calculated by LCF (right) during reduction-reoxidation treatments. a) NiO-Sn; b) NiO. Reaction conditions: T = 500 ºC; (■) ethane/He, 5/25 (mL min^{-1}); (●) O_2/He, 5/25 (mL min^{-1})………………... 212

Figure 6.12. *In situ* time-resolved XANES spectra in the Ni K-edge (left) and their corresponding kinetic curves calculated by LCF (right) during reduction-reoxidation-reduction experiments at different temperatures over NiO-Nb catalysts. a) 400 ºC; b) 450 ºC; c) 500 ºC. Reaction conditions: (1, ■) H_2/He, 25/25 (mL min^{-1}); (2, ●) O_2/He, 5/25 (mL min^{-1}); (3, ▲) ethane/He, 5/25 (mL min^{-1})………… 213

Figure 6.13. *In situ* time-resolved XANES spectra in the Ni K-edge (left) and their corresponding kinetic curves calculated by LCF (right) during reduction-reoxidation-reduction experiments at different temperatures over NiO-Sn catalyst. a) 400 ºC; b) 450 ºC; c) 500 ºC. Reaction conditions: (step 1, ■) H_2/He, 25/25 (mL min^{-1}); (step 2, ●) O_2/He, 5/25 (mL min^{-1}); (step 3, ▲) ethane/He, 5/25 (mL min^{-1})………………………………………………………. 214

Figure 6.14. XANES spectra in the Ni K-edge NiO-Sn recorded after 12 min of reoxidation treatment in O_2/He (5/25 mL min^{-1}) at different temperatures (spectra of metallic Ni and NiO are also shown). a) 400 ºC; b) 450 ºC; c) 500 ºC…………………………………... 215

Figure 6.15. XRD profiles of fresh (*a* and **c**) and used (*b* and *d*) under ethane/He flow (5/95 mL min^{-1} at 450 ºC) of NiO-Sn (*a*, b) and NiO-Nb (*c*, *d*) catalysts………… 217

Figure 6.16. HAADF-STEM images and XEDS maps of NiO-Sn (A) and NiO-Nb (B) catalysts……………………… 218

Figure 6.17. XRD profile (A) and BF-STEM image (B) and the corresponding C-K$_α$ of reduced NiO-Sn catalyst (reduction conditions in Figure 6.3). Symbols: (●) hpc-Ni (JCPDS: 45-1027)………………………… 219

Chapter 7. Reflux-synthesized bulk and supported W-Nb-O and W-V-O

Figure 7.1. Selectivity to ethylene as a function of ethane conversion for NiO-based catalysts. Symbols: NiO (▲); NiO/SiO$_2$ (◘); NiO/PCH-Ti (▽); NiO/TiO$_2$-a (●); NiO/TiO$_2$-P25 (○). Reaction conditions: ethane/O$_2$/He molar ratio of 3/1/26, T = 450 ºC…….. 229

Figure 7.2. XRD profiles of bulk and supported NiO catalysts. a) NiO; b) NiO/SiO$_2$; c) NiO/PCH-Ti; d) NiO/Ti-a; and e) NiO/Ti-P25. Symbols: NiO (●); PCH-Ti (▽); TiO$_2$-anatase (◘); TiO$_2$-rutile (▲)………………….. 231

Figure 7.3. Variation of the catalytic activity with NiO average particle size. Reaction conditions: ethane/O$_2$/He molar ratio of 3/1/26; catalytic activity at 450 ºC at an ethane conversion lower than 5 %............................... 232

Figure 7.4. H_2-TPR profiles of NiO-based catalysts. a) NiO; b) NiO/SiO_2; c) NiO/PCH-Ti; d) NiO/Ti-a; and e) NiO/TiO_2-P25.. 233

Figure 7.5. *In situ* time-resolved XANES spectra in the Ni K-edge during the reduction in H_2/He of NiO-based catalysts. a) NiO; b) NiO/SiO_2; c) NiO/PCH-Ti; d) NiO/TiO_2-P25. Reduction conditions: H_2/He 25/25 (mL min^{-1}) at 450 ºC……………………………………………........ 235

Figure 7.6. A) XANES spectra in the Ni K-edge of NiO and metallic Ni. B) Kinetic curves of reduction in H_2 obtained by linear combination fitting of the corresponding spectra in Figure 7.5. Symbols: NiO (▲); NiO/SiO_2 (◘); NiO/PCH-Ti (▽); NiO/TiO_2-P25 (○) . Reduction conditions: H_2/He 25/25 (mL min^{-1}) at 450 ºC……………………………………… 236

Figure 7.7. Ni $2p_{3/2}$ core level XPS spectra of NiO-based catalysts. a) NiO; b) NiO/SiO_2; c) NiO/PCH-Ti; d) NiO/TiO_2-a; e) NiO/TiO_2-P25. (*) peak due to differential charging……………………………………………... 238

Figure 7.8. Variation of the selectivity to ethylene as a function of Satellite I/Main peak ratio in the Ni $2p_{3/2}$ core level XPS spectra for unsupported and supported NiO catalysts. Symbols: Ti-containing NiO catalysts (●); unsupported NiO (△); NiO/SiO_2 (◘)……………….. 239

Figure 7.9. Module of the Fourier Transform of EXAFS Ni k-edge zone of NiO catalysts. a) NiO; b) NiO/SiO_2; c) NiO/PCH-Ti; d) NiO/TiO_2-a; e) NiO/TiO_2-P25…….. 241

Figure 7.10. Variation of the selectivity to ethylene as a function of the coordination numbers calculated by EXAFS fitting for the 1st (A) and 2nd (B) coordination shells.

Symbols: Symbols: Ti-containing NiO catalysts (●); unsupported NiO (△); NiO/SiO$_2$ (◘)……………….. 242

Figure 7.11. XANES spectra in the Ni K-edge of supported NiO catalysts…………………………………………... 243

Figure 7.12. Variation of the selectivity to ethylene as a function of the normalized intensity of the XANES white line in the Ni K-edge for supported NiO catalysts………... 244

Appendix II

Index of Tables

Page

Chapter 1. Introduction

No Tables.

Chapter 2. Experimental procedure

Table 2.1. Characteristics of metal oxide supports………………… 62

Chapter 3. W-V-O catalysts: Influence of the phase composition on their multifunctional acid-redox properties.

Table 3.1. Precursors used in the hydrothermal synthesis of W-V-O catalysts…………………………………………….. 96

Table 3.2. Physicochemical characteristics of W-V-O catalysts…. 97

Table 3.3. Catalytic properties of W-V-O catalysts in the aerobic transformation of methanol…………………………… 109

Table 3.4. Catalytic properties of W-V-O catalysts in the aerobic transformation of glycerol…………………………….. 113

Chapter 4. W-Nb-O bronzes as catalysts for the valorization of biomass-derived feedstocks.

Table 4.1. Main characteristics of W-Nb-O mixed oxides……….. 127

Table 4.2. Acid characteristics of W-Nb-O mixed oxides catalysts…………………………………………………... 140

Table 4.3. Catalytic properties of W-Nb-O oxides in the aerobic transformation of glycerol………………………….. 149

Table 4.4. BAS/LAS ratio of W-Nb-0 catalyst measured by FTIR of adsorbed pyridine after different sample pretreatment……………………………………………… 152

Table 4.5. Catalytic performance in the valorization of short-chain oxygenates in aqueous phase at 180 ºC………... 156

Table 4.6. Total organic yield as a function of reaction temperature for W-Nb-O catalysts…………………... 156

Chapter 5. Reflux-synthesized bulk and supported W-Nb-O and W-V-O oxide bronzes: Aerobic transformation of alcohols.

Table 5.1. Synthesis method and composition of bulk and supported tungsten bronze catalysts………………… 169

Table 5.2. Textural and acid properties of bulk and supported catalysts……………………………………………... 170

Chapter 6. Promoted NiO catalysts: Studies on the redox and catalytic properties in the ODH of ethane

Table 6.1. Catalytic behavior of unpromoted and promoted NiO catalysts……………………………………………… 197

Table 6.2. Physicochemical features of NiO-based catalysts…….. 201

Table 6.3. Bulk and surface composition of NiO-based catalysts……………………………………………... 203

Chapter 7. Reflux-synthesized bulk and supported W-Nb-O and W-V-O

Table 7.1. Catalytic performance of unsupported and supported NiO catalysts…………………………………………...... 228

Table 7.2. Main physicochemical features of NiO-based catalysts……………………………………………… 232

Table 7.3. EXAFS analysis results for NiO-based catalysts……... 240

Appendix III

List of patents

- Marcelo Eduardo Domine, José Manuel López Nieto, Daniel Delgado Muñoz, Alberto Fernández-Arroyo Naranjo; *Procedimiento para la valorización de compuestos oxigenados presentes en fracciones acuosas derivadas de biomasa*, P201630339, ES2638719 (2017).

- Marcelo Eduardo Domine, José Manuel López Nieto, Daniel Delgado Muñoz, Alberto Fernández-Arroyo; *Method for recovering the oxygenated compounds contained in aqueous fractions derived from biomass*, PCT/ES2017/070167, WO2017162900 (2017).

Appendix IV

List of publications and selected conferences

Publications:

- R. Sanchís, D. Delgado, S. Agouram, M. D. Soriano, M. I. Vázquez, E. Rodríguez-Castellón, B. Solsona, J.M. López Nieto; *NiO diluted in high surface area TiO_2 as an efficient catalyst for the oxidative dehydrogenation of ethane*, Applied Catalysis A: General, 536 (2017) 18.

- N. La Salvia, D. Delgado, L. Ruiz-Rodríguez, L. Nadji, A. Massó, J. M. López Nieto; *V- and Nb-containing tungsten bronzes catalysts for the aerobic transformation of ethanol and glycerol. Bulk and supported materials*, Catalysis Today 206 (2017) 2.

- A. Fernández-Arroyo, D. Delgado, M. E. Domine, J. M. López Nieto; *Upgrading of oxygenated compounds present in aqueous biomass-derived feedstocks over NbO_x-based catalysts*, Catalysis Science & Technology 7 (2017) 5495.

- D. Delgado, B. Solsona, A. Ykreylef, A. Rodríguez-Gómez, A Caballero, E. Rodríguez-Aguado, E. Rodríguez-Castellón, J. M. López Nieto; *Redox and catalytic properties of promoted NiO catalysts for the oxidative dehydrogenation of ethane*, The Journal of Physical Chemistry C 121 (2017) 25132.

- Daniel Delgado, Alessandro Chieregato, M. Dolores Soriano, Elena Rodríguez-Aguado, Lidia Ruiz-Rodríguez, Enrique Rodríguez-Castellón, José M. López Nieto; *Influence of phase composition of bulk tungsten vanadium oxides on the aerobic transformation of methanol and glycerol*, European Journal of Inorganic Chemistry 2018 (2018) 1204.

- L. Nadji, A. Massó, D. Delgado, R. Isaadi, E. Rodríguez-Aguado, E. Rodríguez-Castellón, J. M. López Nieto; *Gas phase dehydration of* *glycerol to acrolein over WO_3-based catalysts prepared by non-hydrolytic sol-gel synthesis*, RSC Advances 8 (2018) 13344.

- D. Delgado, R. Sanchís, J. A. Cecilia, E. Rodríguez-Castellón, A. Caballero, B. Solsona, J. M. López Nieto; *Support effects on NiO-based catalysts for the oxidative dehydrogenation (ODH) of ethane*, Catalysis Today, In press (2018) DOI: 10.1016/j.cattod.2018.07.010.

Selected Conferences:

- Oral: D. Delgado, L. Rodríguez Ruiz, M.D. Soriano, J.M. López Nieto; *Estudio de las propiedades ácidas y redox de bronces hexagonales WNbVO utilizando la transformación selectiva de metanol*, Congreso de la Sociedad Española de Catálisis, Barcelona, 13th-15th July, 2015.

- Poster: D. Delgado, L. Ruiz Rodríguez, M. D. Soriano, A. Chieregato, J. M. López Nieto, *Catalizadores basados en óxidos de wolframio para la transformación selectiva de alcoholes*, II Encuentro de Jóvenes Investigadores de la Sociedad Española de Catálisis, Ciudad Real, 27th-29th June, 2016.

- Oral: D. Delgado, Alberto Fernández-Arroyo, Marcelo E. Domine, E. García-González, J. M. López Nieto; *Nanosized W-Nb-O oxides as effective catalysts for the valorization of light oxygenates in lignocellulosic biomass-derived effluents*, EUROPACAT 2017, EFCATS grant, Florence, 27th-3st August, 2017.

- Oral: D. Delgado, B. Solsona, A. Ykreylef, A. Rodríguez-Gómez, A Caballero, E. Rodríguez-Aguado, E. Rodríguez-Castellón, J. M. López Nieto, *Studies on the redox properties of promoted NiO catalysts for the* *oxidative dehydrogenation (ODH) of ethane,* 8th World Congress on Oxidation Catalysis, Krakow, 3rd-8th September, 2017.

- Oral: D. Delgado, N. La Salvia, L. Ruiz-Rodríguez, A. Massó, P. Concepción, J. M. López Nieto, *KIT-6 supported tungsten oxide bronzes for one-pot glycerol oxidehydration,* 8th World Congress on Oxidation Catalysis, Krakow, 3rd-8th September, 2017.

- Poster: D. Delgado, B. Solsona, A. Ykreylef, A. Rodríguez-Gómez, A Caballero, E. Rodríguez-Aguado, E. Rodríguez-Castellón, J. M. López Nieto, *In situ XAS studies of the redox and catalytic properties of NiO catalysts for the ODH of ethane,* 6th International Congress on Operando Spectroscopy (Operando VI), Estepona (Málaga), 15th-19th April, 2018.

- Oral: D. Delgado, R. Sanchís, J. A. Cecilia, E. Rodríguez-Castellón, A. Caballero, B. Solsona, J. M. López Nieto, *On route to understanding promoter and support effects in NiO-based catalysts for the oxidative dehydrogenation of ethane,* III Encuentro de Jóvenes Investigadores de la Sociedad Española de Catálisis, Valencia, 25th-27th June, 2018.

- Oral: Daniel Delgado, Benjamín Solsona, Rut Sanchís, Patricia Concepción, José M. López Nieto, *Understanding NiO-MeOx interactions in promoted and supported NiO-based catalysts for the ODH of ethane*, The 8th Tokio Conference on Advanced Catalytic Science and Technology (TOCAT8), Yokohama, 5th-10th August, 2018.

- Oral: Daniel Delgado, Segundo Zamora, María Dolores Soriano, Benjamín Solsona, José Manuel López Nieto, *Óxidos W-Ti-O con estructura h-WO_3: Síntesis, caracterización y propiedades catalíticas en la deshidratación de alcoholes,* XXVI Congresso Ibero-americano de Catálise (CICAT 2018), Coimbra, 9th-14th September, 2018.